รายงานวิจัยฉบับสมบูรณ์

โครงการ การใช้กราฟีนเป็นตัวรองรับตัวเร่งปฏิกิริยาคอปเปอร์-ซิงค์ออกไซด์สำหรับการสังเคราะห์เอทานอลจากปฏิกิริยาการเติมไฮโดรเจนของก๊าซคาร์บอนไดออกไซด์: อิทธิพลของการเติมโคบอลต์และเหล็ก

โดย ผศ.ดร.ธงไทย วิฑูรย์ และคณะ

15 มิถุนายน 2559

สัญญาเลขที่ TRG5780258

รายงานวิจัยฉบับสมบูรณ์

โครงการ การใช้กราฟีนเป็นตัวรองรับตัวเร่งปฏิกิริยาคอปเปอร์-ซิงค์ออกไซด์สำหรับการสังเคราะห์เอทานอลจากปฏิกิริยาการเติมไฮโดรเจนของก๊าซคาร์บอนไดออกไซด์: อิทธิพลของการเติมโคบอลต์และเหล็ก

ผศ.ดร.ธงไทย วิฑูรย์ มหาวิทยาลัยเกษตรศาสตร์
รศ.ดร.เมตตา เจริญพานิช มหาวิทยาลัยเกษตรศาสตร์

สนับสนุนโดยสำนักงานกองทุนสนับสนุนการวิจัยและ
มหาวิทยาลัยเกษตรศาสตร์

บทคัดย่อ

รหัสโครงการ : TRG5780258

ชื่อโครงการ : การใช้กราฟีนเป็นตัวรองรับตัวเร่งปฏิกิริยาคอปเปอร์-ซิงค์ออกไซด์สำหรับการสังเคราะห์เอทานอลจากปฏิกิริยาการเติมไฮโดรเจนของก๊าซคาร์บอนไดออกไซด์: อิทธิพลของการเติมโคบอลต์และเหล็ก

ชื่อนักวิจัย : ผศ. ดร.ธงไทย วิฑูรย์

E-mail Address : fengttwi@ku.ac.th

ระยะเวลาโครงการ : 2 ปี ตั้งแต่ 15 กรกฎาคม 2557 ถึง 14 กรกฎาคม 2559

จากความวิตกกังวลเกี่ยวกับปัญหาภาวะโลกร้อนซึ่งมีสาเหตุมาจากการเพิ่มปริมาณของก๊าซคาร์บอนไดออกไซด์ในชั้นบรรยากาศ และการลดลงของแหล่งเชื้อเพลิงฟอสซิล ทำให้มีการสร้างหลากหลายยุทธศาสตร์สำหรับการพัฒนาพลังงานทดแทน การนำก๊าซคาร์บอนไดออกไซด์กลับมาใช้ใหม่เพื่อผลิตเชื้อเพลิงทดแทน เช่น เมทานอลและเอทานอลเป็นแนวทางหนึ่งที่เป็นไปได้ในการแก้ไขปัญหาทั้งสองอย่างนี้ไปพร้อมๆกัน งานวิจัยนี้ศึกษาการใช้กราฟีนออกไซด์เป็นตัวรองรับตัวเร่งปฏิกิริยาคอปเปอร์ออกไซด์-ซิงค์ออกไซด์-เซอร์โคเนีย อิทธิพลของปริมาณกราฟีนออกไซด์ต่อคุณลักษณะทางกายภาพและทางเคมีรวมทั้งประสิทธิภาพในการเร่งปฏิกิริยาไฮโดรจิเนชันของก๊าซคาร์บอนไดออกไซด์เพื่อผลิตเมทานอลถูกตรวจสอบ โดยตัวเร่งปฏิกิริยาที่เตรียมได้ถูกนำมาวิเคราะห์ด้วยเทคนิค การสลายตัวทางความร้อน การรีดิวซ์ตัวเร่งปฏิกิริยาด้วยก๊าซไฮโดรเจน การถ่ายภาพด้วยกล้องจุลทรรศน์อิเล็กตรอนแบบส่องกราด การถ่ายภาพด้วยกล้องจุลทรรศน์อิเล็กตรอนแบบส่องผ่าน และการดูดกลืนรังสีเอ็กซ์ที่ใกล้ขอบ ผลการศึกษาพบว่าการเติมกราฟีนลงไปตั้งแต่ 0.5–5 เปอร์เซ็นต์โดยน้ำหนักช่วยเพิ่มการกระจายตัวของโลหะออกไซด์และช่วยทำให้คอปเปอร์ออกไซด์ถูกรีดิวซ์ได้ง่ายขึ้น อย่างไรก็ตามปริมาณกราฟีนที่มากกว่า 5 เปอร์เซ็นต์โดยน้ำหนัก นำไปสู่การรวมตัวกันเป็นกลุ่มก้อนของกราฟีนทำให้อนุภาคของตัวเร่งปฏิกิริยากระจายตัวไม่สม่ำเสมอ ตัวเร่งปฏิกิริยาคอปเปอร์ออกไซด์-ซิงค์ออกไซด์-เซอร์โคเนียที่ใช้กราฟีนปริมาณ 1 เปอร์เซ็นต์โดยน้ำหนักให้ผลได้ของเมทานอลสูงสุดที่ 274.63 กรัม ต่อกิโลกรัมตัวเร่งปฏิกิริยาต่อชั่วโมง ที่อุณหภูมิในการทำปฏิกิริยา 240 องศาเซลเซียส และความดัน 20 บาร์ เนื่องจากประสิทธิภาพที่ดีที่สุดของตัวเร่งปฏิกิริยาคอปเปอร์ออกไซด์-ซิงค์ออกไซด์-เซอร์โคเนียที่ใช้กราฟีนปริมาณ 1 เปอร์เซ็นต์โดยน้ำหนัก ตัวเร่งปฏิกิริยานี้จึงถูกนำมาปรับปรุงด้วยโลหะโคบอลต์และเหล็กด้วยวิธีการจุ่มชุม เพื่อใช้เป็นตัวเร่งปฏิกิริยาสำหรับผลิตเอทานอลจากปฏิกิริยาไฮโดรจิเนชันของก๊าซคาร์บอนไดออกไซด์ พบว่าการเติมโคบอลต์และเหล็กเพิ่มค่าการแปลงผันของก๊าซคาร์บอนไดออกไซด์ซึ่งเป็นไปได้เนื่องจากการเกิดผลิตภัณฑ์เป็นสารประกอบไฮโดรคาร์บอนมากขึ้นจากกระบวนการไฮโดรจิเนชันของก๊าซคาร์บอนมอนอกไซด์ และตัวเร่งปฏิกิริยาที่ปรับปรุงด้วยโลหะโคบอลต์ 2.5 เปอร์เซ็นต์โดยน้ำหนักให้ค่าการเลือกเกิดเอทานอลสูงที่สุด

คำสำคัญ: ตัวเร่งปฏิกิริยาวิวิธพันธ์; ก๊าซคาร์บอนไดออกไซด์; เมทานอล; เอทานอล; กราฟีนออกไซด์; คอปเปอร์ออกไซด์-ซิงค์ออกไซด์-เซอร์โคเนีย

Abstract

Project Code : TRG5780258

Project Title : Graphene as Cu/ZnO catalyst support for ethanol synthesis from CO_2 hydrogenation: Effect of cobalt and iron addition

Investigator : Asst.Prof.Dr. Thongthai Witoon

E-mail Address : fengttwi@ku.ac.th

Project Period : 2 years from 15 July 2014 to 14 July 2016

Increasing concerns over global warming caused by an increase of atmospheric carbon doxide (CO_2) concentration and depletion of fossil fuel resources have created a large variety of strategic routes for development of renewable. Recycling of CO_2 into alternative fuels such as methanol and ethanol offers a feasible option to tackle both CO_2 emission and demand of energy simultaneously. In this study, we report on the use of graphene oxide as a support for $CuO/ZnO/ZrO_2$ system. The effect of graphene oxide contents on the physicochemical properties of GO-CuZnZr catalysts as well as their catalytic CO_2 hydrogenation to methanol was investigated. The obtained catalysts were characterized by means of thermal gravimetric analysis, H_2-temperature programmed reduction, scanning electron microscope (SEM), transmission electron microscope (TEM) and X-ray absorption near edge spectroscopy (XANES). Graphene oxide contents up to 5 wt% were found to promote the dispersion of metal oxides and enhance the reducibility of copper oxide speices. Higher graphene oxide content (10–20 wt%) led to segregation and inhomogeneous microstructure of the resulting catalyst. The 1GO-CuZnZr catalyst (1 wt% graphene oxide) achieved the highest yield of methanol of 274.63 g kg_{cat}^{-1} h^{-1} at reaction temperature and pressure of 240 ^{o}C and 20 bars. Since the 1GO-CuZnZr catalyst showed the best catalytic performance, this catalyst was selected to impregnate with Co and Fe for the ethanol production from CO_2 hydrogenation. The addition of Co and/or Fe was found to increase the CO_2 conversion which was possibly due to the formation of hydrocarbon from CO hydrogenation reaction. The 1GO-CuZnZr prepared with 2.5 wt% Co was found to be the most selective catalyst for ethanol synthesis from CO_2 hydrogenation.

Keywords: Heterogeneous catalysts; Carbon dioxide; Methanol; Ethanol; Graphene oxide; $CuO-ZnO-ZrO_2$

การใช้กราฟีนเป็นตัวรองรับตัวเร่งปฏิกิริยาคอปเปอร์-ซิงค์ออกไซด์สำหรับการสังเคราะห์เอทานอลจากปฏิกิริยาการเติมไฮโดรเจนของก๊าซคาร์บอนไดออกไซด์: อิทธิพลของการเติมโคบอลต์และเหล็ก

---

1. วัตถุประสงค์การทดลอง

1) เพื่อศึกษาผลของปริมาณกราฟีนออกไซด์ที่ใช้เป็นตัวรองรับตัวเร่งปฏิกิริยาคอปเปอร์ออกไซด์-ซิงค์ออกไซด์-เซอร์โคเนียต่อคุณสมบัติทางกายภาพและทางเคมีของตัวเร่งปฏิกิริยารวมทั้งประสิทธิภาพในปฏิกิริยาการเติมไฮโดรเจนของก๊าซคาร์บอนไดออกไซด์เพื่อผลิตเมทานอล
2) เพื่อศึกษาผลของการเติมโคบอลต์และเหล็กลงตัวเร่งปฏิกิริยาคอปเปอร์ออกไซด์-ซิงค์ออกไซด์-เซอร์โคเนีย-กราฟีน ต่อคุณสมบัติทางกายภาพและทางเคมีของตัวเร่งปฏิกิริยารวมทั้งประสิทธิภาพในปฏิกิริยาการเติมไฮโดรเจนของก๊าซคาร์บอนไดออกไซด์เพื่อผลิตเอทานอล

2. วิธีการทดลอง

2.1 การเตรียมกราฟีนออกไซด์ด้วยการดัดแปลงวิธีของ Hammer

ในการเตรียมกราฟีนออกไซด์ มีสารเคมีที่ใช้ได้แก่ โซเดียมไนเตรต ($NaNO_3$), กรดซัลฟูริก (H_2SO_4), โพแทสเซียมเปอร์แมงกาเนส ($KMnO_4$), ไฮโดรเจนเปอร์ออกไซด์ (H_2O_2), เอทานอล (C_2H_5OH), กรดไนตริก (HNO_3)

กราฟีนออกไซด์จะถูกเตรียมด้วยการดัดแปลงวิธีของ Hammer ในขั้นตอนแรก นำแกรไฟต์กระจายตัวในสารละลายที่ประกอบไปด้วย โซเดียมไนเตรตและกรดซัลฟูริกในสภาวะการกวนที่อุณหภูมิต่ำกว่า 5 องศาเซลเซียส เป็นเวลา 30 นาที จากนั้นเติม โพแทสเซียมเปอร์แมงกาเนสปล่อยทิ้งไว้เป็นเวลา 1 ชั่วโมง หลังจากนั้นเพิ่มอุณหภูมิของสารละลายไปที่ 35 องศาเซลเซียสเป็นเวลา 2 ชั่วโมง แล้วเติมน้ำปราศจากไอออนจำนวน 230 มิลลิลิตร จากนั้นเพิ่มอุณหภูมิไปที่ 98 องศาเซลเซียส เป็นเวลา 15 นาที แล้วเจือจางสารละลายด้วยน้ำปราศจากไอออนปริมาตร 700 มิลลิลิตร แล้วเติม 30 % ไฮโดรเจนเปอร์ออกไซด์ หลังจากนั้นกรองและล้างด้วยน้ำ ปราศจากไอออน หลังจากนั้นทำการอบแห้งภายใต้สภาวะสุญญากาศที่อุณหภูมิ 40 องศาเซลเซียสเป็นเวลา 12 ชั่วโมง

2.2 การเตรียมตัวเร่งปฏิกิริยากราฟีนออกไซด์-คอปเปอร์ออกไซด์-ซิงค์ออกไซด์-เซอร์โคเนียมออกไซด์ ($GO-CuO-ZnO-ZrO_2$)

2.2.1 ชั่งโซเดียมไฮโดรเจนคาร์บอเนตปริมาณ 4.2005 กรัม นำมาละลายด้วยน้ำมาละลายด้วยน้ำกลั่น ปริมาตร 500 มิลลิลิตรในบีกเกอร์ จากนั้นบีกเกอร์ไปใส่ในเครื่องอัลตราโซนิก โดยเติมกราฟีนออกไซด์ลงในสารละลายในปริมาณที่ต้องการ (ร้อยละโดยน้ำหนักของก ราฟีน

ออกไซด์ เท่ากับ 0,0.5,1,2.5,5,10และ20) หลังจากนั้นเปิดเครื่องอัลตราโซนิกเพื่อทำให้แผ่นกราฟีนกระจายตัว

2.2.2 ชั่งคอปเปอร์ไนเตรตไตรไฮเดรต ซิงค์ไนเตรตเฮกซะไฮเดรตและเซอร์โคเนียมออกซิคลอไรด์ออกตะไฮเดรต ในปริมาณที่ต้องการ โดยให้มีอัตราส่วนโดยโมลของ Zn: Cu เท่ากับ 0.75 นำมาละลายด้วยน้ำกลั่นปริมาต 100 มิลลิลิตรในบีกเกอร์ จากนั้นคนจนเป็นเนื้อเดียวกันและนำสารที่ได้เติมลงในสารละลายข้อ 2.2.1 กวนสารละลายผสมด้วยความเร็วรอบ 350 รอบต่อนาที ที่อุณหภูมิห้อง เป็นเวลา 5 นาที

2.2.3 เติมสารละลายโซเดียมไฮโดรเจนคาร์บอเนต ความเข้มข้น 0.1 โมลต่อลิตรลงในสารละลายข้อ 2.2.2 เพื่อปรับความเป็นกรดเบสให้อยู่ในช่วง 7.0-7.5 และทำการปิดผนึกที่บริเวณปากบีกเกอร์ด้วยฟิล์มบางใส หลังจากนั้นทำการกวนสารละลายทิ้งไว้ด้วยความเร็ว 350 รอบต่อนาที ที่อุณหภูมิห้องเป็นเวลา 2 ชั่วโมง

2.2.4 นำสารละลายที่ได้จากข้อ 2.2.3 มาล้างด้วยน้ำกลั่นและเอทานอลปริมาตร 2000 และ 50 มิลลิลิตร ตามลำดับ ผลิตภัณฑ์ที่ได้จะมีลักษณะเป็นตะกอน

2.2.5 นำตะกอนที่ได้ไปอบที่อุณหภูมิ 100 องศาเซลเซียส เป็นเวลา 12 ชั่วโมง

2.2.6 นำสารที่ได้จากข้อ 1.5 มาบดด้วยโกร่งให้ละเอียด และเก็บไว้ในตู้ดูดความชื้น

2.3 การเตรียมตัวเร่งปฏิกิริยาโคบอลต์-เหล็ก-กราฟีนออกไซด์-คอปเปอร์ออกไซด์-ซิงค์ออกไซด์-เซอร์โคเนียมออกไซด์ (Co-Fe/GO-CuO-ZnO-ZrO_2)

การโหลดโลหะโคบอลต์และหรือเหล็กลงบนตัวเร่งปฏิกิริยากราฟีนออกไซด์-คอปเปอร์ออกไซด์-ซิงค์ออกไซด์-เซอร์โคเนียมออกไซด์ จะเตรียมด้วยวิธีจุ่มชุม โดยมีขั้นตอนดังต่อไปนี้

2.3.1 ชั่งโคบอลต์ไนเตรตและเหล็กในเตรตให้ได้ปริมาณตามต้องการ นำไปละลายในน้ำปราศจากไอออนปริมาตร 2 มิลลิลิตร

2.3.2 ชั่ง GO-CuO-ZnO-ZrO_2 จำนวน 1 กรัม แล้วเทลงในสารละลายข้อ 2.3.1 กวนทิ้งไว้ที่อุณหภูมิ 60 องศาเซลเซียส เป็นเวลา 2 ชั่วโมง

2.3.3 อบแห้งสารในข้อ 2.3.2 ที่อุณหภูมิ 100 องศาเซลเซียส เป็นเวลา 12 ชั่วโมง

2.3.4 นำสารที่ได้จากข้อ 2.3.3 มาบดด้วยโกร่งให้ละเอียด และเก็บไว้ในตู้ดูดความชื้น

2.4 การทดสอบประสิทธิภาพในการเร่งปฏิกิริยาการเติมไฮโดรเจนของก๊าซคาร์บอนไดออกไซด์เพื่อผลิตเมทานอล

นำตัวเร่งปฏิกิริยาที่เตรียมได้มาบรรจุในเครื่องปฏิกรณ์แบบเบดนิ่ง จากนั้นรีดิวซ์ตัวเร่งปฏิกิริยาด้วยก๊าซไฮโดรเจนที่อุณหภูมิ 350 องศาเซลเซียส ความดัน 1 บรรยากาศ เป็นเวลา 4 ชั่วโมง จากนั้นลดอุณหภูมิของปฏิกรณ์มาที่ 180 องศาเซลเซียส เมื่อได้อุณหภูมิตามต้องการแล้วเปลี่ยนก๊าซที่ไหลในระบบเป็นก๊าซไฮโดรเจนและก๊าซคาร์บอนไดออกไซด์ที่อัตราส่วน 3ต่อ1 ปล่อยให้ไหลผ่านตัวเร่งปฏิกิริยาทิ้งไว้ 15 นาที แล้วทำการอัดความดันให้ได้ที่ 20 บาร์ พร้อมกับเพิ่ม

อุณหภูมิไปที่ 200 องศาเซลเซียส โดยมีอุณหภูมิที่ใช้ในการศึกษาอีก 4 ค่าได้แก่ 220, 240, 260 และ 280 องศาเซลเซียส ตามลำดับ ก๊าซขาออกที่ได้จะถูกวิเคราะห์ด้วยเทคนิคแก๊สโครมาโทกราฟี

2.5 การวิเคราะห์คุณลักษณะของกราฟีนออกไซด์และตัวเร่งปฏิกิริยา

กราฟีนออกไซด์จะถูกวิเคราะห์ด้วยเทคนิคการถ่ายภาพด้วยกล้องจุลทรรศน์อิเล็กตรอนแบบส่องผ่าน (Transmission electron microscope) เทคนิครามานสเปคโตรสโคปี (Raman spectroscopy) กล้องจุลทรรศน์แรงอะตอม (Atomic-force microscopy) เทคนิคการเลี้ยวเบนของรังสีเอ็กซ์ (X-ray diffraction) และเทคนิคฟูเรียร์ทรานส์ฟอร์มอินฟราเรดสเปคโตรสโคปี (Fourier transform infrared spectroscopy)

ตัวเร่งปฏิกิริยาที่เตรียมได้จะถูกวิเคราะห์ด้วยการสลายตัวทางความร้อนของตัวเร่งปฏิกิริยาด้วยเทคนิคการเปลี่ยนแปลงทางความร้อนด้วยก๊าซชนิดต่างๆ (Thermal gravimetric analysis) วิเคราะห์ความสามารถในการรีดิวซ์และอันตรกิริยาของตัวเร่งปฏิกิริยาด้วยก๊าซไฮโดรเจน (H_2-temperature program reduction) วิเคราะห์องค์ประกอบทางเคมีของตัวเร่งปฏิกิริยาด้วยเทคนิคสเปคโตรสโคปีของอนุภาคอิเล็กตรอนที่ถูกปลดปล่อยด้วยรังสีเอกซ์ (X-ray photoelectron spectroscopy) วิเคราะห์เฟสและขนาดผลึกด้วยเทคนิคการเลี้ยวเบนของรังสีเอ็กซ์ (X-ray diffraction) วิเคราะห์โครงสร้างของตัวเร่งปฏิกิริยาด้วยเทคนิคการถ่ายภาพด้วยกล้องจุลทรรศน์อิเล็กตรอนแบบส่องกราด (Scanning electron microscope) และเทคนิคการถ่ายภาพด้วยกล้องจุลทรรศน์อิเล็กตรอนแบบส่องผ่าน (Transmission electron microscope) วิเคราะห์พื้นที่ผิวและการกระจายตัวของรพรุนด้วยเทคนิคการดูดซับด้วยก๊าซไนโตรเจน (N_2-sorption) วิเคราะห์ความสามารถในการดูดซับของตัวเร่งปฏิกิริยาด้วยก๊าซคาร์บอนไดออกไซด์และก๊าซไฮโดรเจน (CO_2-temperature program desorption, H_2-temperature program desorption)และวิเคราะห์ด้วยเทคนิคการดูดกลืนรังสีเอกซ์โดยใช้การดูดกลืนรังสีเอกซ์ในย่านใกล้ขอบ (X-ray absorption near edge structure, XANES) เพื่อศึกษาโครงสร้างทางของคอปเปอร์

3. ผลการทดลองและการอภิปรายผลการทดลอง

3.1 การวิเคราะห์คุณลักษณะของกราฟีนออกไซด์ที่สังเคราะห์ได้

ภาพที่ 3.1a แสดงภาพถ่ายด้วยกล้องจุลทรรศน์อิเล็กตรอนแบบส่องผ่านของกราฟีนออกไซด์ พบว่ากราฟีนออกไซด์ที่สังเคราะห์มีรอยย่นเนื่องจากการพับของแผ่นกราฟีนบ่งบอกว่ากราฟีนที่สังเคราะห์ได้บางและมีความยืดยุ่น ภาพที่ 3.1b แสดงรามานสเปกตรัมของกราฟีนออกไซด์ซึ่งพบพีคที่ตำแหน่ง 1590 cm-1 และ 1355 cm-1 แสดงถึงกราฟิติกคาร์บอน และบริเวณที่มี defect บนผิวคาร์บอน โดยความหนาของกราฟีนถูกวัดด้วยเทคนิค AFM (ภาพที่ 3.1c) พบว่ามีความหนาประมาณ 0.7 ถึง 1 นาโนเมตร บ่งบอกถึงกราฟีนออกไซด์ที่สังเคราะห์ได้มีแผ่นเดียว (ภาพที่ 3.1d) รูปแบบการเลี้ยวรังสีเอ็กซ์แสดงระนาบ 0 0 1 ที่ 2 theta เท่ากับ 10.9 $^{\circ}$ ซึ่งสัมพันธ์กับระยะห่างระหว่างระนาบเท่ากับ 0.81 นาโนเมตร (ภาพที่ 3.1e) และภาพที่ 3.1f แสดงการมีอยู่ของหมู่

ฟังก์ชันที่มีออกซิเจนเป็นองค์ประกอบ ซึ่งผลที่ได้ทั้งหมดยืนยันว่าสามารถสังเคราะห์แผ่นกราฟีนออกไซด์ระดับนาโนเมตรได้

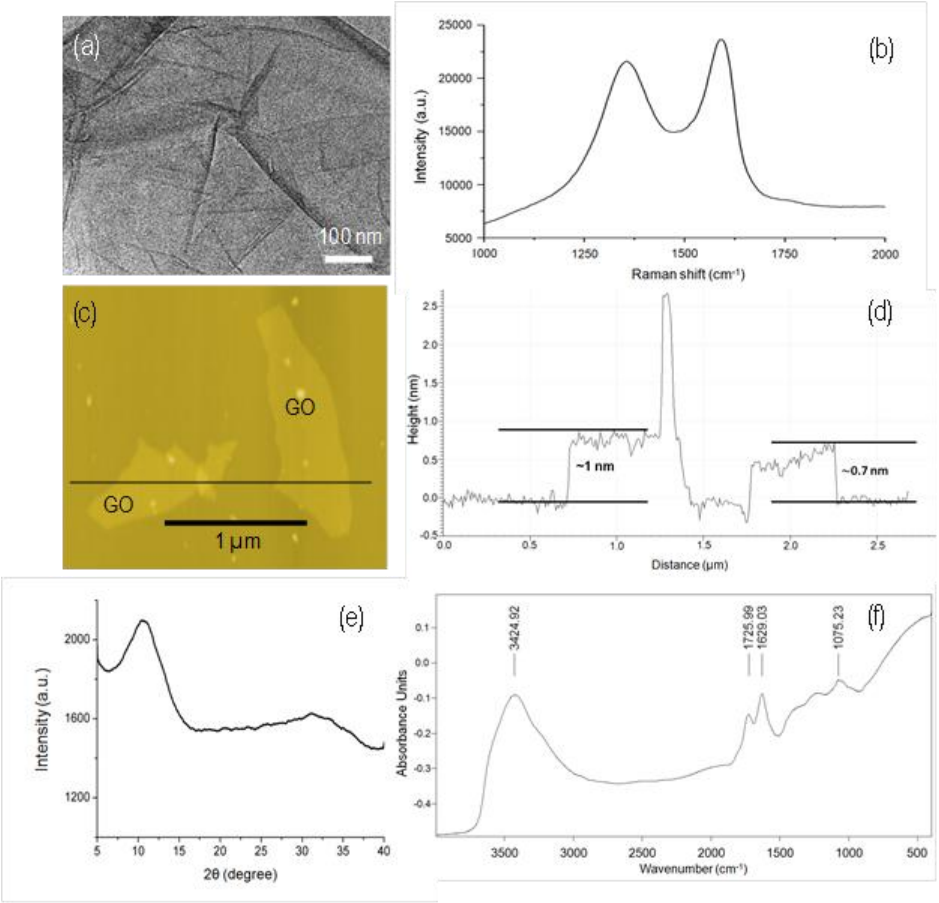

ภาพที่ 3.1 ภาพถ่ายด้วยกล้องจุลทรรศน์อิเล็กตรอนแบบส่องผ่านของกราฟีนออกไซด์ (a), รามานสเปกตรัมของกราฟีนออกไซด์ (b), ภาพถ่ายด้วยกล้องแรงอะตอมของกราฟีนออกไซด์ (c และ d), รูปแบบการเลี้ยวเบนของรังสีเอ็กซ์ของกราฟีนออกไซด์ (e) และฟูเรียร์ทรานส์ฟอร์มสเปกตรัมของกราฟีนออกไซด์ (f)

3.2 การวิเคราะห์คุณลักษณะของตัวเร่งปฏิกิริยา GO-CuO-ZnO-ZrO_2 ที่สังเคราะห์ได้

3.2.1 การวิเคราะห์การสลายตัวทางความร้อนของกราฟีนออกไซด์

เนื่องจากกราฟีนออกไซด์เป็นวัสดุที่ประกอบไปด้วยคาร์บอนและหมู่ออกซิเจนจำนวนมากบนพื้นผิว จึงสามารถเกิดการสลายตัวได้เมื่อสัมผัสกับก๊าซออกซิเจนซึ่งเป็นส่วนประกอบในอากาศ ดังนั้นจึงจำเป็นต้องศึกษาถึงการสลายตัวทางความร้อนภายใต้แก๊สชนิดต่าง ๆ ก่อนว่า กราฟีนที่สังเคราะห์ได้จะยังมีอยู่ภายหลังกระบวนการแคลไซน์

ภาพที่ 3.2 แสดงการเปลี่ยนแปลงน้ำหนักเมื่อได้รับความร้อนของกราฟีนออกไซด์ ภายใต้ก๊าซไฮโดรเจน ก๊าซไนโตรเจน และอากาศ พบว่าการเปลี่ยนแปลงน้ำหนัก 2 ช่วง ช่วงแรกที่อุณหภูมิตั้งแต่ 30 ถึง 150 องศาเซลเซียสซึ่งคิดเป็นเปอร์เซ็นต์การสูญเสียน้ำหนักเท่ากับ 11.23 เปอร์เซ็นต์ เกิดจากการระเหยของน้ำบริเวณผิวนอกและภายในโครงสร้าง และช่วงที่สอง อุณหภูมิ

150 ถึง 400 องศาเซลเซียสซึ่งคิดเป็นเปอร์เซ็นต์การสูญเสียน้ำหนักเท่ากับ77.87 เปอร์เซ็นต์ และเมื่อพิจารณาจากอนุพันธ์ของเปอร์เซ็นต์การเปลี่ยนแปลงทางความร้อน จะพบพีคปรากฏที่อุณหภูมิประมาณ 200 องศาเซลเซียส ซึ่งเกิดมาจากการที่หมู่ฟังก์ชันบนพื้นผิวของกราฟีนออกไซด์สลายตัวออกไปเพื่อเปลี่ยนกราฟีนออกไซด์เป็นกราฟีนรวมกับการสลายตัวของคาร์บอนที่ไม่สเถียรทำปฏิกิริยากับออกซิเจนในอากาศเกิดเป็นแก๊สคาร์บอนมอนออกไซด์และคาร์บอนไดออกไซด์ ส่วนผลของการเปลี่ยนแปลงน้ำหนักตามความร้อนของกรา ฟีนออกไซด์โดยใช้แก๊สไฮโดรเจนและไนโตรเจน พบการเปลี่ยนแปลงที่ใกล้เคียงกัน คือ พบการเปลี่ยนแปลง ทั้งหมด 2ช่วง โดยช่วงแรกมีอุณหภูมิตั้งแต่ 30 ถึง 150 องศาเซลเซียสซึ่งคิดเป็นเปอร์เซ็นต์การสูญเสียน้ำหนักประมาณ 13 เปอร์เซ็นต์ ซึ่งเกิดจากการระเหยของน้ำบริเวณผิวนอกและภายในโครงสร้าง และช่วงที่สองอุณหภูมิ 150 ถึง 400 องศาเซลเซียสซึ่งคิดเป็นเปอร์เซ็นต์การสูญเสียน้ำหนักประมาณ 40 เปอร์เซ็นต์ และเมื่อพิจารณาจากอนุพันธ์ของเปอร์เซ็นต์การเปลี่ยนแปลงทางความร้อน จะพบพีคปรากฏที่อุณหภูมิประมาณ 225 องศาเซลเซียส ซึ่งเกิดมาจากการที่หมู่ฟังก์ชันบนพื้นผิวของกราฟีนออกไซด์สลายตัวออกไปเพื่อเปลี่ยนกราฟีนออกไซด์เป็นกราฟีน จากผลการวิเคราะห์การเปลี่ยนแปลงน้ำหนักตามความร้อน ของกราฟีนออกไซด์ พบว่าการใช้อากาศในการรีดิวซ์กราฟีนออกไซด์ให้เป็นกราฟีนนั้นไม่เหมาะสมเนื่องจากมีหมู่ฟังก์ชันที่หลุดออกไปและ มีคาร์บอนที่ไม่สเถียรภาพหลุดออกไปจำนวนมากด้วย ดังนั้นก๊าซที่เหมาะสมสำหรับการรีดิวซ์กราฟีนเป็นกราฟีนออกไซด์ คือก๊าซไฮโดรเจนกับก๊าซไนโตรเจน เนื่องจากทำให้หมู่ฟังก์ชันบนผิวกราฟีนออกไซด์หลุดออกไปเพียงอย่างเดียว ดังนั้นงานวิจัยนี้จึงเลือกใช้ก๊าซไฮโดรเจนในการรีดิวซ์กราฟีนออกไซด์ให้เป็นกราฟีน และรีดิวซ์คอปเปอร์ออกไซด์ให้เป็นคอปเปอร์ ซึ่งเป็นองค์ประกอบหลักในตัวเร่งปฏิกิริยาในปฏิกิริยาการสังเคราะห์เมทานอลจากก๊าซคาร์บอนไดออกไซด์ภายในขั้นตอนเดียว

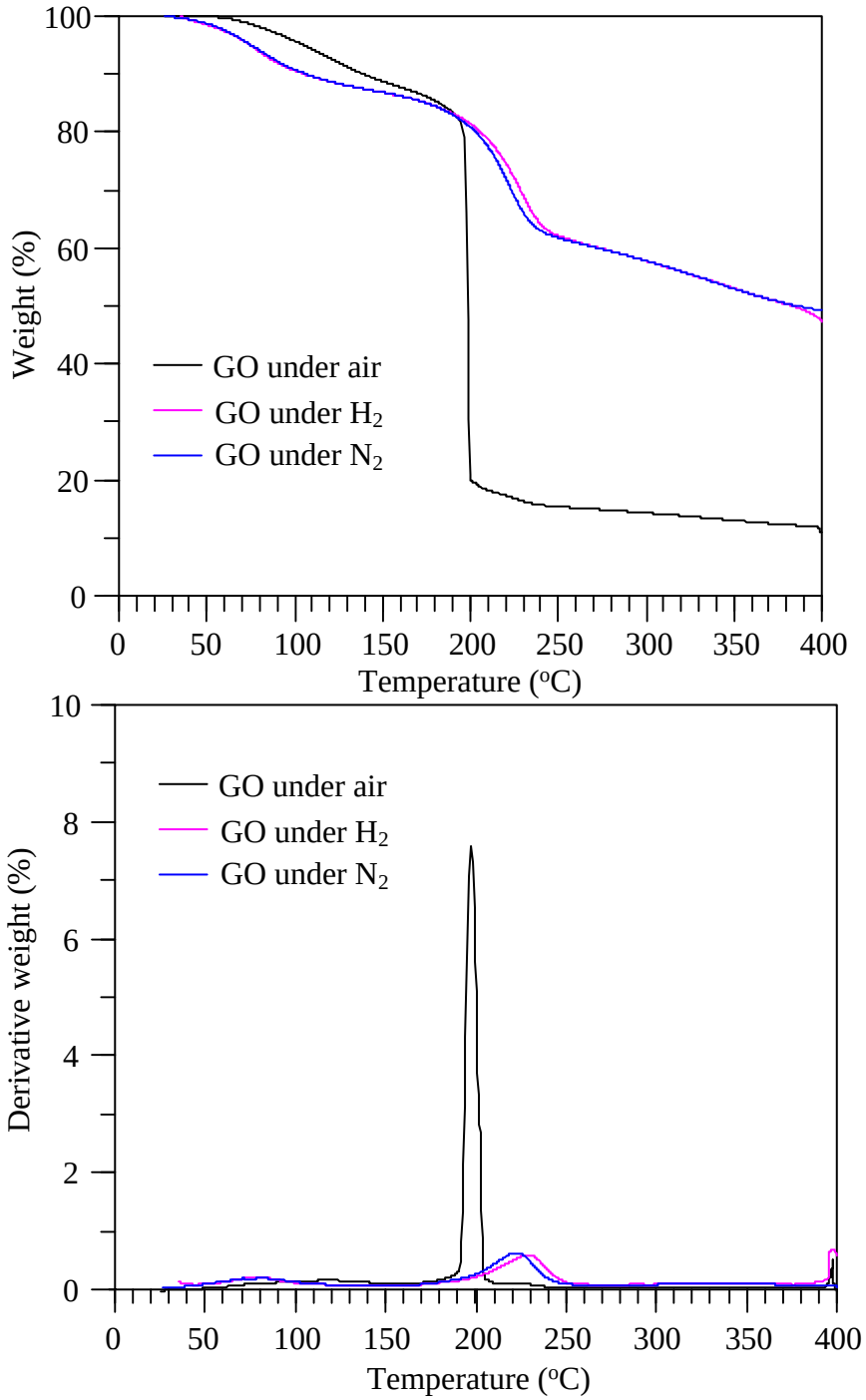

ภาพที่ 3.2 แสดงการเปลี่ยนแปลงน้ำหนักทางความร้อนของกราฟีนออกไซด์ภายใต้ก๊าซที่แตกต่างกัน

ภาพที่ 3.3 แสดงความสามารถในการรีดิวซ์ของตัวเร่งปฏิกิริยา GO-CuO-ZnO-ZrO_2 ที่ผ่านการแคลไซน์ด้วยก๊าซไนโตรเจนก่อนการรีดิวซ์เทียบกับตัวเร่งปฏิกิริยาที่ GO-CuO-ZnO-ZrO_2 ไม่ได้ทำการแคลซิเนชัน พบว่าตัวเร่งปฏิกิริยาที่ทำการแคลไซน์ก่อนที่จะทดสอบความสามารถในการรีดิวซ์ ปรากฏพีคที่ตำแหน่ง อุณหภูมิ 200 องศาเซลเซียส ซึ่งเป็นพีคของการเปลี่ยนคอปเปอร์ออกไซด์เป็นคอปเปอร์ ส่วนตัวเร่งปฏิกิริยาที่ไม่ได้ทำการแคลไซน์พบพีคที่อุณหภูมิสูงกว่า ซึ่งเป็น

พีคที่เกิดจากกราฟีนออกไซด์ถูกรีดิวซ์เปลี่ยนเป็นกราฟีนและสารประกอบคอปเปอร์ออกไซด์ถูกรีดิวซ์ปลี่ยนเป็นคอปเปอร์ร่วมกัน ดังนั้นจากผลความสามารถในการรีดิวซ์ของตัวเร่งปฏิกิริยาที่ทำการการรีดิวซ์เพียงขั้นตอนเดียว สามารถรีดิวซ์กราฟีนออกไซด์และคอปเปอร์ได้เช่นเดียวกับตัวเร่งปฏิกิริยาที่ทำทั้งแคลไซน์และรีดิวซ์ร่วมกัน งานวิจัยนี้จึงเลือกไม่ทำการแคลซิเนชันก่อนการรีดิวซ์ในการเตรียมตัวเร่ง สำหรับใช้ในการศึกษาการทำปฏิกิริยาสังเคราะห์เมทานอลจากก๊าซคาร์บอนไดออกไซด์ เนื่องจากลดกระบวนการในการสังเคราะห์สารรวมถึงช่วยลดการใช้พลังงานจากการที่ไม่ต้องทำการแคลไซน์

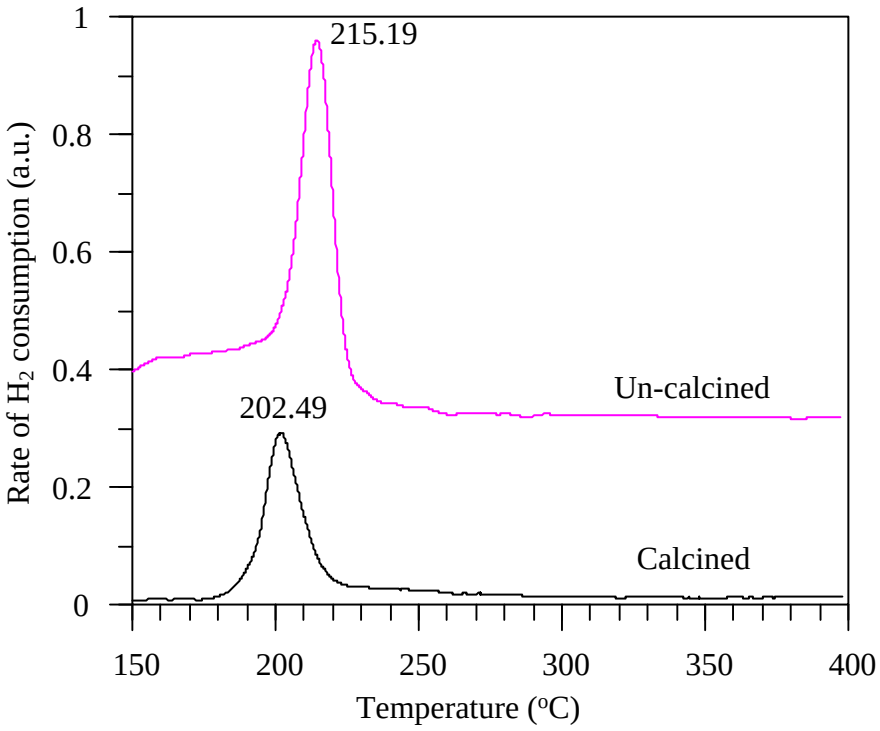

ภาพที่ 3.3 ความสามารถในการรีดิวซ์ของตัวเร่งปฏิกิริยากราฟีนออกไซด์ 5 เปอร์เซ็นต์ใน CuO-ZnO-ZrO_2 ที่ถูกเตรียมด้วยเทคนิคการตกตะกอนร่วม

ภาพที่ 3.4 ผลของการเปลี่ยนแปลงน้ำหนักทางความร้อนของตัวเร่งปฏิกิริยา คอปเปอร์ออกไซด์ซิงค์ออกไซด์เซอร์โคเนียมที่ไม่ได้มีการเติมกราฟีนออกไซด์ภายใต้สภาวะอากาศ พบการเปลี่ยนแปลง ทั้งหมด 3 ช่วง โดยช่วงแรกมีอุณหภูมิตั้งแต่ 30 ถึง 150 องศาเซลเซียส คิดเป็นเปอร์เซ็นต์การสูญเสียน้ำหนักประมาณ 7.79 เปอร์เซ็นต์ ซึ่งเป็นเนื่องจากการสูญเสียน้ำที่ผิวและภายในโครงสร้างของตัวเร่งปฏิกิริยา ช่วงที่สอง อุณหภูมิ 150 ถึง 400 องศาเซลเซียส คิดเป็นเปอร์เซ็นต์การสูญเสียน้ำหนักประมาณ 12.53 เปอร์เซ็นต์ เกิดจากการสลายตัวของสารประกอบคาร์บอเนต สำหรับช่วงที่สาม อุณหภูมิ 400 ถึง 650 องศาเซลเซียส คิดเป็นเปอร์เซ็นต์การสูญเสียน้ำหนักเท่ากับ 6.7 เปอร์เซ็นต์ เกิดจากการสลายตัวเซอร์โคเนียมคาร์บอเนตที่เหลืออยู่ (Dong et al., 2016)

เมื่อเติมกราฟีนออกไซด์ที่ปริมาณต่างๆ พบว่าตัวเร่งปฏิกิริยามีการเปลี่ยนแปลงน้ำหนักทั้งหมด 3 ช่วง โดยช่วงแรกมีอุณหภูมิตั้งแต่ 30 ถึง 150 องศาเซลเซียส เป็นการสูญเสียน้ำหนักเกิดจากการระเหยของน้ำบริเวณผิวนอกและภายในโครงสร้าง ส่วนช่วงที่สอง อุณหภูมิ 150 ถึง 400 องศาเซลเซียส เกิดมาจากการที่หมู่ฟังก์ชันบนพื้นผิวของกราฟีนออกไซด์สลายตัวออกไปเพื่อเปลี่ยนกราฟีนออกไซด์เป็นกราฟีนรวมกับการสลายตัวของคาร์บอนที่ไม่เสถียรทำปฏิกิริยากับออกซิเจนในอากาศเกิดเป็นก๊าซคาร์บอนมอนออกไซด์และคาร์บอนไดออกไซด์ รวมถึงเกิดการสลายตัวของสารประกอบคาร์บอเนต และช่วงสุดท้าย อุณหภูมิ 400 ถึง 650 องศาเซลเซียส เกิดจากกราฟีนออกไซด์เกิดการออกซิเดชันและสลายตัวอย่างสมบูรณ์ รวมกับการสลายตัวเซอร์โคเนียมคาร์บอเนตที่เหลืออยู่ เมื่อพิจารณาจากผลการวิเคราะห์ ที่อุณหภูมิ 1000 องศาเซลเซียส โดยการเผาโดยใช้อากาศนั้นสารประกอบกราฟีนที่อยู่ในตัวเร่งปฏิกิริยาทุกตัวอาจจะสลายตัวออกไปทั้งหมดสอดคล้องกับผลการคำนวณของตารางที่ 3.1 ซึ่งแสดงน้ำหนักของตัวเร่งปฏิกิริยาที่เหลืออยู่หลังจากการเผาที่อุณหภูมิ 1000 องศาเซลเซียส และเมื่อนำน้ำหนักที่เหลืออยู่ของตัวเร่งปฏิกิริยาคอปเปอร์ ซิงค์เซอร์โคเนียม 72.9 เปอร์เซ็นต์ ไปเทียบกับตัวเร่งปฏิกิริยาที่เติมกราฟีนออกไซด์ลงไปนั้นแสดงปริมาณผลต่างในตารางที่ 2 พบว่า ค่าที่ได้คือร้อยละ 0.61, 0.94, 3.52, 4.87, 10.98 และ 25.57 ซึ่งน่าจะเป็นปริมาณกราฟีนออกไซด์ที่อยู่ในตัวเร่งปฏิกิริยาจริงซึ่งมีค่าใกล้เคียงกับปริมาณกราฟีนออกไซด์ที่ใส่ลงไปตอนเตรียมตัวเร่งปฏิกิริยา คือร้อยละ 0.5, 1 ,2.5, 5 ,10 และ 20 ตามลำดับ โดยค่าที่คลาดเคลื่อนไปบ้างเล็กน้อย อาจเกิดจากรูปแบบโครงสร้างและลักษณะการเกาะตัวกันของตัวเร่งปฏิกิริยาในขณะตกตะกอนร่วม

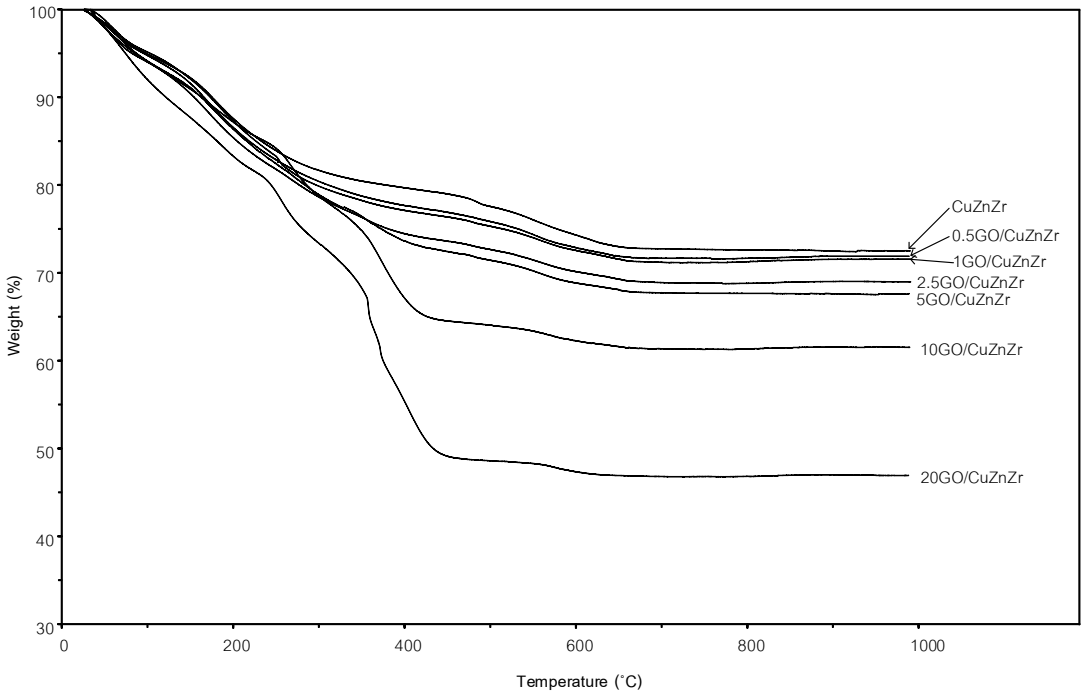

ภาพที่ 3.4 การเปลี่ยนแปลงน้ำหนักทางความร้อนโองตัวเร่งปฏิกิริยาก GO-CuO-ZnO-ZrO_2 ที่ถูกเตรียมด้วยเทคนิคการตกตะกอนร่วมภายใต้อากาศ

ตารางที่ 3.1 น้ำหนักของตัวเร่งปฏิกิริยาปฏิกิริยาก GO-CuO-ZnO-ZrO_2 ภายหลังการวิเคราะห์ด้วยเทคนิคการเปลี่ยนแปลงทางความร้อนโดยใช้อากาศที่ อุณหภูมิ 1000 องศาเซลเซียส

Samples	Weight (%)	Graphen oxide content (%)	Initial amount of GO (wt %)
CuZnZr	72.5	-	0
0.5GO/CuZnZr	71.89	0.61	0.5
1GO/CuZnZr	71.56	0.94	1
2.5GO/CuZnZr	68.98	3.52	2.5
5GO/CuZnZr	67.63	4.87	5
10GO/CuZnZr	61.52	10.98	10
20GO/CuZnZr	46.93	25.57	20

ตารางที่ 3.2 แสดงองค์ประกอบทางเคมีของตัวเร่งปฏิกิริยกราฟีนออกไซด์คอปเปอร์ซิงค์เซอร์โคเนียมที่ถูกเตรียมด้วยเทคนิคตกตะกอนร่วม โดยงานวิจัยนี้กำหนดให้ปริมาณของเซอร์โคเนียมไดออกไซด์มีค่าคงที่เท่ากับ 25 เปอร์เซนต์ โดยน้ำหนัก และอัตราส่วนของซิงค์ต่อคอปเปอร์เท่ากับ 0.75 และทำการศึกษาปริมาณกราฟีนออกไซด์ต่อคอปเปอร์ซิงค์เซอร์โคเนียมออกไซด์ในปริมาณที่แตกต่างกันรวมทั้งสิ้น 7 ตัวอย่าง ผลจากการวิเคราะห์ด้วยเทคนิค XRF พบว่าอัตราส่วนของธาตุคอปเปอร์ ซิงค์ และ เซอร์โคเนียมของตัวเร่งปฏิกิริยาหลังการสังเคราะห์ค่อนข้างมีอัตราส่วนคงที่ สอดคล้องกับการอัตราส่วนในการเตรียมสารตั้งที่กำหนดให้คงที่ และเมื่อมีการเพิ่มปริมาณกราฟฟีนออกไซด์ ค่าองค์ประกอบของธาตุคาร์บอน มีปริมาณเพิ่มขึ้นสอดคล้องกับปริมาณการเตรียมสารตั้งต้น ยกเว้นตัวเร่งปฏิกิริยาที่เติมกราฟีนออกไซด์ ลงไป20เปอร์เซ็นต์ที่ค่าอัตราส่วนมีค่าผิดปกติไป อาจเกิดจากขณะตกตะกอนร่วมเมื่อคาร์บอนมีปริมาณมากทำให้โลหะอื่นๆตกตะกอนลงมาได้ไม่ดี

ตารางที่ 3.2 องค์ประกอบทางเคมีของตัวเร่งปฏิกิริยากราฟีนออกไซด์คอปเปอร์ซิงค์เซอร์โคเนียมที่ถูกเตรียมด้วยเทคนิคการตกตะกอนร่วม

Sample	**Element content (Atom %)**					**Atomic ratio**
	Cu	Zn	Zr	C	O	**Cu : Zn : Zr : C**
CuZnZr	17.55	31.87	15.08	-	35.48	0.55 :1.00:0.47:0.00
0.5GO/CuZnZr	16.82	29.15	16.42	4.57	33.04	0.58:1.00:0.56:0.16
1GO/CuZnZr	15.72	30.60	16.84	5.13	31.70	0.51:1.00:0.55:0.17
2.5GO/CuZnZr	11.11	23.92	14.84	6.82	43.31	0.46:1.00:0.62:0.29
5GO/CuZnZr	16.43	26.61	15.92	8.98	32.07	0.61:1.00:0.59:0.34
10GO/CuZnZr	13.28	23.87	15.39	15.36	32.09	0.56:1.00:0.64:0.64
20GO/CuZnZr	15.67	19.78	10.93	24.89	28.73	0.79:1.00:0.55:1.26

ภาพที่ 3.5 แสดงผลการวิเคราะห์จากเทคนิคการเลี้ยวเบนของรังสีเอกซ์ พบว่าตัวเร่งปฏิกิริยาคอปเปอร์ ซิงค์ออกไซด์ เซอร์โคเนียมไดออกไซด์ มีพีคปรากฏขึ้นที่ตำแหน่ง 2 theta เท่ากับ 35.496, 38.731, 48.727, 66.250 และ 68.091 องศา ตรงกับระนาบผลึกคอปเปอร์ออกไซด์ (11-1),(111),(-202),(-311) และ (-220) ตามลำดับ ส่วนพีคที่ตำแหน่ง 2 theta เท่ากับ 31.772 , 34.420, 36.256, 47.541 และ 56.602 องศา ตรงกับระนาบผลึกของซิงค์ออกไซด์ (100), (002), (101), (102) และ (110) ส่วนพีคที่ตำแหน่ง 2 theta เท่ากับ 30.271, 50.378 และ 60.207 องศา ตรงกับระนาบผลึกของเซอร์โคเนียมไดออกไซด์เฟสเตเตระโกนอล(tetra-ZrO_2) (011),(112) และ (121) โดยเมื่อเติมกราฟีนออกไซด์ลงในตัวเร่งปฏิกิริยาปริมาณ 0.5-1 เปอร์เซ็นต์โดยน้ำหนัก พบว่ายังคงปรากฏพีคที่ตำแหน่งเดิมแต่ความสูงของพีคลดลงบ่งบอกถึงขนาดผลึกที่เล็กลง แต่เมื่อเพิ่มปริมาณกราฟีนออกไซด์มากขึ้น (2.5-10 เปอร์เซ็นต์) พบว่าพีคก็ยังคงปรากฏที่ตำแหน่งเดิมแต่ความสูงของพีคกลับเพิ่มขึ้นแทน ซึ่งบ่งบอกถึงขนาดผลึกที่ใหญ่ขึ้น และตัวเร่งที่มีปริมาณกราฟีนออกไซด์เพิ่มเป็น 20เปอร์เซ็นต์โดยน้ำหนัก พบว่าไม่พบพีคของโลหะทั้ง3ชนิด อาจเนื่องจากการบดบังกราฟีนที่เติมลงไปปริมาณมาก โดยสามารถนำความสูงของพีคหลักมาคำนวณหาขนาดผลึกได้จากสมการของเชอร์เรอร์ (Scherrer's equation) และแสดงผลการคำนวณในตารางที่ 3.3 พบว่าตัวเร่งปฏิกิริยาคอปเปอร์ ซิงค์ออกไซด์ เซอร์โคเนียมไดออกไซด์มีขนาดผลึกของคอปเปอร์ออกไซด์เท่ากับ 9.683 นาโนเมตร โดยเมื่อเติมกราฟีนออกไซด์ลงในตัวเร่งปฏิกิริยาปริมาณ 0.5-1 เปอร์เซ็นต์ โดยน้ำหนัก พบว่าขนาดผลึกของคอปเปอร์ออกไซด์มีค่าลดลงเป็น 9.572 และ 9.357 นาโนเมตรตามลำดับ เนื่องจากโลหะออกไซด์ต่างๆ จะกระจายตัวอยู่บนแผ่นกราฟีน แต่เมื่อเติมกราฟีนออกไซด์ลงในตัวเร่งปฏิกิริยามากขึ้น (2.5-10 เปอร์เซ็นต์โดยน้ำหนัก) มีผลทำให้ขนาดผลึกของคอปเปอร์ออกไซด์มีค่าเพิ่มขึ้น บ่งบอกว่าปริมาณกราฟีนที่มากเกินไปทำให้ เกิดการแยกเฟสของโลหะออกไซด์กับกราฟีน

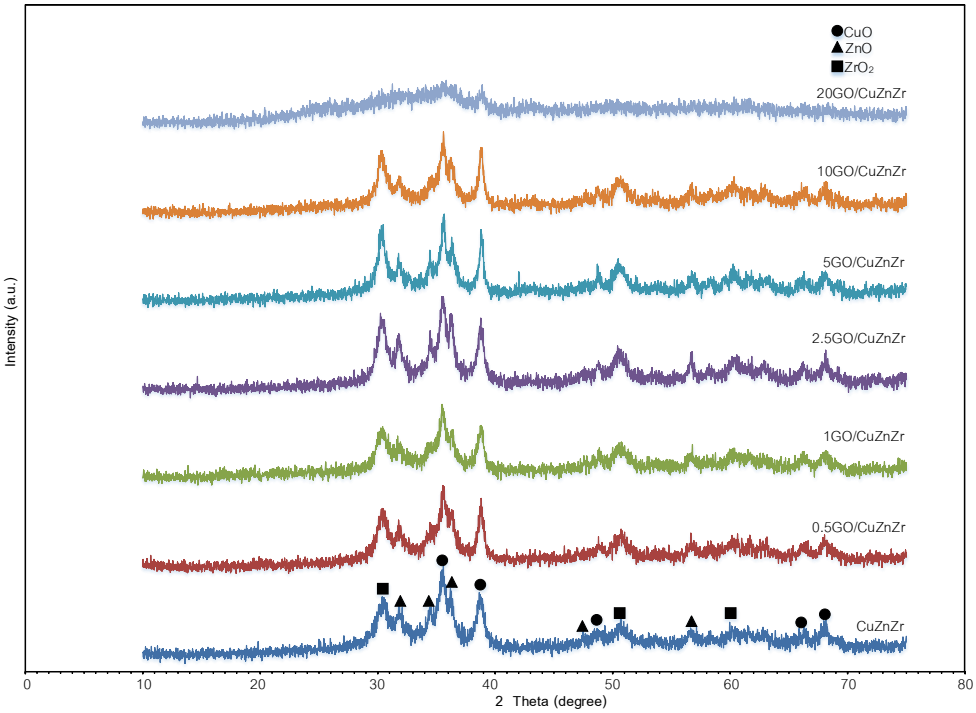

ภาพที่ 3.5 การเลี้ยวเบนของรังสีเอ็กซ์ของตัวเร่งปฏิกิริยากราฟีนออกไซด์ คอปเปอร์ซิงค์และเซอร์โคเนียมที่ถูกเตรียมด้วยเทคนิคการตกตะกอนร่วม

ตารางที่ 3.3 ขนาดผลึกของคอปเปอร์ออกไซด์ของตัวเร่งปฏิกิริยา GO-CuO-ZnO-ZrO_2 ที่เตรียมด้วยปริมาณกราฟีนออกไซด์ต่าง ๆ

Samples	CuO crystallite size (nm)
CuZnZr	9.68
0.5GO/CuZnZr	9.57
1GO/CuZnZr	9.36
2.5GO/CuZnZr	11.90
5GO/CuZnZr	17.35
10GO/CuZnZr	13.43
20GO/CuZnZr	-

ภาพที่ 3.6 แสดงภาพถ่ายด้วยกล้องจุลทรรศน์อิเล็กตรอนแบบส่องกราดของตัวเร่งปฏิกิริยา GO-CuO-ZnO-ZrO_2 ที่เตรียมด้วยปริมาณกราฟีนต่างๆ พบว่าตัวเร่งปฏิกิริยาที่มีปริมาณกราฟีนออกไซด์เท่ากับ 0 เปอร์เซ็นต์โดยน้ำหนัก (ภาพที่ 3.6a) มีการกระจายตัวของอนุภาคคอปเปอร์ ซิงค์และเซอร์โคเนียมขนาดประมาณ10-20 นาโนเมตร ลักษณะของอนุภาคเป็นทรงกลมเชื่อมติดกันอย่างหนาแน่น และเมื่อเพิ่มปริมาณกราฟีนออกไซด์เป็น 0.5 เปอร์เซ็นต์โดยน้ำหนัก(ภาพที่ 3.6b) พบว่า อนุภาคคอปเปอร์ ซิงค์และเซอร์โคเนียมที่มีขนาดประมาณ10-20 นาโนเมตรก่อนหน้านี้นั้นมีขนาดอนุภาคเล็กลงและมีการกระจายตัวอย่างหนาแน่นบนแผ่นของกราฟีนออกไซด์ และเมื่อเพิ่มปริมาณกราฟีนออกไซด์เป็น 1 เปอร์เซ็นต์โดยน้ำหนัก (ภาพที่ 3.6c) พบว่าอนุภาคคอปเปอร์ ซิงค์และเซอร์โคเนียมนั้นมีการกระจายตัวทั้งภายในและภายนอกแผ่นกราฟีนแต่ละแผ่น และยังพบว่า ขนาดอนุภาคคอปเปอร์ ซิงค์และเซอร์โคเนียมบนแผ่นกราฟีนนั้นก็ยังมีขนาดเล็กลงจากตัวเร่งปฏิกิริยาที่ไม่ได้เติมกราฟีนออกไซด์ แต่เมื่อเพิ่มปริมาณกราฟีนเพิ่มขึ้นเป็น 2.5 และ 5 เปอร์เซ็นต์ (ภาพที่ 3.6d และ 3.6e) กลับพบว่า ขนาดอนุภาคของคอปเปอร์ ซิงค์และเซอร์โคเนียมที่กระจายตัวบนแผ่นกราฟีนนั้นกลับมีการรวมตัวกันมากขึ้น จนทำให้มีขนาดอนุภาคใหญ่ขึ้น ทั้งนี้อาจเกิดจากปริมาณที่มากขึ้นของกราฟีนทำให้กราฟีนมีการซ้อนทับกันเองมากขึ้น ซึ่งก็เห็นได้ชัดเจนว่ากราฟีนมีการซ้อนทับกันเองมากขึ้นจริง และเมื่อเพิ่มปริมาณกราฟีนขึ้นเป็น 10 และ 20 เปอร์เซ็นต์ (ภาพที่ 3.6f และ 3.6g) เห็นได้ว่านอกจากขนาดอนุภาคคอปเปอร์ ซิงค์และเซอร์โคเนียมจะใหญ่ขึ้นแล้ว กราฟีนออกไซด์กับคอปเปอร์ ซิงค์และเซอร์โคเนียม ก็มีการแยกจากกันเป็นสองส่วน อาจเนื่องจากการซ้อนทับกันมากขึ้นไปอีกของกราฟีนออกไซด์ ซึ่งผลจากภาพถ่ายอิเล็กตรอนแบบส่องกราดนี้สอดคล้องกับผลขนาดผลึกของคอปเปอร์จากเทคนิคการเลี้ยวเบนของรังสีเอกซ์

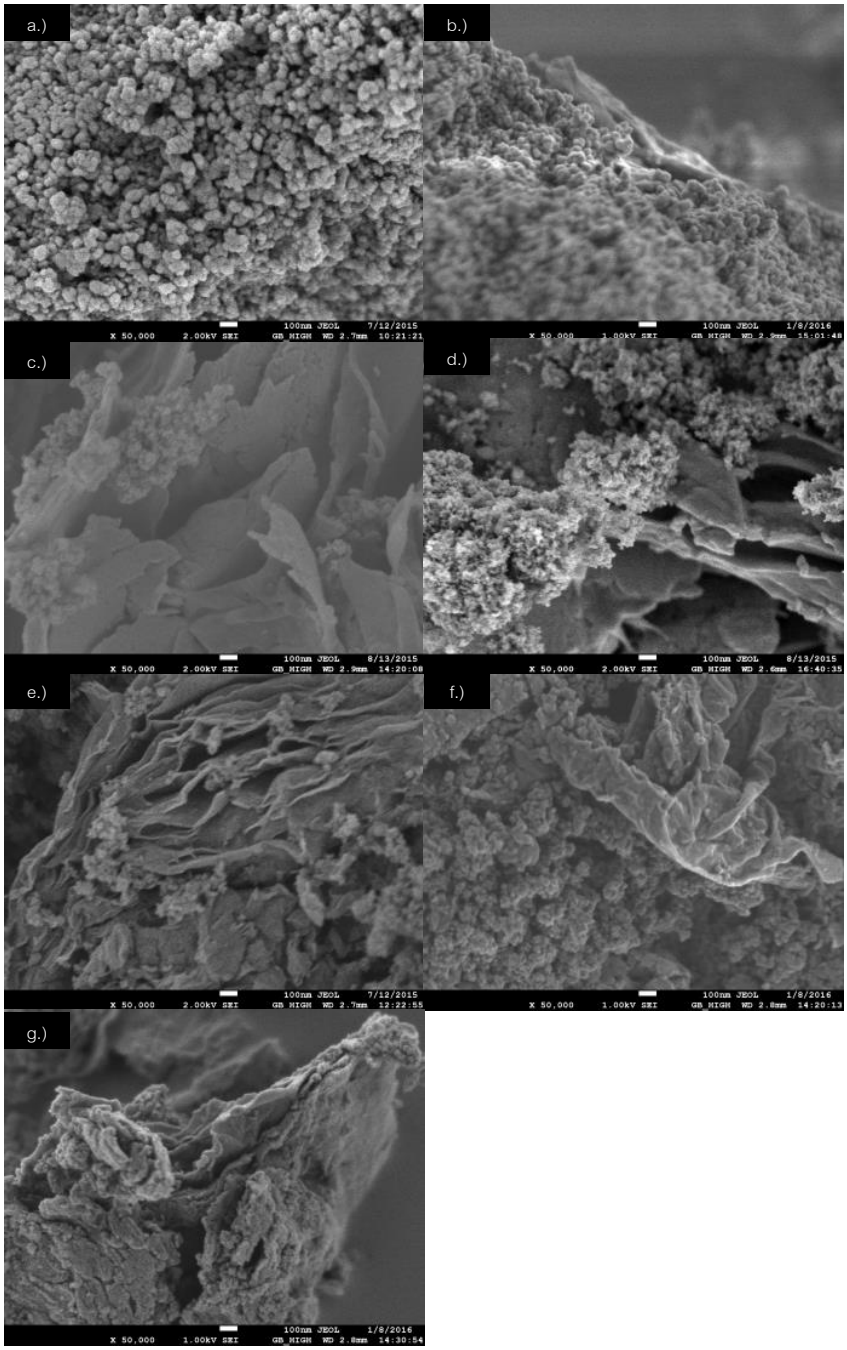

ภาพที่ 3.6 ภาพถ่ายด้วยกล้องจุลทรรศน์อิเล็กตรอนแบบส่องกราดของตัวเร่งปฏิกิริยา GO-CuO-ZnO-ZrO_2 ที่ปริมาณกราฟีนออกไซด์ 0 (a), 0.5 (b), 1 (c), 2.5 (d), 5 (e), 10 (f) and 20 (g) เปอร์เซ็นต์โดยน้ำหนักตามลำดับ

ภาพที่ 3.7 แสดงความสามารถในการรีดิวซ์ของตัวเร่งปฏิกิริยา GO-CuO-ZnO-ZrO_2 พบว่า พบว่าตัวเร่งปฏิกิริยาที่ไม่มีการเติมกราฟีนออกไซด์มีการรีดิวซ์ที่ช่วงอุณหภูมิระหว่าง 210-240 องศาเซลเซียสและมีการใช้ปริมาณก๊าซไฮโดรเจนสูงสุด ณ อุณหภูมิ 225 องศาเซลเซียส เมื่อเติมกราฟีนออกไซด์ลงไป 0.5 และ 1 เปอร์เซ็นต์โดยน้ำหนักพบว่าอุณหภูมิในการรีดิวซ์สูงสุด มีการเลื่อนไปที่บริเวณอุณหภูมิต่ำกว่า บ่งบอกว่าคอปเปอร์ออกไซด์มีการกระจายตัวดีขึ้น แต่เมื่อเติมปริมาณกราฟีนออกไซด์ ปริมาณมากขึ้น เป็น 2.5 และ 5 เปอร์เซ็นต์โดยน้ำหนัก พบว่าอุณหภูมิในการรีดิวซ์สูงสุดมีแนวโน้มเพิ่มขึ้นแต่ยังมีค่าน้อยกว่าตัวเร่งที่ไม่ได้ใส่กราฟีนออกไซด์ ซึ่งน่าจะเกิดจากคอปเปอร์ออกไซด์ที่มีขนาดใหญ่ขึ้นแต่ยังกระจายตัวได้ดีบนตัวรองรับกราฟีนออกไซด์ เมื่อเพิ่มปริมาณกราฟีนออกไซด์เป็น 10และ 20 เปอร์เซ็นต์ จะเห็นได้ว่าอุณหภูมิในการรีดิวซ์สูงสุดเพิ่มขึ้นจนมีค่าใกล้เคียงกับตัวเร่งปฏิกิริยาที่ไม่ได้เติมกราฟีนออกไซด์ ซึ่งอาจเกิดจากการแยกเฟสระหว่างกราฟีนกับโลหะคอปเปอร์ ทำให้กราฟีนไม่ได้ช่วยในการลดอันตรกิริยาของคอปเปอร์เลย ซึ่งก็สอดคล้องกับภาพถ่ายเทคนิคการวิเคราะห์ด้วยกล้องจุลทรรศ์อิเล็กตรอน แบบส่องผ่านและส่องกราดที่มีการซ้อนทับกันของแผ่นกราฟีนและเกิดการแยกเฟสเมื่อเพิ่มปริมาณกราฟีนออกไซด์ปริมาณมากกว่า 10 เปอร์เซ็นต์

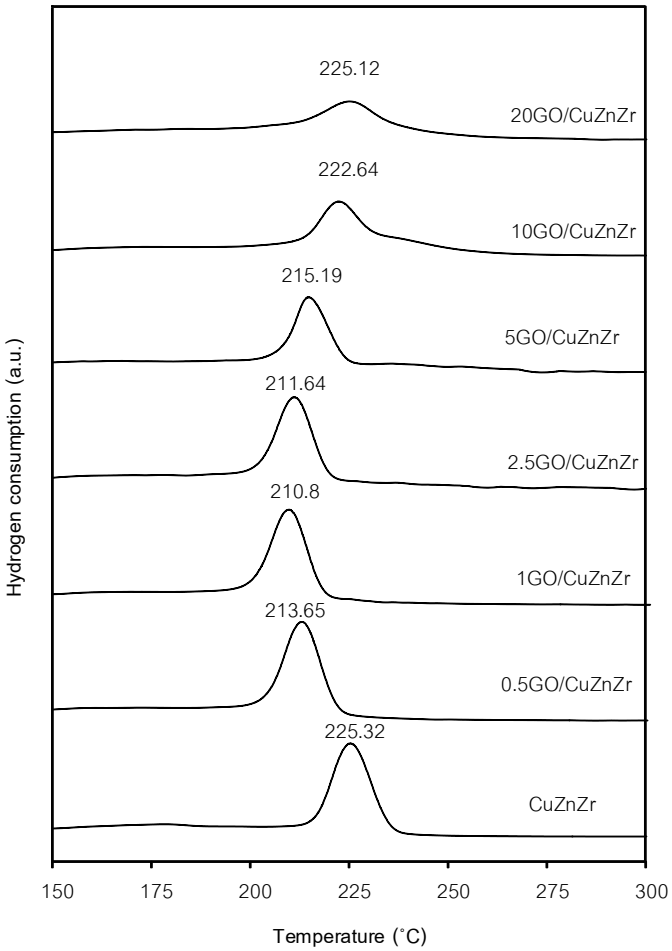

ภาพที่ 3.7 ความสามารถในการรีดิวซ์ของตัวเร่งปฏิกิริยา GO-CuO-ZnO-ZrO2 ที่เตรียมด้วยปริมาณกราฟีนออกไซด์ต่างๆ

ภาพที่ 3.8 (a) แสดงสเปกตรัมการดูดกลืนงสีเอ็กซ์ในย่านใกล้ขอบเค ของตัวเร่งปฏิกิริยา GO-CuO-ZnO-ZrO_2 เตรียมที่ปริมาณกราฟีนออกไซด์ต่างๆ พบว่าลักษณะสเปกตรัมการดูดกลืนรังสีเอ็กซ์ในย่านใกล้ขอบอยู่ในตำแหน่ง 8983.70-8983.90 ซึ่งใกล้เคียงตำแหน่งสารมาตรฐานคอปเปอร์ออกไซด์คือ 8983.20 แสดงให้เห็นว่าคอปเปอร์ซึ่งเป็นองค์ประกอบหลักในตัวเร่งปฏิกิริยาอยู่ในรูป Cu^{2+} เช่นเดียวกับในสารมาตรฐานคอปเปอร์ออกไซด์ ส่วนตัวเร่งปฏิกิริยาที่ทำการเติมกราฟีนออกไซด์ลงไป 20เปอร์เซ็นต์โดยน้ำหนักน มีลักษณะสเปกตรัมการดูดกลืนรังสีเอ็กซ์ในย่านใกล้ขอบอยู่ในตำแหน่ง 8980.50 ซึ่งมีค่าอยู่ระหว่างสารมาตรฐานคอปเปอร์ออกไซด์คือ 8983.20 และสารมาตรฐานคอปเปอร์ไดออกไซด์คือ 8979.80 ซึ่งแสดงให้เห็นว่าตัวเร่งปฏิกิริยาที่ทำการเติมกราฟีนออกไซด์ลงไป 20เปอร์เซ็นต์โดยน้ำหนักอ ยู่ในรูป Cu^{+1} และ Cu^{+2} หรือเป็นเฟสผสมนั่นเองซึ่งอาจเกิดจากปริมาณกราฟีนที่มากเกินไปทำปฏิกิริยากับคอปเปอร์บางส่วนเกิดเป็นสารประกอบอื่นขึ้น และเมื่อพิจารณาผลการวิเคราะห์สเปกตรัมในรูปอนุพันธ์ของการดูดกลืนรังสีเอ็กซ์ในย่านใกล้ขอบ ดังแสดงในภาพที่ 3.8 (b) พบว่าตัวเร่งปฏิกิริยาที่สังเคราะห์ได้ที่ไม่เติมกราฟีนออกไซด์นั้นมีตำแหน่งขอบการดูดกลืนอยู่ที่ 8983.76 ซึ่งเห็นได้ว่ามีการเลื่อนไปเล็กน้อยจากตำแหน่งสารมาตรฐานคอปเปอร์ออกไซด์คือ 8983.20 ทั้งนี้เนื่องมาจากสิ่งแวดล้อมทางเคมีของคอปเปอร์ออกไซด์ ในตัวเร่งปฏิกิริยาอาจแตกต่างจากคอปเปอร์ออกไซด์ซึ่งเป็นสารมาตรฐาน (Velu et al.,2002) ซึ่งแสดงให้เห็นว่าผลที่ได้ยืนยันว่าคอปเปอร์ออกไซด์มีอันตรกิริยากับโลหะออกไซด์ทั้งสอง ชนิด คือ ซิงค์ออกไซด์ และเซอร์โคเนียมไดออกไซด์และเมื่อเพิ่มปริมาณกราฟีนออกไซด์ ขึ้นเป็น 0.5-10 เปอร์เซ็นต์จะพบว่าตำแหน่งขอบการดูดกลืนขยับไปที่ตำแหน่ง 8983.8-8983.9 ซึ่งก็แสดงให้เห็นว่าโลหะคอปเปอร์ก็มีอันตรกิริยากับกราฟีนออกไซด์เช่นกัน และจะเห็นได้อีกว่าอนุพันธ์ของการดูดกลืนรังสีเอ็กซ์ในย่านใกล้ขอบของตัวเร่งปฏิกิริยาที่มีการเติมกราฟีน 5-10 เปอร์เซ็นต์นั้นมีลักษณะความเป็นพีคลดลง อาจเนื่องมาจากกราฟีนนั้นอาจเข้าไปบดบังโลหะคอปเปอร์ ซึ่งก็สอดคล้องกับผลจากเทคนิควิเคราะห์ด้วยเทคนิคภาพถ่ายด้วยกล้องจุลทรรศน์อิเล็กตรอนแบบส่องกราด

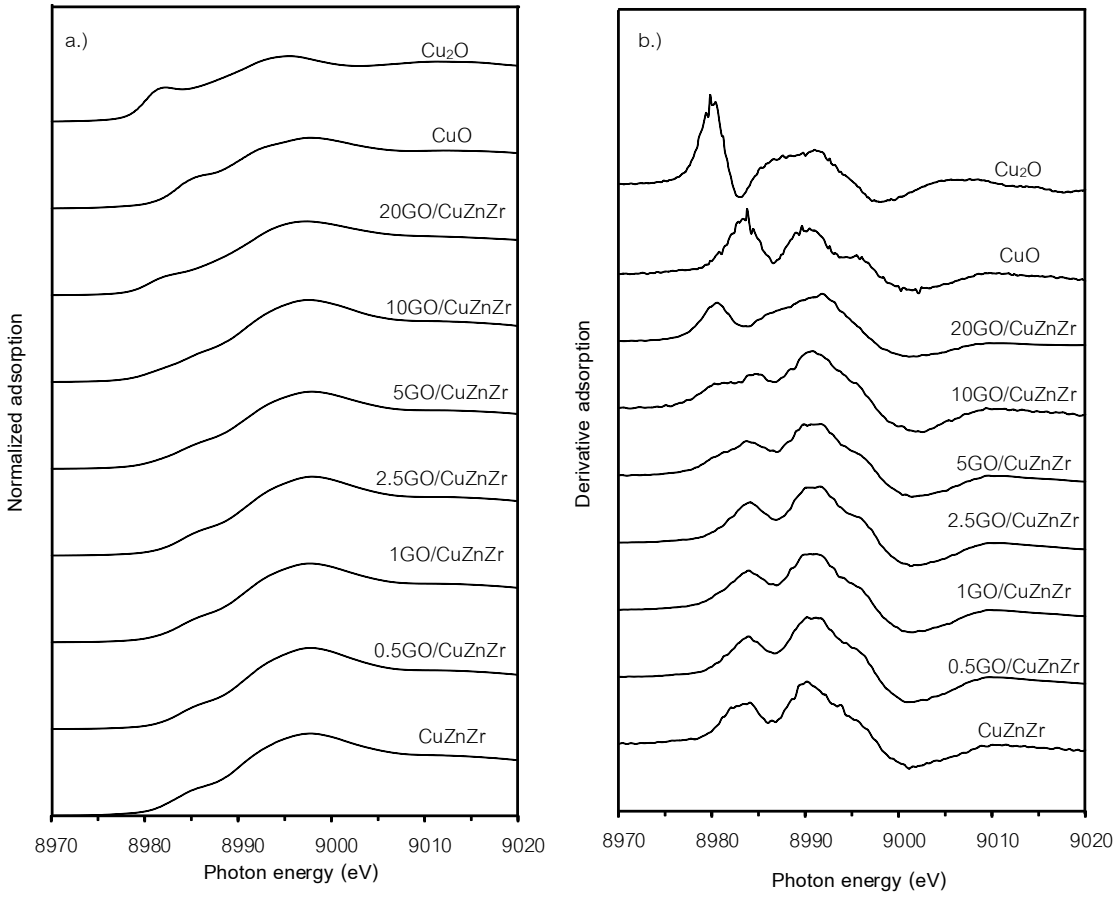

ภาพที่ 3.8 สเปกตรัมการดูดกลืนรังสีเอ็กซ์ในย่านใกล้ขอบที่บริเวณขอบการดูดกลืนเค(K-edge) ของอะตอมคอปเปอร์ (a) และสเปกตรัมในรูปอนุพันธ์ของการดูดกลืนรังสีเอ็กซ์ในย่านใกล้ขอบ(Derivative XANES) (b) ของตัวเร่งปฏิกิริยา GO-CuO-ZnO-ZrO2 ที่เตรียมที่ปริมาณกราฟีนออกไซด์ต่าง ๆ

3.3 การทดสอบประสิทธิภาพของตัวเร่งปฏิกิริยา GO-CuO-ZnO-ZrO_2 ที่เตรียมด้วยกราฟีนปริมาณต่าง ๆ ต่อปฏิกิริยาการเติมไฮโดรเจนของก๊าซคาร์บอนไดออกไซด์เพื่อผลิตเมทานอล

การทดสอบประสิทธิภาพการสังเคราะห์เมทานอลจากก๊าซคาร์บอนไดออกไซด์ของตัวเร่งปฏิกิริยากราฟีนออกไซด์ คอปเปอร์ ซิงค์และเซอร์โคเนียมถูกศึกษาภายในเตาปฏิกรณ์แบบเบดนิ่ง (Fixed bed reactor) โดยใช้อัตราส่วนโดยโมลของก๊าซคาร์บอนไดออกไซด์ต่อก๊าซไฮโดรเจนเท่ากับ 1 ต่อ 3 ที่ความดัน 20 บรรยากาศ และอุณหภูมิที่ทำการศึกษามีค่าเท่ากับ 200, 220, 240, 250, 260 และ 280 องศาเซลเซียส

ภาพที่ 3.9 แสดงอุณหภูมิในการทำปฏิกิริยาต่อร้อยละการแปลงผันของก๊าซคาร์ บอนไดออกไซด์ของตัวเร่งปฏิกิริยากราฟีนออกไซด์ คอปเปอร์ ซิงค์และเซอร์โคเนียมที่ถูกเตรียมด้วยเทคนิคการตกตะกอนร่วมโดยใช้กราฟีนออกไซด์ในอัตราส่วนต่าง ๆ พบว่าทุก ๆตัวเร่งปฏิกิริยาที่ทดสอบมีแนวโน้มของร้อยละการแปลงผันของก๊าซคาร์บอนไดออกไซด์เพิ่มขึ้นเมื่ออุณหภูมิเพิ่มขึ้น

แต่เมื่อพิจารณาตัวเร่งปฏิกิริยาที่มีการเติมกราฟีนออกไซด์ลงไปปริมาณ 0.5-5 เปอร์เซ็นต์โดยน้ำหนัก พบว่ามีค่าร้อยละการแปลงผันของก๊าซคาร์บอนไดออกไซด์มากกว่าตัวเร่งปฏิกิริยาที่ไม่ได้เติมกราฟีนออกไซด์ลงไป แต่เมื่อเพิ่มปริมาณกราฟีนออกไซด์มากขึ้นเป็น 10และ20 เปอร์เซ็นต์โดยน้ำหนัก พบว่าร้อยละการแปลงผันของก๊าซคาร์บอนไดออกไซด์มีค่าน้อยกว่าตัวเร่งปฏิกิริยาที่ไม่ได้เติมกราฟีนออกไซด์ และพบว่าตัวเร่งปฏิกิริยาที่มีการเติมกราฟีนออกไซด์ลงไป 1 เปอร์เซ็นต์ (1GO/CuZnZr) มีค่าร้อยละการแปลงผันก๊าซคาร์บอนไดออกไซด์ดีที่สุด โดยมีค่าร้อยละการแปลงผันก๊าซคาร์บอนไดออกไซด์ที่อุณหภูมิ 200,220,240, 260 และ 280 องศาเซลเซียส เท่ากับ 4.41, 8.88, 15.41, 21.64, 24.55 เปอร์เซ็นต์ตามลำดับ

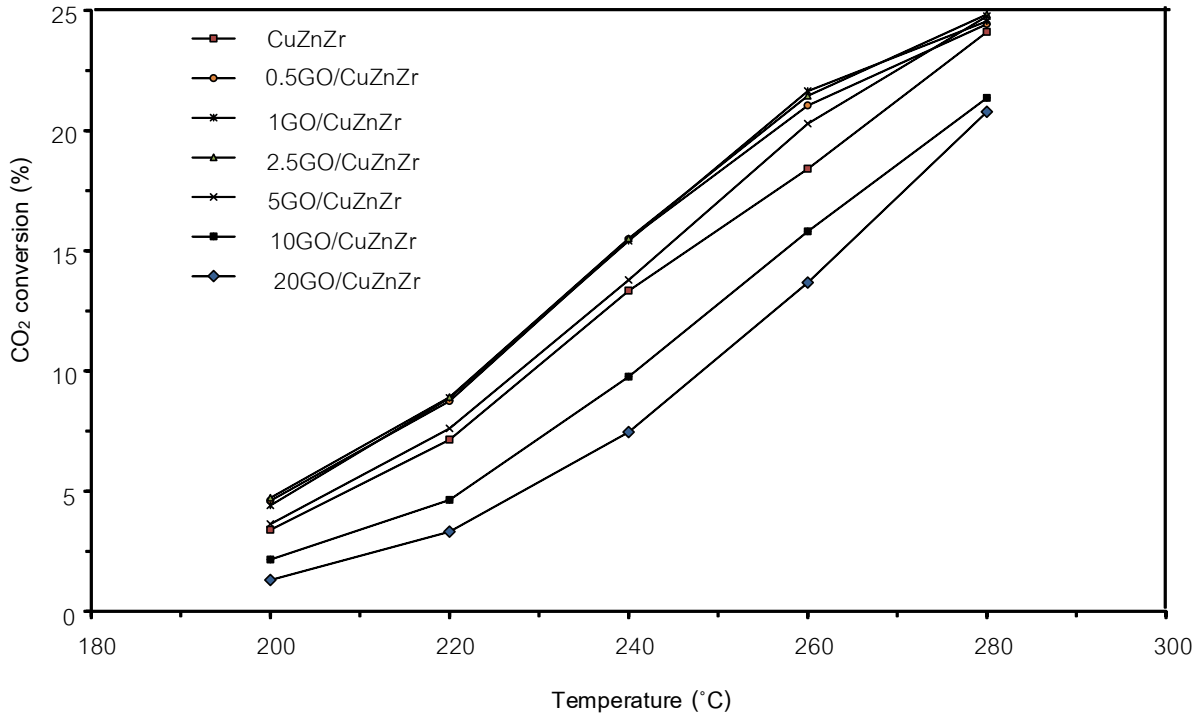

ภาพที่ 3.9 อุณหภูมิในการทำปฏิกิริยาต่อร้อยละการแปลงผันของก๊าซคาร์บอนไดออกไซด์ของตัวเร่งปฏิกิริยากราฟีนออกไซด์ คอปเปอร์ ซิงค์และเซอร์โคเนียมที่ถูกเตรียมด้วยเทคนิคการตกตะกอนร่วม

ภาพที่ 3.10 แสดงอุณหภูมิในการทำปฏิกิริยาต่อการเลือกเกิดเป็นเมทานอลของตัวเร่งปฏิกิริยากราฟีนออกไซด์ คอปเปอร์ ซิงค์และเซอร์โคเนียมเตรียมที่ปริมาณกราฟีนออกไซด์ต่าง ๆ พบว่าในทุก ๆตัวเร่งปฏิกิริยาค่าการเลือกเกิดเป็นเมทานอลลดลงตามอุณหภูมิในการทำปฏิกิริยาที่เพิ่มขึ้น เนื่องจากอัตราการเกิดปฏิกิริยาข้างเคียง Reverse Water-Gas Shift ซึ่งเป็นปฏิกิริยาดูดความร้อนจะเพิ่มมากขึ้น ดังนั้นจะส่งผลให้ก๊าซคาร์บอนไดออกไซด์เลือกที่จะเกิดเป็นคาร์บอนมอนออกไซด์สูงขึ้น เมื่อพิจารณาตัวเร่งปฏิกิริยาที่มีการเติมกราฟีนออกไซด์ลงไป 0-20เปอร์เซ็นต์โดยน้ำหนักพบว่าตัวเร่งปฏิกิริยาที่มีการเติมกราฟีนออกไซด์ลงไปนั้นมีค่าการเลือกเกิดเป็นเมทานอลสูงกว่าตัวเร่งปฏิกิริยาที่ไม่ได้มีการเติมกราฟีนออกไซด์ลงไป โดยตัวเร่งปฏิกิริยาที่มีค่าการเลือกเกิดเม

ทานอลดีที่สุดคือตัวเร่งปฏิกิริยาที่มีการเติมกราฟีน 1 เปอร์เซ็นต์โดยน้ำหนัก(1GO/CuZnZr) โดยมีค่า ร้อยละการเลือกเกิดของเมทานอลที่อุณหภูมิ 200, 220, 240, 260 และ 280 องศาเซลเซียส เท่ากับ 75.88, 56.76, 34.60, 21.51, 7.98 เปอร์เซ็นต์ตามลำดับ

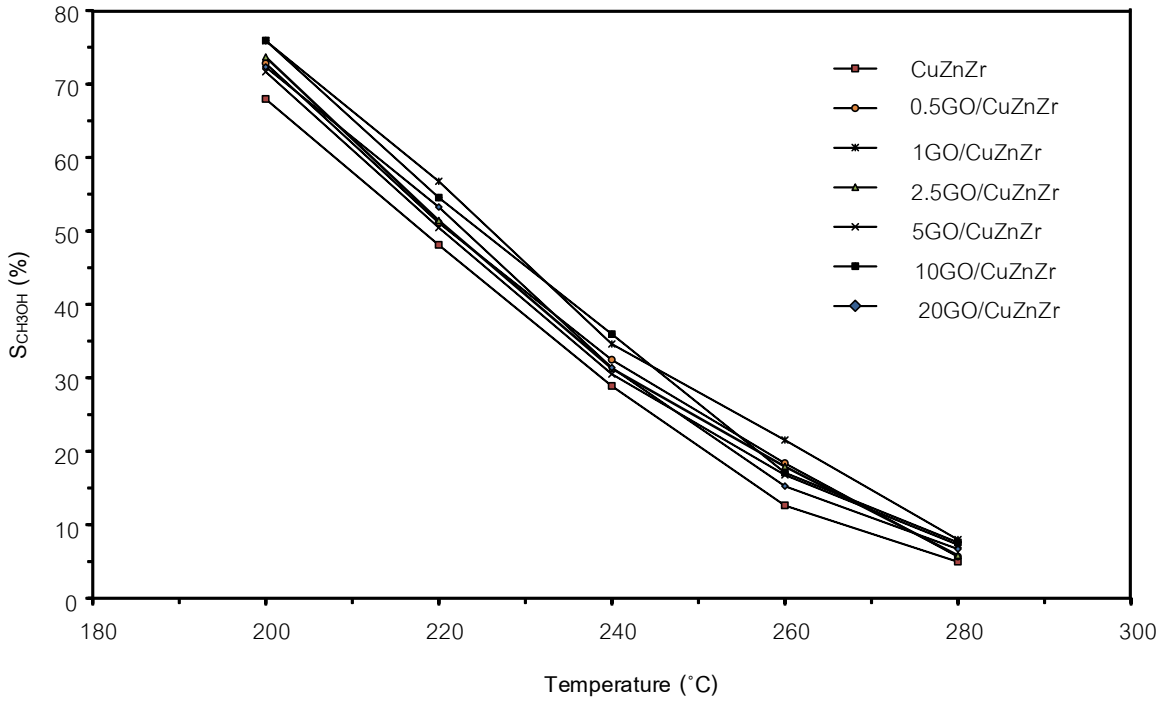

ภาพที่ 3.10 อุณหภูมิในการทำปฏิกิริยาต่อร้อยละการเลือกเกิดของเมทานอลของตัวเร่งปฏิกิริยากราฟีนออกไซด์ คอปเปอร์ ซิงค์และเซอร์โคเนียมที่ถูกเตรียมด้วยเทคนิคการตกตะกอนร่วม

ภาพที่ 3.11 แสดงอุณหภูมิในการทำปฏิกิริยาต่อค่าผลได้ของเมทานอลของตัวเร่งปฏิกิริยา GO-CuO-ZnO-ZrO_2 เตรียมที่ปริมาณกราฟีนออกไซด์ต่างๆ พบว่าทุกๆตัวเร่งปฏิกิริยามีแนวโน้มผลได้ของเมทานอลไปในทางเดียวกันคือมีค่าเพิ่มขึ้นเรื่อยๆจนมีค่าสูงสุดที่อุณหภูมิ 240 องศาเซลเซียส และเมื่ออุณหภูมิเพิ่มมากกว่า 240 องศาเซลเซียส ค่าผลได้ของเมทานอลเริ่มมีค่าลดลง โดยเมื่อพิจารณาตัวเร่งปฏิกิริยาที่เติมกราฟีนลงไป 0-5เปอร์เซ็นต์นั้น พบว่าค่าผลได้ของเมทานอลมีแนวโน้มมาก กว่าตัวเร่งปฏิกิริยาที่ไม่ได้เติมกราฟีนออกไซด์ แต่เมื่อเพิ่มปริมาณกราฟีนออกไซด์มากขึ้นเป็น 10และ 20 เปอร์เซ็นต์โดยน้ำหนัก พบว่าค่าผลได้ของเมทานอลมีแนวโน้มน้อยกว่าตัวเร่งปฏิกิริยาที่ไม่ได้เติมกราฟีนออกไซด์ โดยตัวเร่งปฏิกิริยาที่มีค่าผลได้ของเมทานอลสูงที่สุดคือตัวเร่งปฏิกิริยาที่มีการเติมกราฟีนออกไซด์ลงไป 1เปอร์เซ็นต์ (1GO/CuZnZr) โดยมีค่าผลได้ของเมทานอลที่อุณหภูมิ 200, 220, 240, 260 และ 280 องศาเซลเซียส เท่ากับ 172.48, 259.63, 274.63, 239.78, และ 100.89 กรัมเมทานอลต่อกิโลกรัมตัวเร่งปฏิกิริยาต่อชั่วโมง นอกจากนี้ยังพบว่าเมื่ออุณหภูมิในการทำปฏิกิริยาสูงกว่า 240 องศาเซลเซียส ตัวเร่งปฏิกิริยาที่ใส่กราฟีนลงไปมีแนวโน้มให้ค่าผลได้ของเมทานอลสูงกว่าตัวเร่งปฏิกิริยาที่ไม่ได้ใส่กราฟีนออกไซด์ทั้งนี้น่าจะเป็นเพราะว่า

คุณสมบัติของกราฟีนที่ช่วยให้ไฮโดรเจนอะตอมสามารถเกิดการสปิลโอเวอร์จึงช่วยให้ได้ผลิตภัณฑ์เป็นเมทานอลมากขึ้น

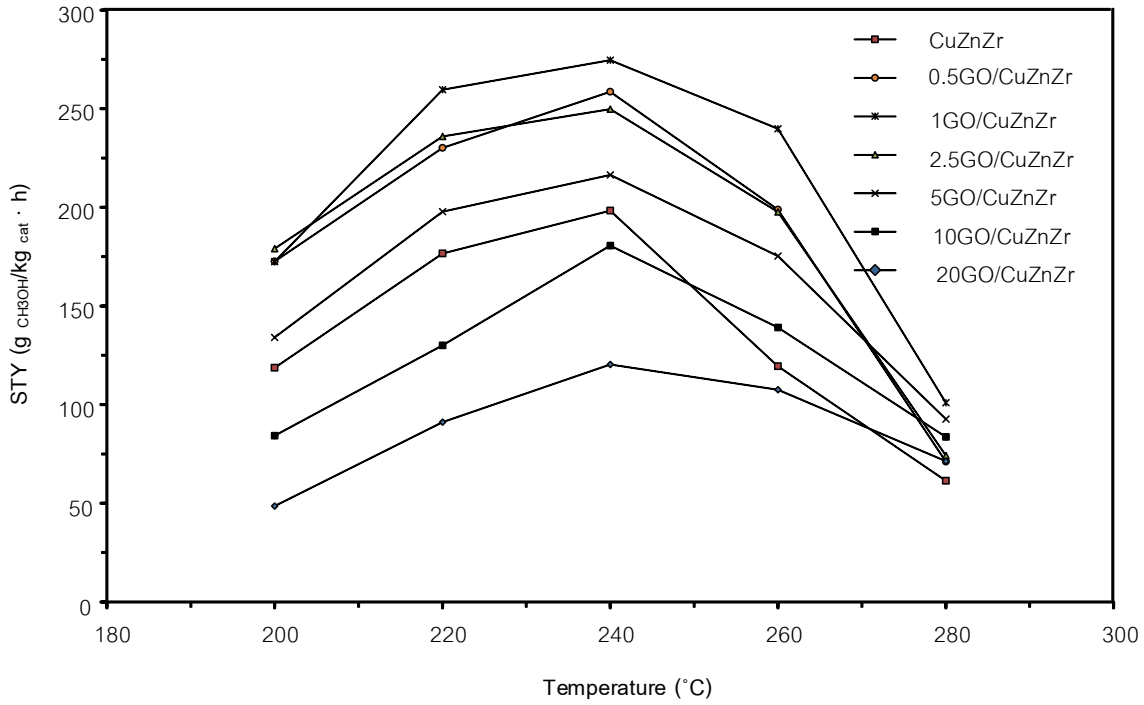

ภาพที่ 3.11 อุณหภูมิในการทำปฏิกิริยาต่อค่าผลได้ของเมทานอลของตัวเร่งปฏิกิริยา กราฟีนออกไซด์ คอปเปอร์ ซิงค์และเซอร์โคเนียมที่ถูกเตรียมด้วยเทคนิคการตกตะกอนร่วม

3.4 การวิเคราะห์คุณลักษณะของตัวเร่งปฏิกิริยา Fe-Co/GO-CuO-ZnO-ZrO_2 ที่สังเคราะห์ได้

จากข้อมูลข้างต้นพบว่าการเตรียมตัวเร่งปฏิกิริยา GO-CuO-ZnO-ZrO_2 ที่มีปริมาณกราฟีนออกไซด์ 1 เปอร์เซ็นต์โดยน้ำหนัก มีการกระจายตัวของโลหะบนตัวรองรับกราฟีนได้ดีที่สุดและให้ค่าผลได้ในการผลิตเมทานอลมากที่สุด จึงนำตัวเร่งปฏิกิริยา GO-CuO-ZnO-ZrO_2 ที่มีปริมาณกราฟีนออกไซด์ปริมาณ 1 เปอร์เซ็นต์โดยน้ำหนัก มาศึกษาเพิ่มเติมในการโหลดโลหะโคบอลต์และเหล็ก เพื่อผลิตเอทานอลจากก๊าซคาร์บอนไดออกไซด์

ภาพที่ 3.12 แสดงผลการวิเคราะห์จากเทคนิคการเลี้ยวเบนของรังสีเอกซ์พบว่าตัวเร่งปฏิกิริยา 1GO-CuZnZr ที่ไม่มีการโหลดโลหะใดๆ แสดงพีคที่บ่งบอกการมีอยู่ของ ZrO_2, CuO, ZnO และ Cu เมื่อเติมโคบอลต์ลงไป 2.5 wt% พบว่า ไม่ปรากฏพีคของโคบอลต์ขึ้น และพีคทุกพีคของโลหะออกไซด์ชนิดอื่นมีความสูงลดลงบ่งบอกว่า โคบอลต์สามารถกระจายตัวได้ดีและ การเติมโคบอลต์ลงไปลดความเป็นผลึกของโลหะออกไซด์ชนิดอื่นๆ ซึ่งอาจจะเป็นไปได้เนื่องจากในขั้นตอนการการจุ่มชุ่มโลหะโคบอลต์เกิดการกระจายตัวของโลหะออกไซด์ชนิดอื่นๆใหม่อีกครั้ง แล้วโคบอลต์ที่มีอยู่ร่วมขัดขวางการรวมตัวกันของโลหะออกไซด์ชนิดอื่นๆทำให้ความเป็นผลึกของโลหะชนิดอื่นเล็กลงไปด้วย เมื่อเติมเหล็กลงไป 2.5 wt% พบว่าให้ผลที่คล้ายคลึงกับการเติมโคบอลต์ แต่

พบพีคของโลหะคอปเปอร์เกิดขึ้น (43.27°; วงกลมสีเขียว) ซึ่งเป็นเนื่องจากตัวเร่งปฏิกิริยามีการรีดิวซ์ก่อนนำมาวิเคราะห์ XRD อย่างไรก็ตามเป็นที่น่าสังเกตว่าตัวเร่งปฏิกิริยา 1GO-CuZnZr (เส้นสีดำ) ที่ผ่านการรีดิวซ์เช่นเดียวกับตัวเร่งปฏิกิริยา 2.5Fe/1GO-CuZnZr กลับไม่มีพีคของโลหะคอปเปอร์ปรากฏอยู่ซึ่งอาจจะเป็นไปได้ว่าการมีอยู่ของโลหะเหล็กทำให้อันตรกิริยาระหว่างโลหะคอปเปอร์กับสารประกอบอื่นๆในโครงสร้างของตัวเร่งปฏิกิริยามีความแข็งแรงขึ้น เมื่อสัมผัสกับอากาศก่อนนำไปวิเคราะห์ด้วยเทคนิค XRD จึงมีโลหะคอปเปอร์เหลืออยู่ เมื่อเติมโคบอลต์ไนเตรตและเหล็กในเตรตอย่างละ 2.5 wt% (2.5Co2.5Fe/1GO-CuZnZr) พบว่า พีคที่แสดงความเป็นผลึกของโลหะคอปเปอร์ มีความชัดเจนมากยิ่งขึ้น ซึ่งเป็นการบ่งบอกว่าการเติมทั้งโคบอลต์และเหล็กลงบนโครงสร้างของ 1GO-CuZnZr ทำให้โลหะคอปเปอร์มีความเป็นผลึกสูงขึ้น

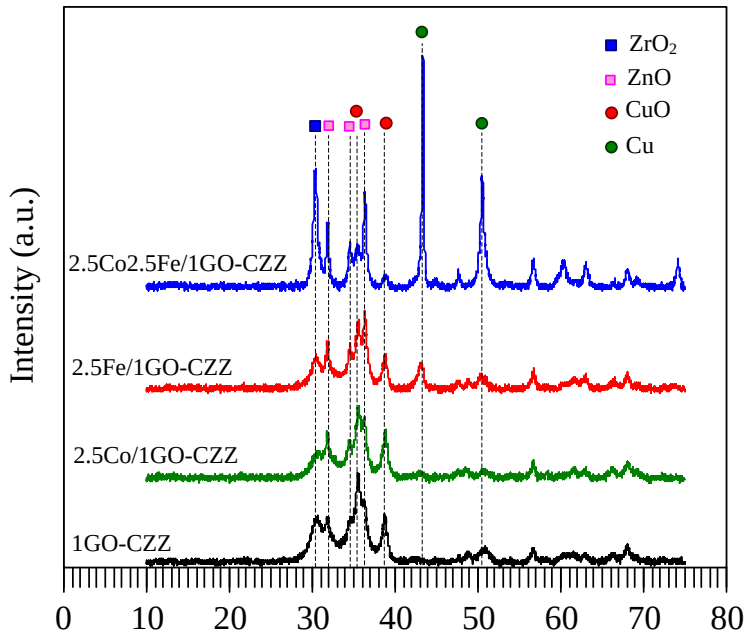

ภาพที่ 3.12 การเลี้ยวเบนของรังสีเอ็กซ์ของตัวเร่งปฏิกิริยากราฟีนออกไซด์คอปเปอร์ซิงค์และเซอร์โคเนียมที่เติมโลหะโคบอลต์ 2.5 wt%, โลหะเหล็ก 2.5 wt% และ โลหะโคบอลต์และเหล็กอย่างละ 2.5 wt%

ภาพที่ 3.13 แสดงภาพถ่ายด้วยกล้องจุลทรรศน์อิเล็กตรอนแบบส่องกราดของตัวเร่งปฏิกิริยา 1GO-CuZnZr ที่โหลดปริมาณโคบอลต์และเหล็กต่างกัน พิจารณา 1GO-CuZnZr พบว่ามีการกระจายตัวของโลหะบนตัวรองรับกราฟีนเป็นอย่างดี เมื่อเติมโลหะโคบอลต์และเหล็กลงไปพบว่าโครงสร้างของตัวเร่งปฏิกิริยามีลักษณะเป็นแผ่นซึ่งเกิดจากการรวมตัวของอนุภาคระดับนาโนเมตร ซึ่งน่าจะเกิดมาจากการที่โลหะออกไซด์กระจายตัวอยู่บนกราฟีนออกไซด์ และเมื่อทำการรีดิวซ์กราฟีนออกไซด์บางส่วนมีการสลายตัว ทำให้ได้โครงสร้างที่มีลักษณะเป็นแผ่น

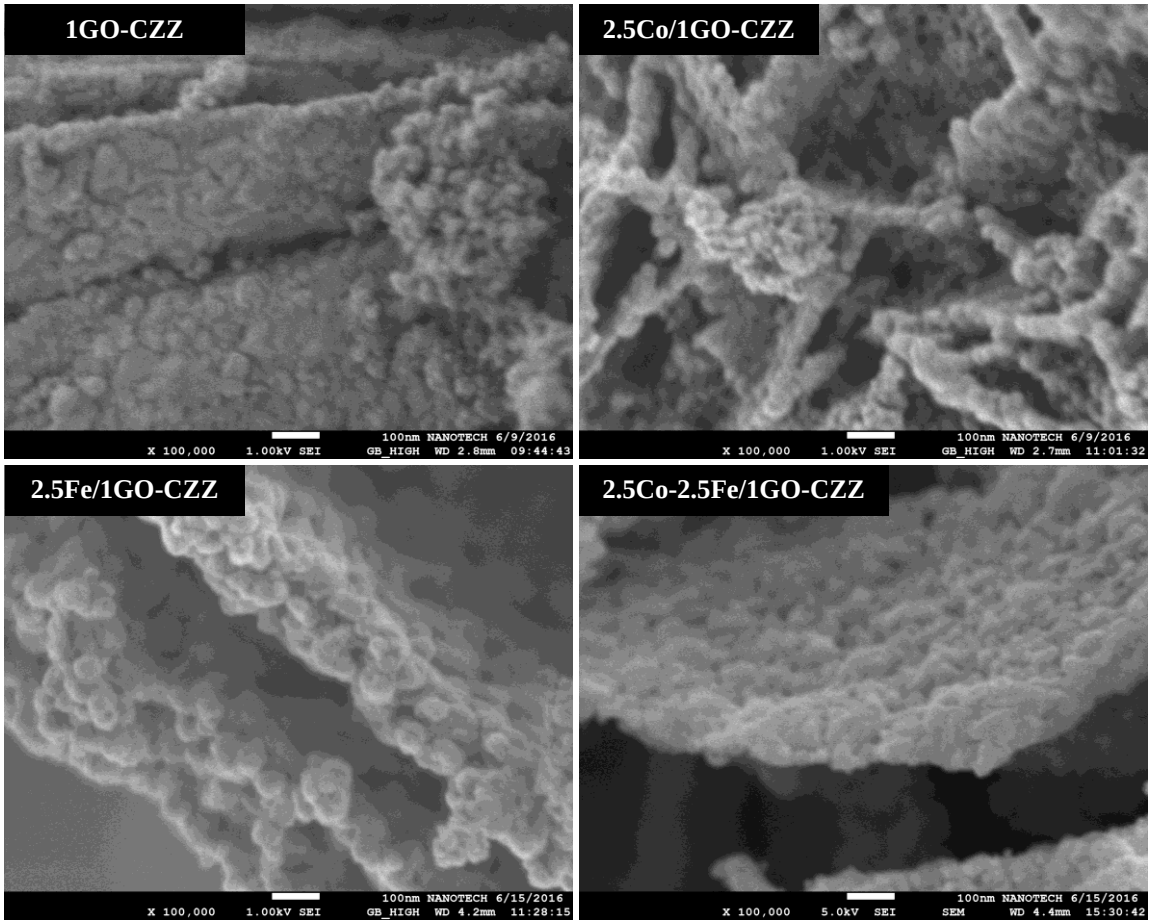

ภาพที่ 3.13 แสดงภาพถ่ายด้วยกล้องจุลทรรศน์อิเล็กตรอนแบบส่องกราดของตัวเร่งปฏิกิริยากราฟีนออกไซด์คอปเปอร์ซิงค์และเซอร์โคเนียมที่เติมโลหะโคบอลต์ 2.5 wt%, โลหะเหล็ก 2.5 wt% และ โลหะโคบอลต์และเหล็กอย่างละ 2.5 wt%

ตารางที่ 3.4 แสดงค่าการแปลงผันของก๊าซคาร์บอนไดออกไซด์ ค่าการเลือกเกิดก๊าซคาร์บอนมอนอกไซด์ ค่าการเลือกเกิดสารประกอบไฮโดรคาร์บอน และการกระจายตัวของผลิตภัณฑ์ไฮโดรคาร์บอน พบว่าการเติมโลหะโคบอลต์ปริมาณ 2.5 wt% (2.5 Co/1GO-CuZnZr) ลงบนตัวเร่งปฏิกิริยา 1GO-CuZnZr ให้ค่าการแปลงผันของก๊าซคาร์บอนไดออกไซด์เพิ่มจาก 12.54 เป็น 16.44 ทั้งนี้เนื่องจาก ก๊าซคาร์บอนมอนอกไซด์สามารถเกิดการไฮโดรจิเนทไปเป็นผลิตภัณฑ์ไฮโดรคาร์บอนได้มากขึ้น และเมื่อพิจารณาการกระจายตัวของผลิตภัณฑ์ไฮโดรคาร์บอนพบว่าให้ผลิตภัณฑ์เป็นมีเทนและเมทานอลที่ใกล้เคียงกัน ร้อยละ 35.15 และ 39.14 ตามลำดับ โดยมีการกระจายตัวของเอทานอลเป็น 10.52 เปอร์เซ็นต์ ในขณะที่เมื่อเติมโลหะเหล็กปริมาณ 2.5 wt% (2.5 Fe/1GO-CuZnZr) พบว่าให้ค่าการแปลงผันของก๊าซคาร์บอนไดออกไซด์เพิ่มขึ้นแต่น้อยกว่าโลหะโคบอลต์คือได้ เท่ากับ 14.21 % ในส่วนของการกระจายตัวของผลิตภัณฑ์เป็นเอทานอลก็ได้ต่ำกว่าตัวเร่งปฏิกิริยา 2.5 Co/1GO-CuZnZr เช่นกันอยู่ที่ ร้อยละ 4.54 และเมื่อทำการเติมโลหะโคบอลต์และเหล็กอย่างละ 2.5 wt% ลงบน 1GO-CuZnZr พบว่าให้ค่าการแปลงผันเพิ่มขึ้นสูงถึงร้อยละ 20.15 และมีค่าการเลือกเกิดสารประกอบไฮโดรคาร์บอนเพิ่มเป็นร้อยละ 64.59 อย่างไรก็ตามกลับ

พบว่าผลิตภัณฑ์ไฮโดรคาร์บอนที่เกิดขึ้นมีมีเทนเป็นองค์ประกอบโดยส่วนใหญ่ และมีเอทานอลอยู่ที่ 4.14% จากผลการทดลองสามารถสรุปได้ว่าการโหลดโคบอลต์ลงบน 1GO-CuZnZr เหมาะสมมากกว่าการใช้เหล็กสำหรับการผลิตเอทานอลจากก๊าซคาร์บอนไดออกไซด์และก๊าซไฮโดรเจน

ตารางที่ 3.4 ค่าการแปลงผันของก๊าซคาร์บอนไดออกไซด์ ค่าการเลือกเกิดก๊าซคาร์บอนมอนอกไซด์ ค่าการเลือกเกิดสารประกอบไฮโดรคาร์บอน และการกระจายตัวของผลิตภัณฑ์ไฮโดรคาร์บอน

Samples	CO_2 conversion (%)	CO selectivity (%)	Hydrocarbon selectivity (%)	Hydrocarbon distribution (%C)				
				Methane	Methanol	Ethanol	$C_{3\text{-}5\ oxygenates}$	$C_{2\text{-}5\ hydrocarbon}$
1GO-CuZnZr	12.54	63.55	36.45	-	100	-	-	-
2.5Co/1GO-CuZnZr	16.44	45.11	54.89	35.15	39.14	10.52	4.10	11.09
2.5Fe/1GO-CuZnZr	14.21	51.33	48.67	30.22	52.11	4.54	2.13	11.00
2.5Co-2.5Fe/1GO-CuZnZr	20.15	35.41	64.59	45.14	30.55	4.14	3.22	16.95

อุณหภูมิในการทำปฏิกิริยาเท่ากับ 250 องศาเซลเซียส, ความดันเท่ากับ 30 บาร์, อัตราส่วนของก๊าซไฮโดรเจนต่อก๊าซคาร์บอนไดออกไซด์เท่ากับ 3:1 และ GHSV เท่ากับ 20,000 ชั่งโมง$^{-1}$

4. ผลการทดลองและการอภิปรายผลการทดลอง

งานวิจัยนี้ศึกษาผลการใช้กราฟีนเป็นตัวรองรับคอปเปอร์ออกไซด์ ซิงค์ออกไซด์และเซอร์โคเนียมไดออกไซด์ โดยศึกษาอิทธิพลของปริมาณกราฟีนที่มีผลต่อคุณสมบัติของตัวเร่งปฏิกิริยาโดยพิจารณาจากคุณสมบัติทางกายภาพและเคมีของตัวเร่งที่ได้สังเคราะห์ขึ้น รวมถึงการศึกษาประสิทธิภาพของการใช้ตัวเร่งปฏิกิริยาดังกล่าวในการเร่งปฏิกิริยาการเติมก๊าซไฮโดรเจนของก๊าซคาร์บอนไดออกไซด์เพื่อผลิตเมทานอล และนำตัวเร่งปฏิกิริยาที่ดีที่สุดไปศึกษาถึงปริมาณการโหลดโคบอลต์และเหล็กต่อประสิทธิภาพในการผลิตเอทานอลจากปฏิกิริยาการเติมไฮโดรเจนของก๊าซคาร์บอนไดออกไซด์ ผลการศึกษาพบว่าในขั้นตอนการเตรียมตัวเร่งปฏิกิริยาสามารถลดขั้นตอนการเตรียมเลยเพียงขั้นตอนเดียวโดยการรีดิวซ์ และไม่ต้องผ่านการแคลไซน์ ซึ่งเป็นวิธีการแบบดั้งเดิมที่ใช้ในการเตรียมตัวเร่งปฏิกิริยา ทำให้มีแนวทางเลือกใหม่ในการประหยัดพลังงานของการเตรียมตัวเร่งปฏิกิริยากลุ่มนี้ ซึ่งผลการศึกษาพบว่าเมื่อเติมปริมาณกราฟีนออก ไซด์ที่เหมาะสมลงในเติมตัวเร่งคอปเปอร์ ซิงค์และเซอร์โคเนียม ส่งผลให้เพิ่มการกระจายตัวของโลหะคอปเปอร์ มีผลให้ขนาดผลึกของคอปเปอร์ออกไซด์เล็กลงและมีผลลดอุณหภูมิในการรีดิวซ์ของคอปเปอร์ออกไซด์ เพิ่มปริมาณไฮโดรเจนบนพื้นผิวซึ่งนำไปสู่การเพิ่มการแตกตัวเป็นไอออนอะตอมของไฮโดรเจนมีผล

ให้การสปิลโอเวอร์ของอะตอมไฮโดรเจนมายังผิวของโลหะออกไซด์เพิ่มขึ้น ซึ่งเมื่อนำตัวเร่งปฏิกิริยามาทดสอบประสิทธิภาพพบว่าปริมาณของกราฟีนออกไซด์ที่เหมาะสมโปรโมทตัวเร่งคอปเปอร์ ซิงค์และเซอร์โคเนียมคือ ร้อยละ1 โดยน้ำหนัก โดยมีร้อยละผลได้ของเมทานอลสูงสุดเท่ากับ 274.63 กรัมเมทานอลต่อกิโลกรัมตัวเร่งปฏิกิริยาต่อชั่วโมง ที่อุณหภูมิของการทำปฏิกิริยา 240 องศาเซลเซียส

เมื่อศึกษาผลการเติมโลหะโคบอลต์และเหล็กลงบนตัวเร่งปฏิกิริยา 1GO-CuZnZr พบว่าให้ค่าการแปลงผันของก๊าซคาร์บอนไดออกไซด์สูงขึ้น และได้ค่าการเลือกเกิดเป็นสารประกอบไฮโดรคาร์บอนมากขึ้น ซึ่งน่าจะมาจากโคบอลต์และ/หรือ ช่วยโปรโมทปฏิกิริยาไฮโดรจิเนชันของก๊าซคาร์บอนมอนออกไซด์ นอกจากนี้พบว่าตัวเร่งปฏิกิริยา 2.5Co/1GO-CuZnZr ให้ค่าการเลือกเกิดเป็นเอทานอลสูงสุด

Output จากโครงการวิจัยที่ได้รับทุนจาก สกว.

ผลงานตีพิมพ์ในวารสารวิชาการนานาชาติ

เรื่องที่ 1

Thongthai Witoon*, Nantana Kachaban, Waleeporn Donphai, Pinit Kidkhunthod, Kajornsak Faungnawakij, Metta Chareonpanich, Jumras Limtrakul, Tuning of catalytic CO_2 hydrogenation by changing composition of CuO-ZnO-ZrO_2 catalysts, Energy Conversion and Management 118 (2016) 21–31. (IF 2015 = 4.801).

เรื่องที่ 2

Thongthai Witoon*, Jiraporn Chalorngtham, Porntipar Dumrongbunditkul, Metta Chareonpanich, Jumras Limtrakul, CO_2 hydrogenation to methanol over Cu/ZrO_2 catalysts: effects of zirconia phases, Chemical Engineering Journal 293 (2016) 327–336. (IF 2015 = 5.310).

เรื่องที่ 3

Thongthai Witoon*, Tinnavat Permsirivanich, Nawapon Kanjanasoontorn, Chalairat Akkaraphataworn, Anusorn Seubsai, Kajornsak Faungnawakij, Chompunuch Warakulwit, Metta Chareonpanich, Jumras Limtrakul, Direct synthesis of dimethyl ether from CO_2 hydrogenation over Cu-ZnO-ZrO2/SO_4^{2-}–ZrO_2 hybrid catalysts: effects of sulfur-to-zirconia ratios, Catalysis Science & Technology 5 (2015) 2347–2357. (IF 2015 = 5.287).

เรื่องที่ 4

Thongthai Witoon*, Sittisut Bumrungsalee, Metta Chareonpanich, Jumras Limtrakul, Effect of hierarchical meso–macroporous alumina-supported copper catalyst for methanol synthesis from CO_2 hydrogenation, Energy Conversion and Management 103 (2015) 886–894. (IF 2015 = 4.801).

เรื่องที่ 5

Porntipar Dumrongbunditkul, **Thongthai Witoon***, Metta Chareonpanich, Thumrongrut Mungcharoen, Preparation and characterization of Co-Cu-ZrO_2 nanomaterials and their catalytic activity in CO_2 methanation, Ceramics International 42 (2016) 10444–10451. (IF 2015 = 2.758).

เรื่องที่ 1

Thongthai Witoon*, Nantana Kachaban, Waleeporn Donphai, Pinit Kidkhunthod, Kajornsak Faungnawakij, Metta Chareonpanich, Jumras Limtrakul, Tuning of catalytic CO_2 hydrogenation by changing composition of CuO-ZnO-ZrO_2 catalysts, Energy Conversion and Management 118 (2016) 21–31. (IF 2015 = 4.801).

Energy Conversion and Management 118 (2016) 21–31

Contents lists available at ScienceDirect

Energy Conversion and Management

journal homepage: www.elsevier.com/locate/enconman

Tuning of catalytic CO_2 hydrogenation by changing composition of CuO–ZnO–ZrO_2 catalysts

Thongthai Witoon [a,b,c,*], Nantana Kachaban [a], Waleeporn Donphai [a,b,c], Pinit Kidkhunthod [d], Kajornsak Faungnawakij [e], Metta Chareonpanich [a,b,c], Jumras Limtrakul [c,f]

[a] Department of Chemical Engineering, Faculty of Engineering, Kasetsart University, Bangkok 10900, Thailand
[b] Center for Advanced Studies in Nanotechnology and Its Applications in Chemical Food and Agricultural Industries, Kasetsart University, Bangkok 10900, Thailand
[c] NANOTEC-KU-Center of Excellence on Nanoscale Materials Design for Green Nanotechnology, Kasetsart University, Bangkok 10900, Thailand
[d] Synchrotron Light Research Institute, Nakhon Ratchasima 30000, Thailand
[e] Nanomaterials for Energy and Catalysis Laboratory, National Nanotechnology Center (NANOTEC), National Science and Technology Development Agency (NSTDA), Khlong Luang, Pathum Thani 12120, Thailand
[f] Department of Materials Science and Engineering, School of Molecular Science and Engineering, Vidyasirimedhi Institute of Science and Technology, Rayong 21210, Thailand

ARTICLE INFO

Article history:
Received 1 January 2016
Received in revised form 21 March 2016
Accepted 25 March 2016
Available online 29 March 2016

Keywords:
CO_2 hydrogenation
Catalyst composition
Nanocrystalline
Mixed oxide

ABSTRACT

CO_2 hydrogenation was carried out over a series of CuO–ZnO–ZrO_2 catalysts prepared via a reverse co-precipitation method. The influence of catalyst compositions on the physicochemical properties of the catalysts as well as their catalytic performance was investigated. The catalysts were characterized by means of N_2-sorption, X-ray diffraction (XRD), inductively coupled plasma optical emission spectrometry (ICP-OES), scanning electron microscopy (SEM), H_2-temperature programmed reduction (H_2-TPR), H_2 and CO_2 temperature-programmed desorption (H_2- and CO_2-TPD). The binary CuO–ZrO_2 (67:33) catalyst exhibits the highest methanol selectivity at all reaction temperature and its maximum yield of methanol (144.5 $g_{methanol}\,kg_{cat}^{-1}\,h^{-1}$) is achieved at 280 °C, owing to the strong basic sites and the largest CuO crystallite size. The addition of Zn to the binary CuO–ZrO_2 catalyst causes a higher Cu dispersion and an increased number of active sites for CO_2 and H_2 adsorption. However, the basic strength of the ternary CuO–ZnO–ZrO_2 catalysts is lower than the binary CuO–ZrO_2 catalyst which provides the maximum yield of methanol at lower reaction tempertures (240 and 250 °C), depending on the catalyst compositions. The optimum catalyst composition of Cu–Zn–Zr (38.2:28.6:33.2) gives a superior methanol productivity of 219.7 $g_{methanol}\,kg_{cat}^{-1}\,h^{-1}$ at 240 °C. The results demonstrate the possibility of controlling catalytic CO_2 hydrogenation via tuning the catalyst composition.

1. Introduction

Industrial revolution and population growth have always been associated with an extensive use of energy. Fossil fuels have been usually the most attractive energy sources because of high-energy concentration, which allows to store a large amount of energy in relatively small volumes. The combustion of fossil fuel is, however, the major source of carbon dioxide (CO_2), which is considered to be the main reason of climate change. Due to scarcity and cost of non-carbon energy sources, fossil fuels will continue to be the dominant source of energy for the next few decades, which is undoubtedly expected to substantially increase the CO_2 emissions [1,2]. CO_2 recycling as a feedstock to produce value added chemicals has received immense research interest as is one of the possible ways to maintain the carbon cycle [3–6]. Among several pathways the hydrogenation of CO_2 to methanol offers a feasible solution for both global warming problem and subtaintial demand of energy because methanol is a convenient liquid fuel and a potential chemical H_2 carrier for fuel cell applications [7,8], in addtion to a vital raw material for synthetic hydrocarbons and their products such as formaldehyde [9], biodiesel [10], acetic acid [11], gasoline [12], olefins [13] and dimethyl ether [14].

Methanol is commercially produced from syngas containing small amount of CO_2 over a Cu/ZnO/Al_2O_3 catalyst [15]. However, this catalyst suffers from a fast deactivation in CO_2-rich syngas feeds because the presence of large amount of water vapor byproduct could negatively affect the physical–chemical properties of the catalysts, e.g., an acceleration of Cu sintering, a partial oxidation of Cu to inactive CuO [16–18]. Alternatively a Cu/ZnO catalyst

* Corresponding author at: Department of Chemical Engineering, Faculty of Engineering, Kasetsart University, Bangkok 10900, Thailand.
E-mail address: fengttwi@ku.ac.th (T. Witoon).

http://dx.doi.org/10.1016/j.enconman.2016.03.075
0196-8904/

containing ZrO_2 has been found to be more active and stable than the conventional $Cu/ZnO/Al_2O_3$ catalyst [19–23]. In recent years, various methods have been developed to prepare $Cu/ZnO/ZrO_2$ catalysts with high copper surface, strong metal-support interactions, and homogeneous components. These properties of the catalysts have been proven to enhance the catalytic activity for methanol synthesis from CO_2 hydrogenation. Gao et al. prepared Cu–ZnO–ZrO_2 catalysts via a glycine–nitrate combustion method [24]. It was found that the catalyst prepared with the stochiometric amount of glycine was equal to 50% had the largest copper surface area, resulting in the highest yield of methanol. Li et al. found that the increase in calcination temperature of the Cu–ZnO–ZrO_2 caused a reduction of the methanol yield due to the enlargement of Cu particles [25]. The catalyst composition is another factor that strongly determines the copper surface area, homogeneity of components as well as the catalytic activity. A variety of CuO–ZnO–ZrO_2 catalyst formulations have been evaluated for CO_2 hydrogenation to methanol. Arena et al. [20] reported that the prepared Cu–ZnO–ZrO_2 catalysts with the Zn/Cu ratio in the range of 0.3–0.7 and constant ZrO_2 loading of ~44 wt% achieved a higher copper surface area and yield of methanol. Khassin et al. [26] studied the effect of Cu content of the binary Cu–Zn catalysts on the methanol synthesis from syngas containing CO_2. The optimum value of Cu content with respect to the catalytic activity was 40 mol%. In a recent report of Jeong and Suh [27], the role of ZrO_2 on the precipitation and formation of Cu–ZnO–ZrO_2 catalysts was examined in detail. They found that no incorporation of Zr^{4+} into the zincian malachite lattice, and ZrO_2 acted as nano-spacer to prevent the sintering of metallic copper particles upon reduction.

Herein, we have studied the effect of chemical compositions of CuO–ZnO–ZrO_2 catalysts in an attempt to develop more efficient catalyst formulations for methanol synthesis from CO_2 hydrogenation. The CuO–ZnO–ZrO_2 catalysts were prepared a reverse co-precipitation method, and characterized by bulk and surface techniques to determine structural and chemical features. The catalytic activity of the catalysts was evaluated in a fixed-bed reactor at different temperatures. The correlations between physicochemical characteristics and catalytic activity of the catalysts were also investigated.

2. Experimental

2.1. Catalyst preparation

A series of CuO–ZnO–ZrO_2 catalysts with different Zn/Cu ratios and ZrO_2 contains were prepared by a reverse co-precipitation method. A metal salts solution (ca. 100 mL) of $Cu(NO_3)_2{\cdot}3H_2O$, $Zn(NO_3)_2{\cdot}6H_2O$ and $ZrOCl_2{\cdot}8H_2O$ (Sigma Aldrich),contained a volume proportion corresponding to the final composition of the catalysts, was slowly added into a 0.1 M $NaHCO_3$ solution (500 mL) under stirring at room temperature. The pH of the solution was adjusted to 7.0 by adding 0.1 M $NaHCO_3$ solution. The mixture was heated to 80 °C under stirring, and kept constant at that temperature for 2 h. The precipitate was filtered and washed with 3000 mL deionized water. Subsequently, the obtained product was dried at 100 °C for 24 h and calcined at 350 °C for 2 h. The catalysts' relative notation is listed in Table 1.

2.2. Catalyst characterization

The BET surface area, pore size distribution and pore volume of all catalysts were determined by N_2-sorption measurement with a Quantachrome Autosorb-1C instrument at −196 °C. Prior to measurements, the samples were degassed at 200 °C for 24 h. Pore size distributions of the samples were determined from the adsorption branch of the isotherms in accordance with the Barrett–Joyner–Halenda (BJH) method. The specific BET (S_{BET}) was estimated for P/P_0 values to be between 0.05 and 0.30. The total pore volume was measured at a relative pressure (P/P_0) of 0.995.

The surface morphology of the studied catalysts was assessed with the application of a scanning electron microscope (SEM; JEOL JSM-7600F). The SEM measurement was taken at 20.0 kV. The samples were sputter–coated with gold prior to analysis.

X-ray diffraction (XRD) patterns of all catalysts were attained on a diffractometer (Bruker D8 Advance) with Cu-Kα radiation. The measurements were made at temperatures in a range of 15–75° on 2θ with a step size of 0.05°. The diffraction patterns were analyzed according to the Joint Committee on Powder Diffraction Standards (JCPDS).

Temperature-programmed reduction (TPR) experiments of the calcained catalysts were carried out by using TA instrument (SDT2960 Simultaneous DTA-TGA Universal 2000). Prior to the reduction, the catalyst (15 mg) was preheated in flowing N_2 at 350 °C for 15 min, and then cooled down to 120 °C. After that, TPR experiment was started with heating rate of 4 °C/min under continuous flow of 10%H_2/He.

H_2 temperature-programmed desorption (H_2-TPD) and CO_2 temperature-programmed desorption (CO_2-TPD) were performed by using the same apparatus for TPR measurements. For H_2-TPD experimental, the sample (15 mg) was reduced in-situ in flowing 10%H_2/He at 300 °C for 2 h. After that, the reduced catalyst was cooled down to 40 °C and then saturated in 10%H_2/He for 1 h, followed by purging with N_2 for 30 min in order to remove any physisorbed molecules. H_2-TPD experiment was then operated at 40–400 °C and heating rate of 5 °C/min in flowing N_2. The area under the first peak of H_2-TPD curve, caused by associative desorption of H_2 from copper metal surface, is used to determine the copper surface area [28,29] from the following equation:

$$\text{Cu surface area}\ \ (\text{m}^2/\text{g}) = \frac{(\text{A}) \times (\text{S}) \times (NA)}{\text{SD}_{\text{Cu}}} \tag{1}$$

where A is amount of H_2 desorbed from the first peak of H_2-TPD curve (mol H_2 g_{cat}^{-1}); S, stoichiometric factor, is 2; *NA* is Avogadro's number (6.022×10^{23} atoms mol^{-1}); SD_{Cu} is copper surface density (1.47×10^{19} atoms m^{-2}).

Copper dispersion, defined as the amount of H_2 desorbed from the first peak of H_2-TPD curve divided by the total copper atoms present in the catalyst, is calculated by using Eq. (2) [15,30].

$$\text{Cu dispersion}\ \ (\%) = \frac{(\text{A}) \times (\text{S}) \times (\text{MW}_{\text{Cu}})}{\text{Cu content}\ \ (\text{wt}\%)} \times 100 \tag{2}$$

where MW_{Cu} is molecular weight of atomic Cu (63.546 g mol^{-1}).

In case of CO_2-TPD experiment, the reduced catalyst was preheated at 400 °C for 30 min in order to clean surface of the catalyst from moisture and other adsorbed gas, and then cooled down to 40 °C. After that, the catalyst was saturated in flowing CO_2 for 1 h and followed by flushing in N_2 for 1 h. The CO_2-TPD measurement was then carried out at 40–400 °C and heating rate of 5 °C/min under continuous flow of N_2.

2.3. Catalytic activity test

CO_2 hydrogenation reaction was carried out in a fixed–bed stainless steel reactor (7.75 mm inner diameter). 0.25 g CuO–ZnO–ZrO_2 catalyst was diluted with 0.75 g inert silica sand (75–150 μm). The catalyst was reduced *in situ* under atmospheric pressure with flowing H_2 (60 mL/min) at 300 °C and a heating rate of 2 °C/min for 4 h. After the reduction, the temperature was cooled to 180 °C under flowing N_2; subsequently a flow of CO_2 and H_2 mixture (CO_2:H_2 molar ratio of 1:3) was fed through the

Table 1
Chemical compositions and textural properties of the CuO–ZnO–ZrO_2 catalyst.

Sample	Starting composition (mol %)			Zn/Cu ratio	Final composition (mol%)[a]			Zn/Cu ratio[a]	Cu surface area (m^2/g)	Cu dispersion (%)
	Cu	Zn	Zr		Cu	Zn	Zr			
CZZ-1	70	–	30	0	67.06	–	32.94	0	32.74	8.94
CZZ-2	60	10	30	0.17	59.58	9.32	31.1	0.16	33.36	10.19
CZZ-3	50	20	30	0.40	48.3	19.17	32.53	0.40	43.43	16.50
CZZ-4	40	30	30	0.75	38.15	28.61	33.24	0.75	52.87	25.16
CZZ-5	35	35	30	1.00	34.6	32.92	32.48	0.95	47.98	25.51
CZZ-6	30	40	30	1.33	27.47	40.08	32.45	1.45	46.97	31.49
CZZ-7	–	70	30	–	–	68.73	31.27	–	–	–
CZZ-8	57.14	42.86	–	0.75	56.99	43.01	–	0.75	35.08	9.64
CZZ-9	45.71	34.29	20	0.75	46.46	35.65	17.89	0.77	49.86	18.89
CZZ-10	34.28	25.72	40	0.75	32.43	22.89	44.68	0.71	32.92	19.69

[a] The chemical compositions of the catalyst were determined by ICP-OES technique.

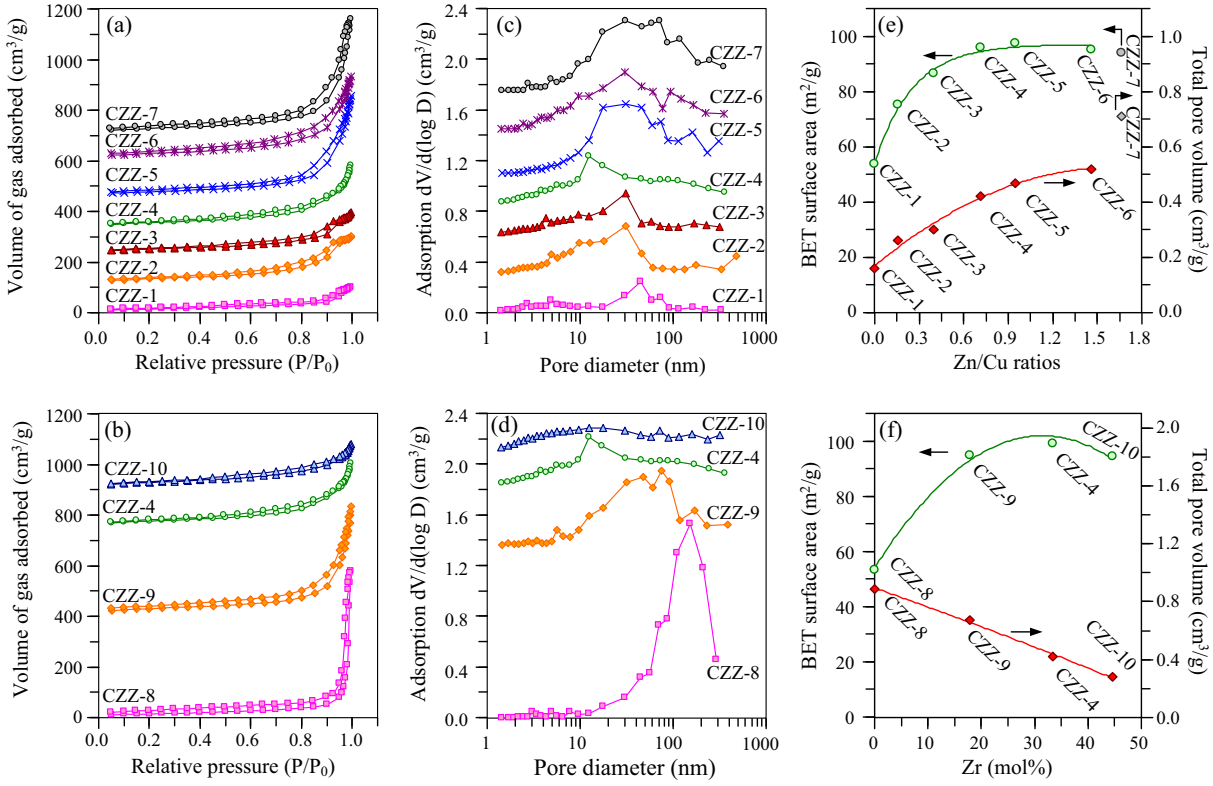

Fig. 1. N_2 adsorption–desorption isotherms (a and b), pore size distribution (c and d) and physical properties (e and f) of the CuO–ZnO–ZrO_2 catalysts prepared with different metal compositions. For clarity, the isotherm of CZZ-1, CZZ-2, CZZ-3, CZZ-4 (a), CZZ-5, CZZ-6, CZZ-7, CZZ-8, CZZ-9, CZZ-4 (b), and CZZ-10 is offset along the vertical axis for 0, 110, 230, 330, 450, 600, 700, 0, 400, 750 and 900 cm^3/g, respectively. The pore size distribution of CZZ-1, CZZ-2, CZZ-3, CZZ-4 (c), CZZ-5, CZZ-6, CZZ-7, CZZ-8, CZZ-9, CZZ-4 (d), and CZZ-10 is offset along the vertical axis for 0, 0.32, 0.63, 0.87, 1.1, 1.45, 1.75, 0, 1.35, 1.85 and 2.15 cm^3/g, respectively.

reactor. The flow rate of carbon dioxide and hydrogen was individually controlled by an electronic mass flow controller (Brooks SLA5850). The feed flow rate was set at 60 mL/min. The reactor pressure was slowly raised to 20 bars, and the reactor was heated to a variety of temperatures (220, 240, 250, 260 and 280 °C). The effluent gaseous products were analyzed by using gas chromatography. Analysis of H_2, CO, CO_2, and N_2 was performed using GC–2014 gas chromatography equipped with a thermal conductivity detector (TCD) and a Unibead-C column. Methanol and other hydrocarbon products were analyzed by using GC 8A equipped with a flame ionization detector (FID) and a Porapak-Q column. The activity-selectivity data were calculated by mass balance from an average of three independent measurements. The errors were within ±2%. CO_2 conversion, CH_3OH selectivity and space–time yield of methanol (grams methanol $catalyst^{-1}$ $time^{-1}$) are defined as follows:

$$CO_2\text{conversion}\ (\%) = \frac{(\text{moles methanol} + \text{moles CO}) \times 100}{\text{moles } CO_{2,in}} \quad (3)$$

$$CH_3OH\ \text{selectivity}\ (\%) = \frac{\text{moles } CH_3OH \times 100}{\text{moles } CH_3OH + \text{moles CO}} \quad (4)$$

$$\text{Space-time yield of methanol} = \frac{\text{moles methanol}}{\text{moles } CO_{2,in} \times \text{total amount of catalyst} \times MV} \times V_{CO_2} \times MW_{methanol} \quad (5)$$

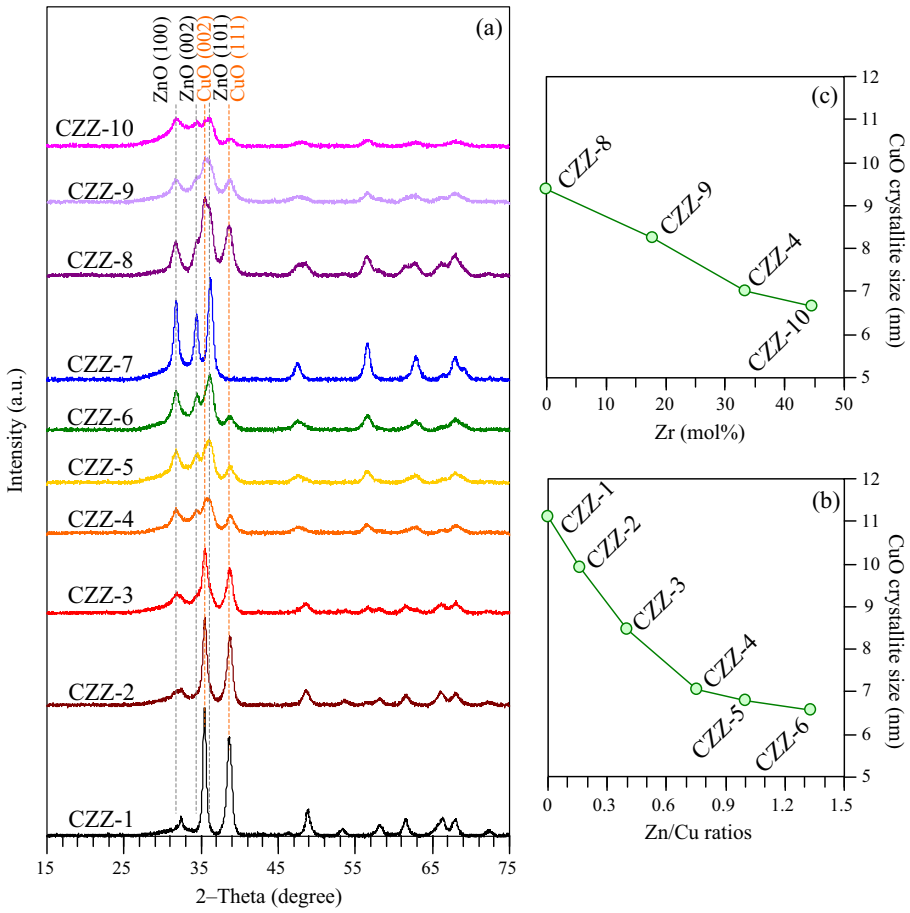

Fig. 2. XRD patterns (a) of the CuO–ZnO–ZrO_2 catalysts prepared with different metal compositions and corresponding CuO crystallite size calculated with the Scherrer Equation (b and c).

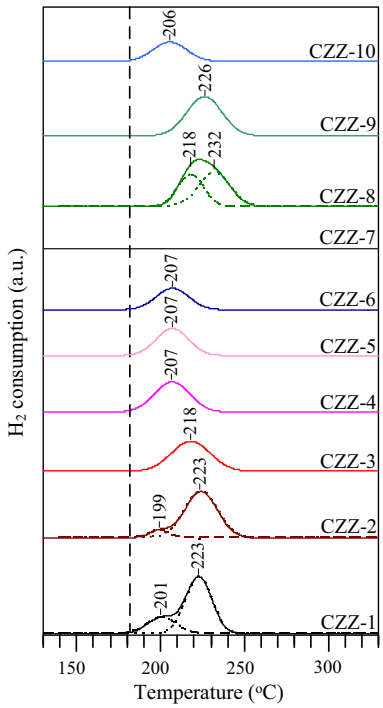

Fig. 3. H_2-TPR profiles of the CuO–ZnO–ZrO_2 catalysts prepared with different metal compositions.

where V_{CO_2} is the volumetric flow of CO_2 ($cm^3\ min^{-1}$), $MW_{methanol}$ is the molecular weight of methanol (grams mol^{-1}), and MV is the molar volume of ideal gas, 22,400 $cm^3\ mol^{-1}$.

3. Results and discussion

The nitrogen adsorption–desorption isotherms and the corresponding pore size distribution curves of the calcined catalysts are displayed in Fig. 1. As shown in Fig. 1a, the isotherm of CZZ-1 belongs to type IV with H3 hysteresis loop, which is the significant feature of the mesoporous materials with slit-shaped pores. However the isotherm is almost flat, indicating the low amount of pores due to a dense agglomeration of metal oxide particles. In comparison to the CZZ-1 sample the isotherm of CZZ-2, CZZ-3, and CZZ-4 is still type IV but the hysteresis loop is changed from H3 to H2, indicating the formation of pores in the form of interstices between closed-packed spherical particles. With yet higher Zn/Cu contents (CZZ-5 and CZZ-6), the type IV isotherm is no longer obtained and instead a type II isotherm is observed, which is indicative of the presence of macropores. Fig. 1c shows a broad pore size distribution with a mean pore size of 40 nm of the CZZ-1 sample, implying that the particle size of metal oxides are larger than 40 nm. Increasing the Zn/Cu ratio to 0.17–0.40 results in the lower mean pore size (~30 nm), indicating a reduction of particle size of metal oxides. The smallest mean pore size of 12.5 nm is obtained when the Zn/Cu ratio is increased to 0.75, suggesting that this ratio provides the homogeneous dispersion of metal oxides. With further increase of Zn/Cu ratio higher than 0.75, the mean pore size shifts toward larger pore size, suggesting that excessive amount of Zn

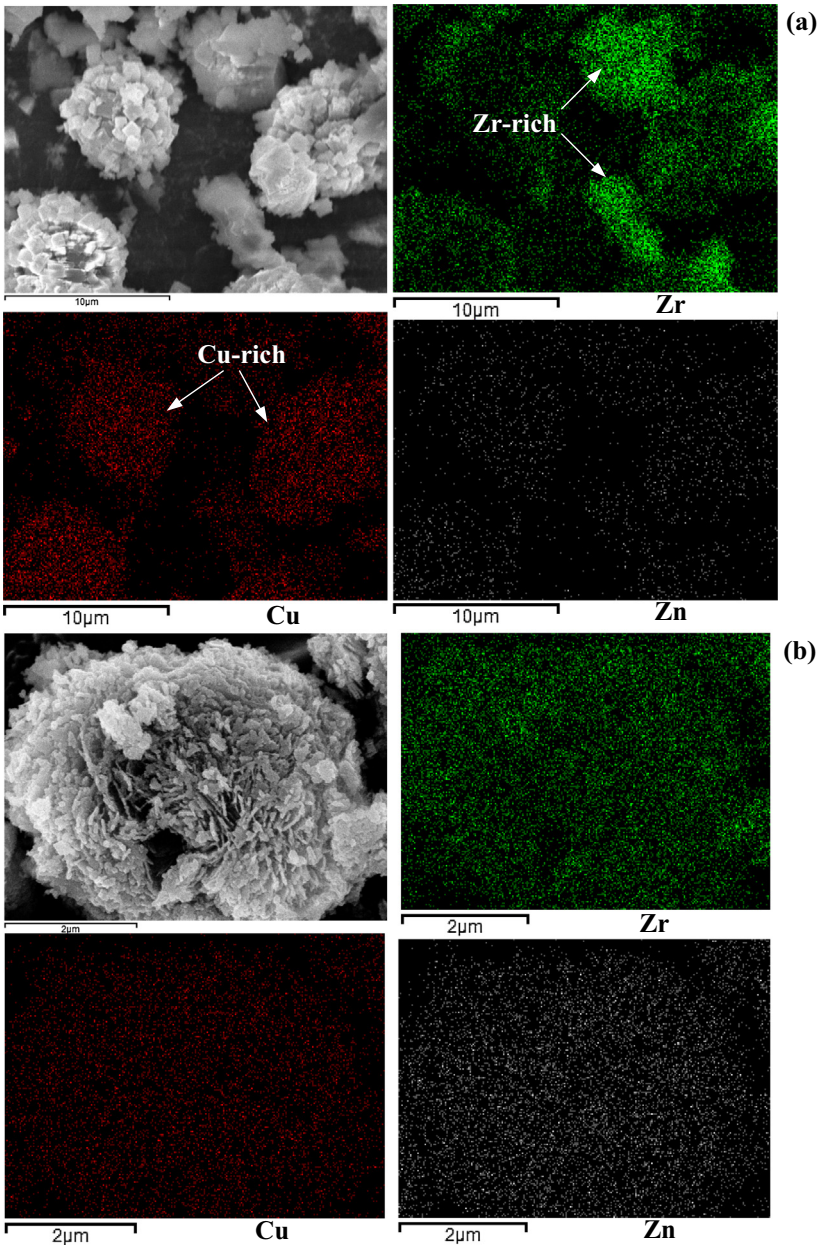

Fig. 4. SEM images of CZZ-2 (a) and CZZ-4 (b).

causes the increase of particle size of metal oxides. As shown in Fig. 1e, the pore volume of the catalysts is found to increase with increasing the Zn content (0.16–0.52 cm^3/g) while the BET surface area of the catalyst significantly increases from 53.18 to 96.12 m^2/g with Zn/Cu ratio ranging from 0 (CZZ-1) to 0.75 (CZZ-4) and then almost constant with further increasing Zn/Cu content.

The catalyst prepared in the absence of Zr (CZZ-8) exhibits type II isotherm (Fig. 1b) with very steep adsorption–desorption, suggesting the presence of the macropores with excellent uniformity in shape. Incorporating Zr (CZZ-9, CZZ-4 and CZZ-10) alters the shape of isotherm from type II to type IV with the shift of condensation step toward lower relative pressure, indicating a reduction of mean pore size. The results suggest different roles of Zn and Zr on the formation of final CuO–ZnO–ZrO_2 catalysts. As well documented, Cu and Zn can co-precipitate in the form of mixed metal hydroxyl carbonate phases such as malachite, zincian malachite and aurichalcite, depending on the nominal metals composition [31–33]. The co-precipitation of Cu and Zn can reduce the formation of individual CuO and ZnO particles and merge the Cu and Zn into a new phase, leading to the formation of the uniform structure as confirmed by the narrow pore size distribution of the CZZ-8 sample (Fig. 1d). The mean pore size distribution is found to shift toward lower pore size (Fig. 1d, CZZ-9, CZZ-4 and CZZ-10) after incorporation of Zr, indicating that the addition of Zr inhibits the growth/crystallization of the new phase resulting in the formation of smaller size of metal oxides. Moreover, Zr incorporates into the space of the new phase (Cu–Zn) as evidenced by a broader pore size distribution with a reduction of pore volume (Fig. 1f).

Fig. 2a shows experimental XRD patterns of the series of calcined Cu–ZnO–ZrO_2 catalysts. Only the diffraction peaks at 2θ values of 32.54°, 35.52°, 38.81°, 48.56° and 61.50° which are indexed to CuO diffractions of (1 1 0), (0 0 2), (1 1 1), (2 0 2) and (1 1 3) planes [34,35], respectively are observed for the catalyst prepared in the absence of Zn (CZZ-1). ZnO–ZrO_2 catalyst (CZZ-7) exhibits three major reflections of 1 0 0, 0 0 2 and 1 0 1 attributed to a hexagonal

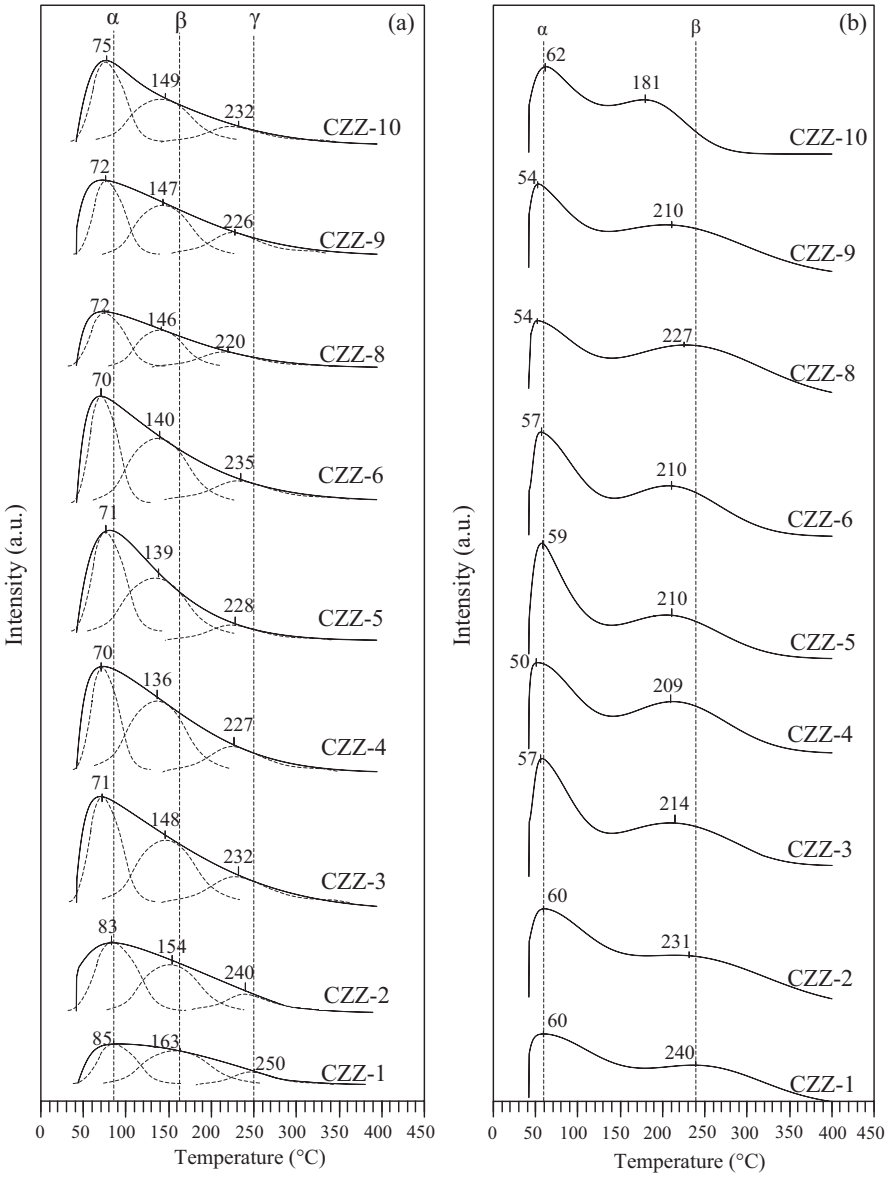

Fig. 5. CO_2-TPD (a) and H_2-TPD (b) profiles of the CuO–ZnO–ZrO_2 catalysts prepared with different metal compositions.

wurtzite ZnO [34,35]. With increasing Zn to Cu content from 0 (CZZ-1) to 0.75 (CZZ-4) a continuous increase in line width of the CuO 002 and 111 reflections is clearly visible. With further increasing Zn to Cu content at higher 0.75 (CZZ-5 and CZZ-6) the CuO 002 and 111 reflections exhibit a minimum in line width and intensity. The line width of the CuO 111 reflection is used to calculate the average CuO crystallite size with the Scherrer Equation; the result is shown in Fig. 2b. The CuO crystallite size dramatically decreases from 11.1 nm at Zn/Cu of 0 (CZZ-1) to 7.03 nm at Zn/Cu of 0.75 (CZZ-4). With further increasing Zn/Cu content from 0.75 (CZZ-4) to 1.45 (CZZ-6) the CuO crystallite size slightly decreases from 7.03 nm to 6.56 nm, suggesting that ZnO and CuO are well amalgamated. The ZnO crystallite site is unable to determine due to the overlapping with CuO reflections. Nevertheless the line width of the ZnO 100, 002 and 101 reflections gradually decreases with increasing Zn/Cu ratio implying the increase of ZnO crystallite size. In addition there is no diffraction peak of all samples (CZZ-1 to CZZ-7) showing crystal structure of ZrO_2, indicating that ZrO_2 is in an amorphous phase. The influence of Zr addition on the crystal structure of the catalysts was investigated at constant Zn/Cu ratio of 0.75. As shown in Fig. 2c, the CuO crystallite size slightly decreased from 9.38 nm to 6.65 nm with the increase of Zr content from 0 to 44.68 mol%.

The reducibility of copper species in the CuO–ZnO–ZrO_2 catalysts prepared at different ratios was investigated by H_2-TPR experiments, and the profiles are shown in Fig. 3. As there is no hydrogen consumption over the ZnO–ZrO_2 sample (CZZ-7), suggesting that ZnO and ZrO_2 are irreducible under the conditions applied in the analysis, the H_2-TPR profiles collected are exclusively indicative of copper surface. The catalysts prepared at Zn/Cu ratio of 0 (CZZ-1) and 0.16 (CZZ-2) exhibit at least two overlapped reduction peaks, suggesting that there are two kinds of reducible CuO species. The peak at lower temperature is attributed to the reduction of highly dispersed CuO species interacting with ZnO and ZrO_2 [35,36] while the higher temperature peak is related to the reduction of bulk-like CuO species [35,36]. SEM-EDS mapping analysis (Fig. 4) of the CZZ-2 sample revealed a segregation and formation of Zr-rich phase (green[1] dot) and Cu-rich phase

[1] For interpretation of color in Fig. 4, the reader is referred to the web version of this article.

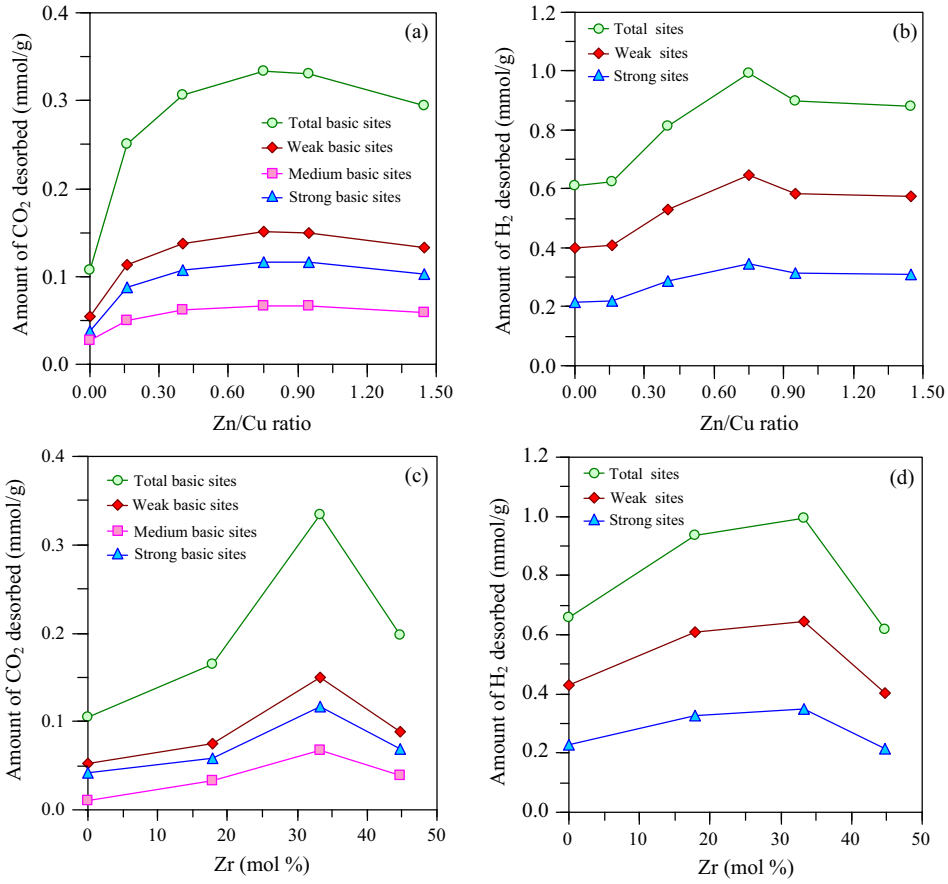

Fig. 6. Amount of CO_2 (a and c) and H_2 (b and d) desorbed of the CuO–ZnO–ZrO_2 catalysts prepared with different metal compositions.

(red dot) within the particles of the final catalyst endorsing the H_2-TPR results for the reduction of CuO at low and high temperature, respectively.

Only one symmetric peak appearing at 218 °C is observed with the catalyst prepared at Zn/Cu ratio of 0.4 (CZZ-3), suggesting the homogeneous dispersion of CuO. With increasing Zn/Cu ratio to 0.75 (CZZ-4), the position of reduction peak shifts toward lower temperature (207 °C), indicating a reduction of CuO particle size compared to that of the CZZ-3. SEM-EDS mapping analysis (Fig. 4) confirmed the homogeneous distribution of the copper element throughout the entire surface of the CZZ-4 sample. With further increasing Zn/Cu ratio to 0.95 (CZZ-5) and 1.45 (CZZ-6) the position of reduction peak slightly shifts toward higher temperature of 208 °C and 209 °C, respectively. This probably explains that the incorporation of excessive Zn increases interaction and obscures the surface of CuO making it even harder to be reduced. In the absence of Zr (CZZ-8), the H_2-TPR profile is asymmetry and it is therefore deconvoluted into two peaks, indicating that the CZZ-8 sample contains two different forms of CuO. Incorporation of 10% Zr (CZZ-9) results in a symmetry H_2-TPR profile, suggesting a homogeneous dispersion of CuO. Increasing Zr content to 25 (CZZ-4) and 40% (CZZ-10) exhibits the similar trend as the larger amount of Zr content is, the lower reduction temperature will be.

In order to study the effect of catalyst compositions on the surface adsorbed CO_2 and H_2, CO_2-TPD and H_2-TPD were performed; the results are shown in Fig. 5a and b, respectively. The CO_2-TPD profile of all catalysts exhibits a broad peak ranging 40–400 °C, suggesting that CO_2 is adsorbed on the surface of the catalysts with different strengths. Since the catalytic activity for methanol synthesis from CO_2 hydrogenation depends on both the number and strength of active sites, an attempt has been made to elucidate the type of active sites for adsorbed CO_2 present on each sample. For this, the CO_2-TPD profiles were deconvoluted into α, β and γ peaks, corresponding to weak, medium and strong basicity, respectively. The weakly basic sites were related to hydroxyl groups, moderately basic sites could be assigned to metal–oxygen pairs, and strongly basic sites were associated with low-coordination oxygen atoms [37,38]. The α, β and γ peaks of the catalyst prepared in the absence of Zn (CZZ-1) are found at 85, 163 and 250 °C, respectively. All desorption peaks are found to shift toward lower region when incorporating Zn into the CuO–ZrO_2 catalysts (CZZ-2, CZZ-3, CZZ-4, CZZ-5 and CZZ-6), which is indicative of the lower interaction between CO_2 molecules and the surface of the catalysts. In contrast to the incorporation of Zn, the interaction between CO_2 and the catalyst surface becomes stronger after the addition of Zr into the CuO–ZnO catalyst (CZZ-8, CZZ-9, CZZ-4, CZZ-10). However, the area under the CO_2-TPD curve of the ternary catalysts is found to be larger than that of the binary catalysts, CuO–ZrO_2 and CuO–ZnO, indicating that the amount of adsorbed CO_2 has been increased.

The H_2-TPD profile of the CZZ-1 exhibits two main hydrogen desorption peaks at around 60 and 240 °C. The first peak at low temperature is attributed to the chemisorbed hydrogen on the highly dispersed copper nanoparticles, which related to number of active sites for dissociation of hydrogen molecule to hydrogen atoms [28,29,39–42]. The second peak can be derived from the hydrogen atom on the surface of metal oxides caused by the spillover of hydrogen from the copper surface [42,43]. The position for the former peak of all catalysts was unchanged after Zn addition (CZZ-2, CZZ-3, CZZ-4, CZZ-5 and CZZ-6), while the latter peak is found to gradually shift toward lower temperature with

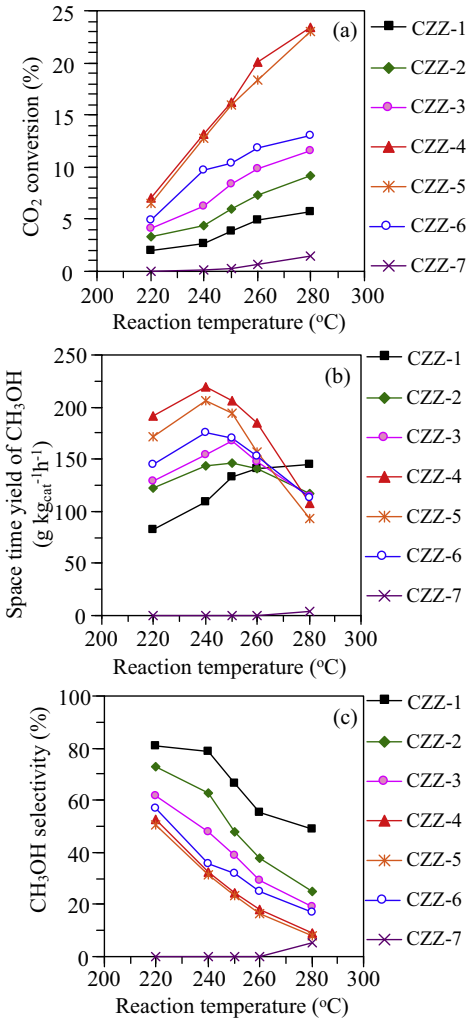

Fig. 7. CO_2 conversion (a), space time yield of methanol (b) and CH_3OH selectivity (c) of the CuO–ZnO–ZrO_2 catalysts prepared with different Zn/Cu ratios.

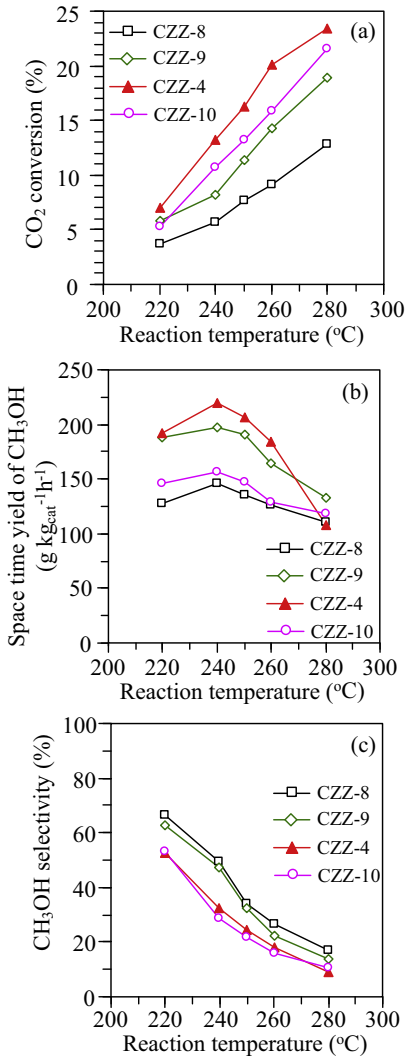

Fig. 8. CO_2 conversion (a), space time yield of methanol (b) and CH_3OH selectivity (c) of the CuO–ZnO–ZrO_2 catalysts prepared with different Zr contents.

increasing Zn/Cu content, indicating a lower adsorption strength of H atom on the surface of metal oxides. The addition of Zr into the CuO–ZnO catalyst follows a trend analogous to that of Zn addition (CZZ-8, CZZ-9, CZZ-4 and CZZ-10).

Fig. 6a–d shows the quantitative data of the amounts of desorbed CO_2 and H_2 of the catalysts prepared with different metal compositions. As shown in Fig. 6a, the total amount of desorbed CO_2 was only 0.11 mmol/g for the catalyst prepared in the absence of Zn (CZZ-1). Incorporating Zn into the Cu/ZrO_2 catalyst at Zn/Cu ratio of 0.16 (CZZ-2) and 0.4 (CZZ-3) extremely increased the total amount of desorbed CO_2 to 0.25 and 0.30 mmol/g, respectively. With a yet higher Zn/Cu ratio, the total amount of desorbed CO_2 remained increased with its maximum (0.33 mmol/g) at Zn/Cu ratio of 0.75. After that the total amount of desorbed CO_2 slightly declined to 0.29 mmol/g at Zn/Cu ratio of 1.45. The amount of desorbed CO_2 correlates to the BET surface area of the catalysts, suggesting that a well dispersion of ternary metal oxides (CuO–ZnO–ZrO_2) is a vital factor determining the number of active sites for CO_2 adsorption.

As shown in Fig. 6b, the binary CuO–ZrO_2 catalyst (CZZ-1) exhibited the lowest amount of H_2 desorbed from the weak site (0.40 mmol/g), which was in good agreement with the XRD and H_2-TPR results. The amount of H_2 desorbed from the weak site was found to increase with increasing Zn/Cu ratio and the highest amount of H_2 desorbed from the weak site was obtained at Zn/Cu ratio of 0.75 (CZZ-4). It is noteworthy that the amount of H_2 desorbed from the weak site of the CZZ-5 and CZZ-6 catalysts is lower than the CZZ-4 catalyst despite the Cu dispersion (Table 1) of the CZZ-5 and CZZ-6 is higher. This suggests that the amount of H_2 desorbed from weak site is a trade-off between the Cu contain and the Cu dispersion. Incorporation of Zn also increases the number of H_2 desorbed from strong site, indicating the enhancement of hydrogen storage on the surface of metal oxides. Regarding to the catalysts prepared with different Zr contents (Fig. 6c and d), the total number of desorbed CO_2 and H_2 exhibits a volcano-shaped trend with respect to the Zr content and its optimum content is 33.24 mol%.

CO_2 hydrogenation was tested over CuO–ZnO–ZrO_2 catalysts in a fixed-bed reactor at 20 bars. The catalytic activities were determined after 3 h on stream at the same GSHV. For all catalysts, methanol and CO were found to be the major products. The catalytic performance of the CuO–ZnO–ZrO_2 catalysts prepared with different chemical composition is shown in Fig. 7 in terms of CO_2 conversion (Fig. 7a), space time yield of methanol (Fig. 7b) and CH_3OH selectivity (Fig. 7c).

CO_2 conversion (Fig. 7a) over all catalysts increased monotonically with ascending reaction temperature. Comparing at identical reaction temperature, the CO_2 conversion greatly increased with increasing Zn/Cu ratio, and the maximum CO_2 conversion was

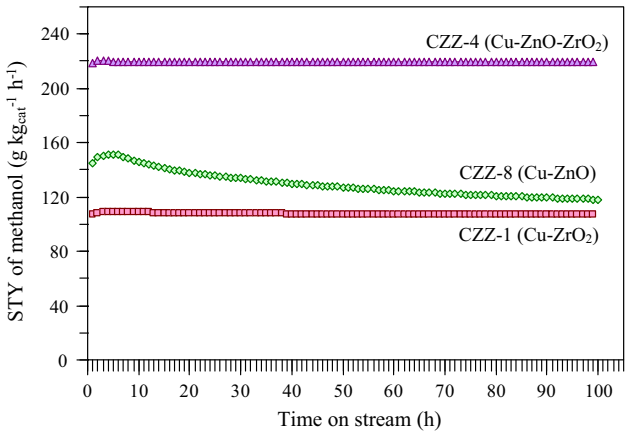

Fig. 9. Space-time yield of methanol as a function of time-on-stream of CZZ-1 (Cu–ZrO_2), CZZ-4 (Cu–ZnO–ZrO_2) and CZZ-8 (Cu–ZnO). Reaction conditions: T = 240 °C, P = 2 MPa, flow rate = 60 mL min^{-1}, the amount of catalyst = 0.25 g.

obtained with the catalyst prepared with Zn/Cu ratio of 0.75. Further increase of Zn/Cu ratio to 0.95 and 1.45 exhibited a decreasing trend in CO_2 conversion but still exceed that of the catalyst prepared with Zn/Cu of 0.4. Note that the catalyst prepared in the absence of Cu (CZZ-7) was almost inactive for CO_2 hydrogenation; the maximum CO_2 conversion was only 1.44% at a reaction temperature of 280 °C.

The CZZ-1 catalyst showed a monotonic increase in space time yield of methanol with increasing reaction temperature (Fig. 7b). The maximum yield of methanol for the CZZ-1 catalyst, 144.5 $g_{methanol}$ kg_{cat}^{-1} h^{-1}, was obtained at 280 °C. The maximum yield of methanol was achieved at a lower reaction temperature as the Zn/Cu ratio is increased; 250 °C at Zn/Cu ratio of 0.16–0.4 and 240°C at Zn/Cu ratio of 0.75–1.45. This is in harmony with the CO_2-TPD results as the strengths between CO_2 molecules (bicarbonate species) and the catalyst surface become gradually weaker when the catalysts are prepared with higher Zn/Cu ratio.

The strength between CO_2 molecules and the catalyst surface play a vital role on the methanol selectivity; the methanol selectivity decreases with decreasing the strength between CO_2 molecules and the catalyst surface (see Figs. 5a and 7c). The generally accepted mechanism has shown that the formation of methanol from CO_2 hydrogenation requires coadsorbed species on the catalyst surface [42,44]. CO_2 adsorbed on the surface of ZnO and ZrO_2 forms a bicarbonate species, while H_2 molecule is dissociatively adsorbed on the metallic Cu existing as copper–hydride species (Cu–H). The bicarbonate species is hydrogenated to produce formate intermediate species via spillover of atomic hydrogen from the metallic copper surface. The stepwise hydrogenation of formate intermediate species leads to the formation of methanol [38]. Alternatively, CO is formed from the decomposition of formate intermediate species [38]. Our result suggests that the strong interaction of bicarbonate species with the catalyst surface is essential to inhibit the decomposition of formate intermediate species. Although the CZZ-1 catalyst achieves the highest methanol selectivity, the CO_2 conversion and space yield of methanol are relatively low compared to those of the CZZ-4 catalyst which is attributed to the large number of active sites for CO_2 and H_2 adsorption of the CZZ-4 catalyst as indicated by CO_2- and H_2-TPD results.

Because of the superiority of the CZZ-4 catalyst (Zn/Cu = 0.75) in terms of the space time yield of methanol as described above, three CuO–ZnO–ZrO_2 catalysts were prepared at different Zr contents while the ratio of Zn/Cu was kept at 0.75. The results of catalytic activity in terms of CO_2 conversion, yield of methanol and methanol selectivity are shown in Fig. 8. Unlike the binary CuO–ZrO_2 catalyst, the binary CuO–ZnO catalyst achieved the maximum yield of methanol at a lower reaction temperature (260 °C), confirming that the strength between bicarbonate species and the catalyst surface is an important parameter promoting the formation of methanol. After the Zr addition, the activities of ternary CuO–ZnO–ZrO_2 catalysts were markedly improved because of the reduced CuO crystallite size and increased CO_2 and H_2 uptakes as compared with those of the binary CuO–ZnO catalyst (CZZ-8). The catalyst prepared with 33.24 mol% Zr (CZZ-4) achieved the highest yield of methanol of 219.7 $g_{methanol}$ kg_{cat}^{-1} h^{-1} at 240 °C.

The methanol selectivity of all catalysts was found to significantly decrease with increasing temperature. Although the addition of Zr increased the strength between CO_2 molecules and the catalyst surface, the higher methanol selectivity was observed for the catalysts prepared with low Zr content (0–17.89 mol%), suggesting that not only the basic strength but also other factors affects the methanol selectivity. Previous works has shown that these is another pathway for the formation of CO, that is, the redox mechanism for the reverse water–gas shift reaction at which the reaction only proceeds over the copper nanoparticles [3]. Karelovic and Ruiz [45] studied the role of copper particle size on the methanol synthesis from CO_2 hydrogenation. They found that the rate of methanol formation expressed per mole surface copper was independent of copper particle size, whereas smaller copper particle was more active for reverse water–gas shift reaction. This can be the reason why the catalysts prepared with low Zr content (0–17.89 mol%) having larger CuO crystallite size exhibited the higher selectivity toward methanol formation.

Fig. 9 shows the space–time yield (STY) versus the time-on-stream of methanol over three catalysts: CZZ-1 (Cu–ZrO_2), CZZ-4 (Cu–ZnO–ZrO_2) and CZZ-8 (Cu–ZnO). For the binary catalyst system, the CZZ-8 catalyst is more active than the CZZ-1 catalyst as the STY of the CZZ-8 is ca. 1.38 times higher than that of the CZZ-1. However, after 100 h of a time-on-stream experiment, the CZZ-8 catalyst loses approximately 18.5% of its initial activity while the CZZ-1 catalyst shows a constant STY of methanol. The fast deactivation of the CZZ-8 (Cu–ZnO) could be due to its low thermal stability [16,46]. The CZZ-4 (Cu–ZnO–ZrO_2) catalyst exhibits the highest STY of methanol of 219.7 $g_{methanol}$ kg_{cat}^{-1} h^{-1} and its activity

Table 2
Comparison of catalytic performance of CuO–ZnO–ZrO_2 catalysts and other catalysts for the methanol synthesis from CO_2 hydrogenation.

Catalyst	Operating conditions		CO_2 conversion (%)	CH_3OH selectivity (%)	Space-time yield of CH_3OH (g kg_{cat}^{-1} h^{-1})	Refs.
	Temperature (°C)	Pressure (bar)				
$Cu/ZnO/Al_2O_3$	240	30	16.2	63.8	130	[18]
In_2O_3	270	40	1.1	54.9	25	[47]
In_2O_3	330	40	7.1	39.7	118	[47]
Cu/Zn/Zr/Al	230	30	23.2	60.3	120	[48]
Pd(0.34)-Cu/SiO_2	250	41	6.6	34	35.8	[49]
La–Mn–Zn–Cu–O	270	50	13.1	54.5	100	[50]
Cu/ZrO_2	240	30	5.1	57.8	76.3	[51]
Cu–ZrO_2	240	20	2.7	78.8	108.9	This work
Cu–ZnO–ZrO_2	240	20	13.2	32.3	219.7	This work

is quite stable during the 100 h time-on-stream. The remarkable improvement of the activity and stability of the methanol catalyst can be attributed to the homogeneous precipitation of ternary oxides which not only enhances the copper surface area but also prevents the sintering of copper nanoparticles. For the relative comparison of the catalyst performances, the CO_2 conversion, CH_3OH selectivity and space–time yield of CH_3OH of other previous work are listed in Table 2 [18,47–51]. Despite the fact that the Cu–ZnO–ZrO_2 catalyst is operated at a lower pressure, it achieves the highest STY of methanol. The results demonstrate that the Cu–ZnO–ZrO_2 catalyst can be considered for practical application.

4. Conclusions

This work discusses the influence of Zn/Cu ratio and ZrO_2 content of CuO–ZnO–ZrO_2 catalysts on the physicochemical properties and the catalytic performance of the catalysts in CO_2 hydrogenation. The microstructure of the catalyst becomes homogeneous when the Zn/Cu ratio is higher than 0.4. Increasing Zn/Cu ratio provides a better inter-dispersion of metal components (Cu, Zn and Zr), leading to a smaller CuO crystallite size, a higher porosity and Cu dispersion of the catalysts as well as an enhancement of number of active sites for CO_2 and H_2 desorption. The increase of Zn/Cu ratio also causes a weaker interaction between CO_2 molecules and the catalyst surface, resulting in a lower methanol selectivity compared to the binary CuO–ZrO_2 catalyst. However, the weaker interaction between CO_2 molecules and the catalyst surface is found to promote the formation of methanol at a lower reaction temperature. The optimum catalyst composition of Cu–Zn–Zr (38.2:28.6:33.2) exhibits a superior performance in terms of CO_2 conversion and space–time yield of methanol.

Acknowledgements

This work was financially supported by the Thailand Research Fund (Grant No. TRG5780258), the Center of Excellence on Petrochemical and Materials Technology (PETROMAT), the National Research University Project of Thailand (NRU), the Nanotechnology Center (NANOTEC), NSTDA, Ministry of Science and Technology, Thailand through its program of Center of Excellence Network, and the Kasetsart University Research and Development Institute (KURDI). The authors would like to thank the support from the Synchrotron Light Research Institute (BL5.2: SUT-NANOTEC-SLRI XAS).

References

[1] Nicoletti G, Arcuri N, Nicoletti G, Bruno R. A technical and environmental comparison between hydrogen and some fossil fuels. Energy Convers Manage 2015;89:205–13.
[2] Lin B, Ouyang X. A revisit of fossil-fuel subsidies in China: challenges and opportunities. Energy Convers Manage 2014;82:124–34.
[3] Wang W, Wang S, Ma X, Gong J. Recent advances in catalytic hydrogenation of carbon dioxide. Chem Soc Rev 2011;40:3703–27.
[4] Goeppert A, Czaun M, Jones JP, Prakash GKS, Olah GA. Recycling of carbon dioxide to methanol and derived products – closing the loop. Chem Soc Rev 2014;43:7995–8048.
[5] Meylan FD, Moreau V, Erkman S. CO_2 utilization in the perspective of industrial ecology, an overview. J CO_2 Util 2015;12:101–8.
[6] Witoon T, Bumrungsalee S, Chareonpanich M, Limtrakul J. Effect of hierarchical meso–macroporous alumina-supported copper catalyst for methanol synthesis from CO_2 hydrogenation. Energy Convers Manage 2015;103:886–94.
[7] Das S, Kumar P, Dutta K, Kundu PP. Partial sulfonation of PVdF-*co*-HFP: a preliminary study and characterization for application in direct methanol fuel cell. Appl Energy 2014;113:169–77.
[8] Kreuer KD. On the development of proton conducting polymer membranes for hydrogen and methanol fuel cells. J Membr Sci 2001;185:29–39.
[9] Zhao Y, Qin Z, Wang G, Dong M, Huang L, Wu Z, et al. Catalytic performance of V_2O_5/ZrO_2–Al_2O_3 for methanol oxidation. Fuel 2013;104:22–7.
[10] Witoon T, Bumrungsalee S, Vathavanichkul P, Palitsakun S, Saisriyoot M, Faungnawakij K. Biodiesel production from transesterification of palm oil with methanol over CaO supported on bimodal meso-macroporous silica catalyst. Bioresour Technol 2015;156:329–34.
[11] Singh AD, Krase NW. Synthesis of acetic acid from methanol and carbon monoxide. Ind Eng Chem 1935;27:909–14.
[12] Li J, Miao P, Li Z, He T, Han D, Wu J, et al. Hydrothermal synthesis of nanocrystalline H[F, Al]ZSM-5 zeolites for conversion of methanol to gasoline. Energy Convers Manage 2015;93:259–66.
[13] Sedighi M, Towfighi J. Methanol conversion over SAPO-34 catalysts; systematic study of temperature, space-time, and initial gel composition on product distribution and stability. Fuel 2015;153:382–92.
[14] Elamin MM, Muraza O, Malaibari Z, Ba H, Nhut JM, Pham-Huu C. Microwave assisted growth of SAPO-34 on β-SiC foams for methanol dehydration to dimethyl ether. Chem Eng J 2015;274:113–22.
[15] Bartholomew CH, Farrauto RJ. Hydrogen production and synthesis gas reactions. In: Bartholomew CH, Farrauto RJ, editors. Fundamentals of industrial catalytic process. New York: John Wiley & Sons, Inc.; 2006. p. 339–486.
[16] Kurtz M, Wilmer H, Genger T, Hinrichsen O, Muhler M. Deactivation of supported copper catalysts for methanol synthesis. Catal Lett 2003;86:77–80.
[17] Zhang Y, Sun Q, Deng J, Wu D, Chen S. A highly activity Cu/ZnO/Al_2O_3 catalyst for methanol synthesis: Preparation and catalytic properties. Appl Catal A: Gen 1997;158:105–20.
[18] Lei H, Hou Z, Xie J. Hydrogenation of CO_2 to CH_3OH over CuO/ZnO/Al_2O_3 catalysts prepared via a solvent-free routine. Fuel 2016;164:191–8.
[19] Sloczyński J, Grabowski R, Kozlowska A, Lachowska M, Skrzypek J. Methanol synthesis from CO_2 and H_2 on Cu/ZnO/Al_2O_3–ZrO_2 catalysts Catalytic activity and adsorption of reactants. Polish J Chem 2001;75:733–42.
[20] Arena F, Barbera K, Italiano G, Bonura G, Spadaro L, Frusteri F. Synthesis, characterization and activity pattern of Cu–ZnO/ZrO_2 catalysts in the hydrogenation of carbon dioxide to methanol. J Catal 2007;249:185–94.
[21] Bonura G, Cordaro M, Cannilla C, Arena F, Frusteri F. The changing nature of the active site of Cu–Zn–Zr catalysts for the CO_2 hydrogenation reaction to methanol. Appl Catal B: Environ 2014;152–153:152–61.
[22] Saito M, Fujitani T, Takeuchi M, Watanabe T. Development of copper/zinc oxide-based multicomponent catalysts for methanol synthesis from carbon dioxide and hydrogen. Appl Catal A: Gen 1996;138:311–8.
[23] Witoon T, Permsirivanich T, Kanjanasoontorn N, Akkaraphataworn C, Seubsai A, Faungnawakij K, et al. Direct synthesis of dimethyl ether from CO_2 hydrogenation over Cu–ZnO–ZrO_2/SO_4^{2-}–ZrO_2 hybrid catalysts: effects of sulfur-to-zirconia ratios. Catal Sci Technol 2015;5:2347–57.
[24] Guo X, Mao D, Lu G, Wang S, Wu G. Glycine-nitrate combustion synthesis of CuO–ZnO–ZrO_2 catalysts for methanol synthesis from CO_2 hydrogenation. J Catal 2010;271:178–85.
[25] Li L, Mao D, Yu J, GuO X. Highly selective hydrogenation CO_2 to methanol over CuO–ZnO–ZrO_2 catalysts prepared by a surfactant-assisted co-precipitation method. J Power Source 2015;279:394–404.
[26] Khassin AA, Pelipenko VV, Minyukova TP, Zaikovskii VI, Kochubey DI, Yurieva TM. Planar defect of the nano-structured zinc oxide as the site for stabilization of the copper active species in Cu/ZnO catalysts. Catal Today 2006;112:143–7.
[27] Jeong C, Suh YW. Role of ZrO_2 in Cu/Zn/ZrO_2 catalysts prepared from the precipitated Cu/Zn/Zr precursors. Catal Today 2016;265:254–63.
[28] Muhler M, Nielsen LP, Törnqvist E, Clausen BS, Topsøe H. Temperature-programmed desorption of H_2 as a tool to determine metal surface areas of Cu catalysts. Catal Lett 1992;14:241–9.
[29] Genger T, Hinrichsen O, Muhler M. The temperature-programmed desorption of hydrogen from copper surfaces. Catal Lett 1999;59:137–41.
[30] Natesakhawat S, Lekse JW, Baltrus JP, Ohodnicki Jr PR, Howard BH, Deng X, et al. Active sites and structure-activity relationships of copper-based catalysts for carbon dioxide hydrogenation to methanol. ACS Catal 2012;2:1667–76.
[31] Behrens M, Brennecke D, Girgsdies F, Kißner S, Trunschke A, Nasrudin N, et al. Understanding the complexity of a catalyst synthesis: Co-precipitation of mixed Cu, Zn, Al hydroxycarbonate precursors for Cu/ZnO/Al2O3 catalysts investigated by titration experiments. Appl Catal A: Gen 2011;392:93–102.
[32] Fujitani T, Nakamura J. The effect of ZnO in methanol synthesis catalysts on Cu dispersion and the specific activity. Catal Lett 1998;56:119–24.
[33] Behrens M. Meso- and nano-structuring of industrial Cu/ZnO/(Al_2O_3) catalysts. J Catal 2009;267:24–9.
[34] Witoon T, Permsirivanich T, Chareonpanich M. Chitosan-assisted combustion synthesis of CuO–ZnO nanocomposites: effect of pH and chitosan concentration. Ceram Int 2013;39:3371–5.
[35] Witoon T, Permsirivanich T, Donphai W, Jaree A, Chareonpanich M. CO_2 hydrogenation to methanol over Cu/ZnO nanocatalysts prepared via a chitosan-assisted co-precipitation method. Fuel Process Technol 2013;116:72–8.
[36] Zhang Y, Fei J, Yu Y, Zheng X. Methanol synthesis from CO_2 hydrogenation over Cu based catalyst supported on zirconia modified γ-Al_2O_3. Energy Convers Manage 2006;47:3360–7.
[37] Tichit D, Das N, Coq B, Durand R. Preparation of Zr-containing layered double hydroxides and characterization of the acido-basic properties of their mixed oxides. Chem Mater 2002;14:1530–8.
[38] Gao P, Li F, Zhan H, Zhao N, Xiao F, Wei W, et al. Influence of Zr on the performance of Cu/Zn/Al/Zr catalysts via hydrotalcite-like precursors for CO_2 hydrogenation to methanol. J Catal 2013;298:51–60.
[39] Natesakhawat S, Ohodnicki Jr PR, Howard BH, Lekse JW, Baltrus JP, Matranga C. Top Catal 2013;56:1752–63.

[40] Tabatabaei J, Sakakini BH, Watson MJ, Waugh KC. The detailed kinetics of the desorption of hydrogen from polycrystalline copper catalysts. Catal Lett 1999;59:143–9.
[41] Dan M, Mihet M, Tasnadi-Asztalos Z, Imre-Lucaci A, Katona G, Lazar MD. Hydrogen production by ethanol steam reforming on nickel catalysts: effect of support modification by CeO_2 and La_2O_3. Fuel 2015;147:260–8.
[42] Guo X, Mao D, Lu G, Wang S, Wu G. The influence of La doping on the catalytic behavior of Cu/ZrO_2 for methanol synthesis from CO_2 hydrogenation. J Mol Catal A: Chem 2011;345:60–8.
[43] Bianchi D, Gass JL, Khalfallah M, Teichner SJ. Intermediate species on zirconia supported methanol aerogel catalysts: I. State of the catalyst surface before and after the adsorption of hydrogen. Appl Catal A: Gen 1993;101:297–315.
[44] Arena F, Italiano G, Barbera K, Bordiga S, Bonura G, Spadaro L, et al. Solid-state interactions, adsorption sites and functionality of Cu–ZnO/ZrO_2 catalysts in the CO_2 hydrogenation to CH_3OH. Appl Catal A: Gen 2008;350:16–23.
[45] Karelovic A, Ruiz P. The role of copper particle size in low pressure methanol synthesis via CO_2 hydrogenation over Cu/ZnO catalysts. Catal Sci Technol 2015;5:869–81.
[46] Szizybalski A, Girgsdies F, Rabis A, Wang Y, Niederberger M, Ressler T. In situ investigations of structure-activity relationships of a Cu/ZrO_2 catalyst for the steam reforming of methanol. J Catal 2005;233:297–307.
[47] Sun K, Fan Z, Ye J, Yan J, Ge Q, Li Y, et al. Hydrogenation of CO_2 to methanol over In_2O_3 catalyst. J CO_2 Util 2015;12:1–6.
[48] Li C, Yuan X, Fujimoto K. Development of highly stable catalyst for methanol synthesis from carbon dioxide. Appl Catal A: Gen 2014;469:306–11.
[49] Jiang X, Koizumi N, Guo X, Song C. Bimetallic Pd–Cu catalysts for selective CO_2 hydrogenation to methanol. Appl Catal B: Environ 2015;170–171:173–85.
[50] Zhan H, Li F, Xin C, Zhao N, Xiao F, Wei W, et al. Performance of the La–Mn–Zn–Cu–O based perovskite precursors for methanol synthesis from CO_2 hydrogenation. Catal Lett 2015;145:1177–85.
[51] Witoon T, Chalorngtham J, Dumrongbunditkul P, Chareonpanich M, Limtrakul J. CO_2 hydrogenation to methanol over Cu/ZrO_2 catalysts: effects of zirconia phases 2016;293:327–36.

เรื่องที่ 2

Thongthai Witoon*, Jiraporn Chalorngtham, Porntipar Dumrongbunditkul, Metta Chareonpanich, Jumras Limtrakul, CO_2 hydrogenation to methanol over Cu/ZrO_2 catalysts: effects of zirconia phases, Chemical Engineering Journal 293 (2016) 327–336. (IF 2015 = 5.310).

Chemical Engineering Journal 293 (2016) 327–336

Contents lists available at ScienceDirect

Chemical Engineering Journal

journal homepage: www.elsevier.com/locate/cej

CO_2 hydrogenation to methanol over Cu/ZrO_2 catalysts: Effects of zirconia phases

Thongthai Witoon [a,b,c,*], Jiraporn Chalorngtham [a], Porntipar Dumrongbunditkul [a], Metta Chareonpanich [a,b,c], Jumras Limtrakul [b,c,d]

[a] Center of Excellence on Petrochemical and Materials Technology, Department of Chemical Engineering, Faculty of Engineering, Kasetsart University, Bangkok 10900, Thailand
[b] Center for Advanced Studies in Nanotechnology and Its Applications in Chemical Food and Agricultural Industries, Kasetsart University, Bangkok 10900, Thailand
[c] NANOTEC-KU-Center of Excellence on Nanoscale Materials Design for Green Nanotechnology, Kasetsart University, Bangkok 10900, Thailand
[d] Department of Materials Science and Engineering, School of Molecular Science and Engineering, Vidyasirimedhi Institute of Science and Technology, Rayong 21210, Thailand

HIGHLIGHTS

- CO_2 hydrogenation to methanol over a-ZrO_2, t-ZrO_2 and m-ZrO_2 supported Cu catalysts.
- Cu–ZrO_2 interaction of Cu/a-ZrO_2 and Cu/t-ZrO_2 is stronger than Cu/m-ZrO_2.
- Cu/a-ZrO_2 catalyst shows a high CO_2 conversion.
- Cu/t-ZrO_2 catalyst shows a high turnover frequency for the formation of methanol.
- The high turnover frequency is defined by a high surface concentration of H_2/CO_2.

GRAPHICAL ABSTRACT

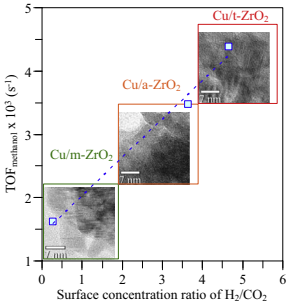

ARTICLE INFO

Article history:
Received 11 September 2015
Received in revised form 8 February 2016
Accepted 19 February 2016
Available online 26 February 2016

Keywords:
CO_2 hydrogenation
Methanol synthesis
Cu-based catalysts
H_2 to CO_2 ratio

ABSTRACT

Structure–activity relationships of amorphous (a-), tetragonal (t-), monoclinic (m-) ZrO_2 phase supported copper catalysts for methanol synthesis from CO_2 hydrogenation were investigated with X-ray diffraction (XRD), high resolution transmission electron microscopy (HR-TEM), N_2O chemisorption, H_2-temperature programmed reduction (H_2-TPR), X-ray absorption spectroscopy (XAS), H_2 and CO_2 temperature-programmed desorption (H_2- and CO_2-TPD). The order of copper surface area is found to be as follows: Cu/a-ZrO_2 > Cu/t-ZrO_2 > Cu/m-ZrO_2. The increased yield of methanol is correlated to the increase of copper surface area. However, normalization of the copper site specific activity ($TOF_{methanol}$) of Cu/t-ZrO_2 is about 1.10–1.50 times and 1.62–3.59 times higher than Cu/a-ZrO_2 and Cu/m-ZrO_2, respectively. The high $TOF_{methanol}$ is caused by a strong Cu–ZrO_2 interaction and a high surface concentration of atomic hydrogen to CO_2.

1. Introduction

As population growth and industrial development, the global demand for energy increases continuously despite of the limited amount of fossil fuels. This unbalanced consumption has significantly caused environmental problems as well: especially the increasing CO_2 emission into the atmosphere which is the main cause of global warming and climate change. Therefore, many attempts have been discovering renewable energy sources and developing alternative fuels from non-fossil fuel sources to solve for both the impending energy shortage and environmental issue [1–11]. One of the feasible and attractive strategies is the utilization of CO_2 waste as reactant to produce methanol because it can

* Corresponding author at: Center of Excellence on Petrochemical and Materials Technology, Department of Chemical Engineering, Faculty of Engineering, Kasetsart University, Bangkok 10900, Thailand. Tel.: +66 2579 2083; fax: +66 2561 4621.
E-mail address: fengttwi@ku.ac.th (T. Witoon).

http://dx.doi.org/10.1016/j.cej.2016.02.069
1385-8947/

be directly used as a fuel additive or a clean fuel, and can be converted to high-octane gasoline [12,13]. Moreover, methanol is also common chemical feedstock for important chemicals such as acetic acid, methyl *tert*-butyl ether (MTBE), formaldehyde and chloromethane [14].

In the decades earlier, the researchers have devoted to the sustainable development for methanol synthesis via CO_2 hydrogenation which focused mainly on improving the performance of the Cu-based catalyst with different oxide additives, e.g., ZnO, Al_2O_3, ZrO_2, Ga_2O_3, Y_2O_3, TiO_2 and SiO_2 [15–21]. Although the conventional Cu/ZnO catalyst was found to be active and selective for methanol synthesis from the hydrogenation of CO_2, it suffered from a fast deactivation due to its low thermal stability [22–24]. Moreover, the Cu/ZnO catalyst could accelerate the reforming of methanol to CO, leading to a lower yield of methanol than that expected from thermodynamic equilibrium [25]. The ZrO_2-supported copper catalyst has been reported to be more selective and stable than the Cu/ZnO catalyst for methanol synthesis from CO_2 hydrogenation [25–31] because of the high thermal stability [32–34] and the high surface basicity of ZrO_2 [35–37]. Therefore, ZrO_2 has been suggested as a structural stabilizer to prevent the sintering of Cu nanoparticles [38–42]. In addition to the structural stabilizer, the surface basicity of ZrO_2 was found to be one of the active sites for CO_2 adsorption [43]. GuO et al. reported that the methanol selectivity linearly increased with the strong basic site on the catalyst surface [44].

ZrO_2 has generally there polymorphs, monoclinic (m-ZrO_2), tetragonal (t-ZrO_2), and cubic (c-ZrO_2), which the different crystal phases of ZrO_2 significantly influence physical properties [45,46]. Pokrovski et al. reported that m-ZrO_2 exhibited a higher concentration and basicity of hydroxyl group as well as the stronger Zr^{4+}/O^{2-} pairs compared to t-ZrO_2, resulting superior CO_2 adsorption capacity [47]. The previous works reported that phase of ZrO_2 affected activity and selectivity for the isosynthesis of higher alcohols [48] and isobutene [49], butane isomerization [50], ethanol dehydration [51] and water gas shift reaction [52]. However, a few studies have investigated the effect of zirconia phase on methanol synthesis from CO_2 hydrogenation [29,53–56] and the roles of ZrO_2 phase in the determination of structure and catalytic activity of Cu/ZrO_2 catalysts are not yet fully understood.

In the present study the effects of ZrO_2 polymorphs including amorphous (-m), tetragonal (-t) and monoclinic (-m) phase on the structure of copper, Cu–ZrO_2 interaction and adsorption–desorption of H_2 and CO_2 were systematically investigated. The catalytic performance in terms of activity, selectivity and normalization of the copper site specific activity (TOF) of the Cu/a-ZrO_2, Cu/t-ZrO_2 and Cu/m-ZrO_2 catalysts is discussed on the basis of their structure and adsorption–desorption properties.

2. Experimental

2.1. Catalyst preparation

Amorphous zirconia (a-ZrO_2) and tetragonal zirconia (t-ZrO_2) were synthesized by precipitation method, according to the experimental procedure as described in Ref. [57]. Initially, 0.1 M $ZrOCl_2 \cdot 8H_2O$ was added into 0.1 M solution of cetyltrimethylamonium chloride, and then the combined solution was stirred for 15 min. Aqueous ammonia (25%) was slowly added under vigorous stirring until pH value of the slurry equal to 11.4–11.5. After precipitation, the mixture was stirred for 1 h and then placed in a water bath at 60 °C under continuous stirring for 94 h. The mixture was then cooled to room temperature, filtered and washed with deionized water and acetone until free of surfactant and then dried at 60 °C for 20 h. The obtained solid powder was calcined in air at 400 and 600 °C for 2 h to produce a-ZrO_2 and t-ZrO_2, respectively.

The procedure for the synthesis of monoclinic zirconia (m-ZrO_2) was modified from the work reported by Jung and Bell [32]. Aqueous ammonia (25%) was added dropwise into 0.5 M solution of $ZrOCl_2 \cdot 8H_2O$ under continuous stirring at room temperature until the pH of solution was 1.5, and then kept stirring for 1 h. After that, the mixture was transferred to Teflon-lined autoclave and heated at 140 °C for 24 h. The obtained mixture was centrifuged and washed with deionized water, dried at 90 °C for 24 h and calcined in air at 400 °C for 4 h.

Cu/ZrO_2 catalysts were prepared by incipient wetness impregnation. Copper nitrate trihydrate ($Cu(NO_3)_2 \cdot 3H_2O$) used as a precursor was dissolved in deionized water and dropped into ZrO_2 supports. After that, the mixture was dried at 100 °C overnight and calcined in air at 350 °C for 2 h. The amount of Cu was ca. 10 wt%. Cu supported on a-ZrO_2, m-ZrO_2 and t-ZrO_2 were denoted as Cu/a-ZrO_2, Cu/m-ZrO_2 and Cu/t-ZrO_2, respectively.

2.2. Catalyst characterization

The crystalline phase of ZrO_2 supports and Cu/ZrO_2 catalysts were investigated by X-ray diffraction spectroscopy (XRD: Bruker D8 Advance) using Cu Kα (λ = 0.15418 nm) radiation source. The intensity data were collected over a 2θ range of 10–75 with 0.02° step size and using a counting time of 1 s per point.

The nanostructure of Cu/ZrO_2 catalysts was investigated by using transmission electron microscopy (TEM: JEOL JEM-2100). The samples were dispersed in ethanol by ultrasonication and dried at room temperature on a copper grid coated with a carbon film.

X-ray absorption near edge structure (XANES) of the calcined Cu/ZrO_2 catalysts was performed on beamline 5 at the Synchrotron Light Research Institute (SLRI), Nakhon Ratchasima, Thailand. The obtained Cu K-edge XANES spectra were measured at room temperature in transmission mode using Ge(220) double-crystal monochromator. Energy range collected was from 8884 to 9104 eV, with 0.2 eV steps from 8954 to 9064 and 10 eV steps outside that range. In this experiment, Cu foil, Cu_2O and CuO were used as standard reference material for comparison. The pre-edge and post-edge background subtractions followed by a normalization procedure of all XANES spectra were achieved using ATHENA program.

Temperature-programmed reduction (TPR) experiments of the calcained catalysts were carried out by using TA instrument (SDT2960 Simultaneous DTA-TGA Universal 2000). Prior to the reduction, the catalyst (15 mg) was preheated in flowing N_2 at 350 °C for 15 min, and then cooled down to 120 °C. After that, TPR experiment was started with heating rate of 4 °C/min under continuous flow of 10% H_2/He.

H_2 temperature-programmed desorption (H_2-TPD) and CO_2 temperature-programmed desorption (CO_2-TPD) were performed by using the same apparatus for TPR measurements. For H_2-TPD experimental, the sample (15 mg) was reduced in-situ in flowing 10% H_2/He at 300 °C for 2 h. After that, the reduced catalyst was cooled down to 40 °C and then saturated in 10% H_2/He for 1 h, followed by purging with N_2 for 30 min in order to remove any physisorbed molecules. H_2-TPD experiment was then operated at 40–400 °C and heating rate of 5 °C/min in flowing N_2. In case of CO_2-TPD experiment, the reduced catalyst was preheated at 400 °C for 30 min in order to clean surface of the catalyst from moisture and other adsorbed gas, and then cooled down to 40 °C. After that, the catalyst was saturated in flowing CO_2 for 1 h and followed by flushing in N_2 for 1 h. The CO_2-TPD measurement was then carried out at 40–400 °C and heating rate of 5 °C/min under continuous flow of N_2.

N_2 adsorption–desorption isotherm were recorded by using a Quantachrome Autosorp-1C instrument at −196 °C. Samples were

degassed at 200 °C prior to sorption measurements. The specific surface area of ZrO_2 supports and Cu/ZrO_2 catalysts was determined by Brunauer–Emmett–Teller (BET) methods. The total pore volume was measured at the relative pressure in range of 0.995–0.998. The copper surface area of the catalysts was determined by N_2O-titration measurements as described elsewhere [16].

2.3. Catalytic activity test

Before testing catalyst performance, the Cu/ZrO_2 sample (0.5 g) was diluted by silicon dioxide (SiO_2: 74–125 μm) with a dilution ratio of 1:1 by mass and packed in stainless-steel fixed bed tubular reactor (3/8″outer diameter). Prior to each experiment, the fresh catalyst was reduced in-situ with pure H_2 at 300 °C for 4 h under atmospheric pressure. After that, the reactor was cooled down to 200 °C in pure N_2 and then the steam of reactant gases (CO_2 and H_2 with molar of 1/3) were introduced into the reactor, raising the pressure to 30 bars. Catalytic activity was measured at 220, 240, 250, 260 and 280 °C. The effluent products were analyzed by using Varian gas chromatography (3800 Varian GC) equipped with thermal conductivity detector (TCD) and CTR I packed column for H_2 CO_2 and CO analysis and Shimadzu gas chromatography (GC-8A) equipped with flame ionization detector (FID) and Porapak-Q packed column for CH_3OH analysis. CO_2 conversion, methanol selectivity, space–time yield of methanol and CO and turnover frequency of methanol are defined as follows [6,58]:

$$CO_2 \text{ conversion } (\%) = \frac{(\text{moles methanol} + \text{moles CO}) \times 100}{\text{moles } CO_{2,in}} \quad (1)$$

$$\text{Methanol selectivity } (\%) = \frac{\text{moles methanol} \times 100}{\text{moles methanol} + \text{moles CO}} \quad (2)$$

$$\text{Space-time yield of methanol } (g_{methanol}\, kg_{cat}^{-1}\, h^{-1}) = \frac{\text{moles methanol}}{\text{moles } CO_{2,in} \times \text{total amount of catalyst} \times MV} \times V_{CO_2} \times MW_{methanol} \quad (3)$$

$$\text{Space-time yield of CO } (g_{CO}\, kg_{cat}^{-1}\, h^{-1}) = \frac{\text{moles CO}}{\text{moles } CO_{2,in} \times \text{total amount of catalyst} \times MV} \times V_{CO_2} \times MW_{CO} \quad (4)$$

where V_{CO_2} is the volumetric flow of CO_2 ($cm^3\, min^{-1}$), $MW_{methanol}$ and MW_{CO} are the molecular weight of methanol and CO ($g\, mol^{-1}$), and MV is the molar volume of ideal gas, 22,400 $cm^3\, mol^{-1}$.

$$TOF_{methanol}\ (s^{-1}) = \frac{SY \times N}{3600 \times MW_{methanol} \times S_{Cu} \times A} \quad (5)$$

where SY is the space-time yield of methanol ($g_{methanol}\, g^{-1}\, h$), $MW_{methanol}$ is the molecular weight of methanol ($g\, mol^{-1}$), N is Avogadro's number (6.023×10^{23}), S_{Cu} is the metallic copper surface area ($m^2\, g^{-1}$) and A is the number of copper atoms (1.469×10^{19} atoms m^{-2}).

3. Results and discussion

3.1. Characterization of catalysts

Fig. 1 shows the XRD pattern of ZrO_2 supports and Cu/ZrO_2 catalysts. ZrO_2 support prepared by precipitation at high pH (11.4) and calcined at 400 °C produced amorphous ZrO_2 (a-ZrO_2). As increasing calcination temperature to 600 °C, the XRD pattern of ZrO_2 support appeared diffraction peaks at 2θ = 30.2, 35.2, 50.2 and 60.1 which are indexed to diffractions from lattice planes (101), (110), (112) and (211) respectively, corresponding to tetragonal zirconia (PDF 01-072-2743). For ZrO_2 support prepared by precipitation at low pH (1.5) and calcined at 400 °C, the diffraction peaks were observed at 2θ = 24.1, 28.2, 31.5, 34.2, 50.1 and 50.3, due to diffraction from lattice planes (110), (−111), (111), (200), (022) and (122), respectively which was consistent with characteristic of monoclinic ZrO_2 (PDF 01-073-8590). Impregnating copper onto the supports did not alter the ZrO_2 phase. Nevertheless, the XRD pattern of Cu/m-ZrO_2 catalyst showed the additional diffraction peaks at 2θ of 35.5° and 38.7°, corresponding to crystalline copper oxide (PDF 01-080-1916), while these peaks were not observed for the XRD pattern of Cu/a-ZrO_2 and Cu/t-ZrO_2 catalysts which could be due to a fine dispersion of CuO on the surface of the a-ZrO_2 and t-ZrO_2 supports [18,59]. This implied that the CuO crystallite size of Cu/m-ZrO_2 catalyst was larger than that of the other catalysts. The XRD results confirm the existence of crystalline phase of ZrO_2 supports used for this study, and reveal the retaining crystalline phase after copper loaded on the ZrO_2 supports.

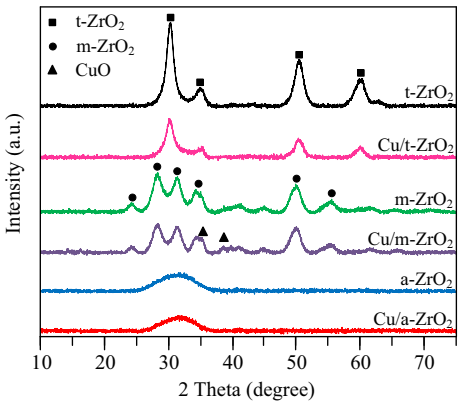

Fig. 1. XRD patterns of ZrO_2 supports and Cu/ZrO_2 catalysts.

To capture the zirconia phase and copper oxide morphology in a more tangible manner, the Cu/a-ZrO_2, Cu/t-ZrO_2, and Cu/m-ZrO_2 samples were visualized by high resolution transmission electron microscopy (HR-TEM). HR-TEM of the Cu/a-ZrO_2 sample (Fig. 2a) showed only one kind of periodicity of lattice fringe with spacing of 0.234 nm, which was compatible with the (11°1) plane of CuO. For the Cu/t-ZrO_2 sample (Fig. 2b), the HRTEM image clearly displayed additional lattice fringes with a spacing of 0.295 nm which was consistent with the (101) plane of tetragonal zirconia (t-ZrO_2). For the Cu/m-ZrO_2 sample (Fig. 2c), the lattice fringes with a spacing of 0.37 nm which was indexed to the (−111) and (111) planes of monoclinic zirconia were clearly visible. The size of copper oxide was in the order of Cu/m-ZrO_2 (~7 nm) > Cu/t-ZrO_2 (~3.5 nm) > Cu/a-ZrO_2 (~2 nm), confirming the previous statement about the well-dispersed copper species on the amorphous and tetragonal zirconia supports as revealed by the XRD data.

The physical properties including BET surface area and total pore volume of ZrO_2 supports and Cu/ZrO_2 catalysts are summarized in Table 1. The BET surface areas of a-ZrO_2, m-ZrO_2 and t-ZrO_2 supports were 272, 174 and 218 m^2/g, respectively, while total pore volume of all ZrO_2 supports were in the range of 0.30–0.34 cm^3/g. After Cu loading, the BET surface area and pore volume of the catalysts were decreased. This observation might originate from Cu metal entered into the pores of ZrO_2 supports during impregnation process [60,61]. The copper surface area (S_{Cu}) of Cu/ZrO_2 catalysts is also listed in Table 1. The copper surface areas follow the order Cu/a-ZrO_2 > Cu/t-ZrO_2 > Cu/m-ZrO_2, varying

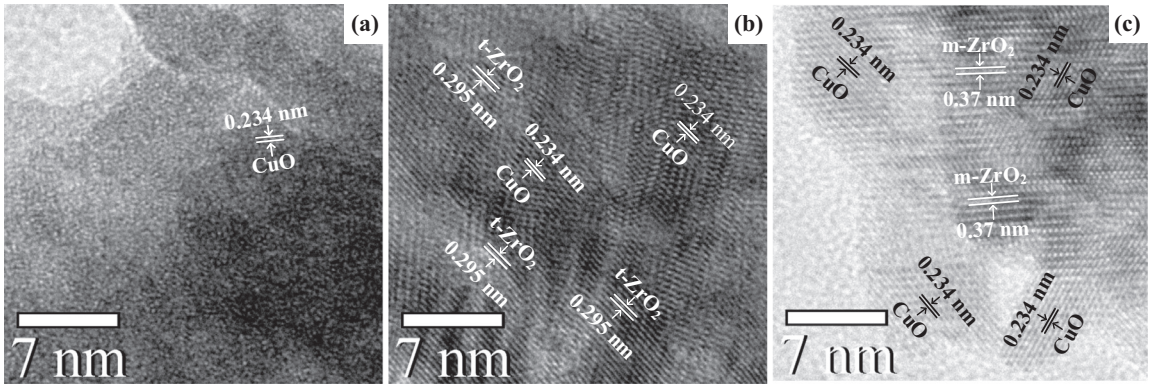

Fig. 2. TEM of (a) Cu/a-ZrO_2, (b) Cu/t-ZrO_2 and (c) Cu/m-ZrO_2 catalysts.

Table 1
Physical properties of ZrO_2 supports and Cu/ZrO_2 catalysts.

Sample	S_{BET}[a] (m^2/g)	V_p[a] (cm^3/g)	S_{Cu}[b] (m^2/g_{Cu})
a-ZrO_2	272	0.31	–
Cu/a-ZrO_2	222	0.27	7.83
m-ZrO_2	174	0.34	–
Cu/m-ZrO_2	111	0.23	2.19
t-ZrO_2	218	0.30	–
Cu/t-ZrO_2	152	0.25	3.71

[a] S_{BET} and V_p represented the BET surface area and total pore volume, respectively.
[b] Cu surface area (S_{Cu}) was determined by N_2O titration.

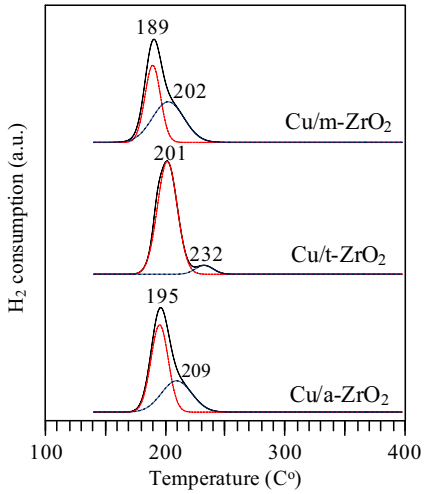

Fig. 3. H_2-TPR profiles of Cu/a-ZrO_2, Cu/t-ZrO_2 and Cu/m-ZrO_2 catalysts.

between 2.19 and 7.83 m^2/g. This result was clearly consistent with the XRD and TEM analyses, i.e. the catalysts with smaller copper oxide particle size had a higher copper surface area.

The reducibility of calcined Cu/ZrO_2 catalysts was carried out by temperature-programmed reduction (TPR); the result is shown in Fig. 3. It was reported that zirconia cannot be reduced under the investigated condition [62]. The results of TPR profile are, therefore, a reduction of CuO species. It can be seen that all catalysts exhibited a broad TPR profile in the range of 160–240 °C. Moreover, the shape of TPR profiles is rather asymmetric with a shoulder or a tail, suggesting the presence of heterogeneous distribution of CuO species [62,63]. In order to clearly distinguish, the TPR profile of all catalysts is deconvoluted, and two peaks denoted as α and β peaks are obtained. The α peak is ascribed to the reduction of highly dispersed of CuO clusters and/or the isolated copper ion (Cu^{2+}), whereas the β peak is attributed to the reduction of CuO species interacting with the support [53,64]. The maximum temperature position of α and β peaks of the Cu/a-ZrO_2 sample appears at 195 and 209 °C, respectively. In comparison to the Cu/a-ZrO_2 sample, the maximum temperature position of α and β peaks of the Cu/t-ZrO_2 sample shifts to 201 and 232 °C, respectively. The harder reduction of copper oxide species loaded on t-ZrO_2 can be attributed to the larger copper oxide particles as evidenced by TEM analysis. In contrast to the Cu/t-ZrO_2, the Cu/m-ZrO_2 sample which had the largest CuO particle size (~7 nm) can be more easily reduced than that over a-ZrO_2 and t-ZrO_2. This implies that the interaction between copper oxide species and m-ZrO_2 is weaker than t-ZrO_2 and a-ZrO_2.

XANES was performed to gain further insight into the interaction of CuO species with different ZrO_2 phases. The normalized Cu K-edge XANES spectra of Cu/ZrO_2 catalysts are shown in Fig. 4. The XANES spectrum of Cu foil exhibits both the absorption edge at 8979 eV, and followed by two characteristic peaks at higher energy position. In the case of Cu_2O and CuO, the XANES spectra show the absorption edge around 8981 and 8983.4 eV, respectively, which could be attributed to the dipole allowed 1s → 4p transition [51,65]. These values for Cu foil and reference compounds are good agreement with previously reported in the literature [66,67]. XANES spectra of all catalysts are similar to CuO reference, indicating the existence of Cu^{2+} specie. However, the XANES spectrum of Cu/m-ZrO_2 catalyst demonstrated explicitly the absorption edge at 8983 eV, indicating that the chemical environment of copper species in Cu/m-ZrO_2 catalyst resemble CuO reference, which its local structure was square-planar coordination geometry [68]. In case of Cu/t-ZrO_2 and Cu/a-ZrO_2 catalysts the absorption edge at 8983 eV was not clearly observed. In order to further identify the absorption edge, the first derivative analyses of the spectra were performed; the result is shown in Fig. 5. The absorption edge of Cu/a-ZrO_2 catalyst and Cu/t-ZrO_2 catalysts were shifted to 8985.6 and 8984.6 eV, respectively, suggesting the change of the geometric coordination of copper sites from square-planar to octahedral structure [68]. This observation indicated that Cu/t-ZrO_2 and Cu/a-ZrO_2 catalysts exhibited the strong interaction between copper oxide species and ZrO_2 supports, which was consistent with the TPR results.

To examine the basicity of the reduced Cu/ZrO_2 catalysts, CO_2 temperature-programmed desorption (CO_2-TPD) measurements were carried out; the results are shown in Fig. 6. The CO_2 desorption profiles of all catalysts exhibited a broad peak with a long tail ranging from 40 to 350 °C which were deconvoluted into three Gaussian peaks, α, β and γ peaks attributing to the desorption of

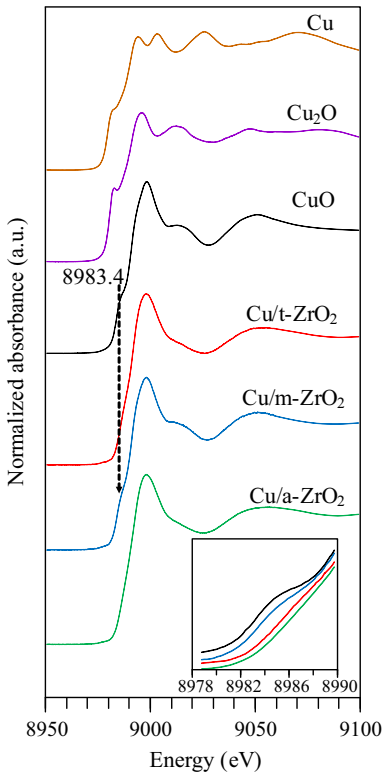

Fig. 4. Cu K-edge XANES spectra of Cu/ZrO_2 catalysts compared with reference compounds.

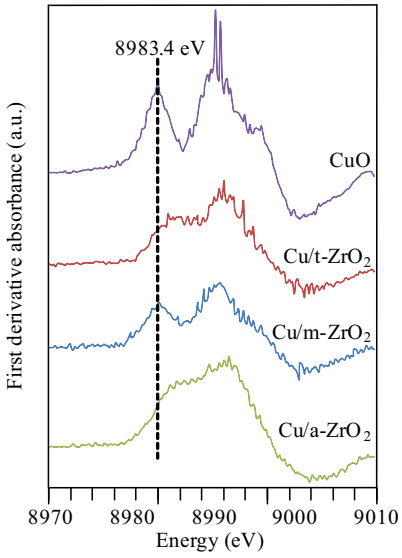

Fig. 5. First derivative XANES spectra of Cu/ZrO_2 catalysts and CuO as a reference.

CO_2 from weak, medium and strong basic sites, respectively. Similar results regarding basic site over Cu/ZrO_2 catalyst were previously reported by Guo et al. [44] that the different strengths parallel the existence of hydroxyl group, cus O^{2-} center and acid-base pair (Zr^{4+}/O^{2-} center) on each ZrO_2 phase [69]. However, the CO_2 adsorbed at strong basic site seems to be more correlated with the active site for methanol synthesis from CO_2 hydrogenation than that from weak and medium basic site, which occur at temperature lower than the reaction temperature performed in the present study (220–280 °C). The maximum temperature

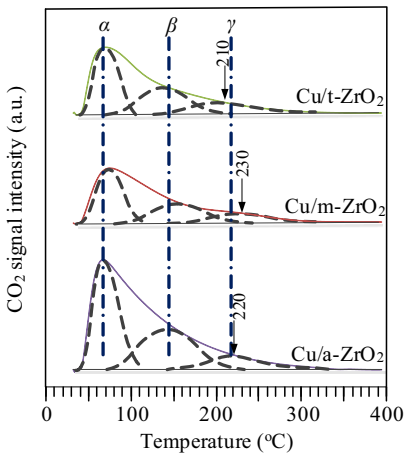

Fig. 6. CO_2-TPD profiles of $Cu/a\text{-}ZrO_2$, $Cu/t\text{-}ZrO_2$ and $Cu/m\text{-}ZrO_2$ catalysts.

position of γ peak of the $Cu/t\text{-}ZrO_2$, $Cu/a\text{-}ZrO_2$ and $Cu/m\text{-}ZrO_2$ catalysts appears at 210, 220 and 230 °C, respectively, indicating that the strength of binding of CO_2 adsorbed on the strong basic site is in sequence of $Cu/m\text{-}ZrO_2 > Cu/a\text{-}ZrO_2 > Cu/t\text{-}ZrO_2$. This finding is in good agreement with earlier studies that monoclinic structure of zirconia had stronger adsorption sites of CO_2 than the tetragonal structure [58,69]. The number of basic sites at different basic strengths of all catalysts is given in Table 2. The total number of basic sites follows the order $Cu/a\text{-}ZrO_2 > Cu/m\text{-}ZrO_2 > Cu/t\text{-}ZrO_2$, while the density of total basic sites (μmol/m^2) was found to be in the same order of strength of adsorption sites ($Cu/m\text{-}ZrO_2 > Cu/a\text{-}ZrO_2 > Cu/t\text{-}ZrO_2$). This suggests that total number of basic sites depends on both basic strength and surface area. Also shown in Table 2 is the number of basic sites from weak (α), medium (β) and strong (γ) sites. As mentioned above, the methanol synthesis from CO_2 hydrogenation proceeded at reaction temperature ranging 220–280 °C, and therefore the number of strong basic site, which was found to be 98.42, 86.43 and 79.09 $\mu mol/g_{catalyst}$ for $Cu/a\text{-}ZrO_2$, $Cu/m\text{-}ZrO_2$ and $Cu/t\text{-}ZrO_2$, respectively, would reasonably responsible as the active site for CO_2 adsorption.

The H_2 temperature-programmed desorption (H_2-TPD) profiles of pre-reduced Cu/ZrO_2 catalysts are presented in Fig. 7. There are two desorption peaks observed for $Cu/t\text{-}ZrO_2$ and $Cu/a\text{-}ZrO_2$ catalysts. The lower temperature peak (α) is ascribed to the desorption of atomic hydrogen on Cu sites, whereas the higher temperature peak (β) is attributed to the desorption of strongly desorbed hydrogen on ZrO_2 surface [43,44,70,71]. The previous work reported that Cu is rather active for adsorption and dissociation of hydrogen while pure ZrO_2 hardly chemisorbs hydrogen, except that addition of small amount of Cu can change ZrO_2 into a reservoir of hydrogen (stored as Zr-OH). This phenomenon can be explained by spillover of atomic hydrogen from Cu as donor onto ZrO_2 as the acceptor oxide, resulting from a synergy of ZrO_2 with Cu [72]. For $Cu/m\text{-}ZrO_2$ catalyst, the additional peak (γ) appears at around 350 °C, which represents the desorption of hydrogen from the bulk of Cu particles [43,70–73]. The quantitative data of the H_2 desorption for Cu/ZrO_2 catalysts are listed in Table 3. The results demonstrated that the amount of hydrogen desorbed from Cu sites (α peak) for $Cu/a\text{-}ZrO_2$ catalyst is ca. 2 and 3.4 times higher than that of $Cu/t\text{-}ZrO_2$ and $Cu/m\text{-}ZrO_2$ catalysts, respectively, corresponding with the variation trend of Cu surface area. Interestingly, the amount of hydrogen desorbed from ZrO_2 sites (β peak) of $Cu/a\text{-}ZrO_2$ (359.48 $\mu mol/g_{catalyst}$) and $Cu/t\text{-}ZrO_2$ (367.72 $\mu mol/g_{catalyst}$) catalysts is ca. 15-fold greater than that of $Cu/m\text{-}ZrO_2$ (24.16 $\mu mol/g_{catalyst}$). This could be explained by the fact that strong interaction between copper and $a\text{-}ZrO_2$ and $t\text{-}ZrO_2$

Table 2
The basic property of Cu/ZrO_2 catalysts.

Catalyst	BET surface area (m^2/g)	Number of total basic sites ($\mu mol/g_{catalyst}$)	Number of basic sites ($\mu mol/g_{catalyst}$)			Density of total basic sites ($\mu mol/m^2$)
			α	β	γ	
$Cu/a\text{-}ZrO_2$	222	1009.06	507.83	402.80	98.42	4.55
$Cu/m\text{-}ZrO_2$	111	613.49	300.97	226.1	86.43	5.55
$Cu/t\text{-}ZrO_2$	152	596.34	294.93	222.32	79.09	3.92

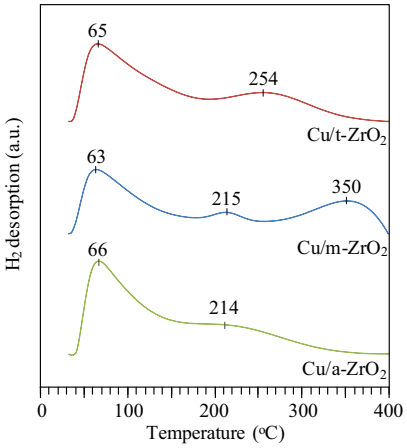

Fig. 7. H_2-TPD profiles of $Cu/a\text{-}ZrO_2$, $Cu/t\text{-}ZrO_2$ and $Cu/m\text{-}ZrO_2$ catalysts.

Table 3
The amounts of H_2 desorption of Cu/ZrO_2 catalysts.

Catalyst	Total H_2 desorbed ($\mu mol/g_{catalyst}$)	Amount of H_2 desorbed from different sites ($\mu mol/g_{catalyst}$)		
		α	β	γ
$Cu/a\text{-}ZrO_2$	1729.13	1369.65	359.48	–
$Cu/m\text{-}ZrO_2$	651.43	396.87	24.16	230.40
$Cu/t\text{-}ZrO_2$	1056.42	688.70	367.72	–

supports as revealed by H_2-TPR and XANES results facilitates the spillover of hydrogen from copper particles onto the zirconia surface.

3.2. Catalytic activity results

The catalytic performance of the Cu/ZrO_2 catalysts is shown in Fig. 8 in terms of CO_2 conversion (a), methanol selectivity (b), space time yield of methanol (c) and space time yield of CO (d). CO_2 conversion of all catalysts monotonically increased with ascending the reaction temperature. At identical reaction temperature, the order of CO_2 conversion was found to be as follows: $Cu/a\text{-}ZrO_2 > Cu/t\text{-}ZrO_2 > Cu/m\text{-}ZrO_2$, indicating that the CO_2 conversion directly related to the copper surface area (Table 1). i.e., a large copper surface area was favorable for a high CO_2 conversion. However, concerning the selectivity to methanol great difference is observed because the methanol selectivity does not follow the trend of copper surface area. The methanol selectivity of $Cu/t\text{-}ZrO_2$ at all reaction temperature is higher compared to those of $Cu/a\text{-}ZrO_2$ and $Cu/m\text{-}ZrO_2$. Nevertheless, there is a marked decrease in the methanol selectivity of $Cu/t\text{-}ZrO_2$ at temperature above 240 °C (from 76.42% to 37.34%). The methanol selectivity of $Cu/a\text{-}ZrO_2$ shows the similar trend with those of $Cu/t\text{-}ZrO_2$ as the methanol selectivity dramatically decreased from 72.3% to 30.61% at temperature 220 to 280 °C. In comparison to $Cu/t\text{-}ZrO_2$ and $Cu/a\text{-}ZrO_2$, the $Cu/m\text{-}ZrO_2$ has the lowest methanol selectivity (60.50%) at 220 °C. However, the methanol selectivity of $Cu/m\text{-}ZrO_2$ slightly decreased with ascending the reaction temperature. At temperature above 250 °C the methanol selectivity of $Cu/m\text{-}ZrO_2$ is higher than $Cu/a\text{-}ZrO_2$. One reasonable probability is the difference in the strength of CO_2 and H_2 adsorption over the different Cu/ZrO_2 catalysts (Figs. 6 and 7), as we will discuss later.

Fig. 8c and d show the rate of the formation of methanol and CO as a function of reaction temperature. The $Cu/a\text{-}ZrO_2$ catalyst demonstrates the highest rates in both CO_2 hydrogenation to methanol and reverse water gas shift reaction at all reaction temperature, followed by $Cu/t\text{-}ZrO_2$ and $Cu/m\text{-}ZrO_2$. Although both methanol and CO formation rate of all catalysts monotonically increased with ascending temperature. The higher rate of CO formation is observed at temperature above 250 °C which could be explained by the fact that reverse water gas shift becomes kinetically much favored at higher temperatures. To gain more information on the formation of methanol and CO over different Cu/ZrO_2 catalysts the apparent activation energies (E_a) for each reaction were determined. Fig. 9a and b show an Arrhenius plot of turnover frequencies for CO and methanol formation, respectively. Activation energies for CO formation derived from the slope were 89.53, 103.86 and 100.32 kJ/mol for $Cu/a\text{-}ZrO_2$, $Cu/t\text{-}ZrO_2$ and $Cu/m\text{-}ZrO_2$, respectively. These activation energies of all catalysts were slightly different which indicated that the reverse water gas shift reaction is slightly sensitive to the structure of catalysts ($Cu/a\text{-}ZrO_2$, $Cu/t\text{-}ZrO_2$ and $Cu/m\text{-}ZrO_2$). In case of methanol formation, the order of activation energy was found to be as follows: $Cu/a\text{-}ZrO_2$ (23.33 kJ/mol) > $Cu/t\text{-}ZrO_2$ (36.43 kJ/mol) ≪ $Cu/m\text{-}ZrO_2$ (63.52 kJ/mol). This indicated a low dependence of the methanol formation rate on the reaction temperature for $Cu/a\text{-}ZrO_2$ and $Cu/t\text{-}ZrO_2$ catalysts, and the methanol formation via CO_2 hydrogenation is strongly sensitive to the structure of the catalysts. The activation energy for the formation of CO was much higher than that for the formation of methanol which means that the reverse water gas shift reaction is very sensible to the temperature, corresponding to the strong increase in the rate of CO formation at higher reaction temperature as shown in Fig. 8c and d.

To gain further insight into the relationship between the activity and the properties of the catalysts, several correlations have been constructed. Fig. 10a shows a plot of the methanol yield and copper surface area. Although a linear correlation between the methanol yield and copper surface area is frequently reported by previous works [58,74,75], the yields of methanol over copper loaded on different ZrO_2 phases described here show no simple linear correlation (R^2 = 0.8106–0.9463), indicating that not only the copper surface area but other factors are involved for the formation of methanol. However, the yields of CO are linearly fixed with the copper surface area, implying that the formation of CO is strongly related to copper surface area. Various mechanisms for the CO_2 hydrogenation to methanol have been studied and proposed. Fisher and Bell [31] proposed that CO_2 adsorbs on ZrO_2 in form of bicarbonate species while hydrogen adsorbs dissociatively on the surface of copper. The atomic hydrogen can transfer to the surface of zirconia-bound carbonaceous species via spillover which undergoes a hydrogenation to produce formate, dioxomethylene,

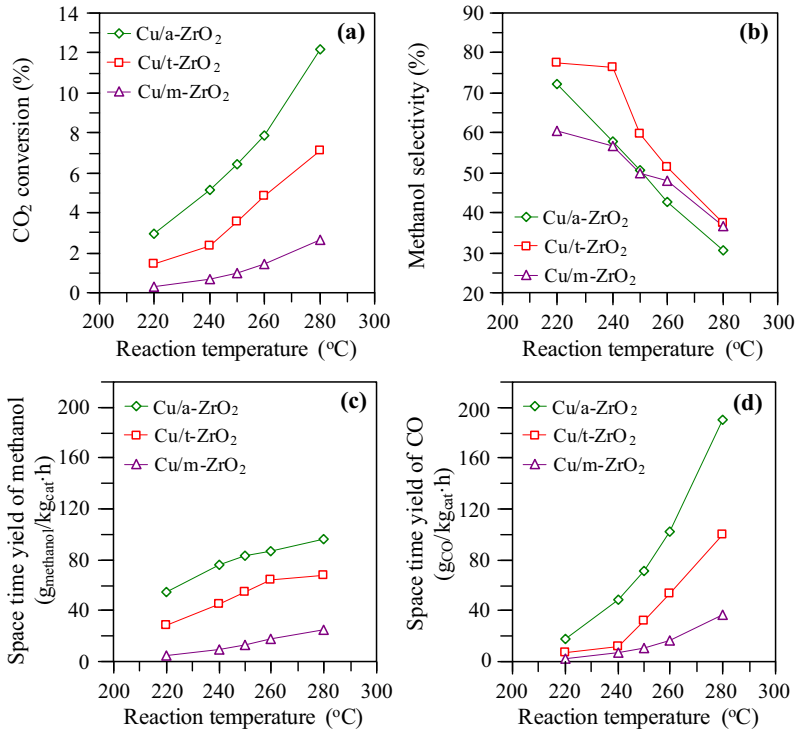

Fig. 8. CO_2 conversion (a), selectivity to methanol (b), space time yield of methanol (c) and space time yield of CO (d).

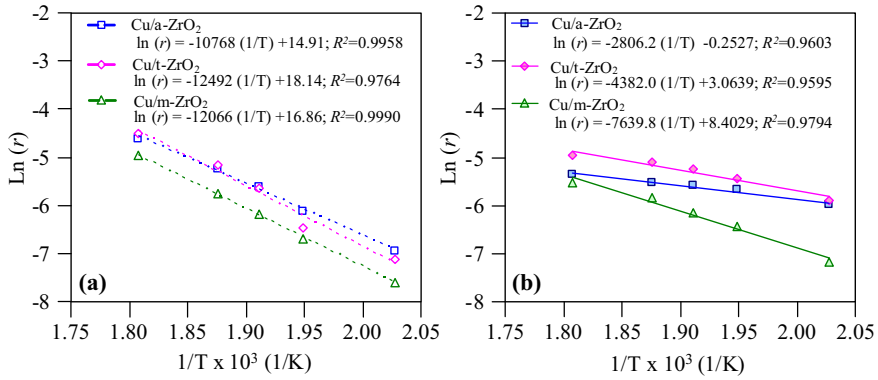

Fig. 9. Arrhenius plots of TOF for the formation of methanol (a) and CO (b) of $Cu/a\text{-}ZrO_2$, $Cu/t\text{-}ZrO_2$ and $Cu/m\text{-}ZrO_2$ catalysts.

and finally methoxide species [72]. In a parallel CO is produced via formate dissociation mechanism [76,77]. Therefore, the strength between CO_2 and basic site must be sufficiently strong to prevent the decomposition of formate to CO. That is why only the fraction of strong basic site (γ peak) is considered to be active site of ZrO_2 for CO_2 adsorption. In addition the hydrogenation of adsorbed formate and dioxomethylene is presumed to be the rate-determining step [72,78], indicating that a fast spillover of atomic hydrogen from the surface of copper to the surface of ZrO_2 and the large quantity of atomic hydrogen under operating conditions are required to enhance the hydrogenation of the adsorbed carbonaceous species. On the basis of TEM, TPR and XANES techniques analyses, $Cu/a\text{-}ZrO_2$ and $Cu/t\text{-}ZrO_2$ exhibited the smaller copper oxide particles and the stronger interaction between copper species and supports when compared to those of $Cu/m\text{-}ZrO_2$, implying that copper particles of $Cu/a\text{-}ZrO_2$ and $Cu/t\text{-}ZrO_2$ achieved a larger interfacial area with zirconia supports, facilitating the spillover of atomic hydrogen. In addition CO_2 hydrogenation to methanol required three molecules of hydrogen per one molecule of CO_2. Therefore the quantity of CO_2 and hydrogen adsorbed under the operating conditions seems to play a decisive role in determining the methanol formation.

The ratio of H_2/CO_2 was calculated based on the amount of H_2 and CO_2 desorbed from β peak and γ peak, respectively. The order of the H_2/CO_2 was as follows: $Cu/t\text{-}ZrO_2$ (4.65) > $Cu/a\text{-}ZrO_2$ (3.65) 8 $Cu/m\text{-}ZrO_2$ (0.28). Fig. 11 shows the dependence of the turnover frequency (TOF) for the formation of methanol on the ratio of H_2/CO_2 at different reaction temperatures. A linear correlation between TOF and ratio of H_2/CO_2 was observed at reaction temperature of 220 and 240 °C, indicating that the ratio of H_2/CO_2 was predominant factor that controls the formation of methanol. However, at temperature above 240 °C, the deviation from the linear correlation was found. This result can be explained on the basis of TPD analysis that the atomic hydrogen adsorbed on $Cu/a\text{-}ZrO_2$ catalyst exhibited a weaker interaction compared to other catalysts. The increase of reaction temperature caused a significant loss of atomic hydrogen, resulting in a reduction of H_2/CO_2 ratio and leading to the lower TOF of methanol. This is the reason why the

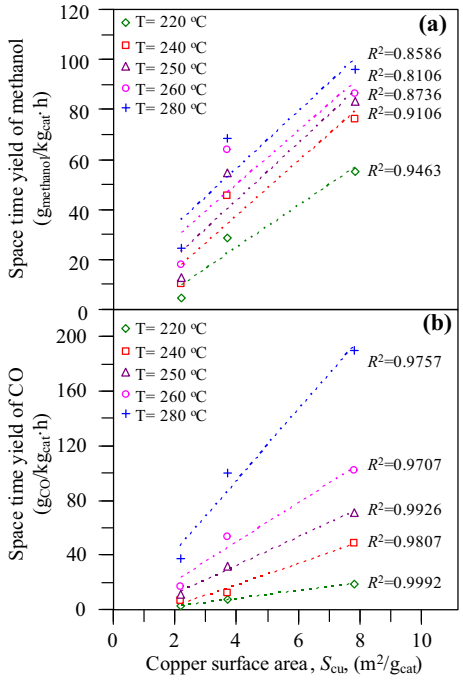

Fig. 10. Space time yields of methanol (a) and CO (b) as a function of copper surface area at different reaction temperatures.

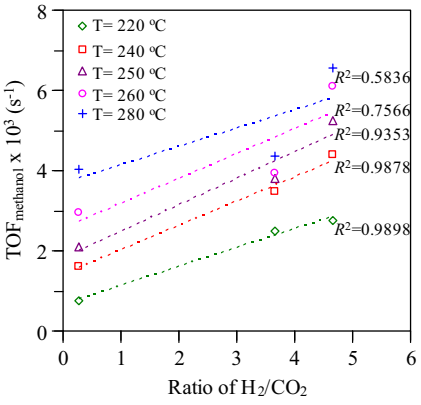

Fig. 11. TOF for the formation of methanol as a function of H_2/CO_2 ratio at different reaction temperatures.

significant reduction of methanol selectivity over Cu/a-ZrO_2 is observed at a higher reaction temperature (Fig. 8b).

Stability is a key factor in determining whether the Cu/ZrO_2 materials can be used as methanol synthesis catalyst for CO_2 hydrogenation reaction in industrial production. Fig. 12 shows the STY versus the time-on-stream of methanol over three catalysts: Cu/a-ZrO_2, Cu/t-ZrO_2 and Cu/m-ZrO_2. The Cu/a-ZrO_2 and Cu/t-ZrO_2 catalysts exhibited the almost constant of the STY of methanol during the 48 h time-on-stream experiment while a slight decrease in STY of methanol from 18.07 to 16.05 g kg^{-1} h^{-1} of the Cu/m-ZrO_2 catalyst was observed. It has been reported that Cu-based catalysts are commonly deactivated by the sintering of copper particles [22]. The higher stability of the Cu/a-ZrO_2 and Cu/t-ZrO_2 catalysts could be attributed to the higher dispersion of copper on the ZrO_2 support and stronger metal-support interaction which could prevent the restructuring effects of the copper particles.

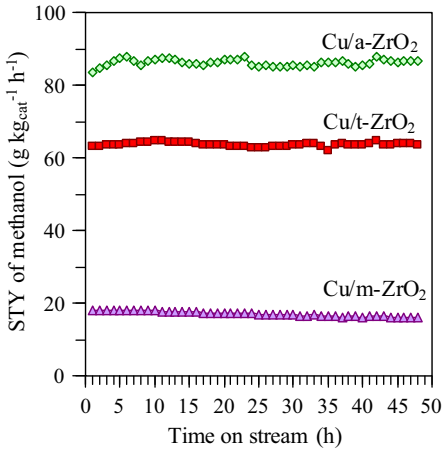

Fig. 12. Space-time yield of methanol as a function of time-on-stream of Cu/a-ZrO_2, Cu/t-ZrO_2 and Cu/m-ZrO_2. Reaction conditions: T = 260 °C, P = 3 MPa, flow rate = 60 mL min^{-1}, the amount of catalyst = 0.5 g.

4. Conclusions

In summary, we demonstrate that the physicochemical properties of copper and the catalytic activity in methanol synthesis from CO_2 hydrogenation are markedly influenced by the kind of zirconia phase. The result of N_2O measurement suggests that the order of copper surface area is as follows: Cu/a-ZrO_2 > Cu/t-ZrO_2 > Cu/m-ZrO_2. The information obtained by H_2-TPR and XANES reveals that the Cu-ZrO_2 interaction of Cu/a-ZrO_2 and Cu/t-ZrO_2 is stronger than that of Cu/m-ZrO_2 which may enhance the spillover of atomic hydrogen from copper surface to the zirconia surface. The CO_2-TPD result indicates that the amount of strong basic site of different Cu/ZrO_2 catalysts is slightly different. Cu/a-ZrO_2 and Cu/t-ZrO_2 exhibited a greater amount of H_2 adsorbed than Cu/m-ZrO_2 when considered at the same temperature range with strong basic site. The copper surface area is found to be the main factor which controls the yields of methanol and CO. However, the higher TOF for the formation of methanol over Cu/t-ZrO_2 implies that the amount of H_2/CO_2 ratio on the surface of catalyst is an important factor to promote the hydrogenation of CO_2 to methanol. This finding provides some guidelines for further development of methanol synthesis catalyst.

Acknowledgements

This work was financially supported by the Thailand Research Fund, the Center of Excellence on Petrochemical and Materials Technology (PETROMAT), the National Research University Project of Thailand (NRU), the Nanotechnology Center (NANOTEC), NSTDA, Ministry of Science and Technology, Thailand through its program of Center of Excellence Network, and the Kasetsart University Research and Development Institute (KURDI). The authors would like to thank the Synchrotron Light Research Institute (BL5.2: SUT-NANOTEC-SLRI XAS) for support in XAS measurement. Financial support for Ms. Porntipar Dumrongbunditkul from Faculty of Engineering, Kasetsart University is also appreciated.

References

[1] W. Wang, S. Wang, X. Ma, J. Gong, Recent advances in catalytic hydrogenation of carbon dioxide, Chem. Soc. Rev. 40 (2011) 3703–3727.
[2] Y. Izumi, Recent advances in the photocatalytic conversion of carbon dioxide to fuels with water and/or hydrogen using solar energy and beyond, Coord. Chem. Rev. 257 (2013) 171–186.

[3] M.J. Bos, D.W.F. Brilman, A novel condensation reactor for efficient CO_2 to methanol conversion for storage of renewable electric energy, Chem. Eng. J. 278 (2015) 527–532.

[4] M. Liu, Q. Bai, H. Xiao, Y. Liu, J. Zhao, W.W. Yu, Selective hydrogenation of o-chloronitrobenzene over tin dioxide supported platinum-ruthenium bimetallic nanocatalysts without solvent, Chem. Eng. J. 232 (2013) 89–95.

[5] E. Anbari, H. Adib, D. Iranshahi, Experimental investigation and development of a SVM model for hydrogenation reaction of carbon monoxide in presence of Co-Mo/Al_2O_3 catalyst, Chem. Eng. J. 276 (2015) 213–221.

[6] T. Witoon, T. Permsirivanich, N. Kanjanasoontorn, C. Akkaraphataworn, A. Seubsai, K. Faungnawakij, C. Warakulwit, M. Chareonpanich, J. Limtrakul, Direct synthesis of dimethyl ether from CO_2 hydrogenation over Cu-ZnO-ZrO_2/SO_4^{2-}-ZrO_2 hybrid catalyst: effects of sulfur-to-zirconia ratios, Catal. Sci. Technol. 5 (2015) 2347–2357.

[7] D. Wu, K. Cao, F. Wang, H. Wang, Z. Gao, F. Xu, Y. Guo, K. Jiang, Two dimensional graphitic-phase C_3N_4 as multifunctional protecting layer for enhanced short-circuit photocurrent in ZnO based dye-sensitized solar cell, Chem. Eng. J. 280 (2015) 441–447.

[8] K.-H. Park, S.J. Kim, R. Gomes, A. Bhaumik, High performance dye-sensitized solar cell by using porous polyaniline nanotubes as counter electrode, Chem. Eng. J. 260 (2015) 393–398.

[9] H. Fei, X. Liu, Z. Li, Hollow cobalt coordination polymer microsphere: a promising anode material for lithium-ion batteries with high performance, Chem. Eng. J. 281 (2015) 453–458.

[10] J. Kim, S.-A. Hong, J. Yoo, Continuous synthesis of hierarchical porous ZnO microspheres in supercritical methanol and their enhanced electrochemical performance in lithium ion batteries, Chem. Eng. J. 266 (2015) 179–188.

[11] Z. Wang, B. Zhang, A.G.L. Borthwick, C. Feng, J. Ni, Utilization of single-chamber microbial fuel cells as renewable power sources for electrochemical degradation of nitrogen-containing organic compounds, Chem. Eng. J. 280 (2015) 99–105.

[12] P. Gao, F. Li, F. Xiao, N. Zhao, W. Wei, L. Zhong, Y. Sun, Effect of hydrotalcite-containing precursors on the performance of Cu/Zn/Al/Zr catalysts for CO_2 hydrogenation: introduction of Cu^{2+} at different formation stages of precursors, Catal. Today 194 (2012) 9–15.

[13] J.F. Haw, W. Song, D.M. Marcus, J.B. Nicholas, The mechanism of methanol to hydrocarbon catalysis, Acc. Chem. Res. 36 (2003) 317–326.

[14] X.-M. Liu, G.Q. Lu, Z.-F. Yan, J. Beltramini, Recent Advances in catalysts for methanol synthesis via hydrogenation of CO and CO_2, Ind. Eng. Chem. Res. 42 (2003) 6518–6530.

[15] K.A. Ali, A.Z. Abdullah, A.R. Mohamed, Recent development in catalytic technologies for methanol synthesis from renewable sources: a critical review, Renewable Sustainable Energy Rev. 44 (2015) 508–518.

[16] F. Arena, K. Barbera, G. Italiano, G. Bonura, L. Spadaro, F. Frusteri, Synthesis, characterization and activity pattern of Cu–ZnO/ZrO_2 catalysts in the hydrogenation of carbon dioxide to methanol, J. Catal. 249 (2007) 185–194.

[17] R. Ladera, F.J. Pérez-Alonso, J.M. González-Carballo, M. Ojeda, S. Rojas, J.L.G. Fierro, Catalytic valorization of CO_2 via methanol synthesis with Ga-promoted Cu–ZnO–ZrO_2 catalysts, Appl. Catal., B 142–143 (2013) 241–248.

[18] S. Natesakhawat, J.W. Lekse, J.P. Baltrus, P.R. Ohodnicki Jr., B.H. Howard, X. Deng, C. Matranga, Active sites and structure-activity relationships of copper-based catalysts for carbon dioxide hydrogenation to methanol, ACS Catal. 2 (2012) 1667–1676.

[19] T. Witoon, S. Bumrungsalee, M. Chareonpanich, J. Limtrakul, Effect of hierarchical meso–macroporous alumina-supported copper catalyst for methanol synthesis from CO_2 hydrogenation, Energy Convers. Manage. 103 (2015) 886–894.

[20] H. Ren, C.-H. Xu, H.-Y. Zhao, Y.-X. Wang, J. Liu, J.-Y. Liu, Methanol synthesis from CO_2 hydrogenation over Cu/γ-Al_2O_3 catalysts modified by ZnO, ZrO_2 and MgO, J. Ind. Chem. Eng. 28 (2015) 261–267.

[21] P. Gao, R. Xie, H. Wang, L. Zhong, L. Xia, Z. Zhang, W. Wei, Y. Sun, Cu/Zn/Al/Zr catalysts via phase-pure hydrotalcite-like compounds for methanol synthesis from carbon dioxide, J. CO_2 Util. 11 (2015) 41–48.

[22] M. Kurtz, H. Wilmer, T. Genger, O. Hinrichsen, M. Muhler, Deactivation of supported copper catalysts for methanol synthesis, Catal. Lett. 86 (2003) 77–80.

[23] A. Szizybalski, F. Girgsdies, A. Rabis, Y. Wang, M. Niederberger, T. Ressler, In situ investigations of structure-activity relationships of a Cu/ZrO_2 catalyst for the steam reforming of methanol, J. Catal. 233 (2005) 297–307.

[24] E. Samei, M. Taghizadeh, M. Bahman, Enhancement of stability and activity of Cu/ZnO/Al_2O_3 catalysts by colloidal silica and metal oxides additives for methanol synthesis from a CO_2-rich feed, Fuel Process. Technol. 96 (2012) 128–133.

[25] Y. Amenomiya, Methanol synthesis from CO_2 + H_2 II. Copper-based binary and ternary catalysts, Appl. Catal. 30 (1987) 57–68.

[26] Y. Nitta, O. Suwata, Y. Ikeda, Y. Okamoto, T. Imanaka, Copper-zirconia catalysts for methanol synthesis from carbon dioxide: effect of ZnO addition to Cu–ZrO_2 catalysts, Catal. Lett. 26 (1994) 345–354.

[27] M.D. Rhodes, K.A. Pokrovski, A.T. Bell, The effects of zirconia morphology on methanol synthesis from CO and H_2 over Cu/ZrO_2 catalysts: Part II. Transient-response infrared studies, J. Catal. 233 (2005) 210–220.

[28] J. Sloczyński, R. Grabowski, P. Olszewski, A. Kozlowska, J. Stoch, M. Lachowska, J. Skrzypek, Effect of metal oxide additives on the activity and stability of Cu/ZnO/ZrO_2 catalysts in the synthesis of methanol from CO_2 and H_2, Appl. Catal., A 310 (2006) 127–137.

[29] K. Samson, M. Śliwa, R.P. Socha, K. Góra-Marek, D. Mucha, D. Rutkowska-Zbik, J.-F. Paul, M. Ruggiero-Mikołajczyk, R. Grabowski, J. Słoczyński, Influence of ZrO_2 structure and copper electronic state on activity of Cu/ZrO_2 catalysts in methanol synthesis from CO_2, ACS Catal. 4 (2014) 3730–3741.

[30] J. Słoczyński, R. Grabowski, A. Kozłowska, P. Olszewski, M. Lachowska, J. Skrzypek, J. Stoch, Effect of Mg and Mn oxide additions on structural and adsorptive properties of Cu/ZnO/ZrO_2 catalysts for the methanol synthesis from CO_2, Appl. Catal., A 249 (2003) 129–138.

[31] I.A. Fisher, A.T. Bell, In-situ infrared study of methanol synthesis from H_2/CO_2 over Cu/SiO_2 and Cu/ZrO_2/SiO_2, J. Catal. 172 (1997) 222–237.

[32] K.T. Jung, A.T. Bell, The effects of synthesis and pretreatment conditions on the bulk structure and surface properties of zirconia, J. Mol. Catal. A: Chem. 163 (2000) 27–42.

[33] W. Li, H. Huang, H. Li, W. Zhang, H. Liu, Facile synthesis of pure monoclinic and tetragonal zirconia nanoparticles and their phase effects on the behavior of supported molybdena catalysts for methanol-selectivity oxidation, Langmuir 24 (2008) 8358–8366.

[34] V.G. Deshmane, Y.G. Adewuyi, Synthesis of thermally stable, high surface area, nanocrystalline mesoporous tetragonal zirconium dioxide (ZrO_2): effects of different process parameters, Microporous Mesoporous Mater. 148 (2012) 88–100.

[35] P. Gao, F. Li, H. Zhan, N. Zhao, F. Xiao, W. Wei, L. Zhong, H. Wang, Y. Sun, Influence of Zr on the performance of Cu/Zn/Al/Zr catalysts via hydrotalcite-like precursors for CO_2 hydrogenation to methanol, J. Catal. 298 (2013) 51–60.

[36] J. Xiao, D. Mao, X. Guo, J. Yu, Effect of TiO_2, ZrO_2, and TiO_2–ZrO_2 on the performance of CuO–ZnO catalyst for CO_2 hydrogenation to methanol, Appl. Surf. Sci. 338 (2015) 146–153.

[37] Y. Zhang, J. Fei, Y. Yu, X. Zheng, Methanol synthesis from CO_2 hydrogenation over Cu based catalyst supported on zirconia modified γ-Al_2O_3, Energy Convers. Manage. 47 (2006) 3360–3367.

[38] P. Gao, F. Li, F. Xiao, N. Zhao, N. Sun, W. Wei, L. Zhong, Y. Sun, Preparation and activity of Cu/Zn/Al/Zr catalysts via hydrotalcite-containing precursors for methanol synthesis from CO_2 hydrogenation, Catal. Sci. Technol. 2 (2012) 1447–1454.

[39] F. Frusteri, G. Bonura, C. Cannilla, G.D. Ferrante, A. Aloise, E. Catizzone, Stepwise tuning of metal-oxide and acid sites of CuZnZr-MFI hybrid catalysts for the direct DME synthesis by CO_2 hydrogenation, Appl. Catal., B 176–177 (2015) 522–531.

[40] Q. Zhang, Y.-Z. Zuo, M.-H. Han, J.-F. Wang, Y. Jin, F. Wei, Long carbon nanotubes intercrossed Cu/Zn/Al/Zr catalyst for CO/CO_2 hydrogenation to methanol/dimethyl ether, Catal. Today 150 (2010) 55–60.

[41] J. Agrell, H. Birgersson, M. Boutonnet, I. Melián-Cabrera, R.M. Navarro, J.L.G. Fierro, Production of hydrogen from methanol over Cu/ZnO catalysts promoted by ZrO_2 and Al_2O_3, J. Catal. 219 (2003) 389–403.

[42] C.C. Chang, C.T. Chang, S.J. Chiang, B.J. Liaw, Y.Z. Chen, Oxidative steam reforming of methanol over CuO/ZnO/CeO_2/ZrO_2/Al_2O_3 catalysts, Int. J. Hydrogen Energy 35 (2010) 7675–7683.

[43] F. Arena, G. Italiano, K. Barbera, S. Bordiga, G. Bonura, L. Spadaro, F. Frusteri, Solid-state interaction, adsorption sites and functionality of Cu–ZnO/ZrO_2 catalysts in the CO_2 hydrogenation to CH_3OH, Appl. Catal., A 350 (2008) 16–23.

[44] X. Guo, D. Mao, G. Lu, S. Wang, G. Wu, The influence of La doping on the catalytic behavior of Cu/ZrO_2 for methanol synthesis from CO_2 hydrogenation, J. Mol. Catal. A: Chem. 345 (2011) 60–68.

[45] M. Rezaei, S.M. Alavi, S. Sahebdelfar, Z.F. Yan, H. Teunissen, J.H. Jacobsen, J. Sehested, Synthesis of pure tetragonal zirconium oxide with high surface area, J. Mater. Sci. 42 (2007) 1228–1237.

[46] M. Mokhtar, S.N. Basahel, T.T. Ali, Effect of synthesis methods for mesoporous zirconia on its structural and textural properties, J. Mater. Sci. 48 (2013) 2705–2713.

[47] K. Pokrovski, K.T. Jung, A.T. Bell, Investigation of CO and CO_2 adsorption on tetragonal and monoclinic zirconia, Langmuir 17 (2001) 4297–4303.

[48] D. He, Y. Ding, H. Luo, C. Li, Effects of zirconia phase on the synthesis of higher alcohols over zirconia and modified zirconia, J. Mol. Catal. A: Chem. 208 (2004) 267–271.

[49] K.-I. Maruya, T. Komiya, T. Hayakawa, L. Lu, M. Yashima, Active sites on ZrO_2 for the formation of isobutene from CO and H_2, J. Mol. Catal. A: Chem. 159 (2000) 97–102.

[50] W. Sitchert, F. Schüth, S. Kuba, H. Knözinger, Monoclinic and tetragonal high surface area sulfated zirconias in butane isomerization: CO adsorption and catalytic results, J. Catal. 198 (2001) 277–285.

[51] A.G. Sato, D.P. Volanti, D.M. Meira, S. Damyanova, D. Longo, J.M.C. Bueno, Effect of the ZrO_2 phase on the structure and behavior of supported Cu catalysts for ethanol conversion, J. Catal. 307 (2013) 1–17.

[52] G. Águila, S. Guerrero, P. Araya, Influence of the crystalline structure of ZrO_2 on the activity of Cu/ZrO_2 catalysts on the water gas shift reaction, Catal. Commun. 9 (2008) 2550–2554.

[53] Z.-Y. Ma, C. Yang, W. Wei, W.-H. Li, Y.-H. Sun, Catalytic performance of copper supported on zirconia polymorphs for CO hydrogenation, J. Mol. Catal. A: Chem. 231 (2005) 75–81.

[54] R.A. Köppel, C. Stöcker, A. Baiker, Copper- and silver–zirconia aerogels: preparation, structural properties and catalytic behavior in methanol synthesis from carbon dioxide, J. Catal. 179 (1998) 515–527.

[55] M.D. Rhodes, A.T. Bell, The effects of zirconia morphology on methanol synthesis from CO and H_2 over Cu/ZrO_2 catalysts Part I. Steady-state studies, J. Catal. 233 (2005) 198–209.

[56] K.T. Jung, A.T. Bell, Effect of zirconia phase on the synthesis of methanol over zirconia-supported copper, Catal. Lett. 80 (2002) 63–68.
[57] M.J. Hudson, J.A. Knowles, Preparation and characterisation of mesoporous, high-surface-area zirconium (IV) oxide, J. Mater. Chem. 6 (1996) 89–95.
[58] I.U. Din, M.S. Shaharun, D. Subbarao, A. Naeem, Synthesis, characterization and activity pattern of carbon nanofibers based copper/zirconia catalysts for carbon dioxide hydrogenation to methanol: Influence of calcinations temperature, J. Power Sources 274 (2015) 619–628.
[59] K.V.R. Chary, G.V. Sagar, C.S. Srikanth, V.V. Rao, Characterization and catalytic functionalities of copper oxide catalysts supported on zirconia, J. Phys. Chem. B 111 (2007) 543–550.
[60] L. Fuxiang, Y. Feng, L. Yongli, L. Ruifeng, X. Kechang, Direct synthesis of Zr-SBA-15 mesoporous molecular sieves with high zirconium loading: characterization and catalytic performance after sulfated, Microporous Mesoporous Mater. 101 (2007) 250–255.
[61] C.-L. Chen, T. Li, S. Cheng, H.-P. Lin, C.J. Bhongale, C.-Y. Mou, Direct impregnation method for preparing sulfated zirconia supported on mesoporous silica, Microporous Mesoporous Mater. 50 (2001) 201–208.
[62] N.F.P. Ribeiro, M.M.V.M. Souza, M. Schmal, Combustion synthesis of copper catalyst for selective CO oxidation, J. Power Sources 179 (2008) 329–334.
[63] X. Guo, D. Mao, G. Lu, S. Wang, G. Wu, CO_2 hydrogenation to methanol over Cu/ZnO/ZrO_2 catalysts prepared via a route of solid-state reaction, Catal. Commun. 12 (2011) 1095–1098.
[64] Y. Zhang, C. Chen, X. Lin, D. Li, X. Chen, Y. Zhan, Q. Zheng, Cu/ZrO_2 catalysts for water-gas shift reaction: nature of catalytically active copper species, Int. J. Hydrogen Energy 39 (2014) 3746–3754.
[65] W. Klysubun, Y. Thongkam, S. Pongkrapan, K. Won-in, J. T-Thienprsert, P. Dararutana, XAS study on copper red in ancient glass beads from Thailand, Anal. Bioanal. Chem. 399 (2011) 3033–3040.
[66] A. Gaur, B.D. Shrivastava, A comparative study of the methods of speciation using X-ray absorption fine structure, Acta Phys. Pol., A 121 (2012) 647–652.
[67] S. Velu, K. Suzuki, C.S. Gopinath, H. Yoshida, T. Hattori, XPS, XANES and EXAFS investigations of CuO/ZnO/Al_2O_3/ZrO_2 mixed oxide catalysts, Phys. Chem. Chem. Phys. 4 (2002) 1990–1999.
[68] D.M. Pickup, I. Ahmed, V. FitzGerald, R.M. Moss, K.M. Wetherall, J.C. Knowles, M.E. Smith, R.J. Newport, X-ray absorption spectroscopy and high-energy XRD study of the local environment of copper in antibacterial copper-releasing degradable phosphate glasses, J. Non-Cryst. Solids 352 (2006) 3080–3087.
[69] B. Bachiller-Baeza, I. Rodriguez-Ramos, A. Guerrero-Ruiz, Interaction of carbon dioxide with the surface of zirconia polymorphs, Langmuir 14 (1998) 3556–3564.
[70] M.-H. Zhang, Z.-M. Liu, G.-D. Lin, H.-B. Zhang, Pd/CNT-promoted Cu-ZrO_2/HZSM-5 hybrid catalysts for direct synthesis of DME from CO_2/H_2, Appl. Catal., A 451 (2013) 28–35.
[71] F. Song, Y. Tan, H. Xie, Q. Zhang, Y. Han, Direct synthesis of dimethyl ether from biomass-derived syngas over Cu–ZnO–Al_2O_3–ZrO_2(x)/γ-Al_2O_3 bifunctional catalysts: effect of Zr-loading, Fuel Process. Technol. 126 (2014) 88–94.
[72] J. Wambach, A. Baiker, A. Wokaun, CO_2 hydrogenation over metal/zirconia catalysts, Phys. Chem. Chem. Phys. 1 (1999) 5071–5080.
[73] H. Wilmer, T. Genger, O. Hinrichsen, The interaction of hydrogen with alumina-supported copper catalysts: a temperature-programmed adsorption/temperature-programmed desorption/isotopic exchange reaction study, J. Catal. 215 (2003) 188–198.
[74] G.C. Chinchen, K.C. Waugh, D.A. Whan, The activity and state of the copper surface in methanol synthesis catalysts, Appl. Catal. 25 (1986) 101–107.
[75] T. Witoon, T. Permsirivanich, W. Donphai, A. Jaree, M. Chareonpanich, CO_2 hydrogenation to methanol over Cu/ZnO nanocatalysts prepared via a chitosan-assisted co-precipitation method, Fuel Process. Technol. 116 (2013) 72–78.
[76] C.-S. Chen, W.-H. Cheng, S.-S. Lin, Study of reverse water gas shift reaction by TPD, TPR and CO_2 hydrogenation over potassium-promoted Cu/SiO_2 catalyst, Appl. Catal., A 238 (2003) 55–67.
[77] J. Yoshihara, C.T. Campbell, Methanol synthesis and reverse water-gas shift kinetics over Cu(110) model catalysts: structural sensitivity, J. Catal. 161 (1996) 776–782.
[78] I.A. Fisher, H.C. Woo, A.T. Bell, Effect of zirconia promotion on the activity of Cu/SiO_2 for methanol synthesis from CO/H_2 and CO_2/H_2, Catal. Lett. 44 (1997) 11–17.

เรื่องที่ 3

Thongthai Witoon*, Tinnavat Permsirivanich, Nawapon Kanjanasoontorn, Chalairat Akkaraphataworn, Anusorn Seubsai, Kajornsak Faungnawakij, Chompunuch Warakulwit, Metta Chareonpanich, Jumras Limtrakul, Direct synthesis of dimethyl ether from CO_2 hydrogenation over Cu-ZnO-ZrO2/SO_4^{2-}–ZrO_2 hybrid catalysts: effects of sulfur-to-zirconia ratios, Catalysis Science & Technology 5 (2015) 2347–2357. (IF 2015 = 5.287).

Catalysis Science & Technology

PAPER

Cite this: *Catal. Sci. Technol.*, 2015, 5, 2347

Direct synthesis of dimethyl ether from CO_2 hydrogenation over Cu–ZnO–ZrO_2/SO_4^{2-}–ZrO_2 hybrid catalysts: effects of sulfur-to-zirconia ratios†

Thongthai Witoon,*[abcd] Tinnavat Permsirivanich,[a] Nawapon Kanjanasoontorn,[a] Chalairat Akkaraphataworn,[a] Anusorn Seubsai,[a] Kajornsak Faungnawakij,[e] Chompunuch Warakulwit,[bc] Metta Chareonpanich*[abcd] and Jumras Limtrakul[bcd]

Received 28th November 2014,
Accepted 26th January 2015

DOI: 10.1039/c4cy01568a

www.rsc.org/catalysis

Sulfated zirconia catalysts were prepared by a direct sulfation method and were admixed with a CuO–ZnO–ZrO_2 catalyst for the direct synthesis of DME from CO_2 hydrogenation. The effects of sulfur-to-zirconia ratios on the physicochemical properties, activity, selectivity and stability of the catalysts were investigated. The sulfur loading content significantly influenced the structure and surface chemistry of the catalysts. The addition of a small amount of sulfur (5–15 wt%) created numerous mesopores on the catalyst surface, remarkably enhancing the surface area and total pore volume. However, at high sulfur loading (20–30 wt%), the mesopores tended to merge and form a larger pore. The detailed characterization by FT-IR, XANES and NH_3-TPD reveals that the sulfated zirconia with low sulfur content (5–10 wt%) mainly contained weak acid sites and acted as Lewis acids. Increasing the sulfur loading (15–30 wt%) resulted in the formation of Brønsted acid sites, thus increasing the acid strengths. The sulfated zirconia catalyst with 20 wt% sulfur loading achieved a superior DME productivity of 236 g_{DME} kg_{cat}^{-1} h^{-1} at a reaction temperature and pressure of 260 °C and 20 MPa. However, after 75 h of a time-on-stream experiment, the sulfated zirconia catalyst lost approximately 16.9% of its initial activity while a commercial H-ZSM-5 catalyst was more stable as only a 2.85% reduction was observed.

1. Introduction

Exploring novel alternative fuels is necessary in order to meet the high global demand for energy and power and to reduce greenhouse gases, especially carbon dioxide (CO_2), released into the atmosphere. The combustion of fossil fuels is the main human activity that causes a drastic increase in the concentration of CO_2 in the atmosphere, which is believed to be the major reason for rapid climate change.[1] For these reasons, the production of alternative fuels obtained from CO_2 is attractive as a prospective solution both for high energy demand and global warming concerns.[2–4] Among the alternative fuels, dimethyl ether (DME) is considered a promising economical transportation fuel because it can be used as an efficient H_2 carrier for fuel cell applications, a fuel source for diesel engines, and a replacement for cooking gas (Liquefied Petroleum Gas; LPG).[5–7] In addition, DME is a clean fuel because the combustion of DME with an excess of oxygen produces no particulate matter and low NO_x emission.

DME can be produced from CO_2 in a single step by mixing a catalyst for methanol dehydration with a catalyst for methanol synthesis successively. This process has received increased attention from researchers because the *in situ* conversion of methanol to DME would become a driving force to overcome the limitation of thermodynamic equilibrium for CO_2 hydrogenation to methanol.[8] In order to obtain a high yield of DME, an excellent catalyst that can effectively convert CO_2 to methanol is required. Many kinds of bimetallic compounds, *e.g.*, Cu–Zn,[9] Pd–Ga,[10] and Ni–Ga,[11] supported on metal oxides have been investigated for methanol synthesis from CO_2 hydrogenation. Among them, the Cu–Zn bimetallic compound has been found to be the most efficient catalyst in terms of performance and cost, and therefore it is

[a] *Center of Excellence on Petrochemical and Materials Technology, Department of Chemical Engineering, Faculty of Engineering, Kasetsart University, Bangkok 10900, Thailand. E-mail: fengttwi@ku.ac.th, fengmtc@ku.ac.th; Fax: +66 2561 4621; Tel: +66 2579 2083*
[b] *Center for Advanced Studies in Nanotechnology and Its Applications in Chemical, Food and Agricultural Industries, Kasetsart University, Bangkok 10900, Thailand*
[c] *NANOTEC-KU-Center of Excellence on Nanoscale Materials Design for Green Nanotechnology, Kasetsart University, Bangkok 10900, Thailand*
[d] *PTT Group Frontier Research Center, PTT Public Company Limited, 555 Vibhavadi Rangsit Road, Chatuchak, Bangkok, 10900, Thailand*
[e] *Nanomaterials for Energy and Catalysis Laboratory, National Nanotechnology Center (NANOTEC), National Science and Technology Development Agency (NSTDA), Khlong Luang, Pathum Thani 12120, Thailand*
† Electronic supplementary information (ESI) available. See DOI: 10.1039/c4cy01568a

considered as the methanol conversion catalyst in this study. To date, several studies have focused on the modification of Cu-based catalysts in order to enhance the catalytic activity and stability. Arena *et al.*[12] showed that ZrO_2-modified Cu–Zn oxide-based catalysts were more active for methanol synthesis from CO_2 hydrogenation than conventional Cu–ZnO–Al_2O_3 catalysts. Wengui *et al.*[13] modified the conventional Cu–ZnO–Al_2O_3 catalyst by adding a small amount of La and found that La could enhance the dispersion of Cu and reduce the CuO crystallite size. Zhang *et al.*[14] reported that by adding 0.5 wt% V_2O_5 onto a Cu–ZnO–ZrO_2 catalyst, CO_2 conversion and DME selectivity increased to 12.5% and 6.7% compared to those for the unmodified Cu–ZnO–ZrO_2 catalyst. However, very few studies have considered the improvement of acid catalysts.[15]

Several solid acid catalysts such as alumina (Al_2O_3), modified alumina, and H-ZSM-5 were extensively studied for the dehydration of methanol. Alumina catalysts exhibited good performance in terms of both methanol conversion and DME selectivity. However, the alumina catalysts rapidly deactivated due to the strong adsorption of water molecules on Lewis acid sites.[16] H-ZSM-5 had a strong resistance towards water adsorption.[17] Nevertheless, H-ZSM-5 usually possessed a narrow pore size, which limited the diffusion of reactant molecules from the surface to the active sites located in the pores. This indicated that only the active sites on the external surface of H-ZSM-5 could be used effectively. Moreover, the presence of strong acid sites on the surface of H-ZSM-5 could lead to the formation of coke and hydrocarbon as secondary products.[17,18] The modified Al_2O_3 catalyst with 1 wt% titania was reported to increase the dehydration rate and minimize the coke formation. However, the optimum operating temperature over this catalyst was *ca.* 400 °C, which was considerably higher than the optimum temperature (220–280 °C) for CO_2 hydrogenation to methanol.[12,19,20] Thus, the development of acidic catalysts for this process is still desired.

Interestingly, sulfated zirconia catalysts have been reported to be super acid catalysts because their catalytic activity is relatively high in alkane isomerization,[21–24] esterification[21,25–29] and alcohol dehydration.[21,30–33] With tunable acid–base properties over sulfur loading content, sulfated zirconia materials could act as bifunctional catalysts for the isomerization of glucose to fructose and the dehydration of fructose to 5-HMF.[34] Despite the significant number of papers reporting the high activity of sulfated zirconia catalysts, a few studies have considered the use of sulfated zirconia as catalysts for DME production *via* methanol dehydration,[30–32] and the performance of a Cu/ZnO/ZrO_2 catalyst mixed with various sulfated zirconia catalysts for the direct synthesis of DME from CO_2 hydrogenation has not yet been reported. In this work, sulfated zirconia catalysts with different sulfur contents were therefore prepared by a direct sulfation method and used in combination with a Cu/ZnO/ZrO_2 catalyst for the direct synthesis of DME from CO_2 hydrogenation. The catalytic performance in terms of activity and stability of the sulfated zirconia catalysts is discussed on the basis of their structure and surface acidity. Moreover, a reaction mechanism for methanol dehydration to DME over the sulfated zirconia catalysts is proposed based on evidence of various characterization techniques.

2. Experimental

2.1. Catalyst preparation

A CuO–ZnO–ZrO_2 catalyst at a Cu : Zn : Zr atomic ratio of ~4 : 2 : 4 was prepared by a reverse co-precipitation method. Note that the effect of metal oxide compositions on the activity and selectivity of methanol production from CO_2 hydrogenation has been primarily investigated and we found that a Cu : Zn : Zr molar ratio of ~4 : 2 : 4 could provide excellent catalytic performance in terms of yield of methanol and stability. As a result, this particular composition was applied in the present study. A metal salt solution (*ca.* 100 mL) of $Cu(NO_3)_2{\cdot}3H_2O$, $Zn(NO_3)_2{\cdot}6H_2O$ and $ZrOCl_2{\cdot}8H_2O$ (Sigma-Aldrich) was slowly added into a 0.1 M $NaHCO_3$ solution (500 mL) under stirring at room temperature. The pH of the solution was adjusted to 7.5 by adding 0.1 M $NaHCO_3$ solution. The mixture was continuously stirred at 400 rpm for 2 h. The precipitate was filtered and washed with 3000 mL of deionized water. Subsequently, the obtained product was dried at 100 °C for 24 h and calcined at 350 °C for 2 h. The textural properties of the prepared catalyst are listed in Table 1.

A series of sulfated zirconia catalysts with different sulfur loadings were obtained according to the procedure described by Sun *et al.*[35] In a typical preparation process, $ZrOCl_2{\cdot}8H_2O$ and $(NH_4)_2SO_2$ were ground in an agate mortar for 20 min at room temperature. After leaving to stand for 18 h at room temperature in air, the sample was calcined at 550 °C for 5 h. The hybrid catalysts were prepared by physically mixing in a mortar the methanol synthesis catalyst and the acid catalyst with a mass ratio of 1 : 2.

A commercial zeolite catalyst (Na^+ZSM-5 with a Si/Al ratio of 24, SH-55 from ALSI-PENTA Zeolithe GmbH (APZ)) was transformed into H-ZSM-5 *via* an ion-exchange method using ammonium nitrate (NH_4NO_3) solution. Typically, 1.5 g of the catalyst was placed in a bottle. 100 ml of 0.1 M NH_4NO_3 solution was added. The exchange process was performed at 80 °C for 2 h under vigorous stirring. After that, the exchanged sample was washed with 100 mL of deionized water to remove the excess NH_4^+ ions. The process was repeated 3 times. Then, the obtained NH_4^+ZSM-5 sample was dried overnight at 110 °C. Finally, the resulting sample was calcined in air at 550 °C for 6 h in order to obtain the H-ZSM-5 catalyst.

2.2. Catalyst characterization

The BET surface area, pore size distribution and pore volume of all catalysts were determined by N_2-sorption measurement with a Quantachrome Autosorb-1C instrument at −196 °C. Prior to measurements, the samples were degassed at 200 °C for 24 h. The pore size distributions of the samples were determined from the adsorption branch of the isotherms in accordance with the Barrett–Joyner–Halenda (BJH) method.

Table 1 Chemical compositions and textural properties of the CuO–ZnO–ZrO_2 catalyst

Catalyst	Chemical composition[a] (mol%)			BET surface area (m^2 g^{-1})	Average pore diameter (nm)	Total pore volume (cm^3 g^{-1})
	CuO	ZnO	ZrO_2			
CuO–ZnO–ZrO_2	37.47	21.53	41.00	142	26.4	0.94

[a] The chemical compositions of the catalyst were determined by the ICP technique.

The specific BET (S_{BET}) was estimated for P/P_0 values between 0.05–0.30. The total pore volume was measured at a relative pressure (P/P_0) of 0.995.

The surface morphology and surface chemical compositions of the sulfated zirconia catalysts were assessed with the application of a scanning electron microscope (SEM; FEI Quanta 450) equipped with an energy-dispersive X-ray spectroscope (EDS). The SEM measurement was taken at 20.0 kV. The samples were sputter-coated with gold prior to analysis.

The X-ray diffraction (XRD) patterns of all catalysts were obtained using a diffractometer (Bruker D8 Advance) with Cu-Kα radiation. The measurements were made at a temperature range of 15–70° on 2θ with a step size of 0.05°. The diffraction patterns were analyzed according to the Joint Committee on Powder Diffraction Standards (JCPDS).

The sulfate content in each sample was determined with a DSC-TGA 2960 thermal analyzer (TA Instruments). A 50 mg sample was loaded into an alumina sample pan. In order to remove the pre-adsorbed H_2O, the sample was heated from room temperature in a flow of pure N_2 (100 mL min^{-1}) at a rate of 10 °C min^{-1} until 400 °C was achieved, then it was kept at that temperature for 30 min. Subsequently, the temperature was linearly raised to 1100 °C at a rate of 10 °C min^{-1}. The sulfate content was calculated from the difference in weight between the sample at 400 °C and 1100 °C.

The FT-IR spectra of the sulfated zirconia catalysts were obtained with a spectrophotometer (Bruker Tensor 27) in the range of 400–4000 cm^{-1} with a resolution of 4 cm^{-1}. The sample preparation included the amalgamation of a fine powder of each sample with KBr powder.

The Sulfur K-edge X-ray Absorption Near Edge Structure (XANES) spectra of the fresh catalysts were recorded at room temperature in the fluorescent mode using a silicon (111) double-crystal monochromator at beamline 5 of the Synchrotron Light Research Institute (SLRI), Nakhon Ratchasima, Thailand. The collected energy range was from 2372 to 2592 eV, with 0.2 eV steps from 2442 to 2552 and 10 eV steps outside that range. Pure $(NH_4)_2SO_4$ was also measured and used as a standard reference material. The pre-edge and post-edge background subtraction followed by a normalization procedure of all XANES spectra was achieved using the ATHENA program.

Acidity measurements were performed by a thermogravimetric technique using ammonia as a probe molecule. A 20 mg sample was pretreated in a flow of He (50 mL min^{-1}) at a rate of 10 °C min^{-1} until 550 °C was achieved; the 550 °C temperature was maintained for 30 min, then the sample was cooled to 100 °C. Once the 100 °C temperature was reached and stabilized, 10% v/v NH_3 (He as a balance gas) with a flow rate of 50 mL min^{-1} was introduced into the system for 1 h. Subsequently, the 10% v/v NH_3 flow was disconnected and a He flow was introduced for 1 h to remove the physisorbed NH_3. NH_3 desorption measurement was conducted in a flow of He (50 mL min^{-1}) at a heating rate of 5 °C min^{-1} from 100 °C to 600 °C. The level of acidity was determined from the weight loss due to the desorption of NH_3.

2.3. Catalytic activity test

CO_2 hydrogenation to DME was carried out in a fixed-bed stainless steel reactor (7.75 mm inner diameter). 0.15 g of the hybrid catalyst was diluted with 1.35 g of inert silica sand (75–150 μm). The catalyst was reduced *in situ* under atmospheric pressure with flowing H_2 (60 mL min^{-1}) at 300 °C and a heating rate of 2 °C min^{-1} for 4 h. After the reduction, the temperature was cooled to 180 °C under flowing N_2; subsequently a flow of CO_2 and H_2 mixture (CO_2 : H_2 molar ratio of 1 : 3) was fed to the reactor. The feed flow rate was set at 60 mL min^{-1}. The reactor pressure was slowly raised to 20 bar, and the reactor was heated to a variety of temperatures (240, 260, 270, 280 and 300 °C). The effluent gaseous products were analyzed by using gas chromatography. Analysis of H_2, CO, CO_2, and N_2 was performed using a GC-2014 gas chromatograph equipped with a thermal conductivity detector (TCD) and a Unibead-C column. Methanol, DME and other hydrocarbon products were analyzed by using a GC 8A equipped with a flame ionization detector (FID) and a Chromosorb WAW (20% PEG) column. The activity–selectivity data were calculated by mass balance from an average of three independent measurements. The errors were within ±2%. CO_2 conversion to oxygenated compounds, yield of DME and yield of CO are defined as follows:

$$\text{CO}_2 \text{ conversion to oxygenated compounds}(\%) = \frac{(\text{moles methanol} + (2 \times \text{moles DME})) \times 100}{\text{moles CO}_{2,\text{in}}} \quad (1)$$

$$\text{Yield of DME } (\%) = \frac{2 \times \text{moles DME} \times 100}{\text{moles CO}_{2,\text{in}}} \quad (2)$$

$$\text{Yield of CO } (\%) = \frac{\text{moles CO} \times 100}{\text{moles CO}_{2,\text{in}}} \quad (3)$$

The stability of the catalysts is presented in terms of the space-time yield of methanol and DME ($g_{\text{methanol or DME}}$

$kg_{catalyst}^{-1}$ h^{-1}) as a function of time-on-stream defined as follows:

$$\text{Space-time yield of methanol} = \frac{\text{moles methanol}}{\text{moles } CO_{2,in} \times \text{total amount of catalyst} \times MV \times V_{CO_2} \times MW_{methanol}} \quad (4)$$

$$\text{Space-time yield of DME} = \frac{\text{moles DME}}{\text{moles } CO_{2,in} \times \text{total amount of catalyst} \times MV \times V_{CO_2} \times MW_{DME}} \quad (5)$$

where V_{CO_2} is the volumetric flow of CO_2 (cm^3 min^{-1}), $MW_{methanol}$ and MW_{DME} are the molecular weight of methanol and DME (g mol^{-1}), and MV is the molar volume of ideal gas, 22 400 cm^3 mol^{-1}. Eqn (1)–(3) and eqn (4)–(5) are used in Fig. 6 and 8, respectively.

3. Results and discussion

3.1 Catalyst characterization

Fig. 1 shows the N_2 adsorption–desorption isotherm (Fig. 1a) and the corresponding pore size distribution (Fig. 1b) of the sulfated zirconia catalysts prepared with different sulfur loading contents. The isotherm of pure ZrO_2 was a typical type IV with a H4 hysteresis loop, a characteristic mesopore structure formed by the aggregates of the plate-like particles giving rise to slit-shaped pores. The pore size distribution of ZrO_2 was broad, ranging from 4 to 30 nm. When 5–15 wt% sulfur was loaded onto ZrO_2, the type IV isotherm was observed, but the hysteresis loop was changed to H2, a characteristic mesopore with an ink-bottle-like structure often generated by compacts of spherical particles of non-uniform size. In comparison with the ZrO_2 product, the mesopores ranging from 2 to 10 nm of the 5S-ZrO_2, 10S-ZrO_2 and 15S-ZrO_2 products became more pronounced. When the sulfur content was increased to 20 wt% (20S-ZrO_2), type IV–II composite isotherms were observed, indicating the presence of both mesopores and macropores. At the highest sulfur content, 30 wt% (30S-ZrO_2), mesopores (2–20 nm) were no longer observed, and instead only macropores were obtained.

Table 2 lists the results regarding the BET surface area, pore volume, and average pore diameter of the sulfated zirconia catalysts. The BET surface area and pore volume of pure ZrO_2 were found to be 26 m^2 g^{-1} and 0.08 cm^3 g^{-1}, respectively. By adding 5–15 wt% sulfur, the BET surface area and pore volume increased remarkably compared to those of pure ZrO_2. 10S-ZrO_2 exhibited the highest BET surface area and the largest pore volume, 89 m^2 g^{-1} and 0.18 cm^3 g^{-1}, respectively. The BET surface area decreased significantly to 36 m^2 g^{-1} and 7 m^2 g^{-1}, when the sulfur content was increased to 20 and 30 wt%, respectively. This discrepancy in the BET surface area can be explained as follows: with 5–15 wt% sulfur content, ammonium sulfate is highly dispersed onto the ZrO_2 surface, creating the numerous mesopores observed after the calcination. However, at high sulfur content (20–30 wt%), the sulfate species might fully cover the ZrO_2 surface, resulting in the reduction of BET surface areas and the generation of larger pores.

The thermal stability and the sulfate content of the sulfated zirconia catalysts, shown in Fig. 2, were analyzed by TG and DTG under nitrogen flow conditions. Every sample showed weight loss at temperatures below 100 °C, a result ascribed to the desorption of physically adsorbed water molecules. The samples prepared with low sulfur contents (5S-ZrO_2 and 10S-ZrO_2) exhibited a small weight loss beginning at about 750 °C and ending at 900 °C, possibly due to the evolution of SO_3 decomposed from the sulfate ion bonded to the zirconia surfaces. With a further increase in the sulfur content (15S-ZrO_2, 20S-ZrO_2 and 30S-ZrO_2), the DTG curve exhibited an additional peak around 726 °C. This implies that the sulfate that forms on the surface of zirconia at high coverage is less stable than that at low coverage. In other words, the number of coordinated configurations between sulfate and zirconia of the catalysts

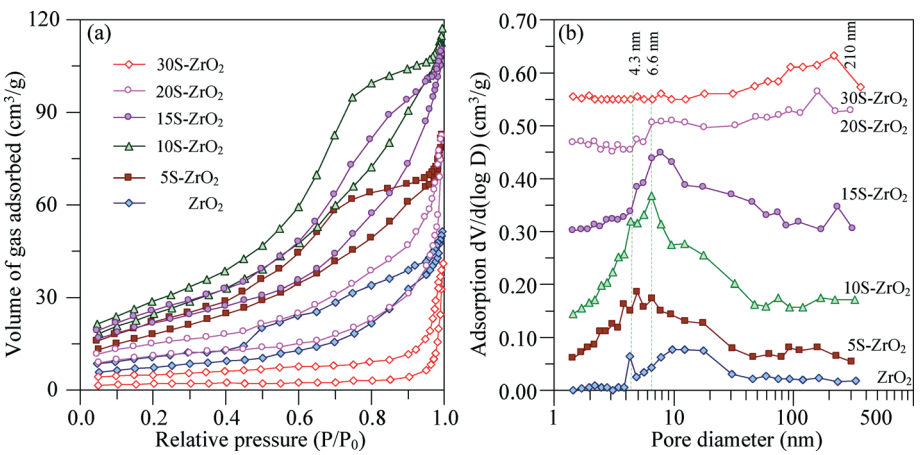

Fig. 1 N_2 adsorption–desorption isotherm (a) and pore size distribution (b) of the sulfated zirconia catalysts calcined at 550 °C.

Table 2 Textural, sulfur content and surface acidic properties of the catalysts

Catalysts	BET surface area ($m^2\ g^{-1}$)	Pore volume ($cm^3\ g^{-1}$)	Sulfur content (wt%)	Weak acid sites ($\mu mol\ g^{-1}$)	Medium acid sites ($\mu mol\ g^{-1}$)	Total acid sites ($\mu mol\ g^{-1}$)
ZrO_2	26.1	0.08	Not detectable	24	—	24
5S-ZrO_2	66.7	0.13	1.00,[a] 0.92[b]	75	20	95
10S-ZrO_2	89.2	0.18	1.20,[a] 1.56[b]	87	42	129
15S-ZrO_2	74.9	0.17	3.20,[a] 4.24[b]	54	160	214
20S-ZrO_2	36.0	0.13	7.00,[a] 12.42[b]	45	261	306
30S-ZrO_2	6.6	0.06	14.00,[a] 17.78[b]	29	140	169

[a] The sulfur content determined by TGA analysis. [b] The sulfur content measured by SEM-EDS analysis.

with high sulfate coverage is lower than that of the catalysts with low sulfate coverage.

TG tests determined the catalysts' sulfur content on the basis of the difference in weights at 200 and 1100 °C. The results are shown in Table 2 together with the sulfur content measured by SEM-EDS. The TG and SEM-EDS measurements agree for the catalysts prepared with low sulfur contents (5S-ZrO_2 and 10S-ZrO_2). However, for the catalysts prepared with higher sulfur contents (15S-ZrO_2, 20S-ZrO_2 and 30S-ZrO_2), the SEM-EDS measurements were appreciably higher than the TG measurements. This suggests that, at high sulfur content, sulfate species almost completely cover the surface of zirconia, preventing the SEM-EDS analysis from detecting ZrO_2. Note that the catalysts' sulfur contents were obviously different from those of the starting composition, which could be due to the fact that the catalysts were pre-calcined at 550 °C prior to the TG and SEM-EDS measurements. Therefore, some sulfate species were decomposed leaving only the stable sulfate species on the surface of the catalysts.

The FT-IR spectra of the sulfated zirconia catalysts prepared with different sulfur contents are shown in Fig. 3. The pure ZrO_2 showed bands between 700 and 418 cm^{-1}, characteristic of crystalline zirconia. 5S-ZrO_2 and 10S-ZrO_2 exhibited bands at 995, 1053, 1136 and 1196 cm^{-1}, characteristic peaks for the S–O stretching vibration modes of the coordinated SO_4^{2-} species on the zirconia surface. The band at 1400 cm^{-1} was assigned to the stretching vibration of the S=O bond in the sulfate groups. The band at 1612 cm^{-1} was attributed to the δ_{O-H} bending frequency of the water molecules associated with the sulfate groups. As the sulfur loading was increased up to 15 wt% (15S-ZrO_2), the distinct peaks between 990–1200 cm^{-1} were no longer observed, and one broad peak appeared instead. With a further increase of the

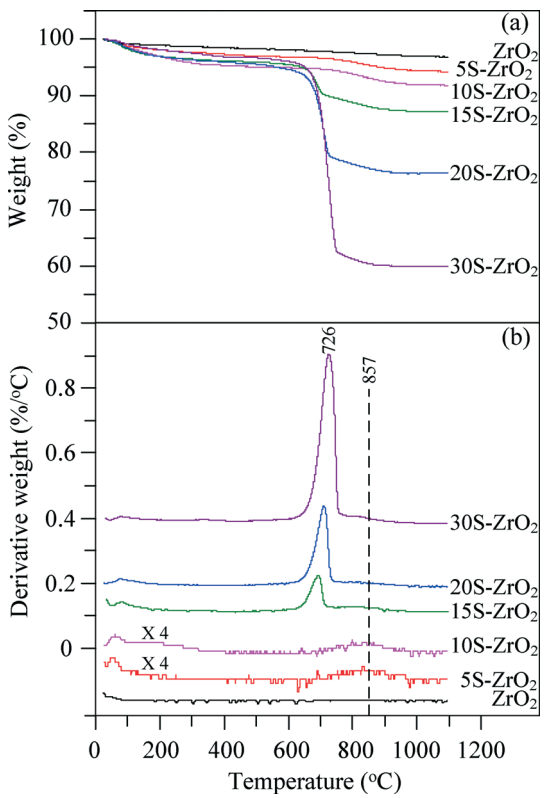

Fig. 2 TG (a) and DTG (b) curves of the sulfated zirconia catalysts calcined at 550 °C.

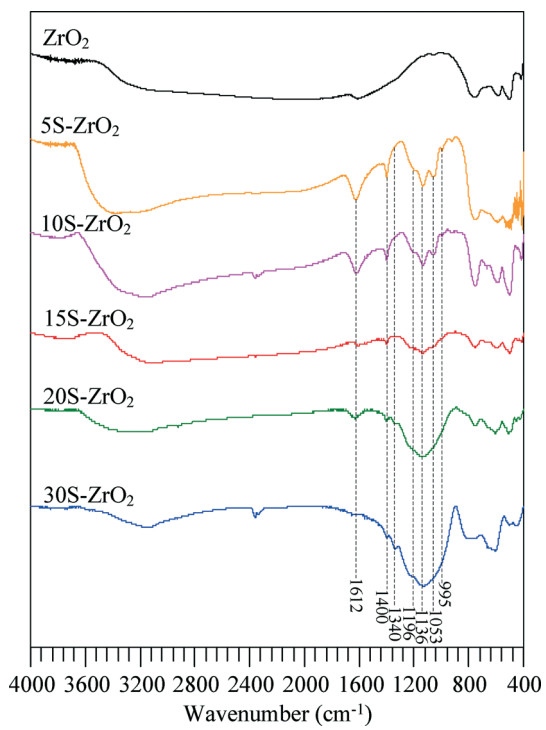

Fig. 3 FTIR spectra of the sulfated zirconia catalysts calcined at 550 °C.

sulfur content from 15 to 30 wt% (20S-ZrO_2 and 30S-ZrO_2), this peak, which indicates a complex poly-sulfate surface species,[36] became more dominant. It was interesting to see that the spectral splitting between the ν(S═O) and ν(S–O) of the 5S-ZrO_2 and 10S-ZrO_2 (200 cm^{-1}) catalysts was much larger than that of the 15S-ZrO_2, 20S-ZrO_2 and 30S-ZrO_2 catalysts, indicating that tridentate sulfate ions coordinated to zirconia at low sulfur contents, while a 2-fold coordinated configuration was formed at high sulfur contents. This FT-IR interpretation was clearly consistent with the TG analysis (Fig. 2), *i.e.* the catalysts with low sulfur contents had a higher coordination configuration. This finding was also supported by the theoretical study by Haase and Sauer.[37] The band at 1340 cm^{-1}, assigned to the bending vibration of Zr–OH groups,[32,38] was observed only for the catalysts with high sulfur contents (15S-ZrO_2, 20S-ZrO_2 and 30S-ZrO_2).

Sulfur K-edge X-ray absorption near edge structure (XANES) spectroscopy was used to investigate the sulfate species. The first derivative analyses of the spectra were performed in order to detect the absorption edges of overlapping species. The sulfur K-edge XANES spectra and first derivative spectra of $(NH_4)_2SO_4$ and sulfated zirconia samples are shown in Fig. 4. $(NH_4)_2SO_4$ showed a white line around 2483.2 eV. The sulfur K-edge XANES spectra of all sulfated zirconia catalysts were similar to that of the $(NH_4)_2SO_4$ sample, indicating that the sulfur species form as a sulfate group. However, the shape of the white line of the sulfated zirconia catalysts was slightly different than that of the $(NH_4)_2SO_4$ sample. In addition to the white line at 2483.2 eV, an absorption peak at 2475.6 eV was present for the sulfated zirconia catalysts with high sulfur contents (15S-ZrO_2, 20S-ZrO_2 and 30S-ZrO_2). This suggests that a portion of the sulfate group was reduced to lower valence states.[39] The first derivative of these spectra showed a more distinctive difference in the white lines of $(NH_4)_2SO_4$ and the catalysts (Fig. 4b). The first derivative of the sulfated-zirconia catalysts had two peaks: one at 2480.2 eV and another at 2483.2 eV. The latter peak was in the same position as that of $(NH_4)_2SO_4$ and the former peak was interpreted as an indication of a protonated sulfate.[40–42] It can be seen that the former peak was much more developed when the sulfur content was increased and that it correlated with the appearance of the FT-IR band at 1340 cm^{-1} (Fig. 3), indicating that the protonated sulfate occurred at high sulfate surface coverage.

The strength and overall concentration of the acid sites of the sulfated zirconia catalysts were determined by NH_3-TPD; the results are shown in Fig. 5. The pure ZrO_2 catalyst showed one broad low-temperature desorption peak ranging from 100 to 200 °C, indicating the presence of weak acid sites. The sulfation treatment at low sulfur content (5S-ZrO_2) increased the number of weak acid sites and also generated medium acid sites, corresponding to the desorption of NH_3, in the range of 240–400 °C, with the maximum at 266 °C. As the sulfur content was increased to 10 wt% (10S-ZrO_2), the second peak appeared to be broader and of somewhat higher intensity than that of the 5S-ZrO_2 catalyst. With an even higher sulfur content (15S-ZrO_2, 20S-ZrO_2 and 30SZrO_2), the second peak shifted towards a higher desorption temperature, indicating an increase in the acid strengths corresponding to the presence of the protonated sulfate species as observed by sulfur K-edge XANES analyses (Fig. 4).

The number of acid sites of all samples is shown in Table 2. The pure ZrO_2 had a low number of total acid sites (24 μmol g^{-1}). The addition of sulfur markedly enhanced the

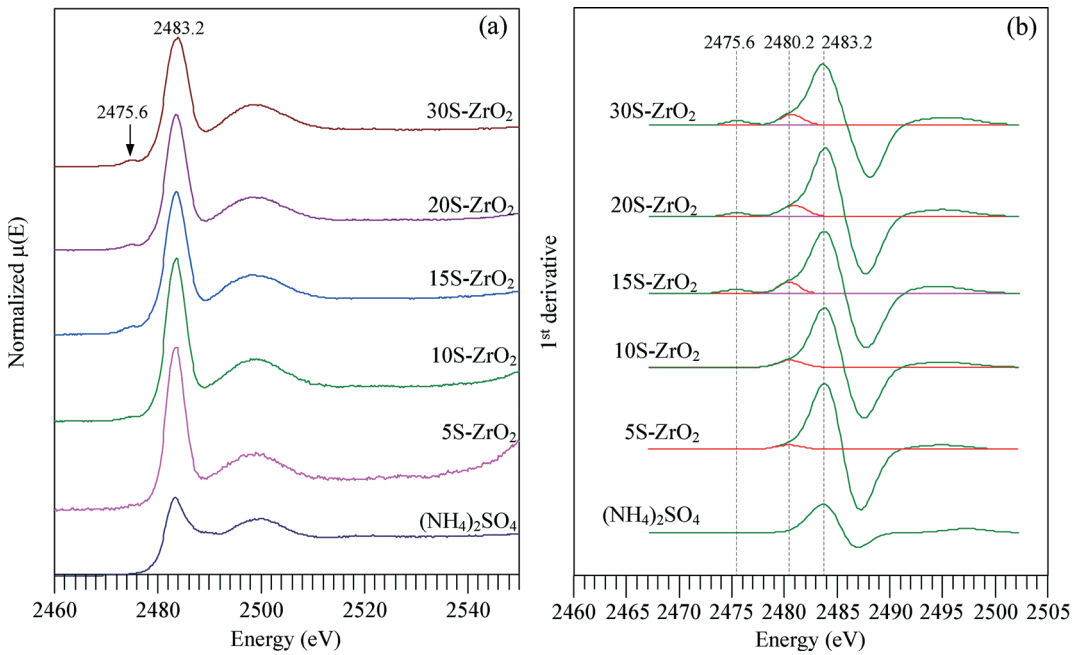

Fig. 4 Raw data (a) and first derivative (b) of sulfur K-edge XANES spectra of $(NH_4)_2SO_4$ and sulfated-zirconia materials.

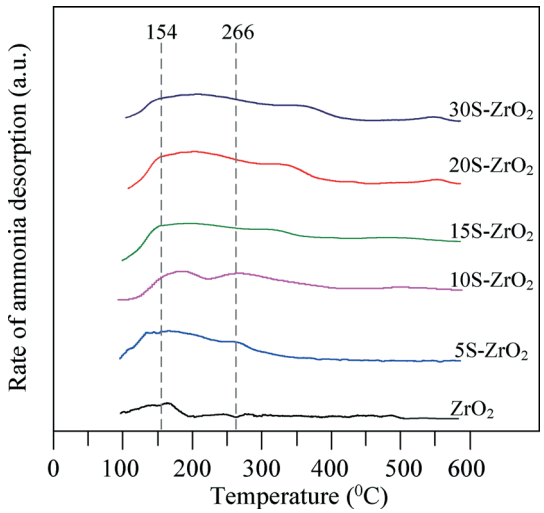

Fig. 5 NH_3-TPD profiles of the sulfated zirconia catalysts calcined at 550 °C.

total number of acid sites. Doping with 5–20 wt% sulfur gave total acid contents 3.96–12.75 times higher than that of the pure ZrO_2. A further increase in the sulfur content to 30 wt% caused a significant decrease in the number of total acid sites, suggesting that some sulfate groups had become embedded in the bulk of the sulfated zirconia catalysts.

3.2 Catalytic activity results

CO_2 hydrogenation was tested over CuO–ZnO–ZrO_2/sulfated-zirconia catalysts in a fixed-bed reactor at 20 bar. The catalytic activities were determined after 3 h on stream at the same GHSV. For all catalysts, CO, methanol and DME were found to be the major products; each also produced a trace amount of methane. The catalytic performance of the sulfated-zirconia catalysts prepared at different ratios is shown in Fig. 6 in terms of CO_2 conversion to oxygenated compounds (Fig. 6a), yield of DME (Fig. 6b) and yield of CO (Fig. 6c). The oxygenated compounds included methanol and DME produced from CO_2 hydrogenation and methanol dehydration, respectively.

Over the sulfur-free catalyst (ZrO_2) and at a reaction temperature of 240 °C, the CO_2-to-oxygenated compound conversion rate (Fig. 6a) was 2.6%. The CO_2 conversion decreased monotonically with increasing temperatures. This could be explained by the fact that CO_2 hydrogenation becomes kinetically less favored at higher temperatures.[43] However, in the presence of sulfated-zirconia catalysts, the CO_2-to-oxygenated compound conversions were considerably higher and followed a volcano-shaped trend with a maximum at a reaction temperature of 260 °C. This observation is potentially explained by the fact that the conversion of methanol to DME increases the equilibrium conversion of CO_2 hydrogenation to methanol.[8]

Fig. 6b shows the performance of the catalysts for converting methanol to DME. The ZrO_2 catalyst was found to be basically inactive for methanol dehydration; the maximum

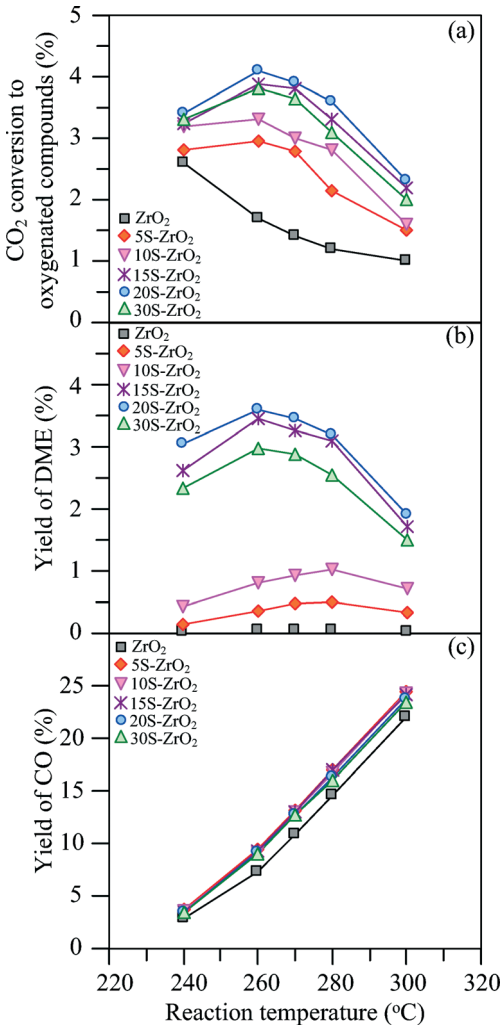

Fig. 6 CO_2 conversion to oxygenated compounds (a), yield of DME (b) and yield of CO (c) of the sulfated zirconia catalysts prepared with different sulfur loading contents.

DME yield was only 0.05% at a reaction temperature of 280 °C. The 5S-ZrO_2 and 10S-ZrO_2 catalysts showed a higher yield of DME compared to the ZrO_2 catalyst. The maximum DME yield for the 5S-ZrO_2 and 10S-ZrO_2 catalysts (0.5% and 1.0%, respectively) was achieved at 280 °C. The catalysts with higher sulfur contents (15S-ZrO_2, 20S-ZrO_2 and 30S-ZrO_2) exhibited a greater DME yield (1.5–3.6%), and these maximum conversions were achieved at a lower reaction temperature (260 °C). This suggests that the formation of DME from methanol dehydration over the two groups of catalysts may have occurred on different active sites.

To gain further insight into the relationship between the catalytic activity and properties of the sulfated zirconia catalysts prepared at different sulfur-to-zirconia ratios, we then attempted to construct a correlation between the DME yield and total number of acid sites of the sulfated zirconia catalysts; the results are shown in Fig. 7. At 240 °C, the DME yield slightly increased from 0.01 to 0.43% when the total number of acid sites was increased from 24 to 129 μmol g^{-1}

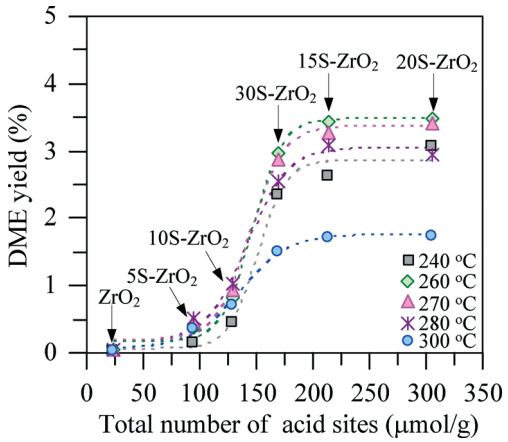

Fig. 7 Correlation of DME yield with the total number of acid sites at different reaction temperatures.

(*i.e.* the catalysts with low sulfur content). By increasing the total number of acid sites from 129 to 169 μmol g^{-1}, a dramatic increase in DME yield was observed. Similarly, the trend was also found for the other reaction temperatures. This implies that the formation of DME over the sulfated zirconia catalysts with low and high sulfur contents occurs *via* different mechanisms. With a further increase in the total acid sites, the DME yield no longer changes which is mainly attributed to the fast rate of methanol dehydration to DME.

Various mechanisms for the dehydration of methanol to DME have been proposed and studied. Bandiera and Naccache[44] proposed that two methanol molecules adsorbed simultaneously on the catalyst surface, forming two surface species ($[CH_3OH_2]^+$ and $[CH_3O]^-$), which then condensed to form DME and a water molecule. Kubelková *et al.*[45] predicted that a surface methoxy species *via* the protonated methanol $CH_3OH_2^+$ was initially formed and another methanol molecule reacted with the methoxy group to produce the DME product. Said *et al.*[32] studied the catalytic performance of sulfated zirconia catalysts and interpreted the mechanism for DME formation in terms of oxidation–reduction reactions in which one molecule of methanol adsorbed on an acid site and another methanol molecule adsorbed on a base site, which then condensed to produce DME and water. We agree that the dehydration of methanol to DME occurs at dual acid–base sites but we suggest that the details of the mechanism differ depending on the sulfur content of the sulfated zirconia catalysts.

Scheme 1 proposes the mechanism for the formation of DME from methanol dehydration over the sulfated zirconia catalysts with low (0–10S) and high (15–30S) sulfur content. The proposed molecular structures and mechanism are based on characterization analyses using FT-IR, TGA, and XANES techniques, performance test results, and previous findings in the literature.[32,44,45] As discussed above in the FT-IR and XANES results, at low sulfur content the sulfate group preferably forms as O=S(–O–Zr–)$_3$ (structure A). Thus, due to the inductive effect of the sulfate group, the zirconium atoms attached to the sulfate group act as Lewis acid sites for DME formation.[21,32] As the sulfur content is increased, the sulfate group forms as –SO_4 (structure B) and seems to cover the surface of the ZrO_2 cluster. It is important to note that the FT-IR and XANES spectra indicate that –Zr–OH (*i.e.* a protonated

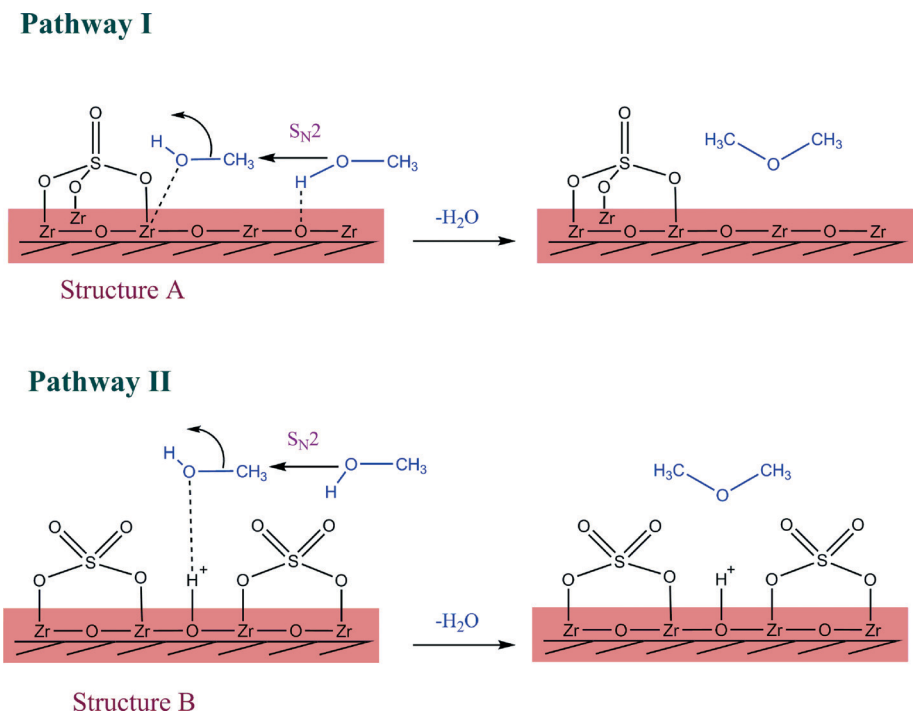

Scheme 1 Proposed mechanism for the formation of DME from methanol dehydration over the sulfated zirconia catalysts at low (pathway I) and high (pathway II) sulfur contents.

oxygen) is present in the high sulfur content catalysts only. This –Zr–OH plays a vital role in increasing DME production in the presence of high $–SO_4$ coverage since $–SO_4$ is a strong electron-withdrawing group. Thus, when $–SO_4$ covers the ZrO_2 surface it induces the neighboring –Zr–OH to become a strong Brønsted acid site, which in turn provides a proton to methanol. Therefore, the methanol-to-DME reaction mechanism at low and high sulfur content follows two separate pathways, as shown in Scheme 1. At low sulfur content (pathway I), one methanol molecule adsorbs on the Lewis acid site, and another methanol molecule adsorbs on a relatively weak Lewis base site (*i.e.* an oxygen atom of –Zr–O–Zr–) and then both undergo a reaction *via* the S_N2 transition state mechanism to produce a DME molecule.[46,47] In contrast, DME molecule generation at high sulfur content (pathway II)[48–50] takes place *via* the strong Brønsted acid site of –Zr–OH. In the first step, one methanol molecule adsorbs on –Zr–OH. Then, it reacts with another methanol molecule from the gas phase *via* the S_N2 type mechanism, resulting in a much higher DME yield than *via* pathway I.

The behavior of CO formation is shown in Fig. 6c. The CO yield of all catalysts was found to significantly increase with increasing temperature. However, only a small difference in the CO yield of all tested catalysts at each reaction temperature was observed. This might be the logical consequence of the fact that the reverse water-gas shift reaction proceeds very fast until equilibrium is achieved over Cu-containing catalysts.[51,52] The equilibrium is shifted towards the formation of CO with increasing temperature. This would explain why all tested catalysts behave more or less the same assuming that the reaction rate of the reverse water-gas shift reaction is much faster than the formation rates of methanol and dimethyl ether.

3.3 Stability of catalysts

Stability is a key factor in determining whether the sulfated-zirconia materials can be used as acid catalysts for dehydration reactions in industrial production. On the basis of the activity test and the proposed mechanism (Fig. 6, 7 and Scheme 1), the dehydration of methanol over the sulfated zirconia catalysts with low and high sulfur contents provided a significant difference in DME yields. Therefore, the stability of the two groups of catalysts was investigated; 10S-ZrO_2 and 20S-ZrO_2 catalysts represented low and high sulfur coverage, respectively, with pure ZrO_2 and H-ZSM-5 used as the reference. Before initiating the experiment, suitable testing conditions must be considered. This is because the direct synthesis of DME from CO_2 hydrogenation requires two functional catalysts: the CuO–ZnO–ZrO_2 catalyst and the sulfated zirconia catalyst. Note that these two catalysts can be deactivated over time. Generally, the deactivation of the Cu-based catalyst for methanol synthesis from CO_2 hydrogenation is caused by the loss of copper surface area due to the low Tammann temperature of copper and the exothermicity of the reaction.[53,54] In order to assess the real performance of the sulfated zirconia catalyst without the imposition of the CuO–ZnO–ZrO_2 catalyst, a stability test must be performed under conditions that can maintain a constant yield of methanol.

Fig. 8 shows the STY *versus* the time-on-stream of DME and methanol over four catalysts: CuO–ZnO–ZrO_2/ZrO_2, CuO–ZnO–ZrO_2/10S-ZrO_2, CuO–ZnO–ZrO_2/20S-ZrO_2 and CuO–ZnO–ZrO_2/H-ZSM-5. The STY of methanol over all catalyst systems was found to be almost constant during the 75 h experiment. This indicated that the methanol catalyst (CuO–ZnO–ZrO_2) had excellent stability. Regarding the STY of DME, the CuO–ZnO–ZrO_2/10S-ZrO_2 catalyst showed a substantial decrease in DME yield *ca.* 41.7% during the 75 h time-on-stream experiment, while the CuO–ZnO–ZrO_2/20S-ZrO_2 catalyst exhibited much greater durability, experiencing only a 16.9% reduction under identical reaction conditions. Saravanan *et al.*[28] reported two possible reasons for the successive decrease in the activity of the sulfated zirconia catalysts: poisoning by water molecules formed during the reaction and leaching of sulfate species from the catalyst in polar alcohol medium. According

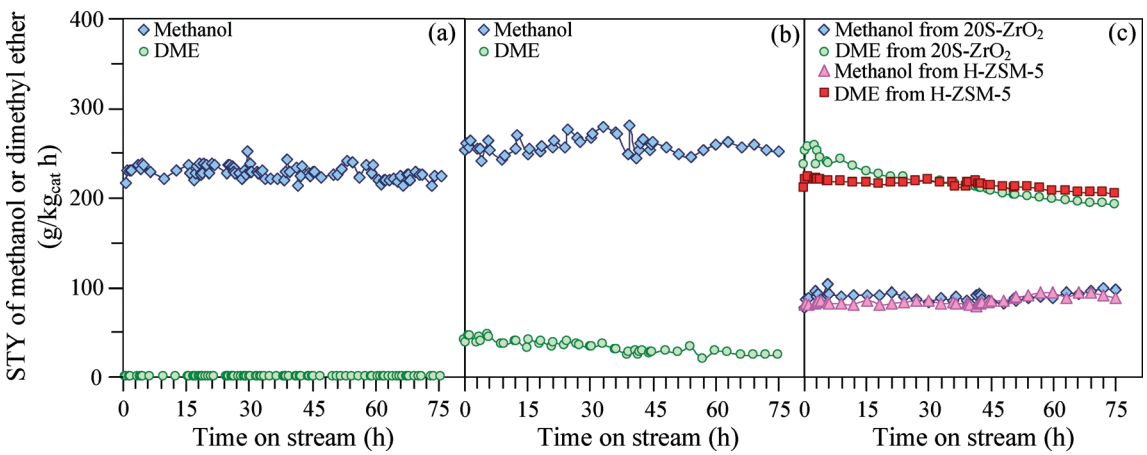

Fig. 8 Space-time yields of methanol and DME as a function of time-on-stream of CuO–ZnO–ZrO_2/ZrO_2 (a), CuO–ZnO–ZrO_2/10S-ZrO_2 (b), and CuO–ZnO–ZrO_2/20S-ZrO_2 and CuO–ZnO–ZrO_2/H-ZSM-5 (c). Reaction conditions: T = 260 °C, P = 2 MPa, flow rate = 60 mL min^{-1}.

to the mechanism we proposed above, for the catalyst with low sulfur content (10S-ZrO_2), methanol dehydrated in the Lewis acid–base sites. This is in harmony with the direct synthesis of DME from CO_2 hydrogenation, which produces a large amount of water when compared to either methanol dehydration or one-step synthesis of DME from syngas.[31,32] This produced water is the major cause of the poisoning at the active sites of the catalysts, since the water molecule competes with the methanol molecule for adsorption onto the Lewis acid sites (Zr^{4+}). This is the reason why the reduction of STY of DME over time is observed and this catalyst provides the maximum yield of DME at a higher reaction temperature (Fig. 6b). When the reaction temperature is increased, the desorption of the water molecules may regenerate the catalyst activity. In contrast, the 20S-ZrO_2 catalyst is mainly composed of Brønsted acid sites, which were slightly affected by the water.[28] Therefore, the deactivation rate of the 20S-ZrO_2 catalyst was much lower than that of the 10S-ZrO_2 catalyst.

CuO–ZnO–ZrO_2 catalysts are commonly deactivated through sulfur poisoning, but we observed no signs of deactivation of our CuO–ZnO–ZrO_2 catalyst. One of the following three hypotheses could explain the durability of this particular Cu-based catalyst. (1) Since the sulfated zirconia – an acid catalyst which was mixed with Cu–ZnO–ZrO_2, a methanol conversion catalyst, to form our catalytic system – was calcined at 550 °C for 2 h, only the stable form of the sulfate remained on the zirconia surface, the sulfate ions are not transferred from the sulfated zirconia to Cu–ZnO–ZrO_2 and therefore do not deactivate it. During the experiment, water and methanol are produced, but they cannot leach out sulfate ions, thus there is no sulfur source to poison the Cu-based catalyst. (2) The presence of ZnO in the catalyst improves sulfur resistance by forming thermodynamically stable ZnS,[9] thus the few sulfate ions that may have been leached out from the sulfated zirconia surface during the reaction are eliminated by Zn and the activity of the Cu-based catalyst remains constant. (3) While the leaching process of sulfate ions is the major cause of sulfated zirconia deactivation, the Cu-based catalyst exhibits excellent stability because the sulfate ions are not changed to H_2S, the most active form for poisoning a metal catalyst. [Note: the spent catalyst should be further characterized for better understanding of the deactivation phenomena, *e.g.*, coke deposition and leaching of sulfate ions.]

A benchmark between the new catalyst and a commercial catalyst is required to allow a straightforward comparison. In the present case, the stability of the 20S-ZrO_2 catalyst is compared to that of the H-ZSM-5 catalyst, as demonstrated in Fig. 8c. The STY of DME over the 20S-ZrO_2 catalyst was found to be higher than that of the H-ZSM-5 catalyst at the beginning of the experiment, indicating that the 20S-ZrO_2 catalyst was more active. However, the 20S-ZrO_2 catalyst exhibited a rapid decrease in the STY of DME while the STY of DME of H-ZSM-5 slightly decreased at approximately 2.85% of 75 h on stream, which was significantly lower than that of the 20S-ZrO_2 catalyst (16.9%). This indicates that the sulfated zirconia catalysts cannot be considered as practical catalysts at this stage since they cannot compete with the commercial H-ZSM-5 catalyst when long-term stability is considered. However, given that the stability of the sulfated zirconia catalyst is improved, it might be considered a good industrial acid catalyst due to its elevated activity and ease of preparation.

4. Conclusions

The physicochemical properties, activity and stability of the sulfated zirconia catalysts were strongly affected by the sulfur content on the zirconia surface. At low sulfur contents (5S-ZrO_2 and 10S-ZrO_2), the tridentate sulfate was formed on the zirconia surface and induced zirconium atoms to act as weak Lewis acid sites. These catalysts were active for methanol dehydration at relatively high reaction temperatures. At high sulfur contents (15S-ZrO_2, 20S-ZrO_2 and 30S-ZrO_2), a protonated sulfate species was formed and donated significant Brønsted acidity, which efficiently catalyzed the methanol dehydration even at relatively low reaction temperatures. In addition, the catalysts with high sulfur contents showed much greater stability than those with low sulfur contents because water molecules preferentially adsorbed on the Lewis acid sites. It was also demonstrated that Brønsted acidity is essentially important for the direct synthesis of DME from CO_2 hydrogenation. These findings may open up new applications of sulfated zirconia catalysts (combined with Cu-based catalysts) in the direct synthesis of DME from CO_2 hydrogenation that could lead to a sustainable fuel in the future.

Acknowledgements

This work was financially supported by the Thailand Research Fund (grant no. TRG5780258), the Center of Excellence on Petrochemical and Materials Technology (PETROMAT), the National Research University Project of Thailand (NRU), the Nanotechnology Center (NANOTEC), NSTDA, the Ministry of Science and Technology, Thailand, through its program of Center of Excellence Network, the Rayong Institute of Science and Technology Foundation, and the Kasetsart University Research and Development Institute (KURDI). The authors would like to thank the Synchrotron Light Research Institute (BL5.2: SUT-NANOTEC-SLRI XAS) for support in XAS measurement. Financial support for Mr. Tinnavat Permsirivanich from the Faculty of Engineering, Kasetsart University is also appreciated.

References

1 D. L. Royer, R. A. Berner and J. Park, *Nature*, 2007, **446**, 530–532.
2 A. Goeppert, M. Czaun, J.-P. Jones, G. K. S. Prakash and G. A. Olah, *Chem. Soc. Rev.*, 2014, **43**, 7995–8048.
3 O. Martin and J. Pérez-Ramírez, *Catal. Sci. Technol.*, 2013, **3**, 3343–3352.
4 E. V. Kondratenko, G. Mul, J. Baltrusaitis, G. O. Larrazábal and J. Pérez-Ramírez, *Energy Environ. Sci.*, 2013, **6**, 3112–3135.

5 K. Sato, Y. Tanaka, A. Negishi and T. Kato, *J. Power Sources*, 2012, **217**, 37–42.
6 T. H. Fleisch, A. Basu and R. A. Sills, *J. Nat. Gas Sci. Eng.*, 2012, **9**, 94–107.
7 G. Thomas, B. Feng, A. Veeraragavan, M. J. Cleary and N. Drinnan, *Fuel Process. Technol.*, 2014, **119**, 286–304.
8 W.-J. Shen, K.-W. Jun, H.-S. Choi and K.-W. Lee, *Korean J. Chem. Eng.*, 2000, **17**, 210–216.
9 M. V. Twigg and M. S. Spencer, *Appl. Catal., A*, 2001, **212**, 161–174.
10 O. Oyola-Rivera, M. A. Baltanás and N. Cardona-Martínez, *J. CO_2 Util.*, 2015, **9**, 8–15.
11 F. Studt, I. Sharafutdinov, F. Abild-Pedersen, C. F. Elkjær, J. S. Hummelshøj, S. Dahl, I. Chorkendorff and J. K. Nørskov, *Nat. Chem.*, 2014, **6**, 320–324.
12 F. Arena, K. Barbera, G. Italiano, G. Bonura, L. Spadaro and F. Frusteri, *J. Catal.*, 2007, **249**, 185–194.
13 G. Wengui, W. Hua, W. Yuhao, G. Wei and J. Miaoyao, *J. Rare Earths*, 2013, **31**, 470–476.
14 Y. Zhang, D. Li, Y. Zhang, Y. Cao, S. Zhang, K. Wang, F. Ding and J. Wu, *Catal. Commun.*, 2014, **55**, 49–52.
15 D. Mao, J. Xia, B. Zhang and G. Lu, *Energy Convers. Manage.*, 2010, **51**, 1134–1139.
16 T. Takeguchi, K.-I. Yanagisawa, T. Inui and M. Inoue, *Appl. Catal., A*, 2000, **192**, 201–209.
17 V. Vishwanathan, K.-W. Jun, J.-W. Kim and H.-S. Roh, *Appl. Catal., A*, 2004, **276**, 251–255.
18 D. Mao and X. Guo, *Energy Technol.*, 2014, **2**, 882–888.
19 G. Bonura, M. Cordaro, C. Cannilla, F. Arena and F. Frusteri, *Appl. Catal., B*, 2014, **152–153**, 152–161.
20 H. Ban, C. Li, K. Asami and K. Fujimoto, *Catal. Commun.*, 2014, **54**, 50–54.
21 G. D. Yadav and J. J. Nair, *Microporous Mesoporous Mater.*, 1999, **33**, 1–48.
22 X. Li, K. Nagaoka and J. A. Lercher, *J. Catal.*, 2004, **227**, 130–137.
23 G. A. Urzhuntsev, E. V. Ovchinnikova, V. A. Chumachenko, S. A. Yashnik, V. I. Zaikovsky and G. V. Echevsky, *Chem. Eng. J.*, 2014, **238**, 148–156.
24 M. A. Ahmed, *Fuel Process. Technol.*, 2011, **92**, 1121–1128.
25 G. D. Yadav and A. D. Murkute, *J. Catal.*, 2004, **224**, 218–223.
26 Y. Zhang, W.-T. Wong and K.-F. Yung, *Appl. Energy*, 2014, **116**, 191–198.
27 M. L. Grecea, A. C. Dimian, S. Tanase, V. Subbiah and G. Rothenberg, *Catal. Sci. Technol.*, 2012, **2**, 1500–1506.
28 K. Saravanan, B. Tyagi and H. C. Bajai, *Catal. Sci. Technol.*, 2012, **2**, 2512–2520.
29 M. Popova, Á. Szegedi, A. Ristić and N. N. Tušar, *Catal. Sci. Technol.*, 2014, **4**, 3993–4000.
30 M. Waqif, J. Bachelier, O. Saur and J.-C. Lavalley, *J. Mol. Catal.*, 1992, **72**, 127–138.
31 F. S. Ramos, A. M. Duarte de Farias, L. E. P. Borges, J. L. Monteiro, M. A. Fraga, E. F. Sousa-Aguiar and L. G. Appel, *Catal. Today*, 2005, **101**, 39–44.
32 A. E.-A. A. Said, M. M. A. El-Wahab and M. A. El-Aal, *J. Mol. Catal. A: Chem.*, 2014, **394**, 40–47.
33 N. A. Khan, D. K. Mishra, I. Ahmed, J. W. Yoon, J.-S. Hwang and S. H. Jhung, *Appl. Catal., A*, 2013, **452**, 34–38.
34 A. Osatiashtiani, A. F. Lee, D. R. Brown, J. A. Melero, G. Morales and K. Wilson, *Catal. Sci. Technol.*, 2014, **4**, 333–342.
35 Y. Sun, S. Ma, Y. Du, L. Yuan, S. Wang, J. Wang, F. Deng and F.-S. Xiao, *J. Phys. Chem. B*, 2005, **109**, 2567–2572.
36 C. Morterra, G. Cerrato, G. Meligrana, M. Signoretto, F. Pinna and G. Strukul, *Catal. Lett.*, 2001, **73**, 113–119.
37 F. Haase and J. Sauer, *J. Am. Chem. Soc.*, 1998, **120**, 13503–13512.
38 X. Dou, D. Mohan, C. U. Pittman Jr. and S. Yang, *Chem. Eng. J.*, 2012, **198–199**, 236–245.
39 S.-Y. Chen, L.-Y. Jang and S. Cheng, *J. Phys. Chem. B*, 2006, **110**, 11761–11771.
40 C. Liu, T. Bolin, P. Northrup, S. Lee, C. McEnally, P. Kelleher, L. Pfefferle and G. L. Haller, *Top. Catal.*, 2014, **57**, 693–705.
41 C. Liu, L. D. Pfefferle and G. L. Haller, *Top. Catal.*, 2014, **57**, 774–784.
42 S. Pin, T. Huthwelker, M. A. Brown and F. Vogel, *J. Phys. Chem. A*, 2013, **117**, 8368–8376.
43 Y. Zhang, Q. Sun, J. Deng, D. Wu and S. Chen, *Appl. Catal., A*, 1997, **158**, 105–120.
44 J. Bandiera and C. Naccache, *Appl. Catal.*, 1991, **69**, 139–148.
45 L. Kubelková, J. Nováková and K. Nedomová, *J. Catal.*, 1990, **124**, 441–450.
46 S. R. Blaszkowski and R. A. van Santen, *J. Am. Chem. Soc.*, 1996, **118**, 5152–5153.
47 H. Yang, H. Song, H. Zhang, P. Chen and Z. Zhao, *J. Mol. Catal. A: Chem.*, 2014, **381**, 54–60.
48 B. C. Gates and L. N. Johanson, *J. Catal.*, 1969, **14**, 69–76.
49 P. K. Kiviranta-Pääkkönen and L. K. Struckmann, *Ind. Eng. Chem. Res.*, 1998, **37**, 18–24.
50 S. Hosseininejad, A. Afacan and R. E. Hayes, *Chem. Eng. Res. Des.*, 2012, **90**, 825–833.
51 J. Yoshihara and C. T. Campbell, *J. Catal.*, 1996, **161**, 776–782.
52 T. Tagawab, G. Pleizier and Y. Amenomiya, *Appl. Catal.*, 1985, **18**, 285–293.
53 F. S. R. Barbosa, V. S. O. Ruiz and J. L. F. Monteiro, *Catal. Lett.*, 2008, **126**, 173–178.
54 T. Witoon, T. Permsirivanich, W. Donphai, A. Jaree and M. Chareonpanich, *Fuel Process. Technol.*, 2013, **116**, 72–78.

เรื่องที่ 4

Thongthai Witoon*, Sittisut Bumrungsalee, Metta Chareonpanich, Jumras Limtrakul, Effect of hierarchical meso–macroporous alumina-supported copper catalyst for methanol synthesis from CO_2 hydrogenation, Energy Conversion and Management 103 (2015) 886–894. (IF 2015 = 4.801).

Energy Conversion and Management 103 (2015) 886–894

Contents lists available at ScienceDirect

Energy Conversion and Management

journal homepage: www.elsevier.com/locate/enconman

Effect of hierarchical meso–macroporous alumina-supported copper catalyst for methanol synthesis from CO_2 hydrogenation

Thongthai Witoon [a,b,c,d,*], Sittisut Bumrungsalee [a], Metta Chareonpanich [a,b,c,d], Jumras Limtrakul [b,c,e]

[a] Center of Excellence on Petrochemical and Materials Technology, Department of Chemical Engineering, Faculty of Engineering, Kasetsart University, Bangkok 10900, Thailand
[b] Center for Advanced Studies in Nanotechnology and Its Applications in Chemical Food and Agricultural Industries, Kasetsart University, Bangkok 10900, Thailand
[c] NANOTEC-KU-Center of Excellence on Nanoscale Materials Design for Green Nanotechnology, Kasetsart University, Bangkok 10900, Thailand
[d] PTT Group Frontier Research Center, PTT Public Company Limited, 555 Vibhavadi Rangsit Road, Chatuchak, Bangkok 10900, Thailand
[e] Department of Materials Science and Engineering, Institute of Molecular Science and Engineering Vidyasirimedhi Institute of Science and Technology, Rayong 21210, Thailand

ARTICLE INFO

Article history:
Received 22 May 2015
Accepted 11 July 2015
Available online 23 July 2015

Keywords:
CO_2 hydrogenation
Hierarchical meso–macroporous alumina
Methanol
Catalyst
Deactivation
Stability

ABSTRACT

Effects of pore structures of alumina on the catalytic performance of copper catalysts for CO_2 hydrogenation were investigated. Copper-loaded hierarchical meso–macroporous alumina (Cu/HAl) catalyst exhibited no significant difference in terms of CO_2 conversion with copper-loaded unimodal mesoporous alumina (Cu/UAl) catalyst. However, the selectivity to methanol and dimethyl ether of the Cu/HAl catalyst was much higher than that of the Cu/UAl catalyst. This was attributed to the presence of macropores which diminished the occurrence of side reaction by the shortening the mesopores diffusion path length. The Cu/HAl catalyst also exhibited much higher stability than the Cu/UAl catalyst due to the fast diffusion of water out from the catalyst pellets, alleviating the oxidation of metallic copper to CuO.

1. Introduction

Concerns over depletion of fossil fuels and rising CO_2 emissions are driving the need for recycling CO_2 into alternative fuels. The catalytic hydrogenation of CO_2 to methanol is considered one of the most promising processes because methanol can be used as an energy carrier for fuel cell application [1–3]. Moreover, methanol can be converted to dimethyl ether (DME) [4,5] which is considered as a feasible fuel for diesel engines [6,7], or into higher hydrocarbons according to methanol-to-olefins (MTO) process [8–11].

The catalysts contained Cu as a main component together with different promoters such as Zn, Zr, Ga, Al, Si and Mg [12–14] were found to be active for CO_2 hydrogenation toward methanol. Along with main component, an appropriate support is of imperative importance because it can act not only as dispersant but also as stabilizer for the main component. Moreover, the interface contact between the main component and the support can cause synergetic effect which provides the active centers for adsorption of reactants and products, enhancing the catalytic performance. As a consequence, most of recent studies have focused on the development of Cu-based catalysts at the nanoscale by means of incorporating promoters [12–15], fine tuning catalyst compositions [12,16] and improving preparation procedure [13,17,18].

Another important impact of supports is the transport of reactants and products. Although the nanoporous catalysts have a large internal surface area which contributes to their high intrinsic catalytic activity per unit catalyst weight, they usually contain small pore size, limiting the molecules' accessibility to the active sites [19–21]. It was reported that the hierarchical meso–macropore structure could diminish diffusion limitations [19,22,23] and extend catalyst lifetime [24–26]. In addition to the activity, the transport of reactants and products within the catalyst pellets might also influence the product selectivity [19,27]. Iglesia [27] proposed that, for Fischer–Tropsch synthesis reaction, the long chain hydrocarbon selectivity was increased by diffusion-enhanced α-olefin re-adsorption phenomena. Despite the significant number of papers reporting the beneficial effect of the hierarchical porous material, its application as supported copper catalyst for methanol synthesis from CO_2 hydrogenation has not yet been studied.

Herein, we report the diffusion-enhanced effects of the hierarchical meso–macroporous structure of Cu/Al_2O_3 catalyst for CO_2 hydrogenation reaction. Cu-loaded unimodal porous alumina catalyst was employed for the purpose of comparison. The physicochemical properties of the catalysts were characterized by means of scanning electron microscope (SEM), N_2-physisorption, mercury porosimetry, X-ray diffraction (XRD), N_2O chemisorption,

* Corresponding author at: Center of Excellence on Petrochemical and Materials Technology, Department of Chemical Engineering, Faculty of Engineering, Kasetsart University, Bangkok 10900, Thailand. Tel.: +66 2579 2083; fax: +66 2561 4621.
E-mail address: fengttwi@ku.ac.th (T. Witoon).

http://dx.doi.org/10.1016/j.enconman.2015.07.033
0196-8904/

H_2-temperature-programmed reduction, pyridine-temperature-programmed desorption.

2. Experimental

2.1. Preparation of alumina supports

Hierarchical meso–macroporous alumina (HAl) was prepared following the method described by Tokudome et al. [28]. In brief, 0.08 g poly(ethylene oxide) (PEO), having viscosity-averaged molecular weight of 1×10^6, was dissolved in a mixture of 4.0 mL ethanol and 5.5 mL deionized water at room temperature for 12 h. Then 4.32 g aluminum chloride hexahydrate ($AlCl_3{\cdot}6H_2O$) was added to the PEO–water–ethanol solution that was being stirred at room temperature until the homogeneous solution was achieved. 3.75 mL propylene oxide (PO) was added into the solution in order to initiate the hydrolysis-condensation reaction. After stirring for 1 min, the resultant homogeneous solution was transferred into the glass tube, sealed and kept at 40 °C for gelation. Subsequently, the wet gel was aged for 24 h and dried at 40 °C. The obtained alumina monolith was calcined at 600 °C in air at heating rate of 10 °C/min for 12 h. Unimodal mesoporous alumina (UAl) was prepared using the similar procedure as mentioned above except the addition of PEO.

2.2. Preparation of copper-loaded alumina catalysts

In order to clearly distinguish the effects of the presence of macropores, the alumina supports were ground and sieved into two fractions, 0.075–0.090 mm and 0.850–2.000 mm denoted as -S and -L, respectively. 10 wt% copper-loaded alumina catalysts were prepared by incipient wetness impregnation method. The calcined unimodal and hierarchical porous alumina supports were impregnated with the desired amount of copper nitrate trihydrate ($Cu(NO_3)_2{\cdot}3H_2O$) in aqueous solution. The slurry mixture was stirred at 60 °C for 2 h, dried at 100 °C for 12 h and calcined at 600 °C and a heating rate of 2 °C/min for 2 h. The copper-loaded unimodal and hierarchical alumina catalysts were designated as Cu/UAl and Cu/HAl, respectively.

2.3. Characterization of copper-loaded alumina catalysts

The surface morphology of the alumina supports was assessed with the application of a scanning electron microscope (SEM; FEI Quanta 450) equipped with energy-dispersive X-ray spectroscopy (EDS). The SEM measurement was taken at 20.0 kV. The samples were sputter–coated with gold prior to analysis.

The elemental analysis of the catalysts was tested with inductively coupled plasma–optical emission spectroscopy (ICP–OES, Optima 4300 DV, Perkin-Elmer).

The macropores size distribution was measured with a mercury porosimetry (PoreMaster 33). The BET surface area, mesopores size distribution and pore volume of the alumina supports and the Cu-loaded alumina catalysts were determined by N_2-sorption measurement with a Quantachrome Autosorb-1C instrument at −196 °C. The copper (Cu^0) surface area of the catalysts was obtained by N_2O-titration measurements as described elsewhere [12].

X-ray diffraction (XRD) patterns of the alumina supports and the Cu-loaded alumina catalysts were attained on a diffractometer (Bruker D8 Advance) with Cu Kα radiation. The measurements were made at temperatures in a range of 15–75° on 2θ with a step size of 0.05°. The diffraction patterns were analyzed according to the Joint Committee on Powder Diffraction Standards (JCPDS).

Temperature programmed reduction (TPR) experiments were conducted using a DSC–TGA 2960 thermal analyzer. A 10 mg sample was pretreated in a flow of N_2 (100 mL/min) at a rate of 10 °C/min until 400 °C was achieved; the 400 °C temperature was maintained for 30 min, then the sample was cooled to 100 °C. Once the 100 °C temperature was reached and stabilized, the sample was heated under flowing 10% v/v H_2 (He as a balance gas) at a heating rate of 4 °C/min from 100 °C to 400 °C.

Temperature programmed desorption (TPD) experiments were performed with the same apparatus as the TPR measurement using pyridine as a probe molecule following the method described by Mohamed and Abu-Zied [29]. Prior to pyridine adsorptions, the alumina supports and the Cu-loaded alumina catalysts were calcined at 400 °C to remove physically and chemically adsorbed water from their surface. Then the samples were transferred into desiccator containing liquid pyridine. The samples were maintained in contact with pyridine vapor at room temperature for a week, prior to acidity measurements. The pyridine desorption measurement was conducted in a flow of N_2 (100 mL/min) at a heating rate of 4 °C/min from room temperature to 600 °C. The amount of acidity was determined from the weight loss due to the desorption of pyridine.

2.4. Catalytic activity test

CO_2 hydrogenation was carried out in a fixed–bed stainless steel reactor (7.75 mm inner diameter). In a typical experiment, 0.5 g catalyst was diluted with 0.5 g inert silica sand. The catalyst was reduced in situ under atmospheric pressure with flowing H_2 (60 mL/min) at 350 °C and a heating rate of 2 °C/min for 4 h. After the reduction, the temperature was cooled to 200 °C under flowing N_2; subsequently a flow of CO_2 and H_2 mixture (CO_2:H_2 molar ratio of 1:3) was fed through the reactor. The feed flow rate was set at 60 mL/min. The reactor pressure was slowly raised to 30 bars, and the reactor was heated to a variety of temperatures (240, 260, 280, 300 and 320 °C). The effluent gaseous products were analyzed by using gas chromatography. Analysis of H_2, CO, CO_2, and N_2 was performed using GC–2014 gas chromatography equipped with a thermal conductivity detector (TCD) and a Unibead-C column. Methanol, DME and other hydrocarbon products were analyzed by using GC 8A equipped with a flame ionization detector (FID) and a Chromosorb WAW (20% PEG) column. The activity–selectivity data were calculated by mass balance from an average of three independent measurements. The selectivity has been calculated taking into account three major products, including methanol, CO and DME, i.e. only a trace amount of methane was observed at 320 °C which was excluded for selectivity calculation. The errors were within ±3%. CO_2 conversion, selectivity to methanol, CO and DME are defined as follows:

$$\text{CO}_2\text{ conversion }(\%) = \frac{(\text{moles methanol} + (2 \times \text{moles DME}) + \text{moles CO}) \times 100}{\text{moles CO}_{2,\text{in}}}$$

$$\text{Methanol selectivity }(\%) = \frac{\text{moles methanol} \times 100}{\text{moles methanol} + (2 \times \text{moles DME}) + \text{moles CO}}$$

$$\text{CO selectivity }(\%) = \frac{\text{moles CO} \times 100}{\text{moles methanol} + (2 \times \text{moles DME}) + \text{moles CO}}$$

$$\text{DME selectivity }(\%) = \frac{2 \times \text{moles DME} \times 100}{\text{moles methanol} + (2 \times \text{moles DME}) + \text{moles CO}}$$

3. Results and discussion

The apparent morphology of alumina supports was examined by means of SEM. Hierarchical meso–macroporous alumina (HAl) sample (Fig. 1a) exhibited the presence of 3-dimentionally

interconnected macropores with a uniform size of ca. 2 μm whereas unimodal mesoporous alumina (UAl) sample (Fig. 1b) showed a dense surface, caused by an aggregation of alumina nanopartciles, and contained no macropores. Hg-porosimetry was conducted to complement the SEM analysis. The HAl sample (Fig. 1c) possessed two different scales of a bimodal pore size distribution: 0.005–0.020 μm and 1–3 μm. The latter scale centered at 1.77 μm corresponding to the macropores as observed by the SEM image (Fig. 1a). The UAl sample (Fig. 1d) showed a broad peak in the region 0.005–0.020 μm (Fig. 1d) representing the interparticle spaces between alumina nanoparticles. The pore size in the mesopores region of both samples was further investigated by N_2-sorption measurement.

Fig. 2a and b shows the N_2 adsorption–desorption isotherm and the corresponding pore size distribution of the UAl and HAl supports and the Cu/UAl and Cu/HAl catalysts. Textural properties of those samples are summarized in Table 1. Both UAl and HAl samples exhibited a type IV isotherm with a H_2 hysteresis loop, indicating that both samples contained mesopores with an ink-bottle structure. After calcination of copper nitrate-loaded alumina supports (Cu/UAl and Cu/HAl catalysts), the type of isotherm for both catalysts was remained the same which was an indication for preservation of the mesopore structure. A monotonic decrease in BET surface areas, pore volumes and pore diameters of Cu/UAl and Cu/HAl catalysts compared to the parent ones could be attributed to the deposition of copper oxide in the mesopores of alumina supports.

XRD pattern of the UAl and HAl samples is shown in Fig. 3. Both samples exhibited two broad peaks centered at 2θ angles of 45.7° and 66.6°, characteristics of an amorphous structure. For Cu/UAl and Cu/HAl catalysts, the XRD patterns were identical to those of the supports, i.e., no discernible peaks associated with copper oxide species were detected. Previous studies have reported that the dispersion capacity of copper oxide on the surface of alumina is 0.75 mmol Cu^{2+}/100 m^2 Al_2O_3 [30,31]. The actual copper loading determined by ICP analysis of the Cu/UAl and Cu/HAl catalysts was about 10.24 and 10.54 wt%, which were equivalent to 0.56 mmol Cu^{2+}/100 m^2 Al_2O_3 and 0.67 mmol Cu^{2+}/100 m^2 Al_2O_3, respectively. This indicated that copper oxide particles highly dispersed in the alumina matrix at the atomic level, consequently, no formation of CuO bulk on the surface of alumina.

The reducibility of CuO over two different supports was observed by H_2-TPR; the result is shown in Fig. 4. The H_2-TPR profile of the Cu/UAl and Cu/HAl catalysts appeared the reduction peak centered at around 261 and 258 °C, an indication of a reduction of highly dispersed CuO nanoparticles [31–33]. Obviously, CuO species were continuously reduced from 290 to 400 °C, indicating a strong interaction between CuO species and alumina supports, i.e., copper was incorporated into the alumina matrix, possibly a formation of a spinel $CuAl_2O_4$ structure [31–33].

Fig. 5 shows pyridine-TPD measurement of the alumina supports and Cu-loaded alumina catalysts. Also, the quantitative estimation of acid sites is shown in Table 1. The UAl and HAl supports exhibited a similar desorption pattern with two distinct regions of 300–390 °C and 400–450 °C, indicating the existence of medium and strong acid sites on the surface of the alumina supports. Adding Cu onto the alumina supports (Cu/UAl and Cu/HAl catalysts) significantly reduced the total number of acid sites and the acid strengths, possibly due to the interaction between CuO and unsaturated aluminum ion. Also shown in Table 1, the Cu surface area of the Cu/UAl catalyst was slightly higher than the Cu/HAl catalyst which could be attributed to the higher surface area of the UAl support. All characterization results clearly indicate that the major difference between Cu/UAl and Cu/HAl catalysts is the presence of macropores in Cu/HAl catalyst.

Fig. 6 shows CO_2 conversion and the production selectivity in terms of methanol, CO and DME. It was found that CO_2 conversion of all catalysts monotonically increased with ascending reaction temperature (Fig. 6a). The CO_2 conversion at each reaction temperature of the Cu/HAl-S catalyst was found to be lower than

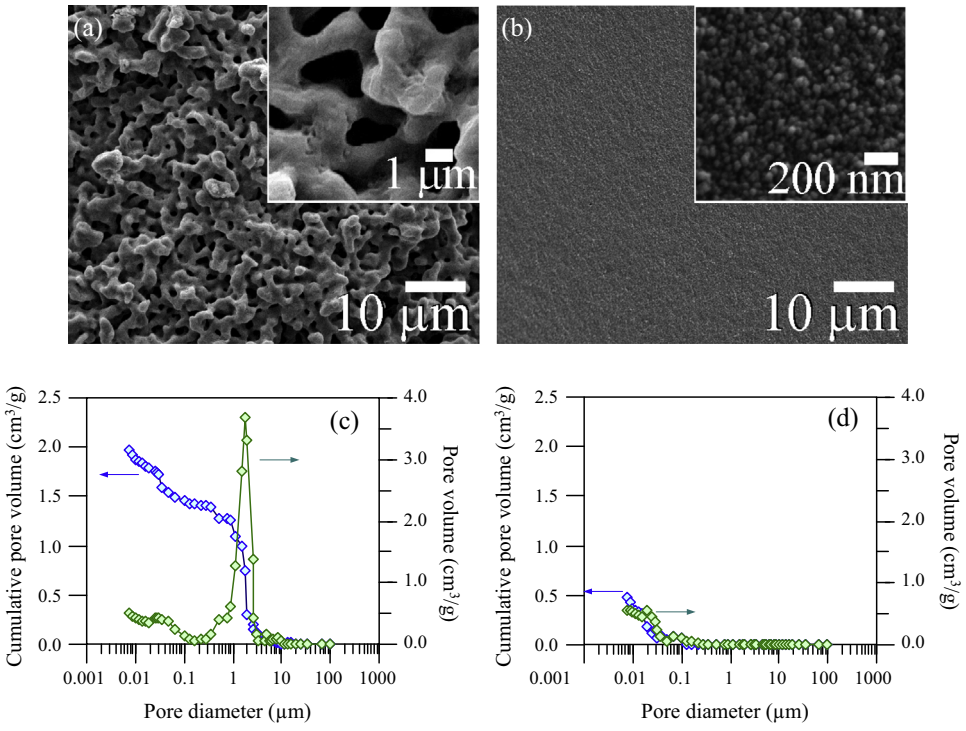

Fig. 1. SEM images (a and b) and pore size distribution measured by mercury porosimetry (c and d) of unimodal mesoporous alumina (UAl) and hierarchical meso–macroporous alumina (HAl) supports.

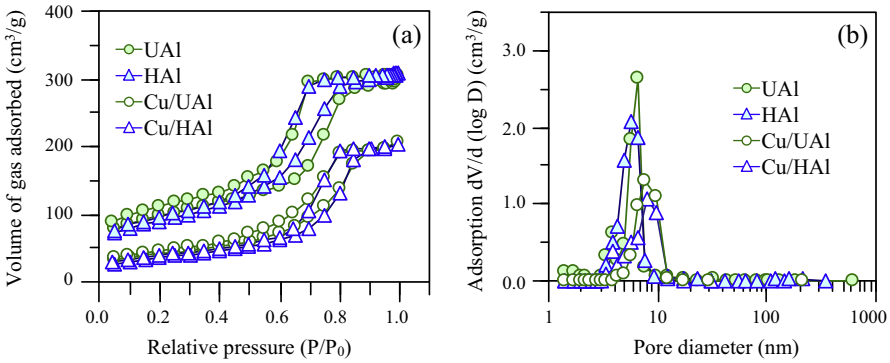

Fig. 2. N_2-sorption isotherms (a) and pore size distribution (b) of UAl and HAl supports and Cu/UAl and Cu/HAl catalysts.

Table 1
Textural properties, copper surface area, and surface acidic properties of the alumina supports and the Cu-loaded alumina catalysts.

Catalysts	BET surface area (m^2/g)	Pore volume (cm^3/g)	Copper surface area (m^2/g)	Medium acid sites (mmol/g)	Strong acid sites (mmol/g)	Total acid sites (mmol/g)
UAl	324	0.51	–	0.37	0.87	1.24
HAl	275	0.45	–	0.22	0.75	0.97
Cu/UAl	154	0.29	1.87	0.15	0.14	0.29
Cu/HAl	124	0.24	1.50	0.12	0.12	0.24

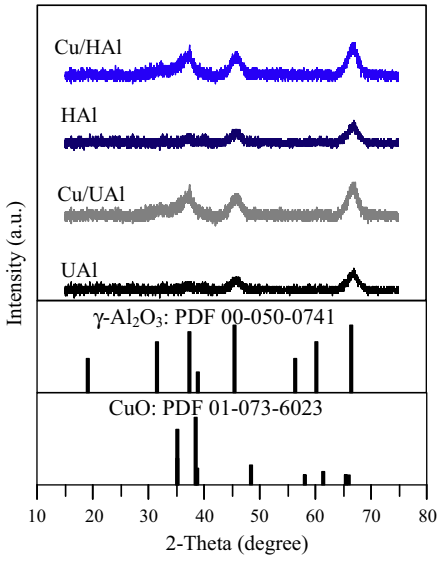

Fig. 3. XRD patterns of UAl and HAl supports and Cu/UAl and Cu/HAl catalysts.

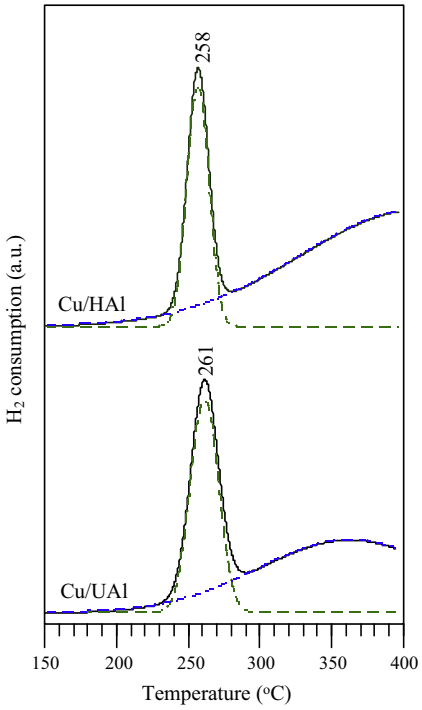

Fig. 4. H_2-TPR profiles of Cu/UAl and Cu/HAl catalysts.

the Cu/UAl-S catalyst due to a lower Cu surface area (Table 1) of the Cu/HAl-S catalyst so that the activity was re-calculated and was defined as CO_2 conversion per Cu surface area which represented the intrinsic activity and the inherent property of the catalysts; the result is shown in Fig. 1S. The slight difference in CO_2 conversion at each reaction temperature was observed when comparing between the Cu/HAl and the Cu/UAl catalysts at the identical particle size. This indicates that the mesopores (~7 nm) of the Cu/HAl and Cu/UAl catalysts are large enough to facilitate diffusion of gas molecules from bulk fluid to active sites located inside the mesopores, i.e., no existence of pore diffusion (internal diffusion) resistance. In other words, the presence of macropores does not significantly contribute to the CO_2 conversion. However, the effect of macropores becomes more pronounced by comparing the results in terms of selectivity. Comparing between the Cu/HAl-S and the Cu/UAl-S catalysts, the Cu/HAl-S catalyst exhibited higher methanol (Fig. 6b) and DME (Fig. 6d) selectivities and lower CO selectivity at any reaction temperature (Fig. 6c). The similar trend was also observed when the catalysts with the larger particle size (Cu/HAl-L and Cu/UAl-L) were compared.

In fact, CO_2 hydrogenation over methanol synthesis catalyst involves two competitive reactions. The first one is the targeted methanol synthesis (Eq. (1)) and the second one is reverse water–gas shift (RWGS) reaction (Eq. (2)). Methanol formed in Eq. (1) can undergoes dehydration to produce DME and water (Eq. (3)) over acidic sites, that present on the surface of the alumina

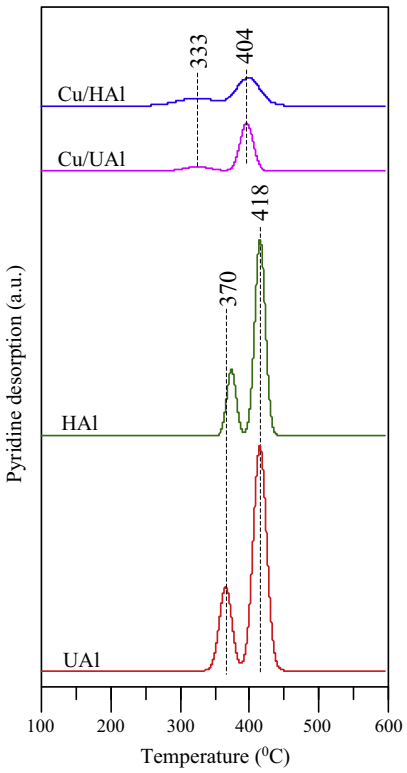

Fig. 5. Pyridine-TPD profiles of Cu/UAl and Cu/HAl catalysts.

supports as indicated by pyridine-TPD. In addition, methanol can subsequently decompose to produce carbon monoxide and hydrogen at a temperature above 200 °C (Eq. (4)) [34,35]. The occurrence of these different pathways strongly influences the product distribution.

$$CO_2 + 3H_2 \leftrightarrow CH_3OH + H_2O \quad \Delta H^\circ = -49.4\ \text{kJ mol}^{-1} \tag{1}$$

$$CO_2 + H_2 \leftrightarrow CO + H_2O \quad \Delta H^\circ = +41.2\ \text{kJ mol}^{-1} \tag{2}$$

$$2CH_3OH \leftrightarrow CH_3OCH_3 + H_2O \quad \Delta H^\circ = -23.4\ \text{kJ mol}^{-1} \tag{3}$$

$$CH_3OH \leftrightarrow CO + 2H_2 \quad \Delta H^\circ = +90.6\ \text{kJ mol}^{-1} \tag{4}$$

It should be mentioned again that the active species between the Cu/HAl and Cu/UAl catalysts are very similar in nature. This indicates that the transport of reactant and products within the catalyst pellet affects the product selectivity. Bonura et al. [35] reported that the space velocity played a vital role on the product selectivity from CO_2 hydrogenation reaction. Increasing the space velocity from 10,000 to 80,000 h^{-1} led to the progressive increase of the methanol selectivity at expense of carbon monoxide which could be due to the potential occurrence of side reactions, i.e., methanol decomposition (Eq. (4)). The similar trend was also observed by Zhang et al. [36] and Gao et al. [37].

Similar to the increase of space velocity, the macropores provided a fast diffusion of methanol out from the catalyst pellets. In addition, the diffusion distance inside the mesopores of the Cu/HAl-S catalyst was shorter than that of the Cu/UAl-S catalyst when compared at the same particle size (see Scheme 1). These

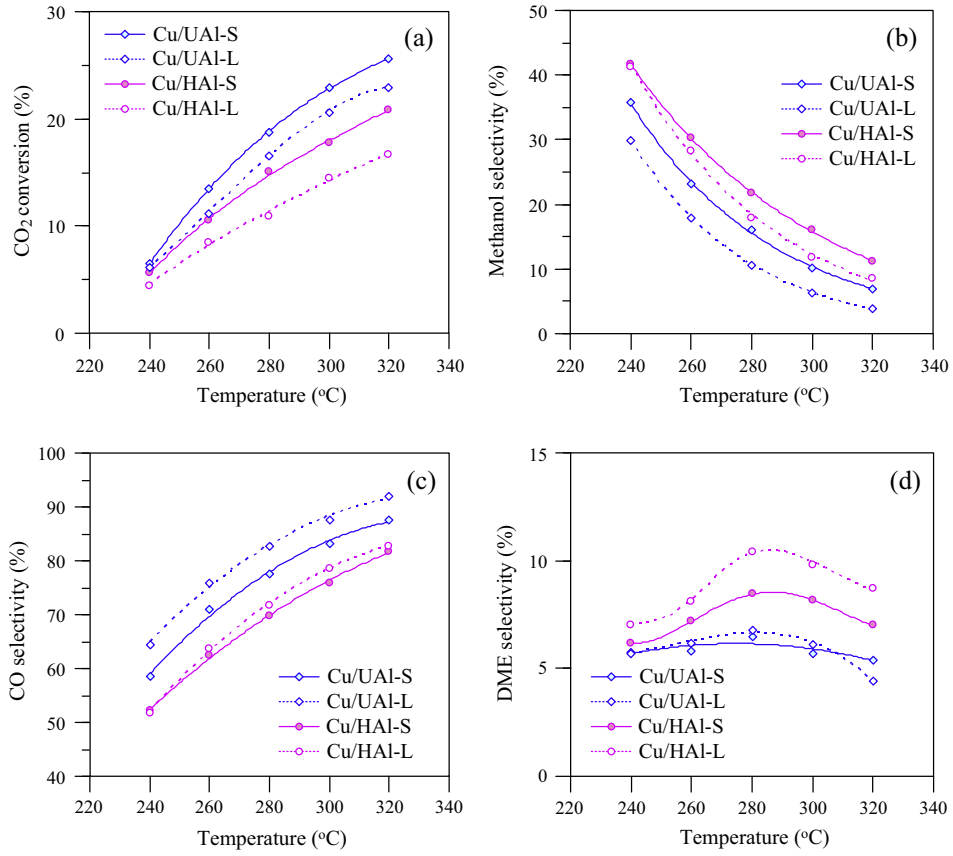

Fig. 6. CO_2 conversion (a), methanol selectivity (b), CO selectivity (c) and DME selectivity (D) as a function of reaction temperature of Cu/UAl-S, Cu/UAl-L, Cu/HAl-S and Cu/HAl-L catalysts. S and L are denoted as the average pellet size of 0.0825 and 1.425 mm, respectively.

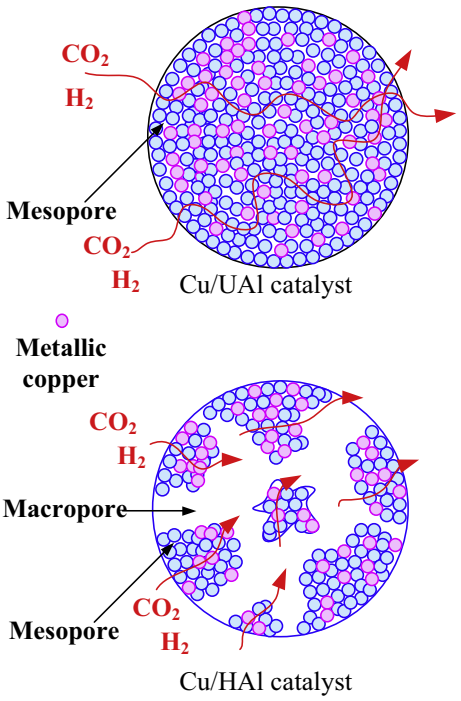

Scheme 1. Illustration of gas diffusion inside mesopores of the Cu/UAl and Cu/HAl catalysts.

Table 2
Effective diffusion coefficients in mesopores and macropores of different catalysts.

Catalysts	Reaction temperature (°C)	Effective diffusion coefficients × 10^3 (cm^2/s)					
		Mesopores			Macropores		
		CO_2	H_2	CH_3OH	CO_2	H_2	CH_3OH
Cu/UAl	240	1.02	2.94	0.97	–	–	–
	260	1.03	3.08	1.01	–	–	–
	280	1.06	3.23	1.05	–	–	–
	300	1.08	3.36	1.09	–	–	–
	320	1.10	3.49	1.12	–	–	–
Cu/HAl	240	0.82	2.38	0.79	10.80	11.54	5.64
	260	0.84	2.49	0.82	11.06	12.42	6.12
	280	0.86	2.61	0.85	11.42	13.36	6.61
	300	0.88	2.71	0.88	11.91	14.29	7.09
	320	0.90	2.82	0.91	12.36	15.23	7.58

probably lessen methanol decomposition reaction (Eq. (4)), and thus provided the higher methanol selectivity compared to the Cu/UAl-S catalyst. With increasing the average catalyst pellet size (from 0.0825 mm to 1.425 mm), the decrease in CO_2 conversion was observed for both Cu/UAl and Cu/HAl catalysts, indicating the existence of diffusion limitation in pores of catalysts. To gain more information, the effective diffusion coefficients (D_e) of reactant and product molecules in mesopores and macropores are calculated by using Eqs. (5)–(10) as shown below [38,39]; and the results are given in Table 2.

$$D_e = \frac{\varepsilon}{\tau} D_{pore} \tag{5}$$

where ε is catalyst porosity; τ is catalyst tortuosity; and D_{pore} represents diffusion coefficient of gas in either mesopores or macropores. Knudsen number was pre-determined to justify the most suitable equation for calculating diffusion coefficient in mesopores and macropores. Knudsen number in mesopores of the reactants and products was found to be in the range of 0.5–1.1, indicating that both molecular diffusion and Knudsen diffusion are important. Thus, the diffusion coefficient in mesopore is calculated by Eq. (6).

$$\frac{1}{D_{pore}} = \frac{1}{D'_A} + \frac{1}{D_K} \tag{6}$$

where D'_A and D_K are molecular diffusion coefficients of component A (cm^2/s) with respect to the total gas mixture and Knudsen diffusion coefficient (cm^2/s), respectively. D'_A and D_K could be calculated from the following equations:

$$D'_A = \frac{1 - y_A}{\frac{y_B}{D_{AB}} + \frac{y_C}{D_{AC}} + \frac{y_D}{D_{AD}} + \cdots} \tag{7}$$

$$D_K = 9700 r_P \left(\frac{T}{M}\right)^{\frac{1}{2}} \tag{8}$$

where D_{AB}, D_{AC}, D_{AD} are respective binary diffusion coefficients; and y_A, y_B, y_C, are mole fractions of the components in the mixture; T is temperature (K); M is molecular weight of gas molecules; and r_p is pore radius (cm). The binary diffusion coefficient (cm^2/s) can be calculated by the following equation:

$$D_{AB} = 0.001858 \frac{T^{\frac{3}{2}} \left(\frac{1}{M_A} + \frac{1}{M_B}\right)^{\frac{1}{2}}}{P \sigma_{AB}^2 \Omega_{AB}} \tag{9}$$

where T is temperature (K); M_A and M_B are molecular weight of components A and B, respectively; P is total pressure (atm); σ_{AB} is effective collision diameter (Å); Ω_{AB} is collision integral. The diffusion coefficient in macropores can be calculated by Eq. (7) because the macropore size is much larger than the mean free path of gas molecules. The catalyst tortuosity (τ) can be calculated from Eq. (10), given by Beckman [40] for heterogeneous catalysts.

$$\tau = \frac{\varepsilon}{1 - (1 - \varepsilon)^{\frac{1}{3}}} \tag{10}$$

Due to the fact that the diffusion coefficient in mesopores of CO_2 was 3-fold lower than that of H_2, this implied the depletion of CO_2 along the intra-pellet pores. In other words, the slower molecular transport of CO_2 to active sites inside the mesopores resulted in lowering the catalyst performance, including the decrease of CO_2 conversion. For the catalyst without macropores (Cu/UAl), methanol selectivity of the catalyst with larger pellet size (Cu/UAl-L) was considerably lower than that of the smaller one (Cu/UAl-S) when compared at the same reaction temperature. This could be attributed to the increase in the residence time of methanol diffusion inside the catalyst pellets, and thus increasing the probability of methanol decomposition. In contrast, for the Cu/HAl-L catalyst with macropores, the methanol selectivity was slightly lower than that of the Cu/HAl-S catalyst when compared at reaction temperature of 240 and 260 °C, suggesting the shorter residence time of methanol diffusion inside the catalyst pellets. However the difference in methanol selectivity between the Cu/HAl-L and Cu/HAl-S catalysts was larger when the temperature was further increased (280 °C, 300 °C, and 320 °C). This could be explained by the fact that methanol decomposition became kinetically more favored at the higher temperature. At higher temperature, the methanol decomposition rate increased more rapidly than the diffusion rate, resulting in the lower methanol selectivity. The CO_2 conversion and methanol selectivity of the Cu/UAl and Cu/HAl catalysts were compared with those of previous works using copper-loaded commercial Al_2O_3 support as the catalyst. The results are shown in Table 3. It was found that the Cu/HAl catalyst possessed a superior performance in terms of methanol selectivity which was 2.4–5.5-fold greater than those catalysts.

Fig. 7 shows the CO_2 conversion and selectivity of methanol, CO and DME *versus* the time-on-stream over the Cu/UAl-S and

Table 3
Comparison of catalytic performance of Cu/HAl and Cu/UAl catalysts and other Cu/Al_2O_3 catalysts for the synthesis of methanol from CO_2 hydrogenation.

Catalysts	Operating conditions		CO_2 conversion (%)	Methanol selectivity (%)	Refs.
	Temperature (°C)	Pressure			
10 wt%Cu/Al_2O_3	250	20 atm	8.98	13.44	[14]
5 wt%Cu/Al_2O_3	220	30 bar	n/a	7.5	[41]
12 wt%Cu/Al_2O_3	240	30 bar	10.7	16.9	[42]
	260	30 bar	15.6	10.7	
10 wt%Cu/UAl	240	30 bar	6.4	35.7	This work
	260	30 bar	13.5	23.1	
	280	30 bar	18.8	16.1	
10 wt%Cu/HAl	240	30 bar	5.6	41.7	This work
	260	30 bar	10.5	30.3	
	280	30 bar	15.0	21.7	

n/a: not available.

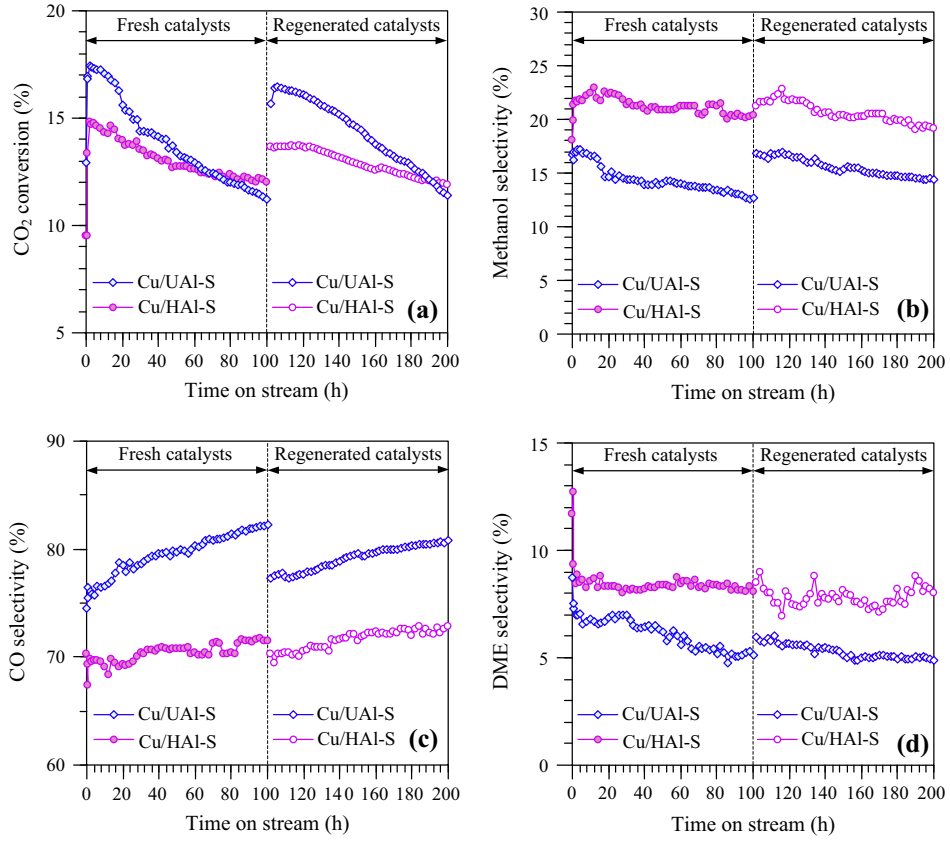

Fig. 7. CO_2 conversion (a), selectivity of methanol (b), CO (c) and DME (d) as a function of time-on-stream of fresh and spent catalysts. Reaction conditions: T = 280 °C, P = 30 bars, flow rate = 60 mL min^{-1}.

Cu/HAl-S catalysts. The CO_2 conversion of the Cu/UAl-S catalyst was first increased from 12.92 to 17.44 within 2 h and then substantial loss its activity *ca.* 6.2% during the 100 h time-on-stream experiment, while the Cu/HAl-S catalyst exhibited much greater durability, experiencing only a 2.77% (14.81% → 12.04%) reduction under identical reaction conditions. This indicated that the Cu/HAl-S catalyst had a higher stability than the Cu/UAl-S catalyst. Regarding the selectivity of methanol and CO, the Cu/UAl-S catalyst lost its selectivity to methanol approximately 4.13% of its initial selectivity while its selectivity to CO progressively increased from 76.48% to 82.24% during the 100 h time-on-stream experiment. For the Cu/HAl-S catalyst the selectivity to methanol and CO were found to be almost constant. The change in product selectivity with time-on-stream suggests the change in the active sites of the catalysts.

The XRD was used to verify phase of the reduced and spent catalysts (Fig. 8). The XRD pattern of the reduced catalysts (Cu/HAl-S and Cu/UAl-S) appeared the peak at 2θ angles of 43° corresponded to the presence of metallic copper (JCPDS 01-089-2838), which was the active phase for methanol synthesis from CO_2 hydrogenation. After the 100 h time-on-stream experiment, the peaks at 2θ angles of 35.5° and 38.6°, which were indexed to the CuO crystal phase, were observed along with the reduction of peak intensity of the metallic copper, indicating the transformation of the metallic copper to the CuO. This could be explained by the fact that a large amount of water produced by the Eqs. (1)–(3) oxidized the

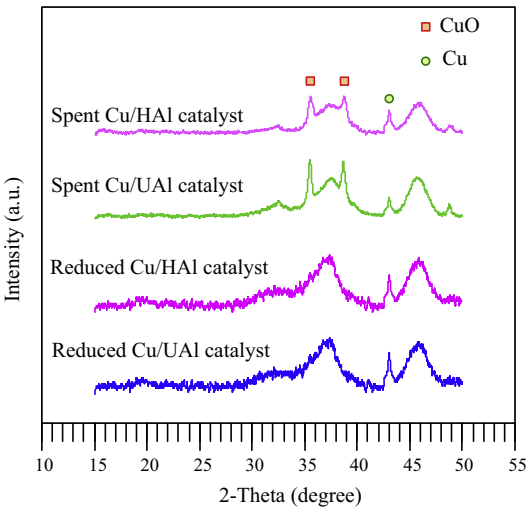

Fig. 8. XRD patterns of reduced and spent catalysts.

metallic copper sites to CuO [43,44]. The XRD pattern of the spent Cu/HAl-S catalyst exhibited the lower peak intensity of CuO and higher peak intensity of Cu compared to those of the spent Cu/UAl-S catalyst, indicating the faster oxidation rate of metallic copper over the Cu/UAl-S catalyst. This is consistent with the faster deactivation of this catalyst. In addition to partial oxidation of metallic copper by water, water has a negative effect for dehydration of methanol over Al_2O_3 catalyst as water molecules could strongly adsorb on the active sites [45–47]. As a result, both Cu/UAl-S and Cu/HAl-S catalysts are commonly deactivated through water poisoning. Interestingly the DME selectivity was almost constant in the case of Cu/HAl-S catalysts, in contrary; it was gradually decreased with time-on-stream over the Cu/UAl-S catalyst. We therefore concluded that the presence of macropores could promote the rate of water removal from catalyst pellets, and thus prolong the lifetime of the catalysts.

As a detectable change of metallic copper to copper oxide in accordance with the substantial decrease of catalytic activity was observed, the spent catalysts after 100 h time-on-stream experiment were reduced with flowing H_2 (60 mL/min) at 350 °C and a heating rate of 2 °C/min for 4 h in order to regenerate and perform the activity test. Note that the effluent gases were analyzed by gas chromatography which would enable to see if carbonaceous species on the catalysts surface are converted to methane during the regeneration process. As a result, no methane formation was observed, indicating that the partial oxidation of metallic copper was the main reason for catalyst deactivation. After regeneration (Fig. 7), almost similar CO_2 conversion and catalyst deactivation trend were observed compared to those of the fresh catalysts. Notably, methanol and DME selectivities over the spent catalysts were restored after regeneration with H_2, indicating that the deactivation phenomena of both catalysts were almost fully reversible.

4. Conclusion

The catalytic activity for methanol synthesis from CO_2 hydrogenation was strongly affected by the pore structure of the catalysts. Cu-loaded hierarchical meso–macroporous alumina catalyst (Cu/HAl) exhibited the higher methanol selectivity and stability than Cu-loaded unimodal mesoporous alumina catalyst (Cu/HAl). The enhanced methanol selectivity and stability can be assigned to the inhibited undesirable reactions induced by the shortened mesopore diffusion path length. This finding emphasizes the importance of transport of reactants and products in pores of the catalysts for methanol synthesis from CO_2 hydrogenation

Acknowledgements

This work was financially supported by the Thailand Research Fund (Grant No. TRG5780258), the Center of Excellence on Petrochemical and Materials Technology (PETROMAT), the National Research University Project of Thailand (NRU), the Nanotechnology Center (NANOTEC), NSTDA, Ministry of Science and Technology, Thailand through its program of Center of Excellence Network, Rayong Institute of Science and Technology Foundation, and the Kasetsart University Research and Development Institute (KURDI). Financial support for Mr. Sittisut Bumrungsalee from Faculty of Engineering, Kasetsart University is also appreciated.

Appendix A. Supplementary material

Supplementary data associated with this article can be found, in the online version, at http://dx.doi.org/10.1016/j.enconman.2015.07.033.

References

[1] Karim NA, Kamarudin SK. An overview on non-platinum cathode catalysts for direct methanol fuel cell. Appl Energy 2013;103:212–20.
[2] Yan XH, Zhao TS, An L, Zhao G, Zeng L. A crack-free and super hydrophobic cathode micro-porous layer for direct methanol fuel cells. Appl Energy 2015;138:331–6.
[3] Baneshi J, Haghighi M, Jodeiri N, Abdollahifar M, Ajamein H. Homogenous precipitation synthesis of $CuO–ZrO_2–CeO_2–Al_2O_3$ nanocatalyst used in hydrogen production via methanol steam reforming for fuel cell applications. Energy Convers Manage 2014;87:928–37.
[4] Witoon T, Permsirivanich T, Kanjanasoontorn N, Akkaraphataworn C, Seubsai A, Faungnawakij K, et al. Direct synthesis of dimethyl ether from CO_2 hydrogenation over $Cu–ZnO–ZrO_2/SO_4^{2-}–ZrO_2$ hybrid catalysts: effects of sulfur-to-zirconia ratios. Catal Sci Technol 2015;5:2347–57.
[5] Ladera RM, Ojeda M, Fierro JLG, Rojas S. TiO_2-supported heteropoly acid catalysts for dehydration of methanol to dimethyl ether: relevance of dispersion and support interaction. Catal Sci Technol 2015;5:484–91.
[6] Park SH, Lee CS. Applicability of dimethyl ether (DME) in a compression ignition engine as an alternative fuel. Energy Convers Manage 2014;86:848–63.
[7] Wei Y, Wang K, Wang W, Liu S, Chen X, Yang Y, et al. Comparison study on the emission characteristics of diesel- and dimethyl ether-originated particulate matters. Appl Energy 2014;130:357–69.
[8] Li J, Miao P, Li Z, He T, Han D, Wu J, et al. Hydrothermal synthesis of nanocrystalline H[Fe, Al]ZSM-5 zeolites for conversion of methanol to gasoline. Energy Convers Manage 2015;93:259–66.
[9] Aghamohammadi S, Haghighi M. Dual-template synthesis of nanostructured CoAPSO-34 used in methanol to olefins: effect of template combinations on catalytic performance and coke formation. Chem Eng J 2015;264:359–75.
[10] Álvaro-Muñoz T, Sastre E, Márguez-Álvarez C. Microwave-assisted synthesis of plate-like SAPO-34 nanocrystals with increased catalyst lifetime in the methanol-to-olefin reaction. Catal Sci Technol 2014;4:4330–9.
[11] Chen J, Li J, Yuan C, Xu S, Wei Y, Wang Q, et al. Elucidating the olefin formation mechanism in the methanol to olefin reaction over AlPO-18 and SAPO-18. Catal Sci Technol 2014;4:3268–77.
[12] Arena F, Barbera K, Italiano G, Bonura G, Spadaro L, Frusteri F. Synthesis, characterization and activity pattern of $Cu–ZnO/ZrO_2$ catalysts in the hydrogenation of carbon dioxide to methanol. J Catal 2007;249:185–94.
[13] Cai W, de la Piscina PR, Toyir J, Homs N. CO_2 hydrogenation to methanol over CuZnGa catalysts prepared using microwave-assisted methods. Catal Today 2015;242:193–9.
[14] Ren H, Xu CH, Zhao HY, Wang YX, Liu J, Liu JY. Methanol synthesis from CO_2 hydrogenation over $Cu/\gamma–Al_2O_3$ catalysts modified by ZnO, ZrO_2 and MgO. J Ind Eng Chem 2015;28:261–7.
[15] Natesakhawat S, Lekse JW, Baltrus JP, Ohodnicki PR, Howard JrBH, Deng X, et al. Active sites and structure–activity relationships of copper-based catalysts for carbon dioxide hydrogenation to methanol. ACS Catal 2012;2:1667–76.
[16] Schumann J, Lunkenbein T, Tarasov A, Thomas N, Schlögl R, Behrens M. Synthesis and characterization of a highly active Cu/ZnO: Al catalyst. ChemCatChem 2014;6:2889–97.
[17] Frusteri F, Cordaro M, Cannilla C, Bonura G. Multifunctionality of $Cu–ZnO–ZrO_2$/H-ZSM5 catalysts for the one-step CO_2 to DME hydrogenation reaction. Appl Catal B Environ 2015;162:57–65.

[18] Witoon T, Permsirivanich T, Donphai W, Jaree A, Chareonpanich M. CO_2 hydrogenation to methanol over Cu/ZnO nanocatalysts prepared via a chitosan-assisted co-precipitation method. Fuel Process Technol 2013;116:72–8.
[19] Witoon T, Chareonpanich M, Limtrakul J. Effect of hierarchical meso–macroporous silica supports on Fischer–Tropsch synthesis using cobalt catalyst. Fuel Process Technol 2011;92:1498–505.
[20] Song D, Li J. Effect of catalyst pore size on the catalytic performance of silica supported cobalt Fischer–Tropsch catalysts. J Mol Catal A Chem 2006;247:206–12.
[21] Khodakov AY, Griboval-Constant A, Bechara R, Zholobenko VL. Pore size effects in Fischer Tropsch synthesis over cobalt-supported mesoporous silicas. J Catal 2002;206:230–41.
[22] Witoon T, Bumrungsalee S, Vathavanichkul P, Palitsakun S, Saisriyoot M, Faungnawakij K. Biodiesel production from transesterification of palm oil with methanol over CaO supported on bimodal meso–macroporous silica catalyst. Bioresour Technol 2014;156:329–34.
[23] Possato LG, Diniz RN, Garetto T, Pulcinelli SH, Santilli CV, Martins L. A comparative study of glycerol dehydration catalyzed by micro/mesoporous MFI zeolites. J Catal 2013;300:102–12.
[24] Tanggarnjanavalukul C, Donphai W, Witoon T, Chareonpanich M, Limtrakul J. Deactivation of nickel catalysts in methane cracking reaction: effect of bimodal meso–macropore structure of silica support. Chem Eng J 2015;262:364–71.
[25] Ramasamy KK, Zhang H, Sun J, Wang Y. Conversion of ethanol to hydrocarbons on hierarchical HZSM-5 zeolites. Catal Today 2014;238:103–10.
[26] Hu Z, Zhang H, Wang L, Zhang H, Zhang Y, Xu H, et al. Highly stable boron-modified hierarchical nanocrystalline ZSM-5 zeolite for the methanol to propylene reaction. Catal Sci Technol 2014;4:2891–5.
[27] Iglesia E. Design, synthesis, and use of cobalt-based Fischer–Tropsch synthesis catalysts. Appl Catal A Gen 1997;161:59–78.
[28] Tokudome Y, Fujita K, Nakanishi K, Miura K, Hirao K. Synthesis of monolithic Al_2O_3 with well-defined macropores and mesostructured skeletons via the sol-gel process accompanied by phase separation. Chem Mater 2007;19:3393–8.
[29] Mohamed MM, Abu-Zied BM. Acidic properties of sulfated ions oxide supported molybdenum catalysts: a differential scanning calorimetry, thermogravimetry and Fourier transform-infrared study. Thermochim Acta 2000;359:109–17.
[30] Xia WS, Wan HL, Chen Y. Cluster model study on the surface interactions of -alumina-supported metal oxides. J Mol Catal A Chem 1999;138:185–95.
[31] Wan H, Wang Z, Zhu J, Li X, Liu B, GaO F, et al. Influence of CO pretreatment on the activities of CuO/γ–Al_2O_3 catalysts in CO+O_2 reaction. Appl Catal B Environ 2008;79:254–61.
[32] LuO MF, Fang P, He M, Xie YL. In situ XRD, Raman, and TPR studies of CuO/Al_2O_3 catalysts for CO oxidation. J Mol Catal A Chem 2005;239:243–8.
[33] Reddy GK, Rao KSR, Rao PK. Effect of support modification by carbon coverage in the dehydrogenation activity of Cu/Al_2O_3 catalyst. Catal Lett 1999;59:157–60.
[34] Li C, Yuan X, Fujimoto K. Development of highly stable catalyst for methanol synthesis from carbon dioxide. Appl Catal A Gen 2014;469:306–11.
[35] Bonura G, Cordaro M, Cannilla C, Arena F, Frusteri F. The changing nature of the active site of Cu–Zn–Zr catalysts for the CO_2 hydrogenation reaction to methanol. Appl Catal B Environ 2014;152–153:152–61.
[36] Zhang Y, Fei J, Yu Y, Zheng X. Study of CO_2 hydrogenation to methanol over Cu-V/-Al_2O_3 catalyst. J Nat Gas Chem 2007;16:12–5.
[37] Gao P, Xie R, Wang H, Zhong L, Xia L, Zhang Z, et al. Cu/Zn/Al/Zr catalysts via phase-pure hydrotalcite like compounds for methanol synthesis from carbon monoxide. J CO_2 Util 2015. 10.1016/j.jcou.2014.12.008.
[38] McCabe WL, Smith JC, Harriott. Unit operations of chemical engineering. 7th ed. New York: McGraw-Hill; 2005.
[39] Fairbanks DF, Wilke CR. Diffusion coefficients in multicomponent gas mixtures. Ind Eng Chem 1950;42:471–5.
[40] Beckman JW. Mathematical description of heterogeneous materials. Chem Eng Sci 1990;45:2603–10.
[41] Bando KK, Sayama K, Kusama H, Okabe K, Arakawa H. In-situ FT-IR study on CO_2 hydrogenation over Cu catalysts supported on SiO_2, Al_2O_3, and TiO_2. Appl Catal A Gen 1997;165:391–409.
[42] Zhang Y, Fei J, Yu Y, Zheng X. Methanol synthesis from CO_2 hydrogenation over Cu based catalyst supported on zirconia modified -Al_2O_3. Energy Convers Manage 2006;47:3360–7.
[43] Arena F, Mezzatesta G, Zafarana G, Trunfio G, Frusteri F, Spadaro L. How oxide carriers control the catalytic functionality of the Cu–ZnO system in the hydrogenation of CO_2 to methanol. Catal Today 2013;210:39–46.
[44] Choi Y, Stenger HG. Fuel cell grade hydrogen from methanol on a commercial Cu/ZnO/Al_2O_3 catalyst. Appl Catal B Environ 2002;38:259–69.
[45] Jun KW, Lee HS, Roh HS, Park SE. Highly water-enhanced H-ZSM-5 catalysts for dehydration of methanol to dimethyl ether. Bull Korean Chem Soc 2003;24:106–8.
[46] Xu M, Lunsford JH, Goodman DW, Bhattacharyya A. Synthesis of dimethyl ether (DME) from methanol over solid-acid catalysts. Appl Catal A Gen 1997;149:289–301.
[47] Akarmazyan SS, Panagiotopoulou P, Kambolis A, Papadopoulou C, Kondarides DI. Methanol dehydration to dimethylether over Al_2O_3 catalysts. Appl Catal B Environ 2014;145:136–48.

เรื่องที่ 5

Porntipar Dumrongbunditkul, **Thongthai Witoon***, Metta Chareonpanich, Thumrongrut Mungcharoen, Preparation and characterization of Co-Cu-ZrO_2 nanomaterials and their catalytic activity in CO_2 methanation, Ceramics International 42 (2016) 10444–10451. (IF 2015 = 2.758).

Ceramics International 42 (2016) 10444–10451

Contents lists available at ScienceDirect

Ceramics International

journal homepage: www.elsevier.com/locate/ceramint

Preparation and characterization of Co–Cu–ZrO_2 nanomaterials and their catalytic activity in CO_2 methanation

Porntipar Dumrongbunditkul [a], Thongthai Witoon [a,b,c,*], Metta Chareonpanich [a,b,c], Thumrongrut Mungcharoen [a]

[a] Department of Chemical Engineering, Faculty of Engineering, Kasetsart University, Bangkok 10900, Thailand
[b] Center for Advanced Studies in Nanotechnology and Its Applications in Chemical Food and Agricultural Industries, Kasetsart University, Bangkok 10900, Thailand
[c] NANOTEC-KU-Center of Excellence on Nanoscale Materials Design for Green Nanotechnology, Kasetsart University, Bangkok 10900, Thailand

ARTICLE INFO

Article history:
Received 16 January 2016
Received in revised form
23 March 2016
Accepted 24 March 2016
Available online 26 March 2016

Keywords:
Nanomaterials
Metal composition
Methane
Mixed oxide
Carbon dioxide

ABSTRACT

In this work, a series of Co–Cu–ZrO_2 nanomaterials with different metal compositions were prepared by a reverse co-precipitation method, and used as catalyst for the production of methane from CO_2 methanation reaction. The physicochemical properties of the catalysts were characterized by means of X-ray fluorescence (XRF), X-ray diffraction (XRD), N_2-physisorption and hydrogen temperature-programmed reduction (H_2-TPR). The binary Co–ZrO_2 catalyst appeared to be predominant in the methanation process. The addition of Cu to the binary Co–ZrO_2 catalyst decreased the reduction temperature of the catalysts and improved the inter-dispersion of mixed metal oxides. The Co–Cu–ZrO_2 catalyst with the ratio of 20:40:40 achieved a superior CH_4 yield of 58% at a reaction temperature and pressure of 300 °C and 3 MPa. Moreover, this catalyst exhibited a great stability as only a 0.6% reduction of initial CH_4 yield was observed after 48 h of a time-on-stream experiment.

1. Introduction

A rapidly growing human population and industrialization has caused an extensive use of different types of energy [1,2]. Fossil fuels such as coal, oil or natural gas have been usually the most attractive energy sources mainly due to their high-energy concentration, which allows storage of large amount of energy in relatively small volume. The burning of fossil fuels is, however, results in the release of carbon dioxide (CO_2) into the earth's atmosphere. The increase of CO_2 concentration in atmosphere has been found to relate with the climate change, especially rising global temperature [3]. Concerns regarding the negative effects of climate change have prompted worldwide efforts to reduce CO_2 emissions by programs for energy saving or improved energy efficiency [4,5]. With the United Nations' prediction of growth in world population to reach 8.7 billion by 2035 [6], the demand for energy is undoubtedly expected to increase substantially, which is certainly to erase any reductions in CO_2 emissions associated with improved energy efficiency. Therefore several alternatives have been proposed to continue using fossil fuels but separating CO_2 from exhaust gases [7–11] by an implementation of carbon capture and storage (CCS) technology with coal-fired power plant which is considered to be the major source of CO_2 emission. However, an expensive cost of CCS technology including a lot of equipment to separate and capture, purify, liquefy, transport and bury CO_2 becomes the major obstacle.

In addition to geological storage, the application of CO_2 as a raw material in other valuable chemical products as well as alternative energy sources not only reduces fossil fuels consumption but furthermore offers an approach for the carbon neutral cycle. Because of the thermodynamic stability of CO_2, the industrial processes using CO_2 as raw material is still limited to the production of urea and its derivatives such as salicylic acid and carbonates [12]. Other products using CO_2 as raw material currently being researched include methane [13,14], methanol [15,16], hydrocarbons [17], dimethyl ether [18,19] and so forth. In comparison to the other products, the transformation of CO_2 to methane offers economically viable prospect in terms of thermodynamics [20].

Methane can be directly synthesized via CO_2 hydrogenation [Eq. (1)], also known as the Sabatier reaction, was first reported in 1902 by Sabatier and Senderens [21].

$$CO_2 + 4H_2 \leftrightarrow CH_4 + 2H_2O;\ \Delta H_{298\,K} = -165.0\ \text{kJ mol}^{-1} \quad (1)$$

According to the stoichiometric ratio of Eq. (1), the CO_2

* Corresponding author at: Department of Chemical Engineering, Faculty of Engineering, Kasetsart University, Bangkok 10900, Thailand.
E-mail address: fengttwi@ku.ac.th (T. Witoon).

http://dx.doi.org/10.1016/j.ceramint.2016.03.193
0272-8842/

methanation reaction has been generally carried out with H_2/CO_2 ratio of 4:1. However, Hoekman et al. has shown that the efficiency of hydrogen utilization significantly improved with decreasing the H_2/CO_2 ratio [22]. Unfortunately, the reduction of the H_2/CO_2 ratio causes a significant decrease in CO_2 conversion [23–25]. To the best of our knowledge, the CO_2 conversion could be enhanced by adjusting the thermodynamic properties. There are several literatures analyzing the effect of pressure on methanation reaction [23–26]. Dorner et al. indicated that only 3.5% of CO_2 conversion was obtained under reaction pressure of 10.34 bars with feed ratio 3:1. When the pressure increased to 17.24, 24.13 and 31.02 bars, the CO_2 conversion considerably increased to 14.7%, 25.8% and 37.7%, respectively. The similar trend was also found for the methane selectivity [23]. Thus, the increase of reaction pressure constitutes a feasible option for improving the CO_2 conversion as well as the methane selectivity. On the basis of these reasons, the pressure of 30 bars with feed ratio H_2:CO_2 of 3:1 is selected in the present work.

The reaction mechanism for the methane production from CO_2 hydrogenation has been usually reported to be similar to that of CO methanation [Eq. (2)] because CO can be an intermediate from reverse water-gas shift reaction [Eq. (3)].

$$CO + 3H_2 \leftrightarrow CH_4 + H_2O; \quad \Delta H_{298\,K} = -206.2\ \text{kJ mol}^{-1} \tag{2}$$

$$CO_2 + H_2 \leftrightarrow CO + H_2O; \quad \Delta H_{298\,K} = +41\ \text{kJ mol}^{-1} \tag{3}$$

For this reason, the active metals (Ni, Co, Fe and Ru) for CO methanation have been used to study for CO_2 hydrogenation to methane [27–30]. Bligaard et al. proposed that the activity during CO methanation was determined by two very critical properties of the catalytic surface: (i) the adsorption enthalpy of the reactants and (ii) the dissociation energy of the C–O bond [31]. On the basis of metals within the group VIII the volcano-shaped curve where Co and Ru exhibited the highest activity was observed. Therefore much less-expensive Co catalyst has become an attractive option. Addition of second metal and support is essential to enhance the activity, selectivity and stability of Co catalyst due to an improvement of metals dispersion and strong metal-support interaction [31]. Regarding to (Eqs. (2) and 3) the second metal and support should be active for the reverse water gas-shift reaction for the production of CO which then undergoes a methanation to form methane. Among several metals and supports, a Cu–ZrO_2 appears as a very attractive catalyst because it can catalyze the reverse water gas-shift reaction at similar conditions at which Co catalyst can provide a high methanation activity. To the best of our knowledge, the CO_2 hydrogenation to methane over a Co–Cu–ZrO_2 catalyst has not yet been reported. In this work, binary (Cu–ZrO_2 and Co–ZrO_2) and ternary (Co–Cu–ZrO_2) catalysts were prepared via a reverse co-precipitation method using sodium hydrogen carbonate ($NaHCO_3$) as a precipitating agent. The influence of catalyst compositions on the physicochemical properties of the catalysts as well as their catalytic activity was investigated.

2. Experiment

2.1. Preparation of Co–Cu–ZrO_2 nanomaterials

The mixed metal oxides with high concentration of active phase are commonly prepared by a co-precipitation method which involves the dissolving metal salts in a deionized water, and then the alkaline solution, i.e., 0.1 M $NaHCO_3$ solution, is added dropwise to induce to formation of mixed metal oxides. However, the distribution of active phase prepared by the conventional co-precipitation method is non-uniform and difficult to control due to the different precipitation kinetics of each cation [32–35]. In contrast to the conventional co-precipitation method, the reverse co-precipitation method has been reported to provide the simultaneous precipitation of cations, resulting in the homogeneous dispersion of the mixed metal oxides [32–35]. Therefore, in this work, the Co-Cu-ZrO_2 nanomaterials with different molar ratios were prepared by the reverse co-precipitation method using sodium hydrogen carbonate ($NaHCO_3$) as a precipitating agent. In a typical synthesis, 100 mL $Cu(NO_3)_2 \cdot 3H_2O$, $Co(NO_3)_2 \cdot 6H_2O$ and $ZrOCl_2 \cdot 8H_2O$ mixture solution was slowly added dropwise into a 0.1 M $NaHCO_3$ solution (500 mL), while the pH of the solution was kept constant at 7.5 by the addition of 0.1 M $NaHCO_3$ solution. Then, the mixed solution was stirred for 2 h at room temperature. The mixture was filtered and washed with deionized water. Finally, the obtain precipitate was dried at 100 °C overnight and calcined at 350 °C for 2 h. The materials' relative notation is listed in Table 1.

Table 1
Chemical compositions and textural properties of the studied catalysts.

Sample	Chemical composition (mol%)[a]			BET surface area (m^2/g)	Total pore volume (cm^3/g)	CuO crystallite size (nm)
	Co	Cu	Zr			
ZrO_2	–	–	100	212	0.31	–
CCZ-1	–	60 (58.7)	40 (41.3)	39	0.05	29.6
CCZ-2	60 (54.4)	–	40 (45.6)	97	0.22	–
CCZ-3	30 (26.6)	30 (29.2)	40 (44.2)	136	0.33	–
CCZ-4	20 (16.4)	40 (38.5)	40 (45.1)	142	0.36	–
CCZ-5	10 (8.9)	50 (47.5)	40 (43.6)	127	0.26	–

[a] Number in parentheses refer to the chemical composition measured by XRF technique.

2.2. Characterization

X-ray diffraction (XRD) patterns of the calcined samples were attained at on a diffractometer (Bruker D8 Advance) with Cu-Kα radiation. The measurements were made at temperatures in a range of 10–75 °C on 2θ with a step size of 0.05°. The diffraction patterns were analyzed with the employment of the Joint Committee on Powder Diffraction Standards (JCPDS). The CuO crystallite size was calculated by means of the Scherrer Equation from the most intense CuO peak at 2θ of 38.81 as shown below:

$$d = \frac{0.89\lambda}{B\cos\theta} \times \frac{180^0}{\pi} \tag{4}$$

where d denotes the mean crystallite diameter, λ the X-ray wave length (1.54 Å), and B the full width half maximum (FWHM) of the CuO diffraction peak.

X-ray fluorescence (PANalytical Epsilon 5) was used for the quantitative analysis of the inorganic compounds in the calcined catalysts.

N_2 adsorption–desorption isotherms of the samples were measured at −196 °C with a Quantachrome Autosorb-1C instrument. Prior to measurements, the samples were degassed at 200 °C for 24 h. Pore size distributions of the samples were determined from the adsorption branch of the isotherms in accordance with the Barrett-Joyner-Hallenda (BJH) method. The specific BET (S_{BET}) was estimated for P/P_0 values to be between 0.05–0.30. The total pore volume of the samples was determined at P/P_0 of 0.995

The reduction of the metal oxides was measured with the thermogravimetric analysis (SDT2960 Simultaneous DTA-TGA Universal 2000) in which the amount and rate of change in the weight is monitored as a function of temperature and time in a

controlled atmosphere. Upon heating a sample containing mixed oxides of Co, Cu and Zr under a flow of H_2, it undergoes a reaction where H_2 molecules react with the oxygen atom to form the water as the following Eqs. (5)–(7):

$$CuO + H_2 \rightarrow Cu^0 + H_2O \quad (5)$$

$$Co_3O_4 + H_2 \rightarrow 3CoO + H_2O \quad (6)$$

$$CoO + H_2 \rightarrow Co^0 + H_2O \quad (7)$$

The weight of the sample decreases due to the loss of oxygen, and thus the weight change of the sample is related to the reduction of metal oxides as well as the hydrogen consumption. Also the rate of change in the weight (derivative of weight: DTW) of the sample is related to the rate of hydrogen consumption. Prior to the reduction process, a calcined sample (15 mg) was preheated in a flow of N_2 from room temperature to 350 °C with a rate of 15 °C/min and kept constant at that temperature for 15 min, and then cooled down to 120 °C. After that, TPR experiment was started with heating rate of 4 °C/min under continuous flow of 10%H_2/He. In order to obtain accurate experimental results, two types of calibration including temperature and weight calibration are performed through the Instrument Control software.

2.3. Activity test

CO_2 methanation reaction was carried out in a fixed–bed stainless steel reactor (7.75 mm inner diameter). 0.25 g catalyst was diluted with 0.75 g inert silica sand (75–150 μm). The catalyst was reduced *in situ* under atmospheric pressure with flowing H_2 (60 mL/min) at 300 °C and a heating rate of 2 °C/min for 4 h. After the reduction, the temperature was cooled to 220 °C under flowing N_2; subsequently a flow of CO_2 and H_2 mixture (CO_2:H_2 molar ratio of 1:3) was fed through the reactor. The feed flow rate was set at 60 mL/min. The reactor pressure was slowly raised to 30 bars, and the reactor was heated to a variety of temperatures (240, 260, 280 and 300 °C). The effluent gaseous products were analyzed by using gas chromatography. Analysis of H_2, CO, CO_2, and N_2 was performed using GC–2014 gas chromatography equipped with a thermal conductivity detector (TCD) and a Unibead-C column. Methane and other hydrocarbon products were analyzed by using GC 8A equipped with a flame ionization detector (FID) and a Porapak-Q column. The activity-selectivity data were calculated by mass balance from an average of three independent measurements. The errors were within ±2%. CO_2 conversion and product selectivity are defined as follows:

$$CO_2 \text{ conversion}(\%) = \frac{\text{moles } CO_{2,in} - \text{moles } CO_{2,out}}{\text{moles } CO_{2,in}} \times 100 \quad (8)$$

$$CH_4 \text{ yield } (\%) = \frac{\text{moles } CH_4 \text{ produced}}{\text{moles } CO_{2,in}} \times 100 \quad (9)$$

$$\text{Product selectivity } (\%) = \frac{P_i}{\sum P_i} \times 100 \quad (10)$$

where P_i stands for the mole of a specific i product (*i.e.,* CH_4, CO, CH_3OH, hydrocarbons).

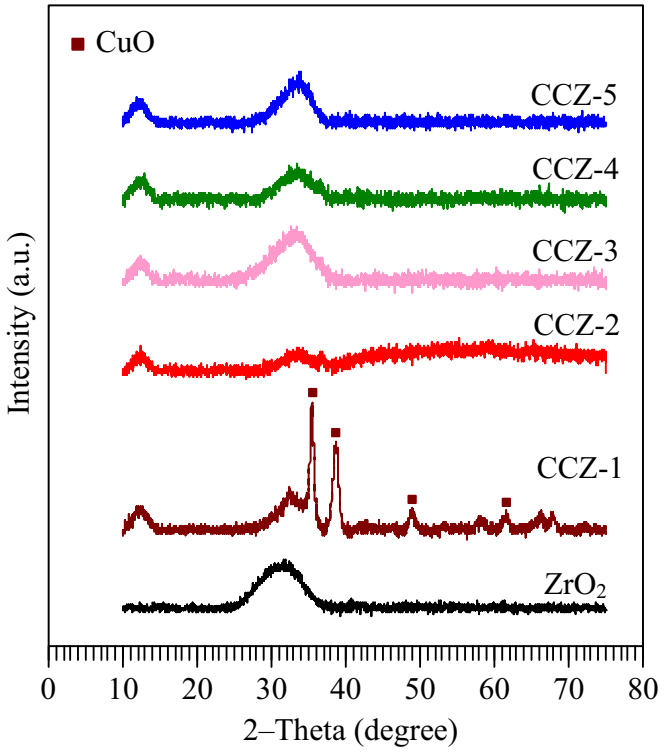

Fig. 1. XRD patterns of ZrO_2 and Co–Cu–ZrO_2 samples prepared with different metal compositions.

3. Results and discussion

3.1. Characterization

The XRD patterns of ZrO_2 sample and the series of the calcined Co–Cu–ZrO_2 catalysts are shown in Fig. 1. The XRD pattern of ZrO_2 exhibits a broad peak, which is a characteristic of an amorphous structure. The XRD pattern of the binary Cu–ZrO_2 catalyst (CCZ-1) shows the diffraction peaks at 2θ values of 35.52°, 38.81°, 48.56° and 61.50° which are indexed to CuO diffractions of (110), (002), (111), (202) and (113) planes, respectively [36]. The average CuO crystallite size calculated via the Scherrer equation is found to be 29.55 nm (Table 1). The binary Co–ZrO_2 catalyst (CCZ-2) exhibits a broad peak, suggesting that cobalt oxide nanoparticles most likely exist as well dispersed small crystallites throughout the bulk. In addition the peak intensities representing the crystallinity of cobalt oxide are possibly smaller than the intensity of broad peak of ZrO_2. On comparison between the binary catalysts (CCZ-1 and CCZ-2) and ternary catalysts (CCZ-3, CCZ-4 and CCZ-5), it can be observed that the CuO diffraction peaks disappear indicating the lower degree of CuO crystallinity and a high dispersion of the metal oxides.

To capture the catalyst morphology in a more tangible manner, the series of the calcined Co–Cu–ZrO_2 samples were visualized by TEM; the results are shown in Fig. 2. Because the ZrO_2 structure is in the amorphous phase, a dense aggregate observed in the TEM image of Cu–ZrO_2 (CCZ-1) belongs to the large crystalline of CuO. In comparison to copper oxide, the cobalt oxide particles have a higher dispersion with the ZrO_2 (CCZ-2) which can be due to a stronger interaction with cobalt oxide species and the surface of ZrO_2 as we will discuss later in the H_2-TPR measurement. It can be clearly seen that the particle sizes (8–15 nm) observed in the ternary catalysts (CCZ-3, CCZ-4 and CCZ-5) are much smaller than the binary catalysts, and the metal oxide particles of the ternary catalysts are homogeneously amalgamated. Note that the particle sizes of 8–15 nm are commonly detected by the XRD

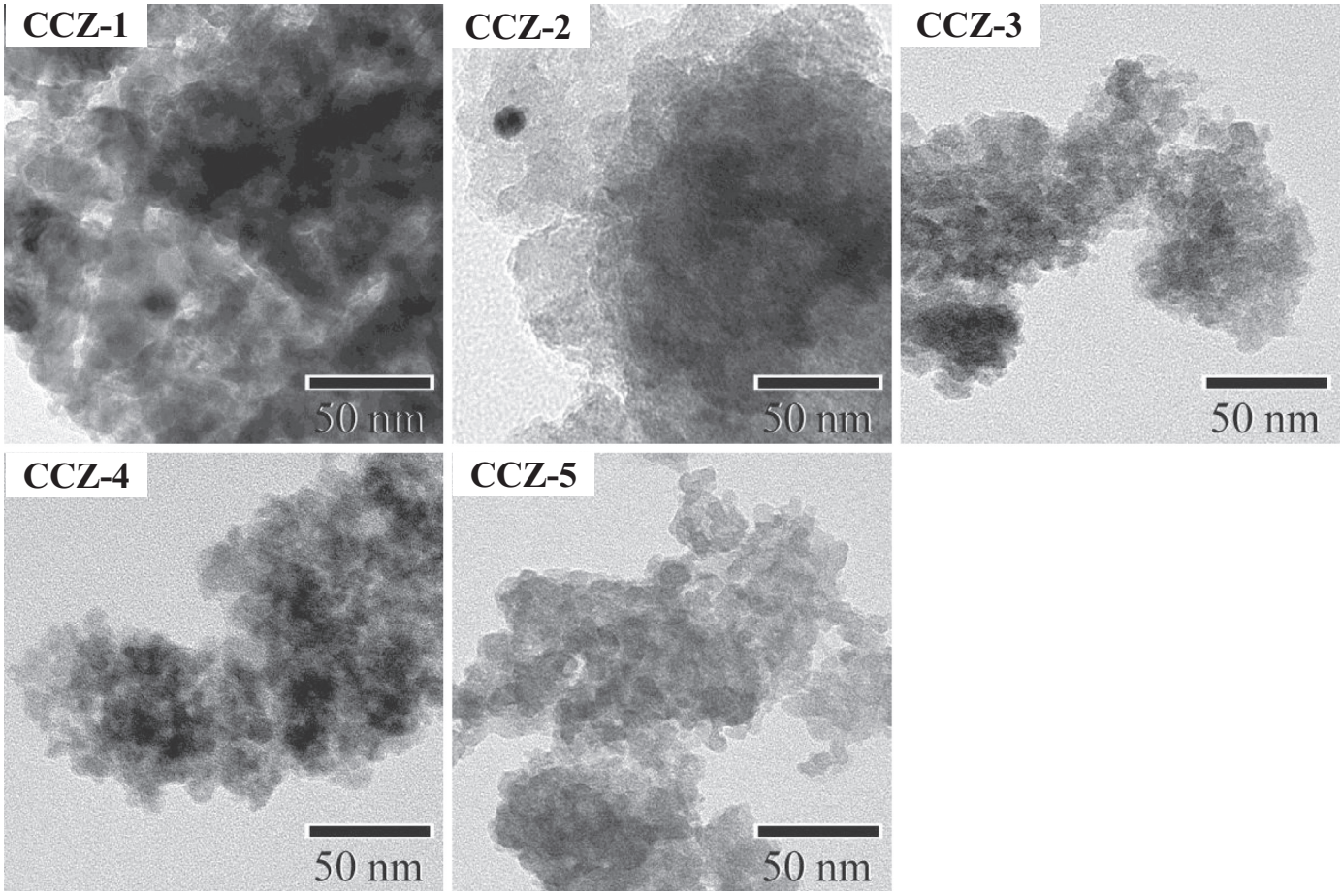

Fig. 2. TEM images of Co–Cu–ZrO_2 samples prepared with different metal compositions.

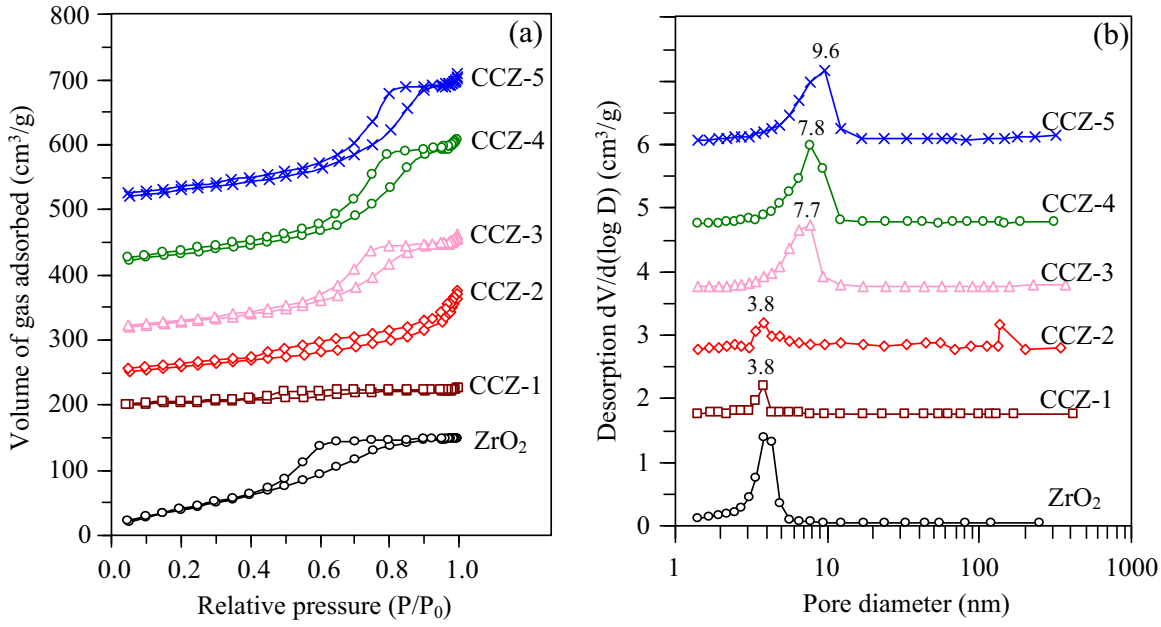

Fig. 3. N_2 adsorption–desorption isotherms (a) and pore size distribution (b) of ZrO_2 and Co–Cu–ZrO_2 samples prepared with different metal compositions.

measurement, but we observed no peaks of the ternary catalysts. This observation can be explained by the fact that the ZrO_2 is in the amorphous phase and the peak intensities of the other metal oxides are possibly low. Therefore the broad peak of ZrO_2 overlays the low intensities peak of the other metal oxides.

The physical properties including pore structure, BET surface area, pore size distribution and total pore volume of the studied catalysts were characterized by means of N_2-physisorption. Fig. 3a shows the N_2 adsorption–desorption isotherm of the studied catalysts. The isotherms have been offset for clarity. The isotherm of

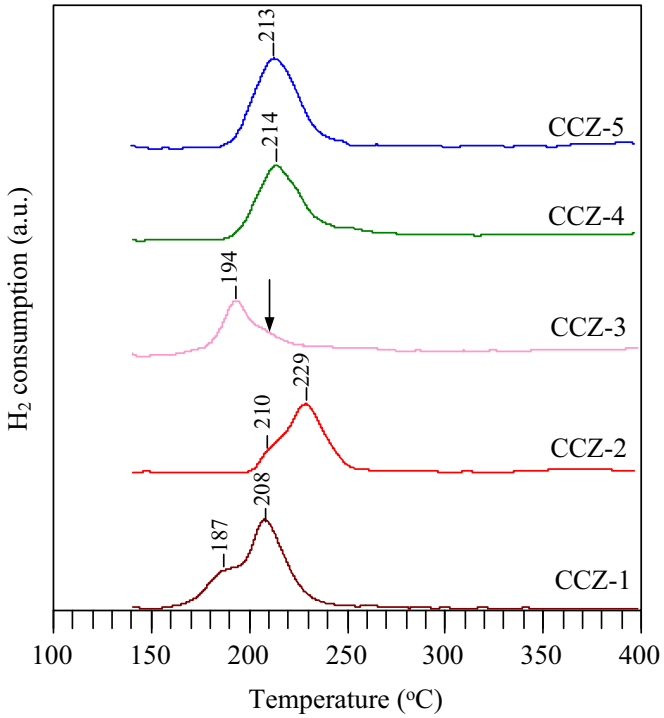

Fig. 4. H_2-TPR profiles of Co–Cu–ZrO_2 samples prepared with different metal compositions.

Cu–ZrO_2 catalyst (CCZ-1) is type IV but it is almost parallel to the *x*-axis, indicating the presence of mesopores in the material with a small amount of pores. The binary Co-ZrO_2 catalyst (CCZ-2) possesses type IV isotherm with H3 hysteresis loop which is typical for mesoporous materials with slit-shaped pores. For the ternary catalysts (CCZ-3, CCZ-4 and CCZ-5) the isotherms remain type IV but the hysteresis loop is changed to H2 which is indicative of the presence of bottle neck shaped pores. The pore size distribution curves of the ternary catalysts are all narrow, and the peaks of the curves are centered at around 7.7, 7.8 and 9.6 nm for the CCZ-3, CCZ-4 and CCZ-5, respectively (Fig. 3b). The narrow pore size distribution of the ternary catalysts can be attributed to a well inter-dispersion of mixed metal oxides. In contrast, the pore size distribution curves of the binary catalyst are broader, and the peaks are smaller.

Table 1 shows the BET surface area and total pore volume of the calcined catalysts. The BET surface area of the binary Cu–ZrO_2 catalyst (CCZ-1) was 39 $m^2\ g^{-1}$, which is consistent with the shape of the isotherm (Fig. 3). The BET surface area of the binary Co-ZrO_2 catalyst (CCZ-2) was 97 $m^2\ g^{-1}$, i.e., 2.5 times higher than the Cu–ZrO_2 catalyst (CCZ-1). The higher surface area of the CCZ-2 catalyst can be attributed to a smaller Co particle sizes and a better dispersion of Co with ZrO_2 as indicated by the XRD result. In comparison to the binary catalysts (CCZ-1 and CCZ-2), the ternary Co–Cu–ZrO_2 catalysts have a higher BET surface area and a larger pore volume, which confirms that all metal oxides are homogeneously dispersed across the whole particle of the catalysts. Among all catalysts, the CCZ-4 catalyst has the highest BET surface area and the largest total pore volume of 142 $m^2\ g^{-1}$ and 0.36 $cm^3\ g^{-1}$, respectively.

Fig. 4 shows the reduction profiles of the calcined catalysts. All the reduction peaks observed in the temperature range of 190–300 °C could be ascribed to the reduction of CuO and Co_3O_4. The binary Cu–ZrO_2 catalyst (CCZ-1) shows one shoulder peak (187 °C) and a major peak (208 °C) which can be related to the reduction of highly dispersed CuO species and the bulk CuO, respectively [37,38]. The binary Co–ZrO_2 catalyst (CCZ-2) also exhibits two peaks at temperature of 210 and 229 °C which can be attributed to two steps reduction of Co_3O_4 to CoO and CoO to Co^0 [39]. Despite the fact the particle size of copper oxide was larger than that of cobalt oxide, the copper oxide can be reduced at a lower temperature, suggesting that the interaction of surface of ZrO_2 with cobalt oxide species is stronger than that with copper oxide species. In contrast to the reduction profile of the binary catalysts, the ternary Co–Cu–ZrO_2 catalysts including CCZ-4 and CCZ-5 exhibit only one reduction peak at 214 and 213 °C, respectively. This suggests a strong interaction between copper and cobalt over zirconia which can lead to the formation of mixed oxides, promoting the reduction of metal oxides via hydrogen spillover mechanism [40]. The reduction profile of the CCZ-3 catalyst is somewhat different. The major peak at 194 °C can be assigned to the combination reduction of cobalt oxide to Co^0 and copper oxide to Cu^0 as mentioned earlier for the CCZ-4 and CCZ-5 catalysts. The broad shoulder above 210 °C can be attributed to the extended reduction of residual cobalt oxide to Co° [40].

3.2. Catalytic activity

The activity and the selectivity of the studied catalysts measured at different reaction temperatures are shown in Fig. 5. CO_2 conversion of all catalysts (Fig. 5a) monotonically increased with increasing the reaction temperature. Among the binary catalysts, the Co–ZrO_2 catalyst (CCZ-2) was found to be more active than the Cu–ZrO_2 catalyst. The CO_2 conversion of the CCZ-2 catalyst was found to be 9.4%, 20.2%, 34.2% and 49.6% at reaction temperature of 240, 260, 280 and 300 °C while that of the CCZ-1 catalyst was 2.7%, 4.4%, 7.0% and 10.9%, respectively. The product selectivities of the CCZ-1 and CCZ-2 catalysts are quite different. The CCZ-1 catalyst mainly produced CO from reverse water-gas shift reaction and exhibited some activity for methanol production from CO_2 hydrogenation [Eq. (11)] but gave no methanation reaction at all reaction temperature. The CCZ-2 catalyst exhibited the great methane selectivity (91.8–95.0%) with trace amounts of hydrocarbons and CH_3OH.

$$CO_2 + 3H_2 \leftrightarrow CH_3OH + H_2O; \quad \Delta H_{298\,K} = -49.5\ kJ\ mol^{-1} \qquad (11)$$

In addition to the large CuO crystallite size, the low metal dispersion and the low BET surface area, the lower thermodynamic equilibrium conversion of (Eqs. (3) and 11) compared to methanation [Eq. (1)] is a reason for the poor activity of the CCZ-1 catalyst.

In comparison to the binary Co–ZrO_2 catalyst (CCZ-2), the ternary Co–Cu–ZrO_2 catalysts provided the lower methane selectivity (Fig. 5b). For example at 260 °C the methane selectivity of the CCZ-3, CCZ-4 and CCZ-5 was found to be 85.6%, 86.3% and 51.9%, respectively, while that of the CCZ-2 was 93.6%. The lower methane selectivity of the ternary catalysts could be due to the lower content of Co which was the main component for methanation reaction. Nevertheless the CCZ-4 catalyst (Co:Cu:Zr = 20:40:40) achieved the highest CO_2 conversion (Fig. 5a) and CH_4 yield (Fig. 5c) at all reaction temperatures due to its high BET surface area and a homogeneous dispersion of mixed metal oxides.

Stability is a key factor in determining whether the Co–Cu–ZrO_2 catalyst can be used for methanation reaction in industrial production. Because of the superior performance of the CCZ-4 catalyst (Co:Cu:Zr = 20:40:40) as described above (Fig. 5), the stability of this catalyst was investigated. Fig. 6 shows the CO_2 conversion and CH_4 yield versus the time-on-stream over the CCZ-4 catalyst. The CO_2 conversion and CH_4 yield over the CCZ-4 catalyst slightly decrease at approximately 1.65% and 0.6% of 48 h on stream. This indicates that the CCZ-4 catalyst can be considered as a practical catalyst for industry.

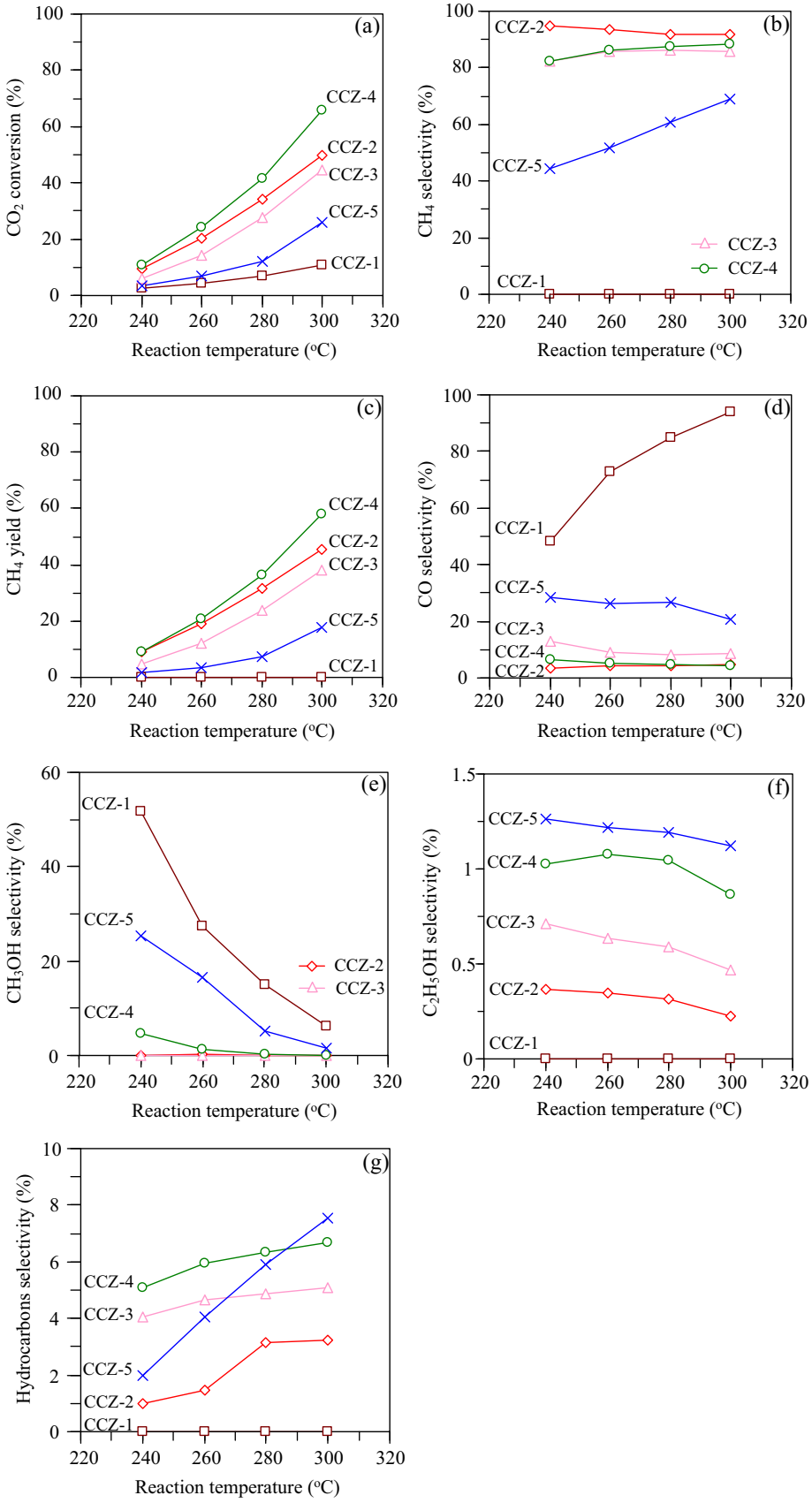

Fig. 5. CO_2 conversion (a), CH_4 selectivity (b), CH_4 yield (c), CO selectivity (d), CH_3OH selectivity (e), C_2H_5OH selectivity (f) and hydrocarbon selectivity (g) of Co–Cu–ZrO_2 catalysts prepared with different metal compositions.

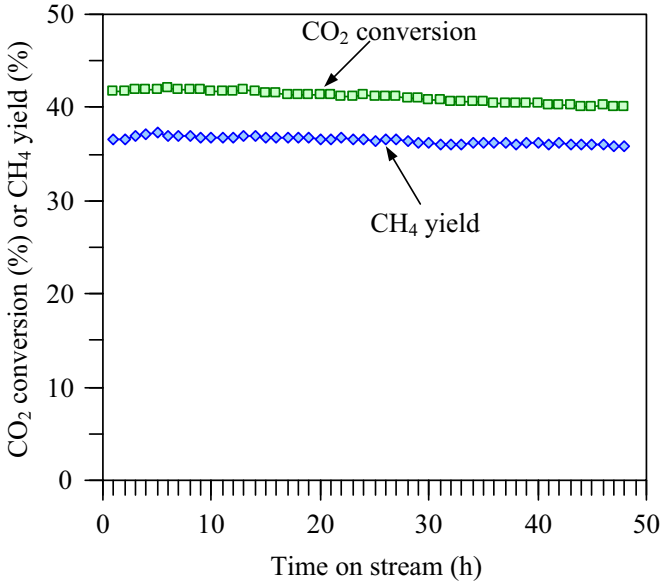

Fig. 6. CO_2 conversion and CH_4 yield as a function of time-on-stream of Co–Cu–ZrO_2 catalyst (Co:Cu:Zr = 20:40:40). Reaction conditions: T=280 °C, P=3 MPa, flow rate = 60 mL min^{-1}.

4. Conclusions

This work discusses the influence of different metal composition of Co–Cu–ZrO_2 nanomaterials on the production of clean fuel from the hydrogenation of CO_2. The characterization results revealed that the Co–ZrO_2 material was amorphous structure while the Cu–ZrO_2 material showed the crystallinity of CuO, indicating a higher dispersion of metal oxides of the Co–ZrO_2 material. The addition of Cu to Co–ZrO_2 material not only improved the dispersion of metal oxides but also changed the reducibility of the cobalt oxides. The Co–ZrO_2 catalyst exhibited the highest methane selectivity (91.8–95.0%). None of the ternary Co–Cu–ZrO_2 catalysts in the present work improved the methane selectivity beyond that of the Co–ZrO_2 catalyst. Nevertheless, the ternary Co–Cu–ZrO_2 catalyst prepared with the Co:Cu:Zr ratio of 20:40:40 (CCZ-4) achieved a superior performance in terms of CH_4 yield. At 300 °C the CH_4 yield of the CCZ-4 catalyst was found to be 58% which was 1.27 times higher than that of the original Co–ZrO_2 catalyst. The enhancement of CH_4 yield can be attributed to the higher BET surface area and the better inter-dispersion of mixed metal oxides. This finding indicates that the Co–Cu–ZrO_2 catalyst constitutes a good candidate as a CO_2 methanation catalyst due to its elevated CO_2 conversion and CH_4 yield, and durability.

Acknowledgements

This work was financially supported by the Thailand Research Fund (Grant no. TRG5780258), the Center of Excellence on Petrochemical and Materials Technology (PETROMAT), the National Research University Project of Thailand (NRU), the Nanotechnology Center (NANOTEC), NSTDA, Ministry of Science and Technology, Thailand through its program of Center of Excellence Network, and the Kasetsart University Research and Development Institute (KURDI). Financial support for Ms. Porntipar Dumrongbunditkul from Faculty of Engineering, Kasetsart University is also appreciated.

References

[1] S. Li, L. Gao, H. Jin, Life cycle energy use and GHG emission assessment of coal-based SNG and power cogeneration technology in China, Energy Convers. Manag. 112 (2016) 91–100.
[2] Z. Liu, T. Zhao, contribution of price/expenditure factors of residential energy consumption in China from 1993 to 2011: a decomposition analysis, Energy Convers. Manag. 98 (2015) 401–410.
[3] D.L. Royer, R.A. Bemer, J. Park, Climate sensitivity constrained by CO_2 concentrations over the part 420 million years, Nature 446 (2007) 530–532.
[4] G.S. Seck, G. Guerassimoff, N. Maïzi, Heat recovery using heat pumps in non-energy intensive industry: are energy saving certificates a solution for the food and drink industry in France? Appl. Energy 156 (2015) 374–389.
[5] S. Li, H. Jin, L. Gao, X. Zhang, Exergy analysis and the energy saving mechanism for coal to synthetic substitute natural gas and power cogeneration system without and with CO_2 capture, Appl. Energy 130 (2014) 552–561.
[6] World Nuclear Association (WNA), available at: ⟨http://www.world-nuclear.org/info/Current-and-Future-Generation/world-Energy-Needs-and-nuclear-power⟩ (accessed 09.01.16).
[7] T. Witoon, Characterization of calcium oxide derived from waste eggshell and its application as CO_2 sorbent, Ceram. Int. 37 (2011) 3291–3298.
[8] S.Y. Shan, Q.M. Jia, L.H. Jiang, Q.C. Li, Y.M. Wang, J.H. Peng, Novel Li_4SiO_4-based sorbents from diatomite for high temperature CO_2 capture, Ceram. Int. 39 (2013) 5437–5441.
[9] M.B. Durán-Guevara, J. Ortiz-Landeros, H. Pfeiffer, M.I. Espitia-Cabrera, M. E. Contreras-García, Potassium-based sorbents using mesostructured γ-alumina supports for low temperature CO_2 capture, Ceram. Int. 41 (2015) 3036–3044.
[10] A. Akgsornpeak, T. Witoon, T. Mungcharoen, J. Limtrakul, Development of synthetic CaO sorbents via CTAB-assisted sol-gel method for CO_2 capture at high temperature, Chem. Eng. J. 237 (2014) 189–198.
[11] T. Witoon, T. Mungcharoen, J. Limtrakul, Biotemplated synthesis of highly stable calcium-based sorbents for CO_2 capture via a precipitation method, Appl. Energy 118 (2014) 32–40.
[12] I. Omae, Aspects of carbon dioxide utilization, Catal. Today 115 (2006) 33–52.
[13] L. Bian, L. Zhang, R. Xia, Z. Li, Enhanced low-temperature CO_2 methanation activity on plasma-prepared Ni-based catalyst, J. Nat. Gas. Sci. Eng. 27 (2015) 1189–1194.
[14] J.Y. Do, Y. Im, B.S. Kwak, S.-M. Park, M. Kang, Preparation of basalt fiber@perovskite PbTiO3 core-shell composites and their effects on CH4 production from CO2 photoreduction, Ceram. Int. ⟨http://dx.doi.org/10.1016/j.ceramint.2015.12.142⟩.
[15] T. Witoon, S. Bumrungsalee, M. Chareonpanich, J. Limtrakul, Effect of hierarchical meso–macroporous alumina-supported copper catalyst for methanol synthesis from CO_2 hydrogenation, Energy Convers. Manag. 103 (2015) 886–894.
[16] E.S. Baeissa, Green synthesis of methanol by photocatalytic reduction of CO_2 under visible light using a graphene and tourmaline co-doped titania nanocomposites, Ceram. Int. 40 (2014) 12431–12438.
[17] M.D. Porosoff, B. Yan, J.G. Chen, Catalytic reduction of CO_2 by H_2 for synthesis of CO, methanol and hydrocarbons: challenges and opportunities, Energy Environ. Sci. 9 (2016) 62–73.
[18] T. Witoon, T. Permsirivanich, N. Kanjanasoontorn, C. Akkaraphataworn, A. Seubsai, K. Faungnawakij, C. Warakulwit, M. Chareonpanich, J. Limtrakul, Direct synthesis of dimethyl ether from CO_2 hydrogenation over Cu–ZnO–ZrO_2/SO_4^{2-}–ZrO_2 hybrid catalysts: effects of sulfur-to-zirconia ratios, Catal. Sci. Technol. 5 (2015) 2347–2357.
[19] G. Bonura, M. Cordaro, C. Cannilla, A. Mezzapica, L. Spadaro, F. Arena, F. Frusteri, Catalytic behaviour of a bifunctional system for the one step synthesis of DME by CO_2 hydrogenation, Catal. Today 228 (2014) 51–57.
[20] T. Inui, T. Takeguchi, Effective conversion of carbon dioxide and hydrogen to hydrocarbons, Catal. Today 10 (1991) 95–106.
[21] S. Saeidi, N.A.S. Amin, M.R. Rahimpour, Hydrogenation of CO_2 to value-added products—a review and potential future developments, J. CO_2 Util. 5 (2014) 66–81.
[22] S. Hoekman, A. Broch, C. Robbins, R. Purcell, CO_2 recycling by reaction with renewably-generated hydrogen, Int. J. Greenh. Gas Control 4 (2010) 44–50.
[23] R. Dorner, D. Hardy, F. Williams, B. Davis, H. Villauer, Influence of gas feed composition and pressure on the catalytic conversion of CO_2 to hydrocarbons using a traditional cobalt-based Fischer-Tropsch Catalyst, Energy Fuel 23 (2009) 4190–4195.
[24] G. Du, S. Lim, Y. Yang, C. Wang, L. Pfefferle, G. Haller, Methanation of carbon dioxide on Ni-incorporated MCM-41 catalysts: The influence of catalyst pretreatment and study of steady-state reaction, J. Catal. 249 (2007) 370–379.
[25] A. Akin, M. Ataman, A. Aksoylu, Z. Onsan, CO_2 fixation by hydrogenation over coprecipitated Co/Al_2O_3, React. Kinet. Catal. Lett. 76 (2002) 265–270.
[26] D. Peebles, D. Goodman, J. White, Methanation of Carbon Dioxide on Ni(100) and the Effects of Surface Modifiers, J. Phys. Chem. 87 (1983) 4378–4387.
[27] S.J.M. Rosid, W.A.W.A. Baker, R. Ali, Physicochemical study of supported cobalt-lanthanum oxide-based catalysts for CO_2/H_2 methanation reaction, Clean Technol. Environ. Policy 17 (2015) 257–264.
[28] Z. Fan, K. Sun, N. Rui, B. Zhao, C.-J. Liu, Improved activity of Ni/$MgAl_2O_4$ for CO_2 methanation by the plasma decomposition, J. Energ. Chem. 24 (2015) 655–659.
[29] G. Garbarino, D. Bellotti, P. Riani, L. Magistri, G. Busca, Methanation of carbon dioxide on Ru/Al_2O_3 and Ni/Al_2O_3 catalysts at atmospheric pressure: Catalysts activation, behavior and stability, Int. J. Hydrog. Energy 40 (2015) 9171–9182.
[30] M.V. Konishcheva, D.I. Potemkin, P.V. Snytnikov, M.M. Zyryanova, V. P. Pakharukova, P.A. Simonov, V.A. Sobyanin, Selective CO methanation in

H_2-rich stream over Ni-, Co- and Fe/CeO_2: effect of metal and precursor nature, Int. J. Hydrog. Energy 40 (2015) 14058–14063.
[31] T. Bligaard, J.K. Nørskov, S. Dahl, J. Matthiesen, C.H. Christensen, J. Sehested, The Brønsted–Evans–Polanyi relation and the volcano curve in heterogeneous catalysis, J. Catal. 224 (2004) 206–217.
[32] L. Liu, H. Jiang, H. Liu, H. Li, Recent advances on the catalysts for activation of CO_2 in several typical processes, in: S.L. Suib (Ed.), New and Future Developments in Catalysis: Activation of Carbon Dioxide, Elsevier, Poland, 2013, pp. 210–214.
[33] F. Huixia, C. Baiyi, Z. Deyi, Z. Jianqiang, T. Lin, Preparation and characterization of the cobalt ferrite nano-particles by reverse coprecipitation, J. Magn. Magn. Mater. 356 (2014) 68–72.
[34] R.T. Figueiredo, H.M.C. Andrade, J.L.G. Fierro, The role of the coprecipitation sequence of salt precursors on the genesis of Cu–ZnO–Al_2O_3 catalysts. Synthesis, characterization and activity for low temperature shift reaction, Braz. J. Chem. Eng. (1998), http://dx.doi.org/10.1590/S0104-66321998000200011.
[35] F. Arena, K. Barbera, G. Italiano, G. Bonura, L. Spadaro, F. Frusteri, Synthesis, Characterization and activity pattern of Cu-ZnO-ZrO_2 catalysts in the hydrogenation of carbon dioxide to methanol, J. Catal. 249 (2007) 185–194.
[36] T. Witoon, T. Permsirivanich, M. Chareonpanich, Chitosan-assisted combustion synthesis of CuO–ZnO nanocomposites: effect of pH and chitosan concentration, Ceram. Int. 39 (2013) 3371–3375.
[37] X. Guo, D. Mao, G. Lu, S. Wang, G. Wu, The influence of La doping on the catalytic behavior of Cu/ZrO_2 for methanol synthesis from CO_2 hydrogenation, J. Mol. Cat. A: Chem. 345 (2011) 60–68.
[38] T. Witoon, T. Permsirivanich, W. Donphai, A. Jaree, M. Chareonpanich, CO_2 hydrogenation to methanol over Cu/ZnO nanocatalysts prepared via a chitosan-assisted co-precipitation method, Fuel Process. Technol. 116 (2013) 72–78.
[39] T. Witoon, M. Chareopanich, J. Limtrakul, Effect of bimodal porous silica on particle size and reducibility of cobalt oxide, J. Porous Mater. 20 (2013) 481–488.
[40] Z. Wang, J.J. Spivey, Effect of ZrO_2, Al_2O_3 and La_2O_3 on cobalt-copper catalysts for higher alcohols synthesis, Appl. Catal. A: Gen. 507 (2015) 75–81.